Sugar Conversion to Hydroxymethylfurfural and Aromatics over Niobium Oxides and Modified Zeolites



Hannah T. Kreissl

Corpus Christi College

University of Oxford

A dissertation submitted for the degree of

Doctor of Philosophy

Inorganic Chemistry Department

2017

Sugar Conversion to Hydroxymethylfurfural and Aromatics over Niobium Oxides and Modified Zeolites

by

Hannah T. Kreissl

Corpus Christi College

Supervisor

Professor S. C. E. Tsang

Internal Assessor

Professor D. O'Hare

A dissertation submitted for the degree of

Doctor of Philosophy

at the Inorganic Chemistry Laboratory,

Department of Chemistry,

University of Oxford

2017

Declaration

I hereby declare that this is my own work and the use of materials from other sources has been properly and fully acknowledged.

Hannah T. Kreissl

Dedication

To my parents

Acknowledgements

First of all, I would like to thank Professor Edman Tsang for giving me the opportunity to join his research group and for his guidance and support throughout the course of my DPhil. Additionally, I would like to thank the University of Oxford, the Engineering and Physical Sciences Research Council and Sinopec China for giving me the opportunity to undertake this project by providing facilities and funding.

The research presented in this thesis would not have been possible without the training and assistance I have received from members of the university and further afield: I would like to thank Dr Stuart Jones, Dr Amy Kolpin and Dr Haohong Duan for their training in and assistance with HPLC, autoclave use and GC-MS, respectively. Further I would like to express my sincere gratitude to Professor Keizo Nakagawa from Kobe University for his support and useful discussions throughout my work with niobium oxides, including synthesis, XRD and surface measurements. I would then like to thank Yung-Kang Peng and Dr Lin Ye for performing TMP NMR analysis, Dr Ashley Shepherd for her assistance with XPS, and Elizabeth Raine for performing TEM measurements and help with XRD analysis. Similarly, I would like to thank Thomas Hooper and Dr John Hanna from Warwick University for solid state NMR analysis of my materials, Dr Gary G.-Z. Chang for TPD measurements, and Tai-Sing Wu and Yun-Liang Soo from Synchrotron Research Center Taiwan for EXAFS work, further Molly M.J. Li for EXAFS data analysis. Thanks must also go to Dr Junlin Zheng and Dr Simon Qi Song from Sinopec for their useful discussions and support throughout my project. For the organisation of general lab matters I would like to thank the past and present postdocs of our group, especially Dr Tugce Ayvali, Dr Ian McPherson, Dr Pu Zhao and Dr Simon Fairclough. Apart from all the above providing support and guidance with scientific matters, I would like to thank the administrative and facilities staff of the Inorganic Chemistry Department, in particular Hillary Fraser, Hazel Osborne, and Aga Borkowska.

Finally I would like to thank all members of the Tsang group, past and present, for their useful discussions and general support, including Dr Tugce Ayvali, Elizabeth Raine, Dr Keizo Nakagawa, Yung-Kang Peng, Ivo Teixeira, Dr Amy Kolpin, Dr Ieuan Ellis, Dr Haohong Duan, Dr Yusuke Koito, Dr Simon Qi Song, Dr Hanif Mahadi, Bin Yu, Elisabeth Wolf, Kirsty Purchase, Molly Li, Dr Ben Lo and Dr Tiantian Jia. I am grateful to all my friends and family for their support throughout my time in Oxford.

Sugar Conversion to Hydroxymethylfurfural and Aromatics over Niobium Oxides and Modified Zeolites

Hannah T. Kreissl

University of Oxford

Abstract

Research in the field of renewable energies is becoming ever more important due to the depletion of fossil fuels and increasing environmental concerns. The upgrading of biomass to commodity and fine chemicals in order to substitute conventional fossil-fuel derived products is a major topic in the area, particularly the upgrading of sugars as the main biomass component. Glucose derived from cellulose is the most abundant sugar and its acid catalysed dehydration yields the platform molecule hydroxymethylfurfural (HMF), a promising precursor for plastics, solvents, fuels and fine chemicals. In this work the conversion of sugars to HMF is studied in water over niobium oxides as solid acid catalysts, presenting an environmentally- and separation-friendly conversion route. An emphasis is put on the reaction mechanistic details and the analysis of catalyst structure in relation to acidity and catalytic performance, as these are key factors in the development of targeted synthesis and improved catalysts. For example, the efficient conversion of glucose to HMF requires the presence of both Lewis acid (LA) and Brønsted acid (BA) sites on the niobium oxides. Large quantities of both LA (exposed Nb centres) and BA (acidic surface hydroxyl) sites are found prominently on the nano-structured niobium oxides compared to their bulk analogues. This results from the large surface areas and structural flexibility of the nano-materials, where LA sites appear to arise from distortions and oxygen defects. Amorphous mesoporous $Nb_2O_5*nH_2O$ shows the best catalytic performance due to the presence of both LA and comparably weak BA sites, where weaker BA sites are formed by protons of terminal surface hydroxyl groups. In addition to sugar conversion to HMF, the conversion of HMF to aromatic hydrocarbons has been addressed, using a two-step reaction route *via* dimethylfuran (DMF) over modified zeolite catalysts. Although there is room for yield improvements, the significant advantage of this route is the use of ethanol as common solvent and sacrificial reagent for both reaction steps, facilitating the combination into a one-batch-process in the future. Aromatics are important fuel additives and precursors for polymers, resins and solvents and are currently fossil-fuel derived, raising the need for such alternative production pathways.

Table of Contents

List of Figures ……...x

List of Schemes ……xii

List of Tables ……xiii

List of Abbreviations ……..……xiv

List of Publications ……xv

1. Introduction ……...1

1.1 Definition of Catalysis ……..2
1.2 History of Catalysis ……..2
1.3 Environmental Catalysis and Renewable Energies ……7
1.4 Biomass Conversion ……11
1.4.1 Sugar Conversion to Hydroxymethylfurfural and Beyond ……..14
1.5 Principles of Catalysis ……18
1.6 Catalysis and Nanoscience ……..23
1.7 Thesis Overview ……...25
1.8 References ……26

2. Analytical Techniques ……..31

2.1 Transmission Electron Microscopy (TEM) ……..32
2.2 X-Ray Diffraction (XRD) ……..34
2.3 Raman and Infrared Spectroscopy ……37
2.4 Temperature Programmed Desorption (TPD) ……...40
2.5 Brunauer-Emmett-Teller (BET)……..43
2.6 X-Ray Photoelectron Spectroscopy (XPS) ……46
2.7 X-Ray Absorption Fine Structure (XAFS) ……49
2.8 Solid State Nuclear Magnetic Resonance (ssNMR) ……52
2.8.1 Trimethylphospine (TMP) ^{31}P ssNMR ……56
2.8.2 ^{93}Nb ssNMR ……..57
2.9 High Pressure Liquid Chromatography (HPLC) ……...58
2.10 Gas Chromatography – Mass Spectrometry (GC-MS) ……63
2.11 References……68

3. Experimental and Characterisation Methods ……...71

3.1 Catalyst Synthesis ……...72
3.1.1 Niobium Oxides ……72
3.1.2 Decoration of Modified Y Zeolites with Ruthenium and Palladium ……74
3.2 Catalyst Characterisation ……...77
3.2.1 TEM ……..77
3.2.2 XRD ……..78
3.2.3 Raman ……..79
3.2.4 TPD ……..79
3.2.5 BET ……..80
3.2.6 XPS ……..80
3.2.7 XAFS ……..81
3.2.8 TMP ^{31}P ssNMR ……82
3.2.9 ^{93}Nb ssNMR ……....84
3.2.10 Hammett Indicator Measurements ……...84
3.3 Catalyst Testing ……87
3.3.1 Sugar Conversion to HMF over Niobium Oxides in Water ……87
3.3.2 HMF to DMF and Further to Aromatics over Ru/Pd on Modified Y Zeolites in Ethanol ……...88
3.4 Product Analysis ……89
3.4.1 HPLC ……..89
3.4.2 GC-MS……..90
3.5 References ……..92

4. Sugar Conversion to Hydroxymethylfurfural over Niobium Oxides in Water: A Mechanistic Study ……93

4.1 Background……..94
4.2 Objectives ……..99
4.3 Experimental ……..100
4.3.1 Synthesis of Niobium Oxides ……...100
4.3.2 Characterisation of Catalyst Acidity ……100
4.3.3 Sugar Reaction to HMF over Niobium Oxides ……101
4.4 Results and Discussion ……...102
4.4.1 Catalyst Acidity ……...102
4.4.2 Sugar Conversion to HMF and Influence of Acidity ……108

4.4.3 Reaction Mechanistic Aspects ……...118
4.5 Conclusions ……..122
4.6 References ……124

5. Niobium Oxides: Structural Studies with Correlation to Acidity ……127

5.1 Background……128
5.2 Objectives ……....132
5.3 Experimental ……..133
5.3.1 Synthesis of Niobium Oxides ……...133
5.3.2 Characterisation of Niobium Oxides ……133
5.4 Results and Discussion ……...134
5.4.1 XRD and TEM ……...134
5.4.2 Raman Spectroscopy ……136
5.4.3 XPS ……139
5.4.4 XAFS ……144
5.4.5 ^{93}Nb ssNMR ……..151
5.4.6 Structure and Acidity Correlations ……....154
5.5 Conclusions ……..159
5.6 References ……161

6. Converting Hydroxymethylfurfural to Dimethylfuran and Further to Aromatic Hydrocarbons ……164

6.1 Background ……..165
6.2 Objectives ……....167
6.3 Experimental ……..169
6.3.1 Catalyst Synthesis: Ru/Pd on Modified Y Zeolites ……169
6.3.2 Reaction of HMF to DMF and Further to Aromatics in Ethanol …169
6.3.3 Product Analysis ……...170
6.4 Results and Discussion ……...171
6.4.1 Conversion of HMF to DMF ……...171
6.4.2 Further Conversion of DMF to Aromatic Hydrocarbons ……..185
6.5 Conclusions ……..188
6.6 References ……190

7. Conclusions and Outlook ……192

7.1 Conclusions and Outlook ……..193

Appendix……....A1

List of Figures

1.1 – One of the oldest examples of catalysis: the energy cycle of photosynthesis and cellular respiration catalysed by enzymes ……3
1.2 – The Haber-Bosch process as an example of heterogeneous catalysis ……5
1.3 – Wilkinson's catalyst as an example of homogeneous catalysis ……7
1.4 – Renewable *versus* Non-Renewable Energies ……...10
1.5 – Decomposition of biomass into the components of cellulose, hemicellulose and lignin as preparation for further chemical conversion ……...13
1.6 – Dehydration of C6 and C5 sugars to HMF and furfural ……...14
1.7 – Application areas of HMF in the chemical industry ……...16
1.8 – Catalysed *versus* non-catalysed reaction pathway, where A = reactant, B = product, M = catalyst……...19
1.9 – Examples of nanomaterial characteristics a) geometric effects b) structural flexibility c) support effects ……...24

2.1 – Schematic drawing of a transmission electron microscope ……...33
2.2 – X-ray diffraction by crystallographic planes according to Bragg's law ……...35
2.3 – Energy level diagram depicting infrared absorption *versus* Raman scattering ……...38
2.4 – TPD spectrum depicting the different molecular adsorption modes of water to a functionalized metal surface ……...42
2.5 – Schematic depiction of multilayer gas adsorption onto solids according to the BET theory ……...43
2.6 – Adsorption-desorption isotherms I to VI obtained for different types of solids ……....45
2.7 – Schematic depiction of photoelectron emission from atomic species due to x-ray absorption ……...47
2.8 – Schematic depiction of x-ray absorption fine structure (XAFS) due to local scattering of excited photoelectrons ……...49
2.9 – Exemplary XAFS spectrum (blue) with marking of the relevant regions (absorption edge, XANES and EXAFS), the threshold absorption intensity $\Delta\mu_0$ and the background function $\mu_0(E)$ ……...50
2.10 – Energy level splitting for spin = ½ nuclei in an external magnetic field ……...53
2.11 – Exemplary ^{1}H NMR spectrum depicting signal splitting due to chemical shift variation and J coupling ……...55
2.12 – Schematic depiction of different column chromatography techniques a) size exclusion chromatography, b) reversed phase chromatography, c) ion exclusion chromatography …...60
2.13 – Schematic depiction of a gas chromatography column with analyte separation …...64
2.14 – Schematic depiction of a GC-MS with a quadrupole mass analyser ……...67

3.1 – Commercial Nb_2O_5 and synthesized niobium oxides ……...74
3.2 – Modified Y zeolite supports before (white) and after decoration with Ru/Pd (black) …...76
3.3 – Experimental set-up for TMP adsorption ……...83
3.4 – NMR peak area calibration line for TMP adsorption ……...84
3.5 – Autoclave reactor set-up ……...87
3.6 – HPLC instrument set-up ……...90
3.7 – GC-MS instrument set-up ……...91

4.1 – a) Exemplary crystal structure of a niobium oxide (HNb_3O_8) where NbO_6 octahedra are shown in green and protons in pink, b) atomic positions and chemical bonds (in bold) for NbO_6, c) depiction of TMP adsorption to different acid sites ……...98
4.2 – a) Surface areas and b) acid site quantities of the niobium oxide catalysts ……104
4.3 – TEM images of a) Nb_2O_5, b) HNb_3O_8, c) hy-Nb, d) hy-Nb-TEOA, e) mesoporous $Nb_2O_5*nH_2O$ ……105
4.4 – TMP ^{31}P NMR spectra of the niobium oxide catalysts displaying BA and LA strength by means of chemical shift, and BA and LA quantity by peak area ……106
4.5 – a) Crystal structure of HNb_3O_8: alternating layers of interconnected NbO_6 octahedra and protons, b) Schematic drawing of bridging and terminal hydroxyl groups giving rise to BA sites on interconnected NbO_6 octahedra, atomic bonds in bold, c) Schematic drawing of distorted NbO_6 octahedra and oxygen vacancies giving rise to LA sites by exposure of the Nb center, atomic bonds in bold, d) Schematic drawing of TMP adsorption on LA and BA sites ….108
4.6 – Profiles of sugar conversion over time: glucose, fructose to HMF and sucrose to glucose, fructose, HMF over a) no catalyst, b) Nb_2O_5, c) HNb_3O_8, d) hy-Nb-TEOA, e) hy-Nb, f) meso Nb_2O_5……...113
4.7 – Maximum HMF yields obtained from glucose, fructose and sucrose over the different niobium oxides ……114

5.1 – Structure of H- Nb_2O_5 ……130
5.2 – Structure of M- Nb_2O_5 ……130
5.3 – Structure of T- Nb_2O_5 ……130
5.4 – Structure of HNb_3O_8 (NbO_6 octahedra in green, protons in pink) ……132
5.5 – XRD patterns of a) Nb_2O_5 (referenced to H-Nb_2O_5 00-005-0379) and mesoporous $Nb_2O_5*nH_2O$, b) HNb_3O_8 (referenced to HNb_3O_8 37-0833), c) hy-Nb and hy-Nb-TEOA (referenced to HNb_3O_8 37-0833) ……....135
5.6 – TEM images of a) Nb_2O_5, b) HNb_3O_8, c) hy-Nb, d) hy-Nb-TEOA, e) mesoporous $Nb_2O_5*nH_2O$ ……136
5.7 – Raman spectra of the different niobium oxides ……137
5.8 – XPS spectra of a.1) Nb_2O_5 single doublet fitting, a.2) Nb_2O_5 triple doublet fitting b) HNb_3O_8, c) hy-Nb, d) hy-Nb-TEOA, e) mesoporous $Nb_2O_5*nH_2O$ ……141
5.9 – XANES Nb K-edge absorption spectra for the different niobium oxides ……145
5.10 – k and R space transformations of Nb K-edge EXAFS spectra of the different niobium oxides for determination of bond distances and coordination numbers ……148
5.11 – ^{93}Nb static NMR spectra of the different niobium oxides with a dotted line through the center-of-gravity position (δ_{CG}) of mesoporous $Nb_2O_5*nH_2O$ ……152

6.1 – DMF and its derivatives MF and MEF ……172
6.2a – TEM images of Ru on modified Y zeolites ……175
6.2b – Particle size distributions for Ru on modified Y zeolites from TEM ……....176
6.2c – TEM images of Pd on modified Y zeolites ……177
6.2d – Particle size distributions of Pd on modified Y zeolites from TEM ……178
6.3a – XRD patterns of Pd/MgO/NaY10 and MgO/NaY10 in comparison to NaY10 ….180
6.3b - XRD patterns of Ru/MgO/NaY10 and MgO/NaY10 in comparison to NaY10 ….180
6.3c – XRD patterns of Pd/NbO/HY10 and NbO/HY10 in comparison to HY10 ……181

List of Schemes

4.1 – Acyclic[1,2] *versus* cyclic[3–6] dehydration pathways of glucose and fructose yielding HMF……..95
4.2 – Experimental overview: sugar conversion to HMF over niobium oxides in water …...99
4.3 – Catalytic steps of sucrose, glucose and fructose conversion to HMF ……119
4.4 – a) Glucose to fructose isomerization *via* LA-1,2-enediol intermediate, b) Fructose to HMF conversion catalysed by BA sites ……121

5.1 – Proposed oxygen vacancy formation based on Raman, XPS and EXAFS results ….143
5.2 – Proposed structure of amorphous mesoporous Nb_2O_5*nH_2O based on EXAFS and XPS results (protons not shown) ……151
5.3 – Proposed oxygen vacancy/LA site formation *via* BA site removal in form of water ….156
5.4 – Proposed oxygen vacancy/LA site formation *via* oxygen removal with Nb^{4+} formation and proton shift ……156
5.5 – Proposed oxygen vacancy/LA site formation upon downscaling from bulk HNb_3O_8 to few- to monolayer hy-Nb and hy-Nb-TEOA ……158
5.6 – Proposed LA and BA site origins in mesoporous Nb_2O_5*nH_2O ……158

6.1 – Conversion pathways and catalysts for DMF and HMF conversion to aromatics ….167
6.2 – Aiming to combine the conversion of HMF to DMF and DMF to aromatics into a one-batch process ……168
6.3 – HMF to DMF reaction scheme ……184
6.4 – Further conversion of DMF to aromatics over Ru/Pd modified HY zeolites ……187
6.5 – Conversion of HMF to aromatics *via* DMF over Ru/Pd on modified Y zeolite in ethanol at 300 °C ……188

List of Tables

4.1 – Surface area and acid site analysis of the niobium oxide catalysts ……103
4.2 – Experimental results of sugar conversion over niobium oxides in water ……110
4.3 – Exemplary product distribution and mass balance from sugar reactions……..111

5.1 – Nb 3d peak position for the different niobium oxides ……142
5.2 – Bond distances and coordination number of the different niobium oxides ……149
5.3 – δ_{CG} and full width at half maximum of the NMR resonances for the different niobium oxides……..153
5.4 - Surface area and acid site analysis for the different niobium oxides ……154

6.1 – Yields of DMF and derivatives obtained over Ru/Pd on modified Y zeolites …….....172
6.2 – Product yield distributions over selected catalysts ……173
6.3 – Average metal particle size and metal surface area obtained from TEM…….....174
6.4 – Acid and base site quantification for the different supports by NH_3 and CO_2 TPD ….179
6.5 – Conversion of HMF to aromatics ……186

List of Abbreviations

BA Brønsted Acid

BET Brunauer Emmett Teller

DMF Dimethylfuran

EXAFS Extended x-ray absorption fine structure

GC-MS Gas Chromatography – Mass Spectrometry

GVL Gamma-valerolactone

HMF Hydroxymethylfurfural

HPLC High Pressure Liquid Chromatography

LA Lewis Acid

MEF Methylethylfuran

MF Methylfuran

Nb Niobium

Pd Palladium

Ru Ruthenium

SA Surface Area

ssNMR Solid State Nuclear Magnetic Resonance

TEM Transmission Electron Microscopy

TMP Trimethylphosphine

TPD Temperature Programmed Desorption

XAFS X-Ray Absorption Fine Structure

XANES X-Ray Absorption Near Edge Structure

XPS X-Ray Photoelectron Spectroscopy

XRD X-Ray Diffraction

List of Publications

Kreissl, H. T.; Nakagawa, K.; Peng, Y. K.; Koito, Y.; Zheng, J.; Tsang, S. C. E. *J. Catal.* **2016**, *338*, 329. Featured Article.

Koito, Y.; Rees, G. J.; Hanna, John, V.; Li, M. J. M.; Peng, Y.-K.; Puchtler, T.; Taylor, R.; Wang, T.; Kobayashi, H.; Teixeira, I. F.; Khan, M. A.; Kreissl, H. T.; Tsang, S. C. E. *ChemCatChem.* **2017**,*9*, 144.

Nakagawa, K.; Yamashita, H.; Saeki, D.; Yoshioka, T.; Shintani, T.; Kamio, E.; Kreissl, H. T.; Tsang, S. C. E.; Sugiyama, S.; Matsuyama, H. *Chem. Commun.* **2017**, *53* (56), 7929.

Kreissl, H. T.; Li, M. M. J.; Peng, Y. K.; Nakagawa, K.; Hooper, T. J. N.; Hanna, J. V.; Shepherd, A.; Wu, T. S.; Soo, Y. L.; Tsang, S. C. E. *J. Am. Chem. Soc.* **2017**, *139* (36), 12670.

Chapter 1

Introduction

Chapter 1 1

1.1 Definition of Catalysis 2

1.2 History of Catalysis 2

1.3 Environmental Catalysis and Renewable Energies 7

1.4 Biomass Conversion 11

1.4.1 Sugar Conversion to Hydroxymethylfurfural and Beyond 14

1.5 Principles of Catalysis 18

1.6 Catalysis and Nanoscience 23

1.7 Thesis Overview 25

1.8 References 26

1.1 Definition of Catalysis

Catalysis is the acceleration of a chemical reaction, where a catalyst is defined as the material which causes this rate acceleration by providing an alternative reaction pathway with a reduced activation energy. The catalyst itself automatically regains its original form upon reaction completion. Many reactions would proceed too slowly without catalysis. It should be noted that while influencing the rate of reaction, a catalyst does not affect the chemical equilibrium.[1,2]

1.2 History of Catalysis

Although the term catalysis was first defined by the Swedish chemist Berzelius in 1835, humans have long exploited the principles of catalysis unknowingly.[3,4] The functioning of the human body is dependent on bio-catalysts called enzymes, which supply us with the energy for living by providing a fast route to convert oxygen and carbohydrates to carbon dioxide and water. This is called cellular respiration, while the reverse or recycling process is plant photosynthesis, also catalysed by enzymes (Figure 1.1). One of mankind's oldest manufacturing processes is fermentation, the bio-catalytic decomposition of sugars to alcohol by yeast or bacteria, dating back far into pre-history. Only much later were the first attempts of inorganic catalysis were reported; in 1552 Valerius Cordus described the conversion of alcohol to ether with the help of sulfuric acid.[5–7]

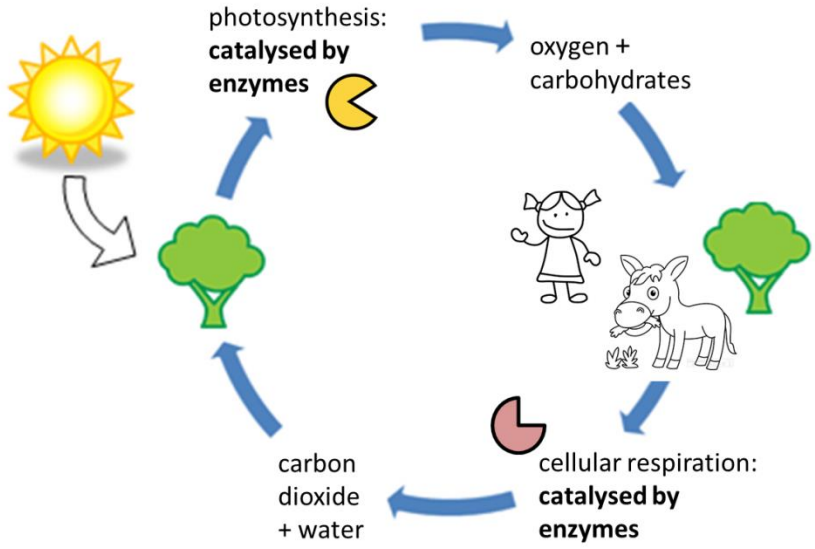


Figure 1.1 – One of the oldest examples of catalysis: the energy cycle of photosynthesis and cellular respiration catalysed by enzymes (reproduced from references[8–10])

The understanding of chemical versus catalytic reactions started only after the alchemical period, with significant advances in scientific knowledge including the conservation of matter postulated by Lavoisier and the atomic model by Dalton.[7] In 1794, Fulhame made an important discovery when she noted that the oxidation of carbon monoxide required small quantities of water which were unaltered by the reaction. Similarly Kirchhoff observed in 1812 that acids he used in the hydrolysis of starch to sugars remained unchanged.[11,12] The work of Sir Humphrey Davy set the basis for modern engine combustion processes, when he reported in 1817 that combustible gases mixed with air in the presence of heated platinum metal exploded below their normal ignition temperature.[13] A number of combustion studies over platinum-based materials followed and in 1834 Faraday documented important facts about the nature of clean versus poisoned platinum surfaces for ignition.[13,14] Today, catalysts in the context of combustion engines are mainly employed to reduce the toxicity of exhaust emissions. In 1835, Berzelius published his definition of catalysis after he systematically studied and compared previous works:

'It is then shown that several simple and compound bodies, soluble and insoluble, have the property of exercising on other bodies and action very different from chemical affinity. The body effecting the changes does not take part in the reaction and remains unaltered through the reaction. This unknown body acts by means of an internal force, whose nature is unknown to us... I will therefore call it the Catalytic Force and I will call Catalysis the decomposition of bodies by this force…' [4,7]

Paired to the advances in other areas of chemistry, a new era of catalysis started, based on systematic scientific study. In 1877, Lemoine and Ostwald proved that a catalyst increases the rate at which the reaction equilibrium is reached, while the equilibrium state itself remains unchanged.[15,16] This important statement was preceded by several discoveries regarding the nature of chemical reactions: In 1850, Wilhelmy showed in his studies on sugar conversion that the rate of reaction is based on the concentration of the reactants, followed by Williamson who formulated the reversibility of reactions.[3,17] In 1862, Berthelot and St. Gilles reported the dependence of the reaction rate on the catalyst concentration based on their studies of acid-catalysed etherification. Following the work of Guldberg and Waage, Van't Hoff established the concept of rate constants in 1877.[3,13,18] The influence of temperature, pressure and concentration on the equilibrium state of a chemical reaction were studied in detail by Le Chatelier. All the above works were followed by the derivation of mathematical expressions to describe reaction rates and equilibria, with important contributions from Gibbs and Nernst.[19–21]

The rapid scientific advances of the 19th century led to the era of large scale industrial production, majorly based on the increasing efficiency of available catalysts. Industrial catalysis between 1900 and 1945 was dominated by the economic and political motives of advancing nutrition, global mobility and warfare.[7] The Haber-Bosch ammonia synthesis process, developed in 1903 and named after its main developers, Fritz Haber and Carl Bosch who industrialized the process in cooperation with BASF, was originally designed to produce fertilizer and thereby

prevent further famines in Europe.[22,23] To this day, ammonia is produced from nitrogen and hydrogen over an iron-based catalyst at high pressures and temperatures. Back in 1914, with the beginning of the First World War, the ammonia process was however entirely designated to the production of explosives, based on Ostwald's work on the oxidation of ammonia to nitric acid from 1902.[24,25] As a side note, all types of catalysts developed around this time were heterogeneous catalysts, where catalyst (solid) and reactants (gas or liquid) are in different phases (Figure 1.2).[26]

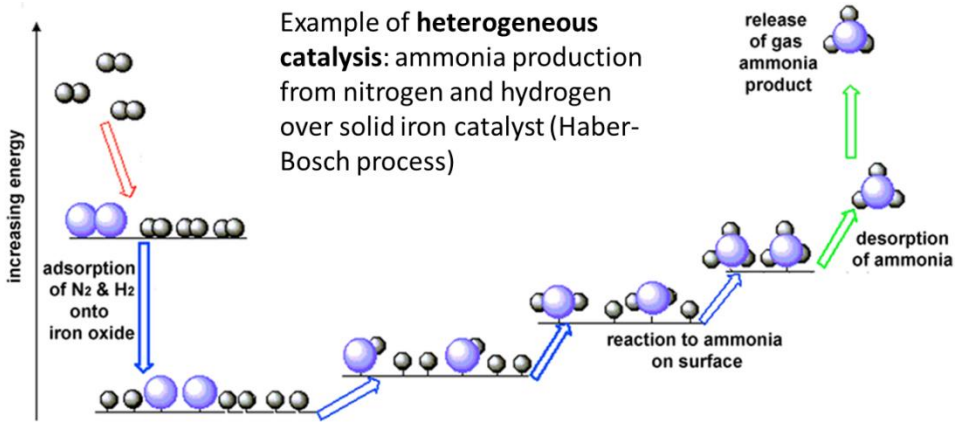


Figure 1.2 – The Haber-Bosch process as an example of heterogeneous catalysis (reproduced from reference[27])

After the First World War, global mobility and the petroleum industry experienced a boom. In 1920, the petroleum company Standard Oil first produced isopropanol from the hydration of propene over an acid catalyst, where propene was obtained from cracking processes of petroleum. Isopropanol was used as a fuel additive and for acetone production.[28] In 1922, Fischer and Tropsch achieved the synthesis of hydrocarbons from carbon monoxide and hydrogen (syngas) over iron- and cobalt-based catalysts. The Fischer-Tropsch process became an important fuel source during the Second World War and until today remains significant fo

r hydrocarbon production. [16,29,30] At the same time, the reversed process yielding hydrogen and carbon monoxide from methane and water (steam reforming) became popular for hydrogen production.

After the Second World War, the catalytic industry shifted towards new production areas. Besides the still booming petroleum industry, the polymer industry emerged rapidly with the production of plastics, rubber and synthetic fabrics. In the 1950s Ziegler and Natta developed the production of polymers from ethylene and propylene over titanium- and aluminium-based catalysts.[31,32] At the same time Philipps Petroleum expanded the use of chromium-based catalyst for polyethylene production. In 1954, Oblad's concept of bifunctional catalysis made an important contribution to petroleum reforming of (cyclo)alkanes to aromatic hydrocarbons.[33] In the 1960s Mobile Oil discovered the huge potential of X zeolites for catalytic cracking, which until today remain the major catalyst class used in the petroleum industry.[34]

With the development of a rhodium complex in solution used for the hydrogenation of olefins, Wilkinson started a new type of catalysis called homogeneous catalysis in 1965.[35] Still today, homogeneous catalysts are particularly important for the pharmaceutical and fine chemical industry due to their high stereo selectivity, enabling the synthesis of highly tailored and pure products (Figure 1.3).[26] Heterogeneous catalysts on the other hand remain market dominating with a share of 85% of all catalysts sold, due to their ease of separation from the product mixture and high durability (Figure 1.2).[36,37]

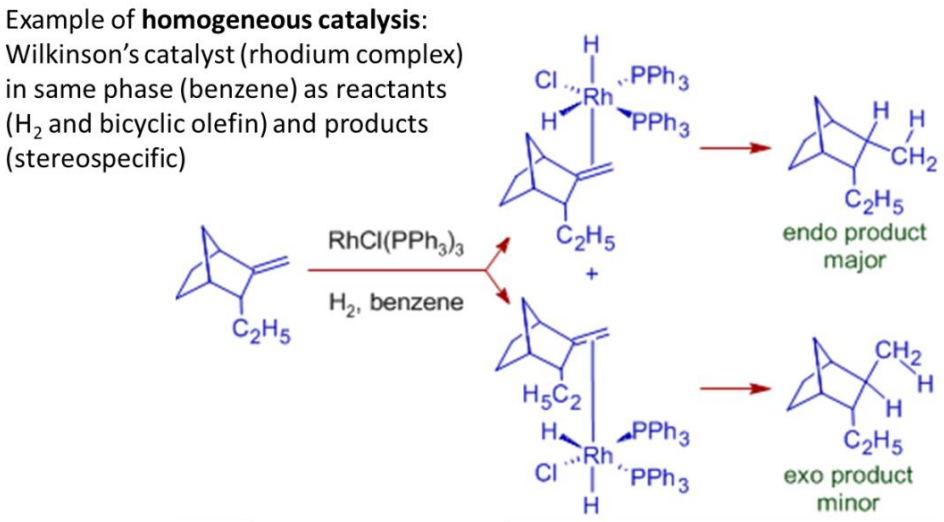


Figure 1.3 – Wilkinson's catalyst as an example of homogeneous catalysis (reproduced from reference[38])

1.3 Environmental Catalysis and Renewable Energies

With the rapidly evolving process industries, environmental pollution became a significant issue and brought forth the areas of environmental and green catalysis. A marked difference of environmental and green compared to traditional catalysis is their aim to protect the environment as well as strengthen industrial growth and quality of life not just in the short-term, but in the long-term.[39–41] The long-term concept came with the fast growth of knowledge in all areas of science. For example, earth science data indicated greenhouse gases from industry emissions as an important factor for climate change. Further it showed the rapid depletion of fossil fuel reserves, raising the need to search for alternative/renewable fuel sources for the future. Advances in medicine proved the hazardous effects of certain substances used in industrial processes, alerting for more care in the choice of chemicals.[40,42,43] These factors led to increased awareness and economic and political regulations in the industrialized countries. While environmental catalysis focuses on the detoxification of produced waste, the approach of green chemistry aims towards avoiding the production of waste in the first place.

The starting point of environmental catalysis in the late 1970s was the discovery of platinum and rhodium based catalysts for the reduction of NO_x with simultaneous oxidation of CO and volatile hydrocarbons, for use in combustion processes. These catalysts importantly reduced the toxicity of exhaust gases from transportation media and industrial plants, causing a significant improvement in air quality.[7,44] Around the same time, tetraethyl lead levels used in combustion engines as anti-knocking agents were decreased under the US Clean Air Act to protect public health and prevent catalyst poisoning. Until today, research in the area of combustion catalysts remains a major field, in terms of both engine efficiency and exhaust fume treatment.[44–46]

Particularly, catalytic technologies for industrial waste treatment are now growing. For example, the slow degradation of polymers with vast amounts of plastic waste accumulating on the land and in the oceans is a big problem to be faced. Current research focuses on the efficient collection, degradation and recycling of polymers, where amongst others the review from Garforth *et al*. presents new strategies for depolymerisation and recycling, as well as the partial oxidation or cracking of polymers to produce fuel additives.[47,48] In addition, new production routes for bio-degradable polymers are explored.[49] The decontamination of waste-water and polluted soils is another important subject, with several catalytic approaches ranging from inorganic to electrochemical and bio-organic. Feng *et al*. reported the efficient degradation of organic material in waste-water by hydroxyl radicals formed over titanium electrodes, while Grady *et al*. present new advances on removal of contaminants by enzymatic and biological oxidation processes.[40,50,51] Very recently, we demonstrated the successful use of niobium oxide nano-materials for waste-water separation membranes (Nakagawa *et al.*).[52]

Particularly important in the area of green catalysis is the development of renewable energies to reduce net CO_2 emissions and replace diminishing fossil fuel reserves. Characteristic of renewable energy sources such as sunlight, wind and water power and fast-growing plant material/biomass, is their continuous energy supply and recycling of emitted CO_2 - unlike fossil fuels which took millions of years to form but only decades to be consumed by mankind.[53–55] One research field in renewable energies is artificial photosynthesis, building on the plant model to generate energy in the form of carbohydrates and oxygen from sunlight, carbon dioxide and water. The area of photo-catalysis further extends the use of sunlight towards a large range of chemical reactions, where many photo-catalysts have been developed over the past years, ranging from inorganic to organic and enzymatic.[56–58] The market for electricity from photovoltaic devices/solar cells is rapidly evolving with an annual world-wide growth rate of 40% from 2010 to 2016. Inorganic solar cells based on doped silicon wafer catalysts are the most widely used type, with installations in industrial plants and on household rooftops.[59]

In case of over-production, the electricity generated from photo-catalysts can be used for other green chemistry applications such as electrochemical water-splitting, where the energy is stored in form of oxygen and hydrogen. Suitable catalysts for the gradual/non-explosive recombination of hydrogen and oxygen to water are researched extensively due to their potential as clean fuels which do not produce CO_2 emissions.[60,61] Unfortunately the large volume and high flammability of hydrogen gas pose difficulties for the use of hydrogen fuel for example in transportation media, giving rise to the search for materials with good hydrogen storage capacity.[62] Currently better developed with a growing market are exhaust-free battery driven vehicles.[55] Electrochemical catalysis further finds increasing research interests regarding ammonia production, with the hope of finding less energy extensive processes to substitute the Haber-Bosch process.[63]

Today fossil fuels still contribute almost 80 % to the world's energy consumption, while renewable energies including biomass, water, wind, solar and geothermal power make up about 20 % (Figure 1.4). From 2010 through to 2015 renewables have seen an average annual growth rate of 15 % which is promising, but there remains a lot to be achieved, especially regarding ambitious goals such as that of the Paris City Hall Declaration: 100 % renewable energy or 80 % reductions in greenhouse gas emissions by 2050, signed by one thousand cities from five continents.[55,64]

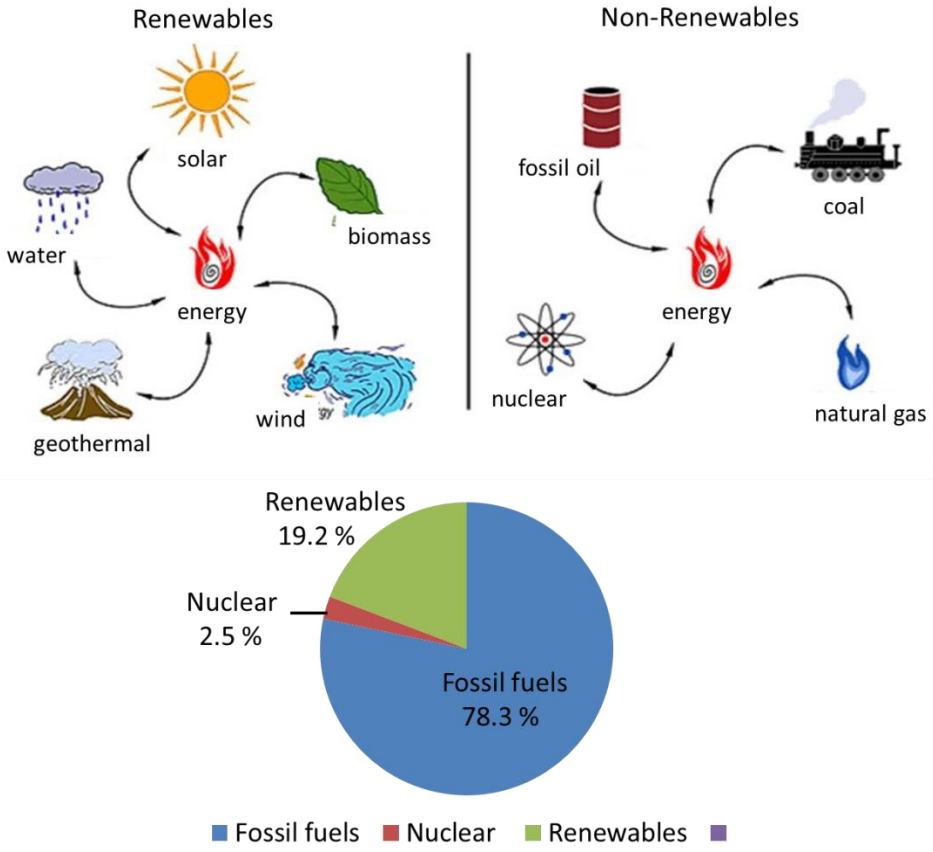


Figure 1.4 – Renewable *versus* Non-Renewable Energies (reproduced from references[55,65])

1.4 Biomass Conversion

Another important topic to be mentioned regarding environmental catalysis and renewable energies is biomass conversion. Biomass conversion refers primarily to the conversion of plant material to commodity chemicals or fuel compounds, ideally using plant waste or fast-growing species which provide a carbon neutral energy source. With the aim to replace fossil fuels, new reaction routes for the biomass-based synthesis of commodity chemicals and biofuels are researched, with promising results in the fields of inorganic, bio-organic and enzyme catalysis.[42,66–68]

Examples of common biomass sources are crops, sugar cane, grass and wood. As the extensive use of these sources requires land which is also needed for food production and biodiversity, it can compromise the original idea of protecting the environment and quality of life. Therefore other biomass sources are more promising, including food, animal and land waste such as weeds, used straw and wood pellets, plant shells and other inedible parts, tea and coffee waste or paper waste.[42,69] Research is also put into harvesting the energy of ocean plant material, particularly that of fast-growing algae.[70]

Plant-derived biomass consists primarily of lignocellulose (~ 95%), while the remaining few percent are made up of proteins, triglycerides, terpenes and minerals. Lignocellulose itself consists of cellulose (~ 50%), hemicellulose (~ 25%) and lignin (~ 25%), where cellulose and hemicellulose are macromolecules made of different sugars, while lignin consists mainly of phenyl based aromatic polymers.[66,67,71,72] There exist different approaches to the decomposition and energy gain from biomass: Thermochemical processes include high-temperature combustion, gasification and pyrolysis of biomass, where combustion produces mainly carbon dioxide and water, gasification proceeds under reduced air conditions yielding mainly carbon

monoxide and hydrogen, and pyrolysis happens in the absence of oxygen yielding gaseous, as well as oily liquid and solid charcoal products.[42,66,73] The use of microorganisms performing aerobic or anaerobic enzyme catalysis provides low-temperature routes for biomass conversion. These include aerobic oxidation by bacteria producing carbon dioxide and water, anaerobic fermentation by yeast producing ethanol or anaerobic digestion by bacteria producing hydrocarbons (mainly methane) and carbon dioxide.[42,70] In general, enzyme catalysis is slower and subject to the availability of an enzyme for the according starting material, but it is also less energy extensive and more specific in its product distribution than inorganic thermochemical catalysis.

For engine efficiency, as well as exhaust control, it is desirable to have fuel mixtures of specific composition, and similarly the synthesis of commodity and fine chemicals requires specific starting materials. Therefore, large research efforts are now put to the efficient separation of biomass into its components and their further conversion to defined fuels and chemicals for industrial synthesis. The separation of biomass into cellulose, hemicellulose and lignin components can be achieved by low-temperature enzymatic processes or by high-temperature solvation and splitting methods, followed by solvent extraction (Figure 1.5).[66,67,71] For example near critical water, supercritical carbon dioxide or gas-expanded liquids can be used to (partially) depolymerize and dissolve the components which can then be separated by polarity based solvent extraction, chromatography or membrane technology. Another possibility is the decomposition using aqueous or solid acid catalysts, where cellulose and hemicellulose are depolymerized and dissolved more rapidly for extraction than lignin.[66,71,74]

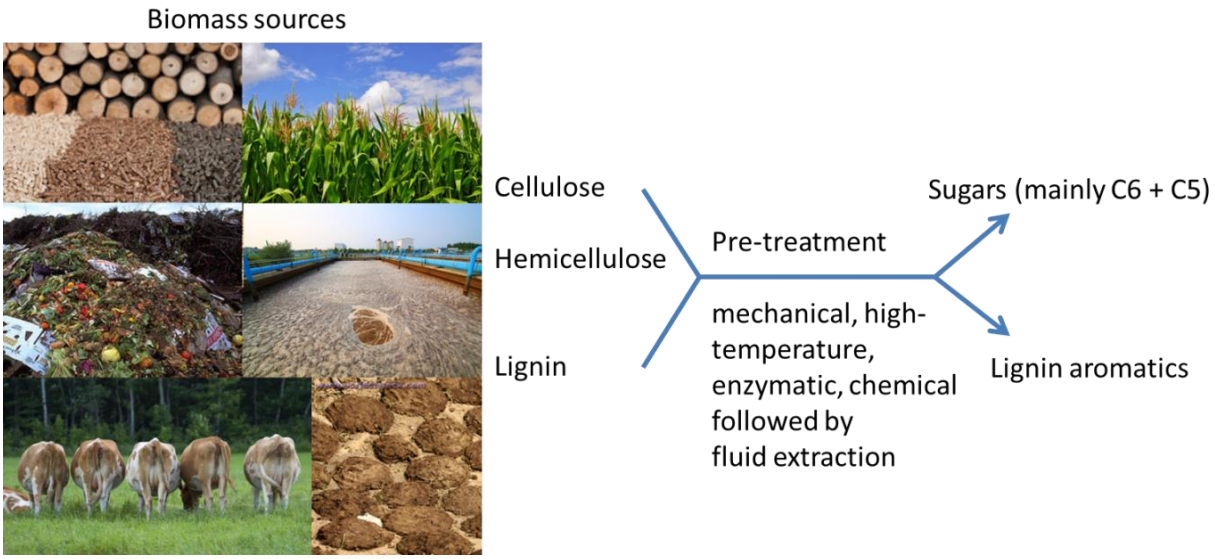


Figure 1.5 – Decomposition of biomass into the components of cellulose, hemicellulose and lignin as preparation for further chemical conversion

Currently, the lignin part is still decomposed mostly thermochemically to generate heat or electricity, although routes for its breakdown into useful aromatic compounds are desirable and researched.[66,75] Cellulose and hemicellulose are decomposed into their individual sugar units. Hemicellulose gives a number of different sugars, mainly C5 and C6 monomers, while cellulose yields the C6 monomer, glucose (Figure 1.5). For both C5 and C6 sugars, successful conversion routes to a number of precursors, also called platform molecules, are already available for use in the laboratory synthesis of commodity and fine chemicals.[66,67,76] The aim is to increase the efficiency of existing as well as develop new conversion routes for suitability on an industrial scale.

As the work of this thesis focuses on sugar conversion to hydroxymethylfurfural and further to aromatics using inorganic catalysts, the background of this particular research field will be discussed here in more detail.

1.4.1 Sugar Conversion to Hydroxymethylfurfural and Beyond

The dehydration of C6 sugars yields hydroxymethylfurfural (HMF), one of the most promising platform molecules in biomass conversion. HMF can be used as a precursor in diverse synthetic processes, including the production of polymers, resins, pharmaceuticals, flavours and fragrances, agro-chemicals and fuel additives. Analogously, the dehydration of C5 sugars yields the structural derivative furfural, with a similar range of applications (Figure 1.6 and Figure 1.7).[74,77,78] HMF and derivatives are naturally occurring in fruit, grains and honey and their ratio is enhanced by heat-processing, with particularly high abundance in processed foods such as coffee, syrup, bread and milk. Accordingly, HMF production on an industrial and laboratory scale from biomass-derived sugars is usually performed at elevated temperatures (100 – 200 °C), but under the further addition of rate- and selectivity-enhancing catalysts.[74,76,79]

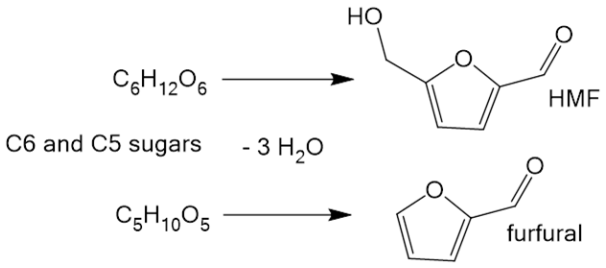


Figure 1.6 – Dehydration of C6 and C5 sugars to HMF and furfural

Sugar dehydration to HMF or furfural is an acid catalysed process and many different types of acid catalysts, heterogeneous and homogeneous, have been developed over the past years with significant improvements in yield and selectivity. Glucose (C6) as the major monomeric biomass component is of interest, and to a lesser extent also xylose (C5). Fructose (C6) is less abundant, but has shown better reactivity and HMF yields.[79–81] The acid catalysed mechanisms proposed in literature for glucose and fructose dehydration to HMF will be discussed in detail in Chapter

4.1. A commonly faced problem in the conversion of sugars and biomass is the complexity of the involved reactions, with a wide product spectrum and low selectivity. For sugar conversion particularly in aqueous solvents, side product formation and HMF degradation play a significant role, leaving room for further catalytic improvements.[76,78,81]

Weingarten *et al*. tested several solid acid catalysts for the conversion of xylose to furfural in water, including Zr-P, SiO_2-Al_2O_3, HY zeolite and WO_x-ZrO_2 with furfural yields of about 20 %, where strongly Brønsted acidic Zr-P gave higher selectivity at lower conversion and more Lewis acidic WO_x-ZrO_2 gave lower selectivity at higher conversion.[82] Nikolla *et al*. achieved significantly higher yields of 50 % HMF from glucose and starch at 70 % selectivity and 75 % conversion, using the Lewis acid catalyst Sn-Beta in a biphasic aqueous/THF system.[83] Biphasic systems are increasingly common as they increase HMF/furfural yield by simultaneous product extraction from the aqueous reaction phase into the organic phase, which reduces product degradation and polymerization.[76,84] Choudhary *et al.* obtained 59 % HMF from glucose over the combined homogeneous acid catalyst $CrCl_3$/HCl in water using THF as extraction phase;[85] similarly Gallo *et al*. reported 62 % HMF from glucose and 79 % from fructose over $AlCl_3$/HCl in a biphasic aqueous/GVL phase.[86] Other common extraction solvents are dimethylsulfoxide and dimethylformamide, which however provide difficulties with product separation due to their high boiling points and thermal instability of HMF.[78,79,84] The same problem occurs with the use of ionic liquids, which otherwise have shown very good conversion yields, as reported for example by Zhao *et al.* with 68 % HMF from glucose over $CrCl_2$ in [EMIM]Cl.[87]

HMF and furfural product separation generally proves very cost-intensive, and besides yield optimisation is an important issue in large scale industrial production. Currently the main techniques employed are neutralisation, filtration, distillation, crystallisation and

chromatography to obtain pure HMF and furfural. For their future potential as biomass-derived synthesis precursors and energy carriers it is important to both reduce production costs and find environmentally-friendly conversion routes, which is challenging.[74,76,79] One concept for further development is the use of water in combination with a heterogeneous solid acid catalyst. This is advantageous from both the product separation and environmental point of view, but requires significant yield improvements to become cost-effective. Chapter 4 of this thesis will focus on the potential of niobium oxides for sugar conversion to HMF in water, including reaction mechanistic investigations.

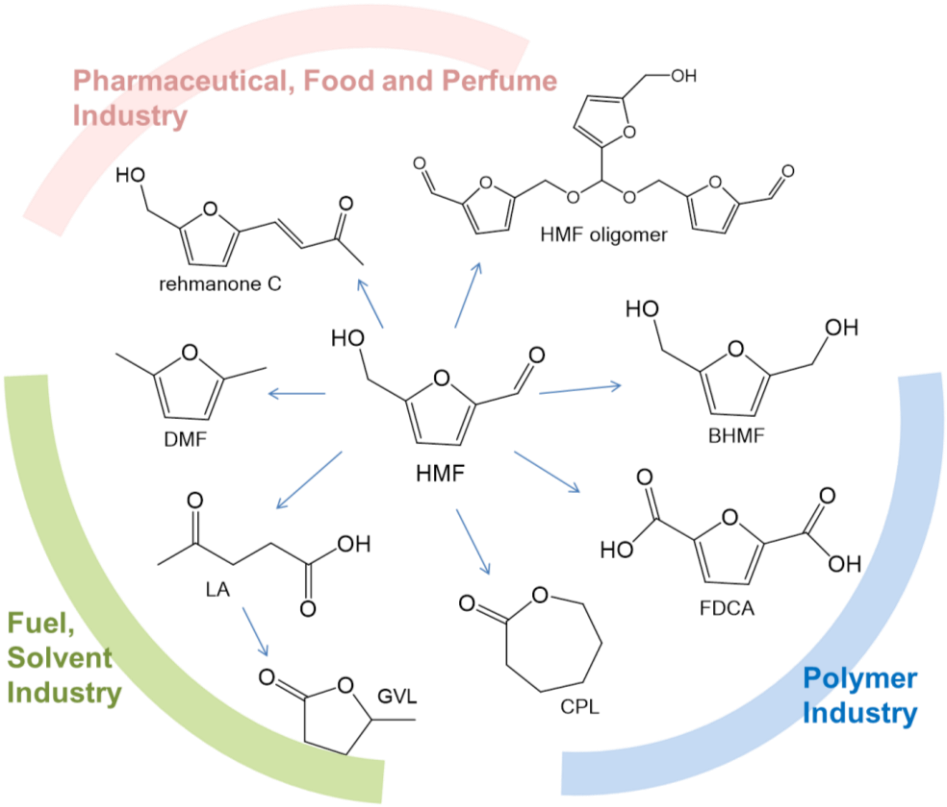


Figure 1.7 – Application areas of HMF in the chemical industry

As mentioned earlier, HMF is a promising starting material for a number of areas in synthetic chemistry and the fuel industry (Figure 1.7). Oxidation of HMF yields 2,5-furandicarboxylic acid (FDCA) which is an important polymer building block, used for example in the production of

polyethylene furanoate (PEF), a replacement polymer for fossil-fuel based polyethylene terephthalate (PET).[72,76,78] Hydrogenation of HMF yields 2,5-*bis*-hydroxymethylfuran (BHMF), which by etherification can be used as a component of polyurethane foams. HMF is also interesting for the production of bio-polymers such as polycaprolactone from caprolactone (CPL) with applications in drug delivery and tissue engineering.[72,79] An attractive fuel component in the replacement of conventional fuels is 2,5-dimethylfuran (DMF), synthesized from HMF *via* hydrogenation. Of interest here are also coupling reactions of HMF derivatives, leading to longer carbon chain products for example *via* aldol condensation.[77,79] Other application areas of HMF coupling reactions and aldol condensations are the food and pharma industry. For example HMF oligomers can be used in food flavouring, while aldol condensation of HMF and acetone gives the biologically active compound rehmanone C.[78,79] HMF hydrolysis produces formic and levulinic acid (LA) with high yields, where levulinate esters are widely used in the food industry and as plasticisers and solvents. Gamma-valerolactone (GVL) is obtained from the reduction of levulinic acid and finds applications in the solvent and perfume industry.[74,88]

As can be seen, HMF has a wide range of applications and new synthetic routes are currently researched. Chapter 6 of this thesis investigates the development of a synthetic route to produce aromatic hydrocarbons from HMF *via* DMF.

1.5 Principles of Catalysis

The rate of any chemical reaction is dependent on its activation energy, the energy barrier that needs to be overcome to convert reactant(s) into product(s). Raising the temperature is a way to enhance the reaction rate, but many reactions would require high temperatures to proceed, which is undesirable due to the large amounts of energy invested; further the reaction equilibrium is affected by temperature. The relation between rate constant k, activation energy E_a and temperature T is generally described by the Arrhenius equation, where further R is the gas constant and A the pre-exponential or reaction intrinsic factor (Equation 1.1).[89,90]

$$k = Ae^{-\frac{E_a}{RT}} \qquad Equation\ 1.1$$

Catalysts are convenient as they accelerate the reaction by providing a different pathway for the reaction to proceed, at a lower activation energy E_a. At the same time they do not affect the total energy change ΔG of the reaction, which is the difference in energy between the reactants and products.[91] Figure 1.8 depicts how a catalyst influences the reaction proceedings, by the example of reactant A being converted to product B over catalyst M. The reduction in activation energy results from transition-state stabilising interactions between the catalyst, reactant and product, where the different interaction stages can be described as follows: Reactant A binds to catalyst M to form adsorption complex AM, followed by the conversion of A to B *via* the catalyst-stabilised transition state AM*. The resulting product complex BM is dissociated by product desorption to give B and M. The same basic concept also applies to multiple reactants and products.[26,91]

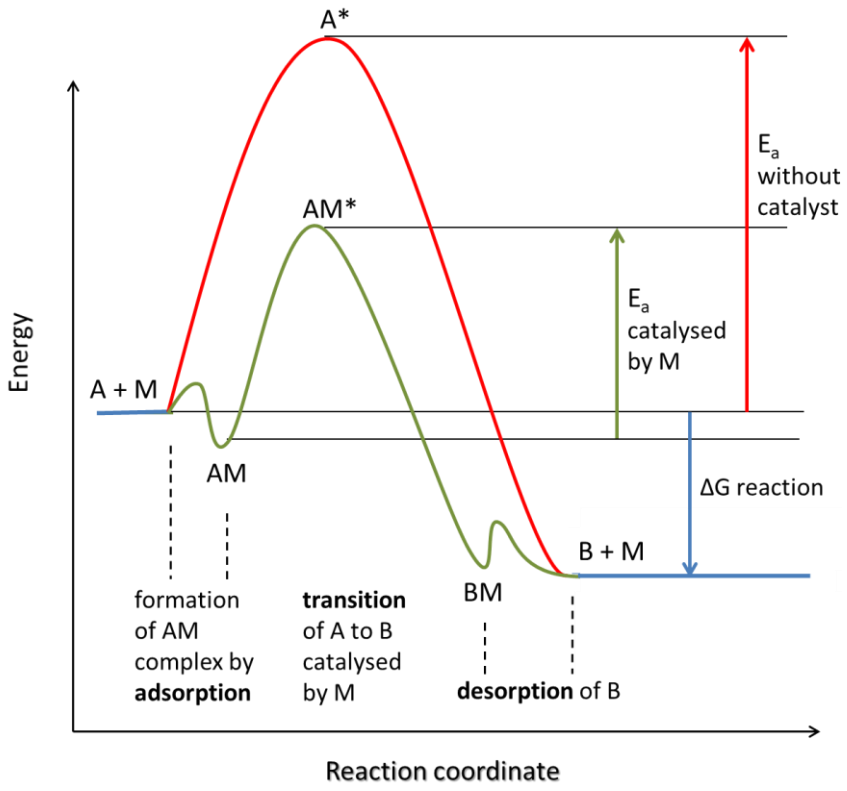


Figure 1.8 – Catalysed *versus* non-catalysed reaction pathway, where A = reactant, B = product, M = catalyst

The term active site is important in catalysis, as often not the whole catalyst surface is active but only specific sites on which the reaction proceeds. A solid Brønsted acid for example has H^+ active sites, which can bind to OH groups of the reactant (in analogy to adsorption complex AM), thereby weakening the internal R-OH bonds of the reactant, which in turn lowers the activation energy for R-OH bond breakage (AM*) and accelerates the rate of dehydration.[92] Depending on the chemistry, there are many different types of reactant-active site interactions to enhance reactivity. These include weaker dispersive forces as well as stronger dipole or hydrogen bonding, as often observed in enzymatic catalysis, or even ionic interactions, such as in the case of solid acid and base catalysis. For typical transition metal catalysts such as iron, zinc, copper or the more noble ruthenium and palladium, electronic d-band interactions dominate. In

shape-selective catalysis, as for enzymes and zeolites, the spatial arrangement of the active site fits that of the reactant(s) to accommodate and convert.[26,93]

$$A + M \underset{k_{reverse}}{\overset{k}{\rightleftarrows}} B + M \qquad Equation\ 1.2$$

$$A + M \underset{k_{1\,reverse}}{\overset{k_1}{\rightleftarrows}} AM \underset{k_{2\,reverse}}{\overset{k_2}{\rightleftarrows}} BM \underset{k_{3\,reverse}}{\overset{k_3}{\rightleftarrows}} B + M$$

As can be seen in Figure 1.8, the different stages involved in a catalysed reaction each have their own energy transition/activation energy, which can be depicted by individual reaction rates and equilibria (Equation 1.2).[89,94] For example, the rate constant for the adsorption of A onto M is given by k_1, the rate constant for the conversion of AM to BM by k_2 and the rate constant for desorption of B by k_3. As every reaction can also proceed backwards and the speed depends on the respective activation energy, the according rate constants are given by $k_{1\,reverse}$, $k_{2\,reverse}$ and $k_{3\,reverse}$. For the given reaction profile, the backward reactions are more "uphill" in terms of energy and therefore slower than the forward reactions, causing the individual and overall equilibrium to be product-oriented. This is reflected by the total energy change ΔG and the equilibrium constant K of the reaction, where k is the forward rate constant and $k_{reverse}$ the backward rate constant of the overall reaction A to B, [A] is the concentration of reactant A and [B] the concentration of product B (Equation 1.3).[20,89]

$$K = \frac{k}{k_{reverse}} = e^{\frac{-\Delta G}{RT}} = \frac{[B]}{[A]} \qquad Equation\ 1.3$$

According equations can be set up for the individual reaction stages from Equation 1.2, with equilibrium constants K_1, K_2 and K_3. Determining product concentrations for each of the interdependent reaction stages gets quite complex when many stages and equilibrium constants

are involved. It can therefore be useful to work with approximations and simplified equations. In a typical catalytic reaction, the rates of reactant adsorption and product desorption are much faster than the rate of transition from AM to BM (Figure 1.8), which is therefore also called the rate-determining step. Accordingly, the following reaction rate approximation can be set up (Equation 1.4).[94]

$$r = k_2[AM] \approx k_2 K_1[A][M] \qquad Equation\ 1.4$$

$$\text{where } K_1 = \frac{[AM]}{[A][M]}$$

At first sight, it appears from here that the higher the concentration of AM, the faster the rate of AM to BM conversion. This is only partially true, as a high equilibrium concentration of AM also means a strongly stabilised adsorption complex with a significant energy gain/negative ΔG. This on the other hand enlarges the activation energy of AM to BM transition, meaning a lower rate constant k_2 which reduces the overall reaction rate. Therefore an intermediate adsorption strength of the reactants to the catalyst is most efficient (Sabatier principle).[16,95] Similarly, the product complex BM should not be too stable due to very slow desorption of product B, while an unstable product complex BM would increase the backward reaction rate. Overall, relatively fast adsorption and desorption processes with intermediate adsorption and desorption strength are ideal in catalysis. Most enzymes, being among the oldest and most evolved catalytic species, function according to these principles.[26] However, a catalyst cannot change the fact that many reactions are energetically unfavourable; it can only optimise the transition process, as mentioned earlier. To obtain decent product yields even for reactions with a positive ΔG, techniques such as product extraction from the reaction mixture can be used to shift the reaction equilibrium towards the product side.[91,96]

Another important topic in catalysis are competitive reactions, particularly in the conversion of biomass where many reactants and reaction pathways are involved. If for example reactant C competes with reactant A for active sites M, the competitive adsorption equilibrium $K_{competitive}$ can be described as follows (Equation 1.5), where K_C is the equilibrium constant of adsorption of C onto M.[94]

$$K_{competitive} = \frac{[CM][A]}{[AM][C]} = \frac{[M][A]}{[MA]} \frac{[CM]}{[C][M]} = \frac{K_C}{K_1} \qquad Equation\ 1.5$$

The rate slowing effect of C on the reaction of A is less pronounced for low reactant concentrations and high active site concentrations, as only few active sites M are occupied. Competitive reactions further include side reactions, where reactant A undergoes transitions to different products, occurring mainly for reactions which are catalysed by the active sites M to a similar extent. Overall, it is always desirable to develop a reaction-specific catalyst that is primarily active for the reaction of interest, in order to reduce competitor effects and side reactions and thereby increase product yield and selectivity.[91,97]

1.6 Catalysis and Nanoscience

Over the last few decades nanoscience catalysis has become of major interest. It refers to the application of nano-structured materials as catalysts, covering the size regime of 1 to 100 nm. Nanomaterials have much larger surface areas than their respective bulk materials, resulting in high active site concentrations and making them particularly useful in catalysis. Nanomaterials can be synthesized *via* a top-down approach, where the bulk material is broken down into smaller parts, or *via* a bottom-up approach, where the nanomaterial is directly synthesized from precursors.[95,98]

Besides their high surface areas, there are other significant differences in nanomaterials compared to bulk. Geometric effects are important, where the reduced particle size leads to different surface site configurations (Figure 1.9 a). A large metal sphere for example possesses an almost flat surface from the point of view of an adsorbing molecule, while a spherical metal nanoparticle has many stepped surface sites. Further there is the increased flexibility of nanomaterials, where for example 2D-nanomaterials are easier to bend and structurally deform (Figure 1.9 b), sometimes with strong effects on the nature of catalytic sites, or where metal nanoparticles experience less added strain upon doping and are therefore easier to modulate than the respective bulk materials.[98–100] An important factor are also electronic effects, particularly pronounced for metals and semiconductors, where a reduction in particle size leads to an increased band gap between valence and conduction band, with effects on surface-adsorbate interactions and photocatalytic behaviour. Further the reduced size of nanomaterials tends to lead to transverse effects of any supporting materials in use, where the support takes influence on shape, structure and electronic properties (Figure 1.9 c).[98,101,102] Overall, there are many distinct features to nanostructure catalysis and it has become an important research field in chemistry, physics and material sciences.

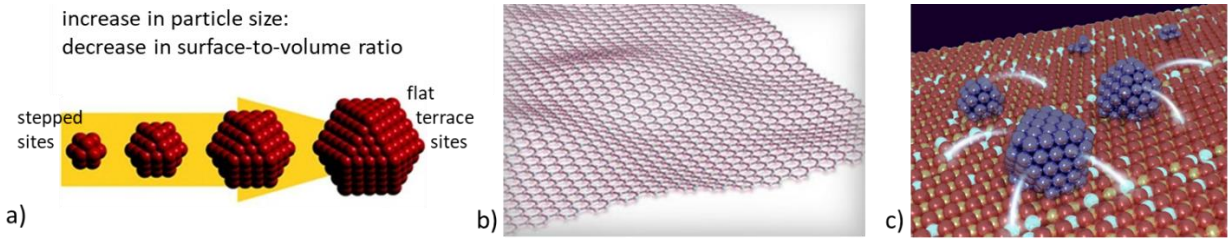


Figure 1.9 – Examples of nanomaterial characteristics a) geometric effects (reproduced in part from reference[103] (doi 10.1039/c1cp22048a) with permission of the PCCP Owner Societies). b) structural flexibility (reproduced from reference)[104] c) support effects (reprinted by permission from Macmillan Publishers Ltd. from reference[105] (doi 10.1038/nmat4500))

Chapter 5 of this thesis focuses on structural studies of 2D-nanosheet compared to bulk niobium oxides. The 2D-nanosheets are synthesized *via* a bottom-up approach from niobium precursor under the addition of surfactant (see Chapter 3.1.1 for experimental details). Surfactants are typically bulky organic molecules which adsorb onto the nanoparticle surface and thereby act as stabilizers to prevent nanoparticle aggregation.[106–108] The properties of a suitable surfactant are dependent on the nature of both solvent and nanomaterial surface. For example, the niobium oxide nanosheet synthesis in aqueous solution is performed under addition of the base triethanolamine (TEOA) which adsorbs onto the acidic nanosheet surface. As mentioned earlier, the use of supporting materials is further a common approach to stabilise the formation of separate nanoparticles by particle immobilisation on the support surface.[109,110] In Chapter 6, ruthenium and palladium nanoparticles supported on zeolites are synthesized *via* wet impregnation of the support with metal precursor, followed by reduction and metal nanoparticle formation under hydrogen at elevated temperatures (see Chapter 3.1.2 for experimental details). For the synthesis of porous nanomaterials the use of organic templates is common, where template removal by calcination or irradiation gives rise to according pores.[111,112] The amorphous mesoporous Nb_2O_5*nH_2O in Chapter 5 on the other hand is synthesized *via* a top-down approach, where parts of the formed niobium oxide network are removed by acid etching (see Chapter 3.1.1 for experimental details).

1.7 Thesis Overview

This thesis consists of seven chapters, where chapters three to seven detail the research conducted during the course of this DPhil.

Chapter One: This chapter introduces the principles of catalysis and the story of its origins until today, with an emphasis on the newer fields of environmental catalysis and biomass conversion. Sugar conversion as the topic of this thesis is presented in additional detail.

Chapter Two: The background and theory of the analytical techniques employed to characterize the catalysts and conversion processes in this work are presented.

Chapter Three: A detailed description of the experimental techniques used in this work is given, including catalyst synthesis and characterization as well as product analysis procedures.

Chapter Four: The experimental results of sugar conversion to hydroxymethylfurfural (HMF) over niobium oxides in water are presented and discussed. An emphasis is put on environmental aspects and underlying reaction mechanisms, which is important to improve catalyst design.

Chapter Five: A detailed study on the structure of different niobium oxide catalysts with an emphasis on the relation of structure to acidity is presented. A structural understanding of the material is important for targeted synthesis and catalytic improvements, in analogy to the work from Chapter Four.

Chapter Six: This chapter details the experimental results of the conversion of hydroxymethylfurfural (HMF) to dimethylfuran (DMF) and further to aromatic hydrocarbons. New synthesis routes for aromatics from alternative sources such as sugars become increasingly important with the depletion of fossil fuels.

Chapter Seven: The final chapter presents the conclusions and the future outlook of this work.

1.8 References

(1) Thomas, J. M.; Thomas, W. J. *Principles and Practice of Heterogeneous Catalysis*; Wiley VCH Verlag GmbH & Co. KGaA, 1997.

(2) *Oxford Dictionaries Catalyst Definition*; Oxford Dictionaries, 2013.

(3) Green, S. *Industrial Catalysis*; Macmillan Company, 1928.

(4) Berzelius, J. J. *Arsberattelsen om framsteg i fysik och kemi*; Royal Swedish Academy of Sciences, 1835.

(5) Galgani, J.; Ravussin, E. *Int. J. Obes.* **2008**, *32* (7), 109.

(6) McGovern, P. E. *Uncorking the Past: The Quest for Wine, Beer, and Other Alcoholic Beverages*; Berkeley: University of California Press, 2009.

(7) Lindström, B.; Pettersson, L. J. *Cattech* **2003**, *7* (4), 130.

(8) Stewart, M. https://sites.google.com/site/mrstewartjfr/matter-energy-in-cells-notes.

(9) http://clipartsign.com/image/37567/.

(10) https://stickfiguresclipart.com/wp-content/gallery/family-stick-figures/.

(11) Mellor, J. *J. Phys. Chem.* **1903**, *7*, 557.

(12) Kirchhoff, G. M. *Schweigger's J.* **1812**, *4*, 108.

(13) Partington, J. R. *A History of Chemistry*, Vol. 4.; Macmillan, 1964.

(14) Faraday, M. *Phil. Trans.* **1834**, *55*, 124.

(15) Lemoine, G. *Ann. Chim. Phys.* **1877**, *12*, 45.

(16) Ertl, G.; Knözinger, H.; Weitkamp, J. *Handbook of Heterogeneous Catalysis*, Vol. 1.; Wiley VCH Verlag GmbH & Co. KGaA, 1997.

(17) Wilhelmy, L. F. *Pogg. Ann.* **1850**, *81*, 413.

(18) Guldberg, C. M.; Waage, P. *Forhandlinger i Videnskabs-Selskabet i Christiania*; Brögger & Christiers Bogtrykkeri, 1865.

(19) Le Chatelier, H.; Boudouard, O. *Bull. Soc. Chim. Fr.* **1898**, *19*, 483.

(20) Atkins, P.; De Paula, J. *Atkins' Physical Chemistry*; Oxford University Press, 2010.

(21) Atkins, P. *The Elements of Physical Chemistry*; Oxford University Press, 1993.

(22) Haber, F.; van Oordt, G. *Z. Anorg. Chem.* **1905**, *44*, 341.

(23) Bosch, C. *Die Chem. Fabrik* **1933**, *12*, 127.

(24) Mittasch, A. *Geschichte der Ammoniaksynthese*; Weinheim VCH Verlag, 1951.

(25) Anderson, J. R.; Boudart, M. *Catalysis Science and Technology*, Vol.7.; Springer, 1981.

(26) Swiegers, G. F. *Mechanical Catalysis: Methods of Enzymatic, Homogeneous, and Heterogeneous Catalysis*; Wiley VCH Verlag GmbH & Co. KGaA, 2008.

(27) Licht, S.; Comanescu, J. http://technologies.research.gwu.edu/technologies/014-025-licht_a-simple-one-pot-chemistry-to-produce-ammonia-from-air-and-water-without-emitting-carbon-dioxide.

(28) Wittcoff, M. M.; Green, H. A. *Organic Chemistry Principles and Industrial Practice*; Wiley VCH Verlag GmbH & Co. KGaA, 2003.

(29) Fischer, F.; Tropsch, H. DEP 484337 [Patent], 1925.

(30) Fischer, F.; Tropsch, H. DEP 531004 [Patent], 1925.

(31) Ziegler, K.; Gellert, H. G. DEP 883067 [Patent], 1953.

(32) Natta, G. DEP 1094985 [Patent], 1955.

(33) Bowden, M. E. *Chemical Achievers*; Chemical Heritage Foundation, 1997.

(34) Rosinski, C. J.; Edward, J. GBP 1039345 [Patent], 1964.

(35) Wilkinson, G. *Platin. Met. Rev.* **1968**, *12*, 50.

(36) Rothenberg, G. *Catalysis: Concepts and Green Applications*; Wiley VCH Verlag GmbH & Co. KGaA, 2008.

(37) Hagen, J. *Industrial Catalysis: A Practical Approach*; Wiley VCH Verlag GmbH & Co. KGaA, 2006.

(38) Vutturi, A. V. http://www.adichemistry.com/inorganic/organometallic/catalysis/wilkinson/wilkinsons-catalyst.html.

(39) Garin, F. *Catal. Today* **2004**, *89*, 255.

(40) Centi, G.; Ciambelli, P.; Perathoner, S.; Russo, P. *Catal. Today* **2002**, *75* (1–4), 3.

(41) Crabtree, R. H. *Handbook of Green Catalysis*; Wiley VCH Verlag GmbH & Co. KGaA, 2009.

(42) Saidur, R.; Abdelaziz, E. A.; Demirbas, A.; Hossain, M. S.; Mekhilef, S. *Renew. Sustain. Energy Rev.* **2011**, *15* (5), 2262.

(43) Fatsikostas, A. N.; Kondarides, D. I.; Verykios, X. E. *Catal. Today* **2002**, *75* (1–4), 145.

(44) Farrauto, R. J.; Heck, R. M. *Catal. Today* **1999**, *51* (3–4), 351.

(45) Armor, J. N. *Catal. Today* **2011**, *163* (1), 3.

(46) Armor, J. N. *Appl. Catal. B Environ.* **1992**, *1*, 221.

(47) Parker, L. *National Geographic*. 2015,.

(48) Garforth, A. A.; Ali, S.; Hernández-Martínez, J.; Akah, A. *Curr. Opin. Solid State Mater. Sci.* **2004**, *8* (6), 419.

(49) Mohanty, A. K.; Misra, M.; Hinrichsen, G. *Macromol. Mater. Eng.* **2000**, *276–277*, 1.

(50) Feng, C.; Sugiura, N.; Shimada, S.; Maekawa, T. *J. Hazard. Mater.* **2003**, *103* (1–2), 65.

(51) Grady, C.; Daigger, G.; Love, N.; Filipe, C. *Biological Wastewater Treatment*, 3rd editio.; CRC Press, 2011.

(52) Nakagawa, K.; Yamashita, H.; Saeki, D.; Yoshioka, T.; Shintani, T.; Kamio, E.; Kreissl, H. T.; Tsang, S. C. E.; Sugiyama, S.; Matsuyama, H. *Chem. Commun.* **2017**, *53* (56), 7929.

(53) Panwar, N. L.; Kaushik, S. C.; Kothari, S. *Renew. Sustain. Energy Rev.* **2011**, *15* (3), 1513.

(54) Herzog, A. V.; Lipman, T. E.; Kammen, D. M. *Encycl. Life Support Syst.* **2001**, 1.

(55) REN21 Secretariat. *Renewables 2016 Global Status Report*; 2016.

(56) Hoffmann, M. R.; Martin, S.; Choi, W.; Bahnemann, D. W. *Chem. Rev.* **1995**, *95* (1), 69.

(57) Aresta, M.; Dibenedetto, A.; Baran, T.; Angelini, A.; Łabuz, P.; Macyk, W. *Beilstein J.*

Org. Chem. **2014**, *10*, 2556.

(58) Fujishima, A.; Zhang, X.; Tryk, D. A. *Surf. Sci. Rep.* **2008**, *63* (12), 515.

(59) Fraunhofer Institute for Solar Energy Systems. *Photovoltaics Report*; 2017.

(60) Kudo, A.; Miseki, Y. *Chem. Soc. Rev.* **2009**, *38* (1), 253.

(61) Osterloh, F.; Parkinson, B. *MRS Bull.* **2011**, *36* (1), 17.

(62) Schlapbach, L.; Züttel, a. *Nature* **2001**, *414* (6861), 353.

(63) Montoya, J. H.; Tsai, C.; Vojvodic, A.; Norskov, J. K. *ChemSusChem* **2015**, *8* (13), 2180.

(64) International Energy Agency. *Renewable energy medium-term market report 2015. Market Analysis and Forecasts to 2020 - Executive Summary*; 2015.

(65) http://www.keepbanderabeautiful.org/renewable.html.

(66) Sheldon, R. A. *Green Chem.* **2014**, *16* (3), 950.

(67) Stöcker, M. *Angew. Chemie - Int. Ed.* **2008**, *47* (48), 9200.

(68) McKendry, P. *Bioresour. Technol* **2002**, *83* (1), 37.

(69) Hoogwijk, M.; Faaij, A.; van den Broek, R.; Berndes, G.; Gielen, D.; Turkenburg, W. *Biomass and Bioenergy* **2003**, *25* (2), 119.

(70) Demirbaş, A. *Energy Convers. Manag.* **2001**, *42* (11), 1357.

(71) Ragauskas, A. J.; Williams, C. K.; Davison, B. H.; Britovsek, G.; Cairney, J.; Eckert, C. A.; Frederick, W. J.; Hallett, J. P.; Leak, D. J.; Liotta, C. L.; Mielenz, J. R.; Murphy, R.; Templer, R.; Tschaplinski, T. *Science* **2006**, *311* (5760), 484.

(72) Isikgor, F. H.; Remzi Becer, C. *Polym. Chem.* **2015**, *6*, 4497.

(73) McKendry, P. *Bioresour. Technol.* **2002**, *83* (1), 47.

(74) Chen, S. S.; Maneerung, T.; Tsang, D. C. W.; Ok, Y. S.; Wang, C.-H. *Chem. Eng. J.* **2017**, *328*, 246.

(75) Zakzeski, J.; Bruijnincx, P. C. A.; Jongerius, A. L.; Weckhuysen, B. M. *Chem. Rev.* **2010**, *110*, 3552.

(76) Teong, S. P.; Yi, G.; Zhang, Y. *Green Chem.* **2014**, *16* (4), 2015.

(77) Climent, M. J.; Corma, A.; Iborra, S. *Green Chem.* **2014**, *16* (2), 516.

(78) Rosatella, A. A.; Simeonov, S. P.; Frade, R. F. M.; Afonso, C. A. M. *Green Chem.* **2011**, *13* (4), 754.

(79) Van Putten, R. J.; Van Der Waal, J. C.; De Jong, E.; Rasrendra, C. B.; Heeres, H. J.; De Vries, J. G. *Chem. Rev.* **2013**, *113* (3), 1499.

(80) Kuster, B. F. M. *Starch - Stärke* **1990**, *42* (8), 314.

(81) de Souza, R. L.; Yu, H.; Rataboul, F.; Essayem, N. *Challenges* **2012**, *3* (2), 212.

(82) Weingarten, R.; Tompsett, G. A.; Conner, W. C.; Huber, G. W. *J. Catal.* **2011**, *279* (1), 174.

(83) Nikolla, E.; Román-Leshkov, Y.; Moliner, M.; Davis, M. E. *ACS Catal.* **2011**, *1* (4), 408.

(84) Román-Leshkov, Y.; Chheda, J. N.; Dumesic, J. A. *Science* **2006**, *312* (5782), 1933.

(85) Choudhary, V.; Mushrif, S. H.; Ho, C.; Anderko, A.; Nikolakis, V.; Marinkovic, N. S.; Frenkel, A. I.; Sandler, S. I.; Vlachos, D. G. *J. Am. Chem. Soc.* **2013**, *135* (10), 3997.

(86) Gallo, J. M. R.; Alonso, D. M.; Mellmer, M. A.; Dumesic, J. A. *Green Chem.* **2013**, *15*

(1), 85.

(87) Zhao, H.; Holladay, J. E.; Brown, H.; Zhang, Z. C. *Science* **2007**, *316* (5831), 1597.

(88) Girisuta, B.; Janssen, L. P. B. M.; Heeres, H. J. *Ind. Eng. Chem. Res.* **2007**, *46* (6), 1696.

(89) House, J. *Principles of Chemical Kinetics*, 2nd ed.; Elsevier Science, 2007.

(90) Soustelle, M. *An Introduction to Chemical Kinetics*; Wiley VCH Verlag GmbH & Co. KGaA, 2013.

(91) Beller, M.; Renken, A.; van Santen, R. *Catalysis: From Principles to Applications*; Wiley VCH Verlag GmbH & Co. KGaA, 2012.

(92) Caratzoulas, S.; Davis, M. E.; Gorte, R. J.; Gounder, R.; Lobo, R. F.; Nikolakis, V.; Sandler, S. I.; Snyder, M. A.; Tsapatsis, M.; Vlachos, D. G. *J. Phys. Chem. C* **2014**, *118* (40), 22815.

(93) Ennaert, T.; Van Aelst, J.; Dijkmans, J.; De Clercq, R.; Schutyser, W.; Dusselier, M.; Verboekend, D.; Sels, B. F. *Chem. Soc. Rev.* **2016**, *45* (3), 584.

(94) http://faculty.gvsu.edu/mcbaneg/chm358wi02.pdf.

(95) Prins, R.; Wang, A.; Li, X. *Introduction to Heterogeneous Catalysis*; Imperial College Press, 2016.

(96) Wirth, T. *Microreactors in Organic Chemistry and Catalysis*; Wiley VCH Verlag GmbH & Co. KGaA, 2013.

(97) Behrens, M.; Datye, A. *Catalysis for the Conversion of Biomass and its Derivatives*; Edition Open Access, 2013.

(98) Roduner, E.; Cronin, L. *Nanoscopic Materials: Size-Dependent Phenomena*; Royal Society of Chemistry, 2006.

(99) Hornyak, G.; Tibbals, F.; Dutta, J.; Moore, J. *Introduction to Nanoscience & Nanotechnology*; CRC Press, 2008.

(100) Bhattacharyya, D.; Schäfer, T.; Wickramasinghe, S.; Daunert, S. *Responsive Membranes and Materials*; Wiley VCH Verlag GmbH & Co. KGaA, 2012.

(101) Kolasinski, K. *Surface Science: Foundations of Catalysis and Nanoscience*, 3rd ed.; Wiley VCH Verlag GmbH & Co. KGaA, 2012.

(102) Tiwari, A.; Titinchi, S. *Advanced Catalytic Materials*; Wiley VCH Verlag GmbH & Co. KGaA, 2015.

(103) Sonström, P.; Bäumer, M. *Phys. Chem. Chem. Phys.* **2011**, *13* (43), 19270.

(104) Ricci, T. https://www.asme.org/engineering-topics/articles/nanotechnology/2d-nanomaterials-revolutionizing-device-design.

(105) Lykhach, Y.; Kozlov, S. M.; Skála, T.; Tovt, A.; Stetsovych, V.; Tsud, N.; Dvořák, F.; Johánek, V.; Neitzel, A.; Mysliveček, J.; Fabris, S.; Matolín, V.; Neyman, K. M.; Libuda, J. *Nat. Mater.* **2016**, *15* (3), 284.

(106) Astruc, D. *Nanoparticles and Catalysis*; Wiley VCH Verlag GmbH & Co. KGaA, 2008.

(107) Johnson, S. R.; Evans, S. D.; Brydson, R. *Langmuir* **1998**, *14* (23), 6639.

(108) Mévellec, V.; Mattioda, C.; Schulz, J.; Rolland, J. P.; Roucoux, A. *J. Catal.* **2004**, *225* (1), 1.

(109) Johnston, R. L.; Wilcoxon, J. P. *Metal Nanoparticles and Nanoalloys*; Elsevier Ltd, 2012.

(110) Campelo, J. M.; Luna, D.; Luque, R.; Marinas, J. M.; Romero, A. A. *ChemSusChem* **2009**, *2* (1), 18.

(111) Van Bommel, K. J. C.; Friggeri, A.; Shinkai, S. *Angew. Chemie - Int. Ed.* **2003**, *42* (9), 980.

(112) He, J.; Yang, X.; Evans, D. G.; Duan, X. *Mater. Chem. Phys.* **2003**, *77* (1), 270.

Chapter 2

Analytical Techniques

Chapter 2 31

2.1 Transmission Electron Microscopy (TEM) 32

2.2 X-Ray Diffraction (XRD) 34

2.3 Raman and Infrared Spectroscopy 37

2.4 Temperature Programmed Desorption (TPD) 40

2.5 Brunauer-Emmett-Teller (BET) 403

2.6 X-Ray Photoelectron Spectroscopy (XPS) 46

2.7 X-Ray Absorption Fine Structure (XAFS) 49

2.8 Solid State Nuclear Magnetic Resonance (ssNMR) 52

2.8.1 Trimethylphosphine (TMP) ^{31}P ssNMR 56

2.8.2 ^{93}Nb ssNMR 57

2.9 High Pressure Liquid Chromatography (HPLC) 58

2.10 Gas Chromatography - Mass Spectrometry (GC-MS) 63

2.11 References 68

2.1 Transmission Electron Microscopy (TEM)

Transmission electron microscopy (TEM) is an imaging technique using a beam of accelerated electrons instead of light to picture a specimen. This gives the advantage of a much higher spatial resolution (x 10^5 that of visible light) down to near atomic scale of about 0.1 nm. Together with the different imaging modes possible, it makes TEM a major analytical technique in today's physics, chemistry and biology.[1,2]

The maximum resolution d which can be obtained by a microscope is limited by the wavelength λ and the numerical aperture NA, where n is the refractive index of the medium the lens is working in and α is the maximum half-angle of the cone of light that can enter the lens (Equation 2.1).[1]

$$d = \frac{\lambda}{2n \sin \alpha} = \frac{\lambda}{2NA} \qquad (Equation\ 2.1)$$

The wavelength of electrons is related to their kinetic energy as given by the de Broglie equation. Further applying a relativistic correction factor, since the electrons used in TEM approach the speed of light, the following equation for the electron wavelength λ_e is obtained, where h is Planck's constant, p is momentum, m_0 is the electron rest mass, E is the accelerated electron energy and c is the speed of light (Equation 2.2).[3]

$$\lambda_e = \frac{h}{p} = \frac{h}{\sqrt{2m_0E\left(1 + \frac{E}{2m_0c^2}\right)}} \qquad (Equation\ 2.2)$$

In TEM the electrons are usually generated by an electron gun where a high voltage (100-300 kV) is applied to a filament resulting in the emission of electrons, which are then accelerated by applying an electric potential. The instrument is operated at high vacuum (at least 10^{-4} Pa) in

order to allow for the application of a high acceleration voltage without arc generation and further to minimise electron collision with gas molecules. Focussing of the electron beam is achieved by lenses consisting of electromagnetic fields which direct the electrons. This allows for much more rapid changes in optical configuration than with a light microscope, such as fast magnification and beam shifting/ specimen scanning. Typically TEMs consist of three groups of lenses, further including apertures which are annular metallic plates used for additional beam filtering (Figure 2.1). The condenser lenses are responsible for primary beam directing, the objective lenses focus the beam that goes through the specimen itself, and the projector lenses expand the beam onto the imaging device. The imaging device can consist of a fluorescent screen, photographic film or charge-coupled sensor.[2,3]

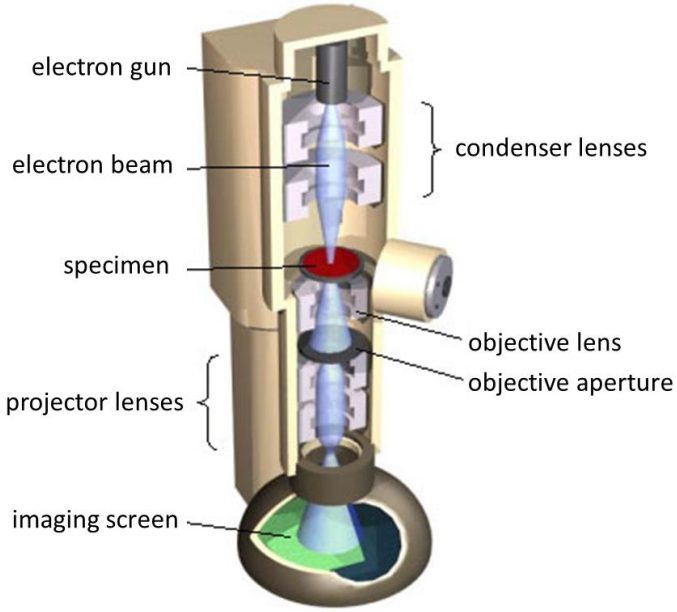


Figure 2.1 – Schematic drawing of a transmission electron microscope (reproduced from reference[4])

TEM specimens are typically less than 100 nm thick sections or suspensions which are prepared on 3 mm diameter holey mesh grids made of copper or gold. For imaging, the grids are placed in the TEM sample stage holder which can be moved and tilted in several directions for optimal

location within the beam. Limitations of TEM include the rather extensive sample preparation with possible structural changes, a small imaging area which may not be representative of the whole sample and sample damaging by the electron beam.[2,3]

Several operational modes are possible in TEM, the most common mode being bright field imaging. In this mode a contrast is created by the varying amounts of electrons penetrating the sample due to differences in sample thickness or electron density. Thin or electron poor parts appear bright, while thick or electron rich part appear dark. Another mode is known as dark field imaging, where the secondary electrons scattered by the sample are detected. Regions of thin sample or out of plane appear dark while regions in scattering plane appear bright, making this mode especially useful for surface analysis. More advanced operating modes include the following: High resolution transmission electron microscopy (HRTEM) which is able to depict crystal structure in more detail using complex phase shift analysis; electron energy loss spectroscopy (EELS) which is used to analyse atomic composition, oxidation and bonding states within the sample; as well as energy dispersive X-ray spectroscopy (EDX) for analysis of atomic composition, which measures x-rays created due to core electron holes.[3,5]

2.2 X-Ray Diffraction (XRD)

X-ray diffraction (XRD) is one of the most basic analysis techniques to determine the atomic structure of a crystalline material. It is based on the principles of elastic scattering of light by atomic planes, also called diffraction planes of a material, which more specifically is caused by the electrons surrounding the atoms. In order to determine structures on an atomic level, short wavelengths in the order of magnitude of atomic plane spacing are required, therefore X-rays are

used. A unique diffraction pattern is obtained for each material due to the different orientations and spacing of atomic planes, making it a powerful tool of identification (Figure 2.2).[6,7]

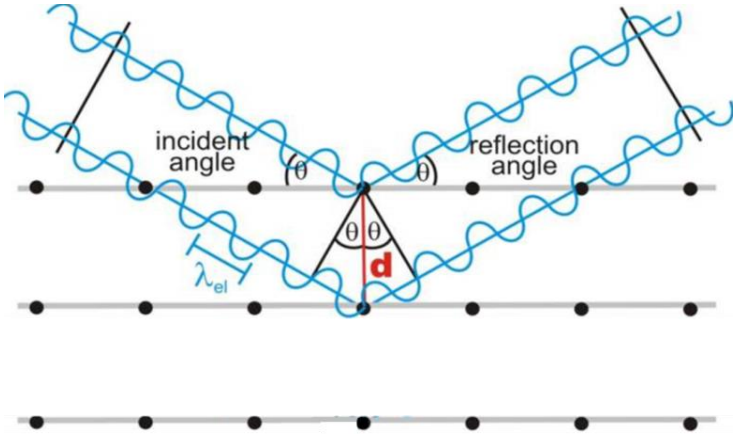


Figure 2.2 – X-ray diffraction by crystallographic planes according to Bragg's law (reproduced from reference[8])

The diffraction pattern is caused by constructive and destructive interference of parallel light waves hitting the atomic planes, resulting in dark and bright spots on the detector. Depending on the atomic spacing d and the angle θ of the incoming light beam, the condition for constructive interference is given by Bragg's law, where n is an integer multiple of the wavelength λ (Equation 2.3).[6]

$$2dsin\theta = n\lambda \qquad (Equation\ 2.3)$$

X-ray diffractometers consist of three main parts: X-ray tube, sample holder and X-ray detector. X-rays are generated in a cathode ray tube, where firstly electrons are generated by thermal emission from a high-voltage filament and are further accelerated towards a metal target by applying an electric potential. When the electrons hit the target with sufficient speed to dislocate inner core electrons, X-ray spectra characteristic of the material are produced. Additional filtering using optical prisms or gratings and collimating is required to produce the required monochromatic and parallel X-rays for diffraction. Cu K_α radiation with λ = 1.5418 Å is the

most commonly used X-ray, produced from a copper target. The geometry of the diffractometer is such that the sample holder rotates at an angle θ in the path of the collimated X-ray beam and the detector arm rotates accordingly to collect the diffracted X-rays. Typical detectors are photographic films or charge-coupled devices. A challenge in the interpretation of interference patterns is the phase problem, meaning that the X-rays hitting the detector are of unknown phase and not all synchronised.[7,9]

The data collected from a diffraction experiment is a two-dimensional or reciprocal representation of the three dimensional real space, requiring the use of Fourier transformation. Each reflection point corresponds to a set of parallel atomic lattice planes. Data interpretation is typically done by comparison to well-known structures and lattice types, which are also used to help overcome the phase problem. Indexing of the reflections is done where the direction of the reciprocal lattice vector is perpendicular to the lattice planes in real space. This information is denoted in so-called Miller indices for each sample structure. Information on space group, unit cell dimensions and atomic positions can be obtained from here further using knowledge of the experimental parameters.[6,10]

Powder XRD, where crystallites are oriented at random, is most widely used as it is fast, non-destructive and sample preparation is a lot easier than for single-crystal diffraction. Powder XRD is useful for any material identification and structural comparison that does not require a detailed structural and atomic position analysis. In a powder XRD pattern signal intensity is plotted versus beam angle and the obtained peaks represent the different lattice planes and their respective spacing. According Miller indices are assigned and in many cases unit cell dimensions can further be obtained from here. The higher the sample crystallinity, the narrower the resulting peaks, while defects and very small particles <100 nm cause peak broadening. The degree of

peak broadening can be useful to calculate the average particle size of nanocrystallites present, where the relation between the crystallite size τ and the peak broadening β (full width at half maximum intensity, FWHM) is given by the Scherrer equation (Equation 2.4).[9,10]

$$\tau = \frac{K\lambda}{\beta\cos(\theta)} \qquad Equation\ 2.4$$

Further, K is a dimensionless shape factor, λ the x-ray wavelength and θ the Bragg angle. It should be noted that the crystallite size obtained from the Scherrer equation provides a lower boundary to the crystallite size - meaning that the actual particle size can be larger, as peak broadening is also caused by other factors than size, such as crystallite defects and strain.[11]

2.3 Raman and Infrared Spectroscopy

Raman spectroscopy is an analysis technique involving the inelastic scattering of light to study rotational and vibrational modes in a molecule or atomic system. It is closely related to Infrared spectroscopy and often the two techniques are used complimentary. In Infrared spectroscopy the frequencies of absorbed light are directly related to according rotational/vibrational modes and are monitored, while Raman spectroscopy uses laser excitation (usually in the range of visible light) of a molecule to a virtual energy state. Most of this energy is released unchanged (Rayleigh scattering), but a small proportion of molecules occupy a different rotational/vibrational mode than beforehand, causing a shift (Stokes or Anti-Stokes) in the energy of emitted light. This difference in energy is equal to the frequency of the according rotational/vibrational mode (Figure 2.3).[12,13]

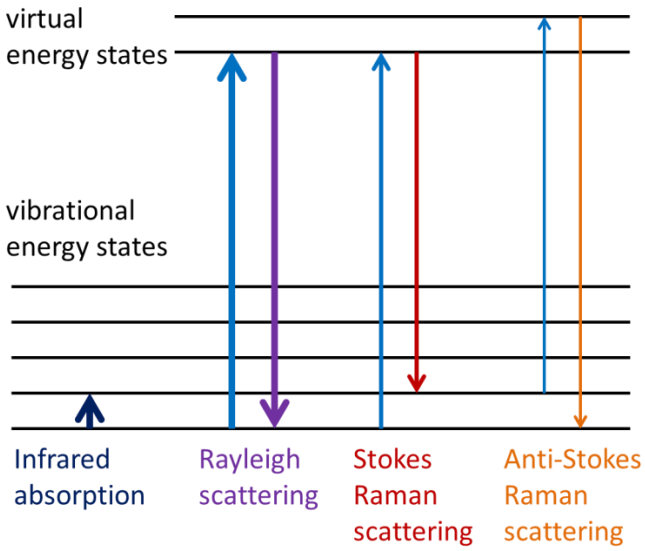


Figure 2.3 – Energy level diagram depicting infrared absorption *versus* Raman scattering (reproduced from references[14,15])

Raman and Infrared spectroscopy provide complimentary information since there are selectivity rules for excitation: Infrared light is only absorbed if there is a change in the molecular dipole moment, while Raman laser excitation occurs when the molecule's polarizability changes. Often the absorption intensities of a specific mode are high in one and low using the other technique, meaning that different absorption spectra are obtained for Infrared and Raman. Symmetrical stretches and vibrations of heavier atoms tend to give strong Raman bands, while modes of low symmetry molecules tend to be both Raman and Infrared active but with differing band intensities.[12,16]

The frequency of a mode basically depends on the nature of the mode (rotation < bending < stretching frequency), the atomic mass and the bond strength. Taking the simplest case of two atoms connected by a bond, this frequency can be approximated by the formula of harmonic oscillation, where ν is the oscillation frequency/frequency of absorbed light, k the bond force constant and μ the reduced mass (Equation 2.5).[13]

$$\nu = \frac{1}{2\pi}\sqrt{\frac{k}{\mu}} \qquad (Equation\ 2.5)$$

$$\text{where } \mu = \frac{m_1 m_2}{m_1 + m_2}$$

When considering more complicated cases of larger molecules or solid atomic systems, these frequency relations become more complicated due to long range interactions, symmetry related vibrations and coupling between neighbouring entities. This can make assignment of bands to certain modes difficult, but at the same time these so-called 'fingerprint' regions are highly characteristic of the material looked at, which is useful for identification purposes. Other bands can clearly be assigned to specific entities, such as functional groups of organic molecules or inorganic surface species, and are therefore useful for structural studies.[13,17]

Raman and Infrared spectrometers each consist of three main parts: a light source, a sampling apparatus and a detector. In Raman spectroscopy, a laser is used to produce the monochromatic light required for accurate determination of the frequency shift. The monochromatic light is focused onto the sample through an optical lens system and the light scattered by the sample is passed through a notch filter. This is done to improve the detection capability as only Stokes and Anti-Stokes wavelengths can pass the filter, while the large amount of elastically scattered Rayleigh light is blocked. A Raman spectrum is obtained as a plot of absorption intensity against wavenumber, where the wavenumbers are calculated from the frequency shifts. In Infrared spectroscopy, a beam of infrared light is passed through the sample and the amount of transmitted light is recorded by a detector. Usually a blank run in comparison to sample transmission is used to obtain a plot of the sample's absorbed light against wavenumber. A measurement can be obtained two ways: Either the required wavelength range is scanned using a monochromator and light transmission for each wavelength is recorded consecutively, or Fourier

transform infrared spectroscopy is used. Here transmission of the whole wavelength range is measured at once using a Fourier transform of the recorded signal.[12,18]

2.4 Temperature Programmed Desorption (TPD)

Temperature programmed desorption (TPD) uses the heat controlled removal of adsorbate species from a surface to measure surface characteristic features. Depending on the experimental set-up, properties such as surface area and geometry, the amount of a surface species or the binding strength of an adsorbate can be determined. The underlying principle of TPD is the variation in adsorbate-substrate binding strength, which is dependent on the properties of both the adsorbate molecule and the substrate/surface material. The weakest attractive interaction formed between two particles is due to so-called dispersion forces, which are temporarily induced dipole interactions. Such weaker binding interactions with dissociation energies of up to 50 kJ mol^{-1} are typically classified as physisorption. Chemisorption occurs when an orbital overlap between the adsorbate molecule and surface atoms leads to the formation of a chemical bond, usually exceeding a binding strength of 50 kJ mol^{-1}. Common adsorbates to probe surfaces are gases such as carbon monoxide and dioxide, hydrogen, oxygen and ammonia.[19–21]

Upon gradually heating a sample, the additional kinetic energy of the particles causes bond dissociation; firstly physisorptive bonds and at higher temperatures chemisorptive bonds are broken by overcoming the required bond activation energies. The relation between rate of desorption r, temperature T and activation energy E_a is described by the Polanyi-Wigner equation (Equation 2.6).[19]

$$r = -\frac{d\sigma}{dt} = v_n(\sigma)\,\sigma^{n(\sigma)}\,e^{-\frac{E_a(\sigma)}{RT}} \qquad (Equation\ 2.6)$$

R is the gas constant and further factors to be taken into account are n the order of desorption, σ the surface coverage and v_n the pre-exponential factor. The order of desorption in the case of pure molecular adsorption is usually 1, while molecular adsorption involving subsequent bond dissociation to atomic species (such as for hydrogen adsorption to metallic surfaces) can give orders of desorption of 2 or larger. The reason why the order of desorption and the activation energy are both dependent on the surface coverage is that molecular adsorption to surfaces can occur in several layers. The first molecular layer interacts strongest with the surface and therefore has the highest bond activation energy, possibly also involving dissociation into atomic species. Second and third layers on the other hand have weaker interactions and their behaviour is typically compared to that of liquids. A TPD spectrum shows signal intensity (amount of desorbed gas) plotted against temperature (using a fixed heating rate), where the rate of desorption at each point is proportional to the signal intensity. Integrating a TPD signal curve gives the amount of total adsorbate while the curve shape and desorption temperature give information about the adsorbate-surface interaction and the activation energy for desorption. There can even be different adsorption modes of one adsorbate molecule to a specific surface, giving rise to more than one signal curve (Figure 2.4). As can be seen from the above rate equation, calculations can get very complex and are usually done using computer programs, where more advanced and accurate modelling is based on Monte Carlo algorithms.[19–22]

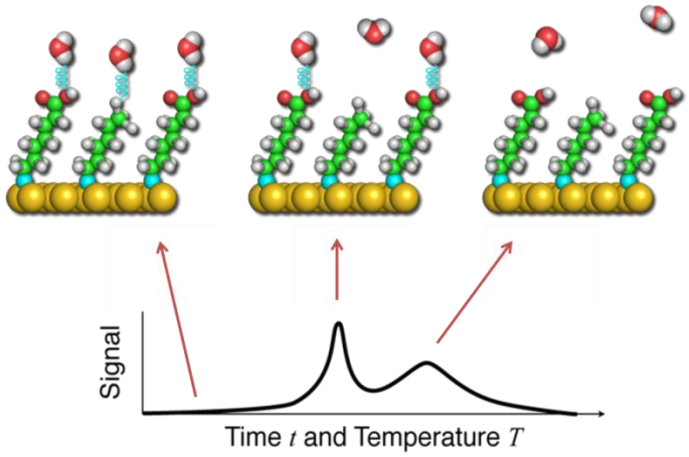


Figure 2.4 – TPD spectrum depicting the different molecular adsorption modes of water to a functionalized metal surface (reproduced from reference[23])

The exact instrumental set-up of a TPD machine depends on the specific measurements performed, but the general features are as follows: There are gas in- and outlets for one or more adsorbate gases and an inert carrier gas, a sample stage or tube holder and a mass spectrometer consisting of an ultra-high vacuum chamber and a mass spectrometry detector. Before a measurement the sample is typically weighed and purged under inert gas such as helium to clean the sample surface and equilibrate the system. Afterwards the sample surface is saturated with adsorbate by passing the according adsorbate gas(es) over the sample. The desorption process itself is performed under the flow of an inert carrier gas and heating the sample at a specific ramp rate, while measuring the amount of desorbed gas(es) by mass spectrometry detection.[20,24]

2.5 Brunauer-Emmett-Teller (BET)

The BET theory describes multilayer gas adsorption processes occurring on a homogeneous sample surface. It is named after its founders Brunauer, Emmett and Teller and is an extension of the Langmuir theory which deals with monolayer adsorption. The BET theory derived equations are a commonly used tool for surface area analysis, based on the following assumptions:[25,26]

1. The gas molecules adsorb onto a homogeneous surface where all surface sites have the same adsorption energy/heat of adsorption.
2. Gas adsorption occurs in multiple layers and the monolayer heat of adsorption E_1 is higher than for the following layers, where the heat of adsorption E_L is considered to equal the heat of liquefaction.
3. The formation of a new layer starts before completion of the previous layer and there are longitudinal but no lateral interactions between the adsorbent molecules.
4. The uppermost molecules are in equilibrium with the gas phase, where the rate of adsorption equals the rate of desorption.
5. At the saturation pressure p_0 the number of layers formed tends to infinity, resulting in the formation of a liquid adsorbent phase surrounding the sample.

A simplified depiction of gas adsorption onto a solid surface according to the BET theory is shown below (Figure 2.5).

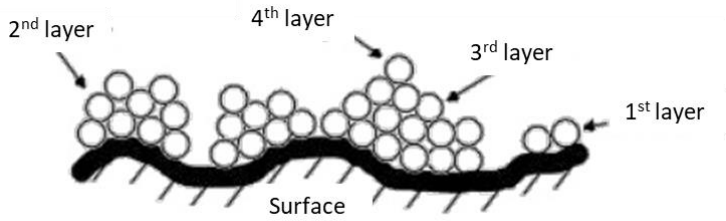


Figure 2.5 – Schematic depiction of multilayer gas adsorption onto solids according to the BET theory (reproduced from reference[27])

To determine the surface area of a sample, the volume of adsorbed gas V_{ads} needs to be measured with respect to relative gas pressure (p/p_0), where p is the applied and p_0 the saturation pressure. Typically an inert gas such as nitrogen is used and the measurement is performed at T equal to its boiling point temperature. From a vessel with liquid nitrogen, nitrogen is introduced into the previously evacuated sample tube step-wise to give according relative pressures, until p_0 (liquefaction) is reached. Afterwards, a desorption measurement is performed according to the adsorption measurement and V_{ads} is plotted against p/p_0 for both processes, giving a so-called adsorption-desorption isotherm. Using the isotherm data and the equations derived from above BET theory, the sample surface area can now be calculated. Firstly, a BET plot of $p/(v(p_0 - p))$ against p/p_0 is done, giving rise to a linear plot in the range of about $0.05 < p/p_0 < 0.35$. From the y-intercept I and the slope A of the line, the monolayer volume v_{mono} of adsorbent can be obtained according to Equation 2.7.[25,28]

$$\frac{p}{v(p_0 - p)} = \frac{C - 1}{v_{mono}C}\frac{p}{p_0} + \frac{1}{v_{mono}C} \qquad Equation\ 2.7$$

$$where \quad C = 1 + \frac{A}{I}$$

$$and \quad v_{mono} = \frac{1}{I + A}$$

From the adsorbent monolayer volume v_{mono} and the sample weight m, the specific surface area S_{BET} of the sample can then be derived (Equation 2.8), where further V is the molar volume of the adsorbent, m is the sample mass, N is Avogadro's number and a is the area occupied by one adsorbent molecule.[25,28]

$$S_{BET} = \frac{v_{mono}\,Na}{Vm} \qquad Equation\ 2.8$$

General information on the nature of a solid (surface area, porosity) can already be obtained from the shape of the measured adsorption-desorption isotherm. Six different types of solid giving rise to according adsorption-desorption isotherms (Figure 2.6) are classified, although in practice many variations and overlapping types are observed.[29,30]

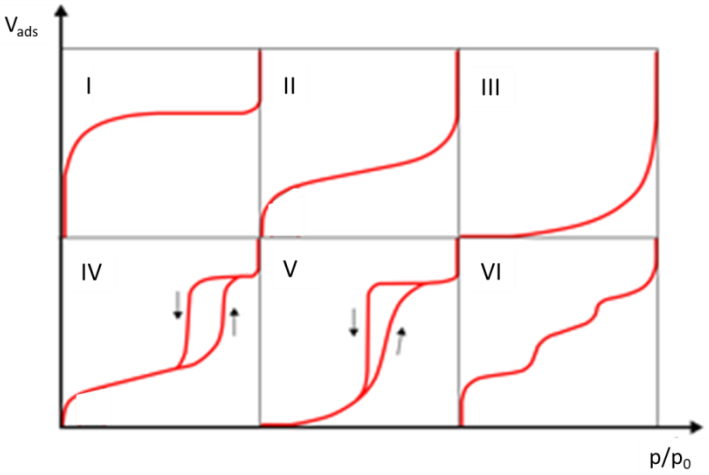


Figure 2.6 – Adsorption-desorption isotherms I to VI obtained for different types of solids (reproduced from reference[31])

Typically, V_{ads} in the low-end pressure region ($p/p_0 < 0.05$) represents monolayer coverage and therefore the higher V_{ads} here, the larger the surface area. In case of porous materials however, the micropore region (0 – 2 nm, $p/p_0 < 0.5$) can sometimes overlap with the monolayer region, typically giving rise to a less sharp slope transition in this region, as observed for type I: highly microporous or gel-like solids. Type II and III represent non-porous or macroporous solids where III has a low surface area (low initial values for V_{ads} and low slope for $0.05 < p/p_0 < 0.5$) or alternatively very weak surface-adsorbent interaction. Type IV and V represent mesoporous solids displaying a hysteresis loop in the mesopore region (2 – 50 nm, $p/p_0 > 0.5$) due to capillary forces acting within the pores. In terms of surface area, type IV is similar to type II and type V similar to type III, with differences occurring only in the high pressure/mesopore region. Type VI is hardly observed in practice; it shows distinguishable adsorption of first, second and third layer as for highly uniform, non-porous surfaces with strong adsorption. For all types, V_{ads} tends

towards infinity at pressures close to p_0 (liquefaction), and macroporous solids are typically not distinguishable from non-porous materials due to the weak additional interactions resulting from the large pore width.[29,30]

2.6 X-Ray Photoelectron Spectroscopy (XPS)

X-ray photoelectron spectroscopy is a surface analysis technique commonly used to determine the elemental composition of a sample, as well as the oxidation state and local environment of the chemical species present. X-rays of a fixed energy are directed onto the sample surface to remove electrons from the atomic core shells, based on the photoelectric effect. The kinetic energy E_{kin} of the emitted electrons is measured and given by the energy difference between the incident x-ray energy E_{photon} and the binding energy E_{bind}. The x-ray energy is further proportional to its frequency ν, and h is the Planck constant (Equation 2.9).[32,33]

$$E_{kin} = E_{photon} - E_{bind} \qquad (Equation\ 2.9)$$

$$\text{where } E_{photon} = h\nu$$

The main contribution to E_{bind} is the core binding energy of the electron to its atomic core, in solids a small additional contribution comes from stabilisation inside the material's conduction band, also called the work function. A plot of signal intensity against binding energy shows atom specific signal bands as a result of the electrons occupying discrete energy levels within each atom (Figure 2.7). A typical binding energy spectrum ranges from about 0 to 1200 eV and most signals can accordingly be allocated to a specific core shell/orbital of a specific element. There are some exemptions where a signal arises due to secondary electron emission, as is the case with Auger electrons from core-hole formation or electrons generated from plasmon resonance, while satellite peaks correspond to electron emission from non-monochromatic x-rays.[32,34,35]

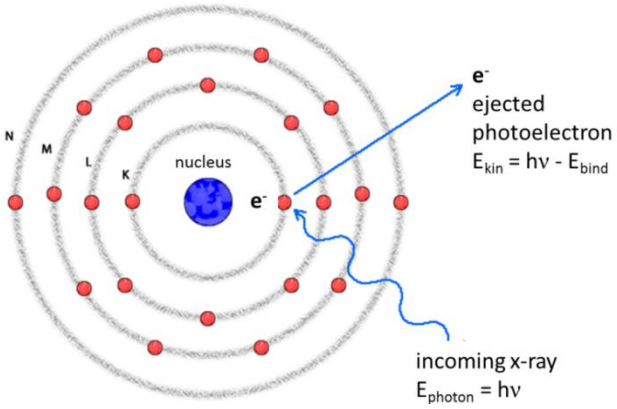


Figure 2.7 – Schematic depiction of photoelectron emission from atomic species due to x-ray absorption (reproduced from reference[36])

After identification of the element-specific signals, quantitative analysis is possible from signal area integration, however it is not straightforward and corrections have to be made. One issue is the non-trivial XPS background. Inelastic scattering and kinetic energy loss of the emitted electrons while travelling through the surface lead to these electrons being 'falsely' interpreted as higher binding energy electrons, causing an uneven background signal. Inelastic scattering is also the reason why XPS can only analyse surfaces up to a depth of about 10 nm. Quantitative analysis is usually done with the help of tabulated relative sensitivity factors which are available for various elements and orbitals, and take into account correction factors such as amount of electrons, lifetime of the excited state and background deduction.[37]

Taking a closer look at individual XPS signals shows that s orbitals give rise to single peaks, while p and d orbitals give rise to doublets of specific intensity ratios. These doublets represent small energy splittings due to spin-orbit coupling. During the process of removing a core-shell electron, an excited atomic state is formed which consists of an unpaired electron of spin $s = \pm ½$ interacting with its orbital's angular magnetic moment of $L = 0, \pm1, \pm2$, etc. Depending on the orientation of the interaction which can be expressed in terms of the different values of s and L,

different energy states are formed. Some of these energy states are degenerate, which explains why p and d orbitals only give rise to a doublet of energy splitting. The degeneracies are reflected by the relative intensities of the two peaks in the doublet.[32,34]

Oxidation and chemical state analysis is done by studying the XPS signals of a particular atomic species in detail. The oxidation state can be determined from small variations in the binding energy, where a peak shift to higher binding energies reflects a higher oxidation state, resulting from a stronger electrostatic interaction upon removal of a core electron. It should be noted that such peak shifts also occur for non-conducting samples due to surface charging during XPS measurements. A flood gun providing low energy electrons can be used to partially balance the charge; further a general correction of the peak shift is required during data analysis, usually done with reference to the C 1s peak, before analysing individual peak shifts. Extending the identification to types of neighbouring atoms, bond lengths and coordination numbers is more difficult as the inferred energy differences tend to be very small. Sometimes comparative rather than individual studies can help to visualize small differences in peak shape and position, and thereby give structural insights.[37]

An XPS analysis system consists of three main parts: an x-ray source, an ultra-high vacuum chamber and an electron energy analyser. Monochromatic x-rays are typically generated by bombarding an aluminium or magnesium foil with high-voltage electrons to yield x-rays of a specific wavelength, such as 8.3386 Å for Al K_{α}. The produced x-rays are focused onto the sample inside an ultra-high vacuum chamber to minimise energy loss of the emitted electrons due to particle collisions. The emitted electrons are then separated inside an electron energy analyser according to their kinetic energies by applying an external electric field, before being measured by a detector.[34,38]

2.7 X-Ray Absorption Fine Structure (XAFS)

X-ray absorption fine structure analysis is based on the absorption of x-rays by atoms in a material due to the excitation of core-shell electrons. As discussed in the previous XPS section, there are fixed energy level transitions for each element and core-shell, resulting in discrete absorption signal spectra. While XPS is concerned with overall binding energies of electrons ejected from the material, XAFS focuses on the analysis of signal fine structure from electron excitation into the atomic neighbourhood/conduction band of the material. While XPS uses x-rays of a fixed wavelength, XAFS samples are scanned over a range of x-ray wavelengths to detect electronic transitions from a specific core-shell (usually K or L) to a range of available states in the atomic neighbourhood. These states arise from scattering interactions between the excited electron and the surrounding atoms (Figure 2.8). As the observed energy and intensity differences are very small compared to the total energy defined by the core-shell binding energy, a synchrotron radiation source is required to produce high intensity x-rays over a narrow range of well-defined energies.[39–41]

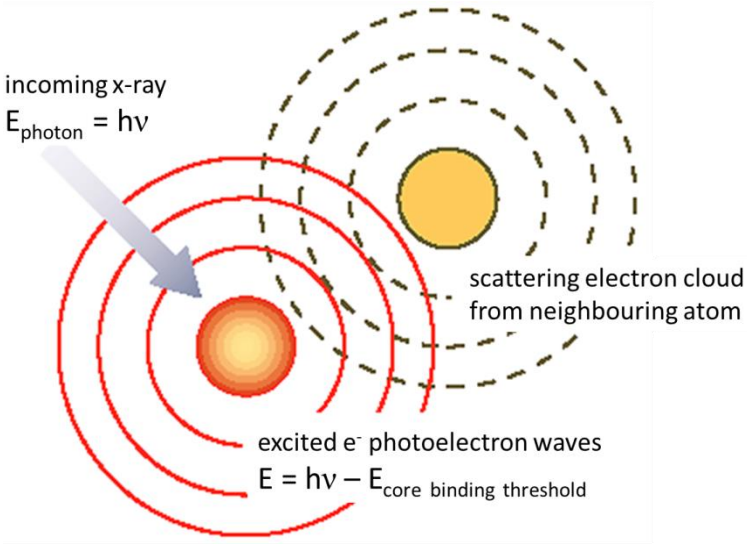


Figure 2.8 – Schematic depiction of x-ray absorption fine structure (XAFS) due to local scattering of excited photoelectrons (reproduced from reference[42])

A XAFS spectrum for a specific element's core-shell is a plot of normalized absorption intensity μ(E) against absorption energy E, expressed in electron volt rather than x-ray frequency as it refers to the electronic transition (Figure 2.9). There are three main regions to a spectrum: the absorption edge, the x-ray absorption near edge structure (XANES) and further the extended x-ray absorption fine structure (EXAFS). The absorption edge is the large increase in absorption intensity due to the first allowed energy transitions from the core-shell to the atom's unoccupied outer shells, which in solids refers to states around the Fermi level. A shift observed in the absorption edge energy represents a change in oxidation state for that element, due to a variation in strength of the Coulombic interaction. The XANES region is dominated by multiple scattering interactions between the electron and several of its neighbours which makes structural interpretation challenging, modelling atomic cluster size is a key step. Usually structural analysis starts with the EXAFS region which is easier to model due to being dominated by single scattering interactions with individual neighbouring atoms at different radial distances.[41,43]

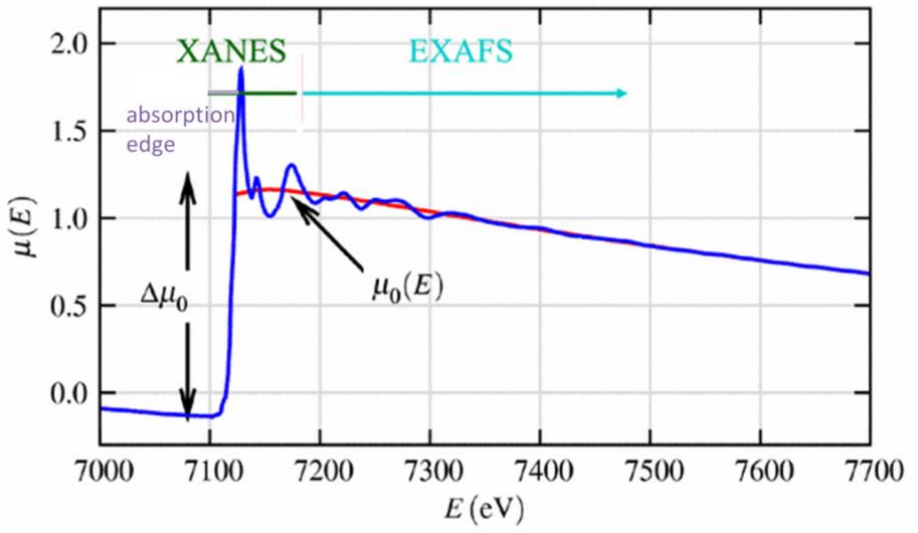


Figure 2.9 – Exemplary XAFS spectrum (blue) with marking of the relevant regions (absorption edge, XANES and EXAFS), the threshold absorption intensity $\Delta\mu_0$ and the background function μ_0(E) (reproduced from reference[43])

As mentioned earlier XAFS measurements are quite extensive as they require fine-tuned x-rays and samples are usually analysed at synchrotron radiation facilities. The tuned x-rays are passed through the sample and the amount of transmitted photons I is compared to the initial beam intensity I_0. The absorption intensity is proportional to $\log(I_0/I)$ (Beer's law) and for XAFS analysis the absorption coefficient μ(E) is further obtained by normalizing the absorption intensity, which corrects for different factors such as sample thickness, element concentration and detector dead time (Equation 2.10).[43]

$$\mu(E) = log\frac{I_0}{I} \qquad (Equation\ 2.10)$$

For EXAFS analysis, the fine structure wave function χ(E) is obtained by subtracting a smooth background function $\mu_0(E)$ - which relates to the absorption of an isolated/averaged surroundings atom - from μ(E), and further normalizing for the threshold absorption intensity $\Delta\mu_0(E)$ (Figure 2.9 and Equation 2.11).[39,43]

$$\chi(E) = \frac{\mu(E) - \mu_0(E)}{\Delta\mu_0(E)} \qquad (Equation\ 2.11)$$

The fine structure wave function χ(E) is then re-scaled to χ(k) which refers to the wavenumber k of the excited electron, where further m is the electron mass, E_0 the threshold/absorption edge energy and ħ the reduced Planck constant (Equation 2.12).[39,43]

$$k = \sqrt{\frac{2m(E - E_0)}{\hbar^2}} \qquad (Equation\ 2.12)$$

The EXAFS function χ(k) is usually multiplied by k^2 or k^3 to emphasize the oscillations before further analysis. The amplitude and shift of the oscillations described by χ(k) contains the wave-interference patterns resulting from electron scattering, which in turn can be related to the distance and number of neighbouring atoms. Data fitting and interpretation is usually done using

data fitting programs such as FEFF, EXCURVE or GNXAS. These programs work with both *ab initio* methods to calculate the fitting parameters from the experimental absorption spectrum and model compounds of known structure for further calibration. Fourier transform is used to transfer $\chi(k)$ information to the $\chi(R)$ regime which is better to visualize and work with, as $\chi(R)$ is a plot of scattering amplitude against radial distance from the atom studied. Thereby the distance to neighbouring atoms can be determined with high accuracy (0.01-0.02Å), while in many cases coordination numbers can only be determined to ±1. Further it should be noted that the obtained data is an average over all atoms and local environments of the atomic species looked at. Despite these limitations, EXAFS is an important tool for structural analysis of non-crystalline systems, particularly regarding bond length determination, where traditional methods suffer.[43–45]

2.8 Solid State Nuclear Magnetic Resonance (ssNMR)

Solid state nuclear magnetic resonance is a specific type of NMR whose spectra analysis is more complex than that for liquids, as a result of anisotropic (orientation-dependent) interactions. NMR in general is used for structural analysis based on short-range atomic interactions, giving insights into molecular structure and atomic environment. It is based on the magnetic properties of atomic nuclei which vary with the type of atom/nucleus and can be described by their magnetic susceptibility or gyromagnetic ratio. Upon exposure to an external magnetic field, any nuclei with net spinning charge(s) can either spin-align or spin-oppose the external magnetic field, also referred to as spin up or down, which leads to a splitting into two energy states (Figure 2.10). The resulting energy gap ΔE (radiofrequency range) is proportional to the nuclei's gyromagnetic ratio γ and the external magnetic field B_0. Using radiation of the matching frequency v_0 (Larmor frequency), more nuclei from the equilibrium state (spin populations about

1:1 in equilibrium) can be excited/spin-flipped to oppose the external magnetic field (Equation 2.13).[46–48]

$$\Delta E = h\nu_0 = h\frac{\omega_0}{2\pi} \qquad (Equation\ 2.13)$$

$$\text{where } \omega_0 = \gamma B_0$$

Upon relaxation, the remitted radiation in form of magnetic oscillations is measured with respect to time and Fourier transformed to obtain a NMR spectrum. The spectrum reflects the different energy gaps/frequencies and thereby the different nuclei and their chemical environment.[49]

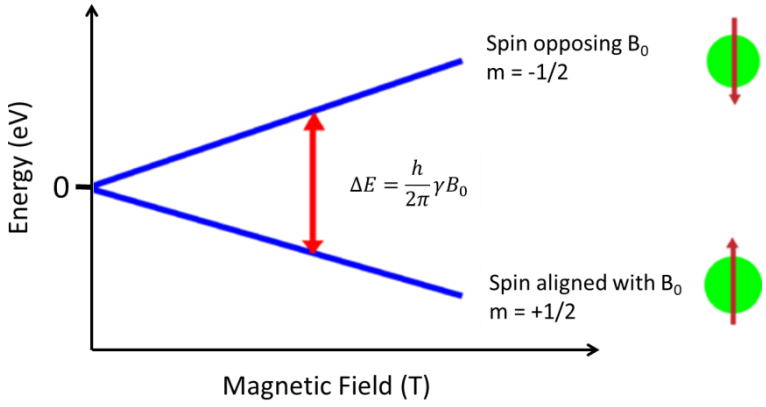


Figure 2.10 – Energy level splitting for spin = ½ nuclei in an external magnetic field (reproduced from reference[47])

As relaxation times and optimum experimental conditions vary significantly amongst different atomic types, only one type of atomic nuclei (e.g. ^{1}H, ^{13}C, ^{31}P or ^{93}Nb) is analysed per session. Some sessions are quick (^{1}H nuclei) while others take hours and several pulse-relaxation sequences to complete with a decent signal-to-noise ratio, influenced by several factors such as the relaxation time (dependent on the Larmor frequency), the sample state (liquid or solid) and concentration, the nuclear abundance and nuclear environment.[50]

As discussed earlier, the main energy gap relating to a specific frequency is that arising from the gyromagnetic ratio and the external magnetic field, which would yield only one signal per nuclei type (e.g. ^{1}H nuclei) in a measurement. No significant information would be obtained from here; it is the further energy splitting which is of importance for structural analysis. The largest frequency differences arise from the chemical shift (Figure 2.11): Depending on the type of bonding and atoms attached, the local magnetic field strength exerted on the nuclei varies, with electron-donating groups shielding and electron-withdrawing groups deshielding the nuclei, resulting in different energy gaps and therefore different chemical shifts/frequencies. The shielding effect (upfield shift) of a larger electron density arises from an induced electronic current due to the external magnetic field, which creates a small opposing magnetic field, which in turn leads to a weakened local magnetic field acting on the nucleus. There are other factors leading to further energy splitting of the chemical shift signal. Such are nuclei with spin > ½ (more than one spinning charge), where the magnetic field exerted on the spin to be flipped depends on the orientation of the remaining spins (up or down) and the signal splitting is determined by the possible spin combinations. Similarly, the spins of neighbouring nuclei interact, called dipolar coupling (through space) or J coupling (through bonds, Figure 2.11). However the interaction strength and therefore the coupling/signal splitting decreases rapidly with distance, which is why NMR is a short-range structural analysis method.[48,51]

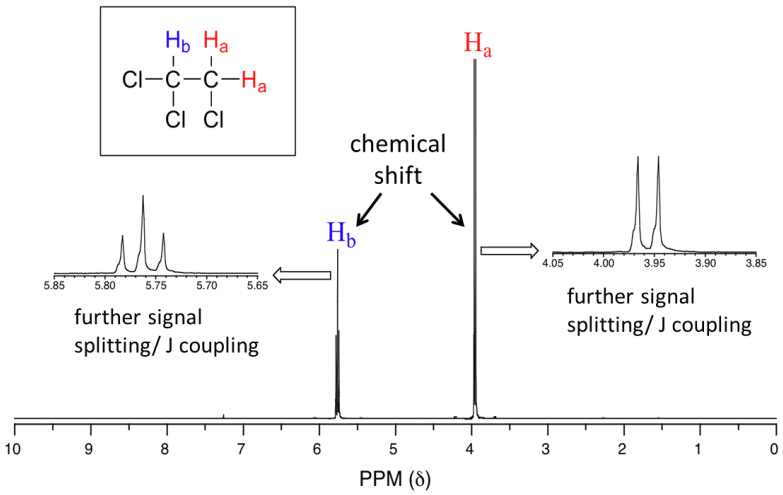


Figure 2.11 – Exemplary ^{1}H NMR spectrum depicting signal splitting due to chemical shift variation and J coupling (reproduced from reference[52])

Coming back to solid state *versus* solution NMR, the following differences are important: In solution, particle movement is rapid compared to the NMR time scale, which averages the directional dependence, yielding an isotropic signal. In solids on the other hand, the directional component (anisotropic) leads to additional signal splitting, which is especially apparent in the case of asymmetric molecules and units. Considering the chemical shift, for an aspherical distribution of surrounding electrons/bonds the orientation within the external magnetic field has a significant effect on the magnitude of the created opposing magnetic field. This leads to further splitting of the chemical shift signal in solid state compared to solution NMR, especially for powders where the orientation of units is random. Further signal splitting also applies for the dipolar and J coupling, where the angular orientation of neighbouring nuclei towards the spin-flip nucleus determines the magnitude of their magnetic field effect, as well as for quadrupolar nuclei (spin > ½) which have a non-spherical nuclear charge distribution interacting with the surrounding electron cloud. All these additional splitting factors often lead to significant broadening of ssNMR spectra with low signal-to-noise ratios. In terms of time and experimental effort this is a disadvantage, while the additional information on structural orientation can be of

advantage. Techniques to improve the resolution of ssNMR spectra have been developed quite recently, some of which will be discussed in section 2.7.1 and 2.7.2.[46,53]

The NMR spectrum of a sample is a plot of signal intensity against chemical shift which is the normalized frequency (radiofrequency divided by magnetic field frequency) in ppm (Figure 2.11). The expression in ppm (parts per million) is useful because the frequency variations created by the different chemical environments of a nuclei type are very small compared to the external magnetic field strength.[50]

2.8.1 Trimethylphosphine (TMP) ^{31}P ssNMR

Trimethylphosphine (TMP) is an organic base useful to probe the surface acidity of solids. This is due to the variations in interaction strength between adsorbed TMP and different acid sites, including Brønsted *versus* Lewis acids as well as varying strengths amongst each acid type. The bond between acid site and TMP is formed via the lone electron pair of phosphorus (P) and the according proton H^+ (Brønsted) or exposed positively charged metal centre M^{n+} (Lewis). Due to the variations in electron-withdrawing character amongst the acid sites, different chemical shifts are obtained from ssNMR of the ^{31}P nuclei. In terms of signal-to-noise ratio, the high isotopic abundance (100%), relatively high gyromagnetic ratio and spin = ½ (no quadrupolar broadening) are advantageous for ^{31}P ssNMR. High external magnetic field strengths and a large number of scans (800) are used to increase the resolution and enable accurate peak area analysis for quantification of the respective acid sites. To average out the orientation dependent interactions and thereby reduce the chemical shift signal splitting, magic angle spinning (MAS) is used. In MAS, the sample is rotated at high frequency at 54.74° with respect to the external magnetic field. To further prevent dipolar and J coupling of the ^{31}P nuclei to their main signal splitting

neighbours, the ^{1}H nuclei from trimethyl groups and protons, proton decoupling is applied. Proton decoupling uses high pulses of the according ^{1}H radio frequencies during data acquisition, which induces rapid spin flipping of the ^{1}H nuclei and thereby averages out their interfering magnetic fields.[46,54,55]

2.8.2 ^{93}Nb ssNMR

^{93}Nb ssNMR can be used for structural analysis of niobium containing solids such as niobium oxides. In terms of signal-to-noise ratio, the high isotopic abundance (100%) and relatively high gyromagnetic ratio are advantageous for ^{93}Nb ssNMR. So is the nuclear spin of 9/2 regarding total signal intensity, however the significant quadrupolar splitting leads to undesirable line broadening. High external magnetic field strengths (14.1 T) and a large number of scans (8061) are used to reduce relaxation times and increase resolution. In niobium oxides where Nb-O-Nb bonds dominate, no significant dipolar or J coupling is observed due to the low abundance (0.038%) of ^{17}O nuclei and the relatively large distances between neighbouring ^{93}Nb nuclei. However the structural comparison between niobium oxides consisting mainly of NbO_6 and some NbO_5 and NbO_4 units still proves difficult. Magic angle spinning (MAS) could be used to average out the chemical shift orientation dependence, but the simultaneous averaging of the quadrupolar orientation dependence requires non-trivial additional spinning modes. Overall, the large quadrupolar splitting and the small chemical shift differences between NbO_6, NbO_5 and NbO_4 units lead to very broad ssNMR line shapes. In some cases it is possible to differentiate between NbO_6 units of varying bond lengths/chemical shift, whose high symmetry causes orientation effects to be low. NbO_5 and NbO_4 units are of lesser symmetry and their broad signals tend to underlie these of NbO_6. Further the presence of lower oxidation state Nb^{4+} besides Nb^{5+} species can lead to significant paramagnetic broadening due to an unpaired

electron. Paramagnetic signal shifting is caused by the increase in local magnetic field strength nearby high-spin unpaired electrons, as well as the fast electron relaxation times.[56–59]

2.9 High Pressure Liquid Chromatography (HPLC)

High pressure liquid chromatography is a widely used technique for compound separation, identification and quantification. The separation procedure is based on compound nature, leading to variations in interaction strength between the compound and the mobile *versus* the stationary phase. The mobile phase is a polar or non-polar solvent which is pumped through the stationary phase, also called chromatography column, using high pressures (50-350 bar). The stationary phase consists of a porous filling of sorbent particles (beads) packed into a long column tube of dimensions typically ranging from 2 to 10 mm diameter and 50 to 300 mm length, whose polarity characteristics differ from these of the solvent. When a compound mixture is injected into the mobile phase and subsequently pumped through the column, some compounds preferably remain in the mobile phase and reach the end of the column faster, while others interact stronger with the stationary phase and are retained longer on the column. This results in different retention times for different compounds. Under appropriate measurement conditions full separation of the compounds in a mixture is achieved, with each compound giving rise to a clear and separate detector signal when monitoring the mobile phase effluent over time.[60–62]

In order to optimise compound separation, several factors need to be considered. For example, very strong interactions between compound and stationary phase can be undesirable due to very long retention times which are time consuming and further lead to signal broadening. On the other hand, very short retention times can be inefficient for mixtures containing many compounds, as poor separation with overlapping peak signals is likely an issue. There are several

instrumental possibilities to influence compound retention time. Such is changing the pump pressure, where an increase in pressure and mobile phase flow rate leads to shorter retention times. Similarly increasing the column temperature causes an increased flow rate (at constant pressure) and shorter retention times due to a decrease in viscosity and column backpressure. It is further possible to use a so-called gradient elution, where the pressure, temperature or mobile-phase composition are changed throughout the measurement, which is especially useful as it can target the retention time of certain compounds rather than affecting all.[60,61]

Before adjusting retention times with the help of the discussed experimental parameters, it is important to consider the choice of column. Many different types of columns exist for use with different mobile phases, each designed to meet the separation requirements for a specific compound class or type of mixture. Just to discuss a few examples, there are normal phase and reversed phase chromatography, displacement, size exclusion and ion exclusion chromatography (Figure 2.12).[61,63,64]

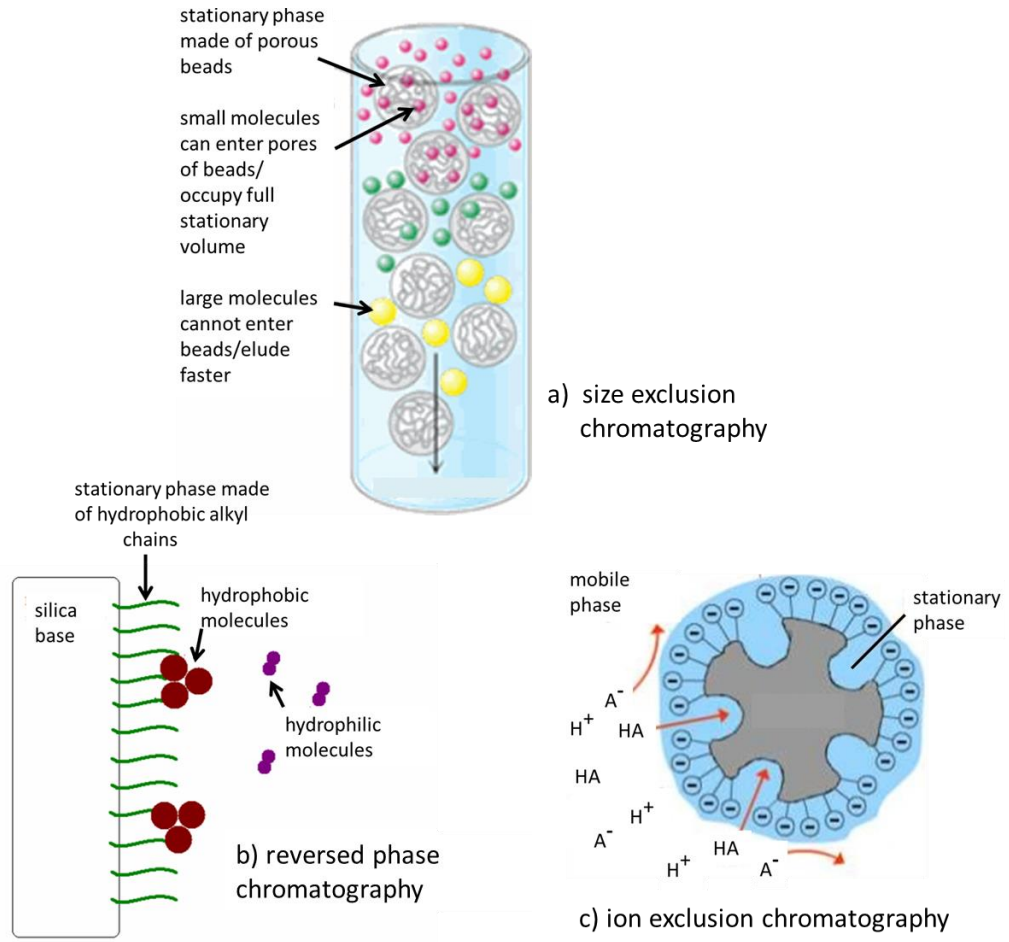


Figure 2.12 – Schematic depiction of different column chromatography techniques a) size exclusion chromatography[65], b) reversed phase chromatography[66], c) ion exclusion chromatography[67] (all reproduced from respective references[65–67])

In normal phase chromatography a polar stationary phase made of silica is used in combination with a non-polar mobile phase, making it useful mainly for analysis of low-polarity compounds. Reversed phase chromatography is more common and uses a non-polar stationary phase made of silica decorated with long hydrophobic alkyl chains and a polar, typically aqueous mobile phase. It is useful for the separation of water-soluble compounds with varying degrees of polarity, where less polar compounds are retained longer in the stationary phase. Displacement chromatography is substance specific and typically used in the separation of biomolecules. It is based on the high-affinity binding of a compound to stationary sites, which retain the compound until a substance of higher affinity is added for replacement. Size exclusion chromatography

separates compounds according to size, where small molecules are retained longer as they can enter pores unavailable to larger molecules. Ion exclusion chromatography is useful for the separation of weak acids or bases according to their dissociation strength in an aqueous mobile phase. The ionic outer surface of the stationary phase rejects dissociated acid or base molecules and thereby prevents them from passing through to the inner hydrophobic surface where non-dissociated acid or base molecules are retained.[61,63,64]

As can be seen, compound retention times are determined by a variety of factors influencing the partitioning of a compound between mobile and stationary phase. There are column-mobile phase specific features such as hydrophilic and -phobic as well as ionic, dipole-dipole and dispersion interactions, next to steric effects and stationary phase volume. Further instrumental factors such as pressure and temperature are important. This makes the calculation of retention times non-trivial, meaning that for compound identification and quantification, previous calibration of the HPLC system in use is required. Running a measurement with a known pure compound gives its retention time, while injecting different concentrations of the compound changes the signal intensity/peak area. Once calibrated with all compounds of interest, the HPLC system can be used to identify and quantify these compounds in unknown mixtures.[60,61]

High pressure liquid chromatography is much more efficient for compound separation than liquid chromatography (only using gravitational force) as longer columns can be used giving narrower and better separated peaks. An HPLC instrument operates on the following basis: The mobile phase is pumped through the system at high pressure, firstly passing the sample injection valve for sample take-up. This is followed by a degasser to remove any air trapped in the mobile phase, which can cause pressure and retention time fluctuations as well as an unstable detector baseline. Afterwards the mobile phase containing the sample is passed through the column,

followed by the detector, which is typically UV-vis absorption or refractive index based and produces an according compound signal.[60,63]

The retention time t_R of a compound is referred to as the time between the injection and detection. A common way to compare the retention times of different compounds on a column is using the retention factor k, which is defined as the adjusted retention time t'_R (compound retention t_R minus mobile phase retention t_M) divided by the mobile phase retention time t_M (Equation 2.14).[61,68]

$$k = \frac{t'_R}{t_M} = \frac{t_R - t_M}{t_M} = \frac{[C_S]}{[C_M]} \qquad (Equation\ 2.14)$$

$$K = \frac{[C_S]_0}{[C_M]_0} = \frac{[C_S]}{[C_M]} \frac{V_M}{V_S}$$

The mobile phase retention t_M refers to the time it takes an un-retained compound to travel through the void volume of the system without stationary phase interaction. This means the retention factor gives the ratio of time a compound spends in the stationary compared to the mobile phase, which can also be expressed as the concentration of the compound in the stationary compared to the mobile phase, $[C_S]/[C_M]$. After correcting for the phase volumes V_S and V_M, the partition equilibrium constant K can be obtained from here, which is useful for compound comparison as it is independent of column length and phase volumes.[61,68]

2.10 Gas Chromatography - Mass Spectrometry (GC-MS)

Gas Chromatography coupled to Mass Spectrometry (GC-MS) is a very useful analysis technique as both compound separation (GC) and structural identification (MS) are possible within the same measurement. A measurement run consists of injecting a liquid or gaseous sample into the gas chromatograph inlet, where it is vaporized if necessary before take-up into the carrier gas stream. The inert carrier gas transports the sample through the chromatography column with the help of a pressure gradient and the sample components are separated according to their column affinity, which is mainly boiling point dependent. After passing the column, the gas stream containing the separated sample components is led into the mass spectrometer. Here each sample component is ionized, typically under harsh conditions involving the break-down into several ionic species. These species are further separated according to their mass/charge ratio using electric and magnetic fields under high vacuum conditions. The resulting mass spectrum contains structural information about the investigated compound and typically an internal compound library is used to identify the compound name/structure. Further the amount of each compound is detected (in form of ionic species concentration) and converted into a signal peak at the according retention time, which is the time passed between compound injection and detection.[69,70]

Gas chromatography (GC) has many similarities to the previously discussed high pressure liquid chromatography (HPLC) and equivalent scientific terms are used. The column contains the stationary phase which adsorbs and retains the compound depending on the interaction strength, whereas the mobile phase carries the compound through the column. The column in GC can be either capillary or packed. In capillary columns the walls are coated with the stationary phase, which consists either of porous fused silica or fused silica coated in a thin layer of liquid, with column dimensions of 0.1 – 0.5 mm internal diameter and 10 – 100 m length (Figure 2.13).

Packed columns have dimensions of 1 – 4 mm internal diameter and 1 – 10 m length and are packed with sorbent particles made of steel or glass. Overall capillary columns are used more frequently as they provide better compound separation with narrower peak signals.[69,71]

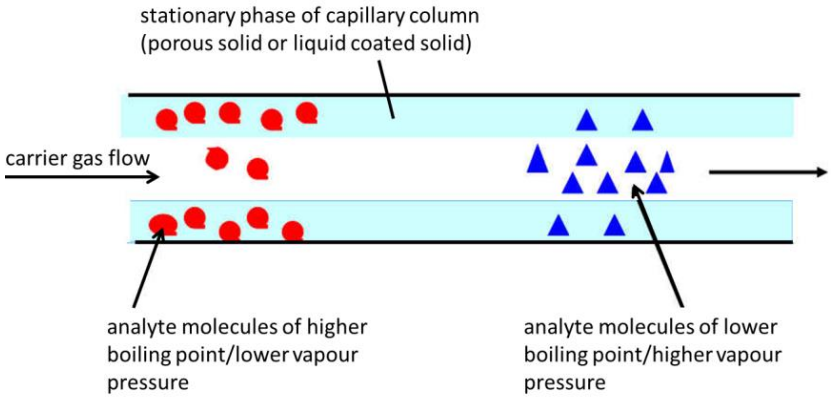


Figure 2.13 – Schematic depiction of a gas chromatography column with analyte separation (reproduced from reference[72])

The mobile phase in GC consists of an inert carrier gas such as helium, nitrogen, hydrogen or argon, which hardly interact with the sample apart from flow rate transport. One of the major differences between HPLC and GC is the design of the mobile and stationary phase, which in HPLC is compound specific and involves a variety of interactive forces. In GC the interactive forces of the compound and mobile phase are minimal and kept to more general dispersive forces for the stationary phase. These properties make GC retention times mostly boiling point dependent, miming the compound's liquid to gas transition inside the column. This means sample components with a low boiling point/high vapour pressure elude faster than those with a high boiling point/low vapour pressure (Figure 2.13). At constant column temperature, the ratio of adjusted retention time t'_R to mobile phase retention t_M is equal to the ratio of compound concentration in the stationary phase [C_S] to the mobile phase [C_M] (compare HPLC section and Equation 2.15), which in turn is inversely related to the compound vapour pressure.[70,73]

$$k = \frac{t'_R}{t_M} = \frac{t_R - t_M}{t_M} = \frac{[C_S]}{[C_M]} \qquad (Equation\ 2.15)$$

When analysing samples with structurally different components and a larger range of boiling point temperatures, the use of a temperature gradient is common. This significantly improves the resolution compared to an isothermal measurement, where choosing a low column temperature leads to very long retention times and diffusion related signal broadening for the high boiling components, while a high column temperature leads to signal overlapping for the low boiling point components. Besides the column temperature, the carrier gas pressure/flow rate can be adjusted, where higher flow rates reduce compound retention times.[69,71]

The carrier gas stream containing the sample eluent is directly analysed by the mass spectrometer (MS) after leaving the GC column (Figure 2.14). As the manipulation of ionic species from their formation to their mass/charge separation requires ultra-high vacuum conditions (10^{-5} to 10^{-8} torr), only a small fraction of the eluent gas stream is allowed to pass through into the mass spectrometer after complete vaporization at high temperatures. The first chamber is that for ionic species formation, which is typically done by electron impact ionization. The sample is bombarded with accelerated electrons produced from a high voltage filament and in the collision process electrons are removed from the sample molecules, sometimes under covalent bond fragmentation. The resulting cationic species are accelerated towards slits by an electric field, while anionic species are repelled and discarded together with neutral species under the applied vacuum. The cations passing through the slits reach the mass analyser, where they are accelerated and deflected under the application of electric and magnetic fields, resulting in different trajectories which are determined by the species' mass/charge ratio. A general description of this directional acceleration is reached by combining the force laws of Newton and Lorentz (Equation 2.16), where F is the force acting on the cation, a is the cation

acceleration, m its mass, Q its charge, v its velocity, E is the applied electric field and B the applied magnetic field.[70,74,75]

$$F = ma = Q(E + v \times B) \qquad (Equation\ 2.16)$$

$$\left(\frac{m}{Q}\right) a = E + v \times B$$

A typical mass analyser is a quadrupole mass analyser, where electric and magnetic fields are created between four parallel rods using radiofrequency voltages (Figure 2.14). Depending on the applied voltages, only one mass/charge species is stabilized and passes between the rods through to the detector, while the remaining species are destabilized and collide with the rods. The rapid switching between voltages allows for scanning of a wide range of mass/charge ratios. The detector itself is usually an electron multiplier which is sensitive even for small quantities of a particular species. Mass spectra depicting the signal intensity against the mass/charge ratio are obtained, each covering a small window in time and thereby monitoring the GC sample elution over time. On one hand a plot of signal intensity/peak area, which results from the concentration of ionic species detected, against retention time can be retrieved from here, while the ion fragmentation pattern itself gives information on compound structure. Compound names and structures are usually obtained with the help of an internal compound library which matches experimental to reported structures.[73,75]

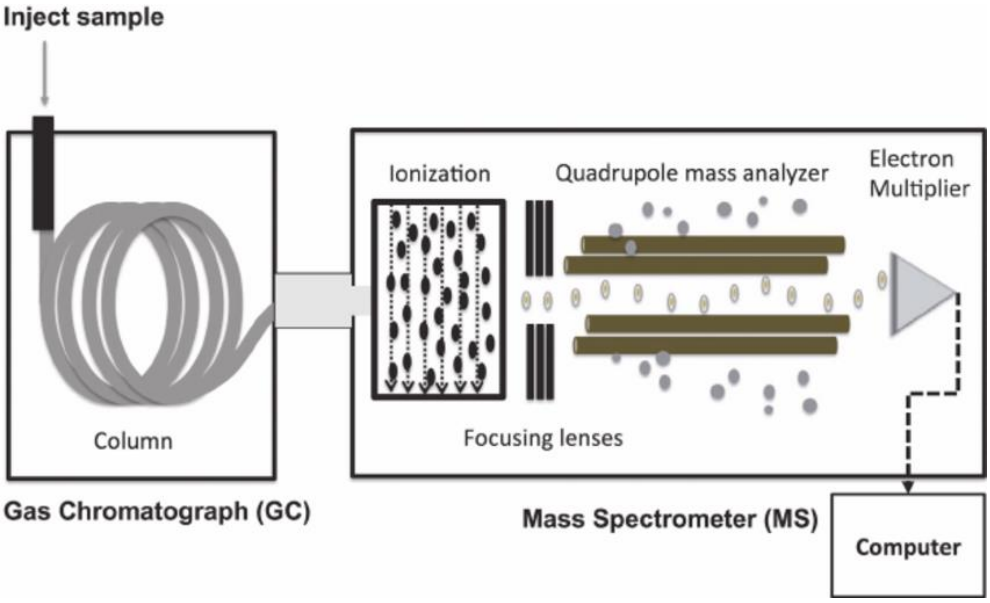


Figure 2.14 – Schematic depiction of a GC-MS with a quadrupole mass analyser (reproduced from reference[76] (doi 10.1038/emm.2015.97) licensed under creativecommons.org/licenses/by/4.0/)

Finally, compound quantification is also possible with GC-MS, based on previous calibration of the instrument with known concentrations of the compound of interest. The obtained calibration curve of signal peak area against concentration can then be used to determine the concentration of unknown samples.[69]

2.11 References

(1) Fryer, J. *The Chemical Applications of Transmission Electron Microscopy*; Academic Press, 1979.

(2) Nessler, R. https://cmrf.research.uiowa.edu/transmission-electron-microscopy.

(3) Reimer, L.; Kohl, H. *Transmission Electron Microscopy*, 5th ed.; Springer, 2008.

(4) Barrett, C. J. http://barrett-group.mcgill.ca/tutorials/nanotechnology/nano02.htm.

(5) Fultz, B.; Howe, J. *Transmission Electron Microscopy and Diffractometry of Materials*, 4th ed.; Springer, 2013.

(6) Ooi, L. *Principles of X-Ray Crystallography*; Oxford University Press, 2010.

(7) Smyth, M. S.; Martin, J. H. *J. Clin. Pathol. Mol. Pathol.* **2000**, *53* (1), 8.

(8) Krumeich, F. http://www.microscopy.ethz.ch/bragg.htm.

(9) Woolfson, M. *An Introduction to X-Ray Crystallography*; Cambridge University Press, 1997.

(10) Ladd, M. *Structure Determination by X-Ray Crystallography: Analysis by X-Rays and Neutrons*; Springer, 2013.

(11) Jenkins, R.; Snyder, R. *Introduction to X-Ray Powder Diffractometry*; Wiley VCH Verlag GmbH & Co. KGaA, 1996.

(12) Schrader, M. *Infrared and Raman Spectroscopy: Methods and Applications*; Wiley VCH Verlag GmbH & Co. KGaA, 1995.

(13) Colthup, B.; Daly, L.; Wiberley, E. *Introduction to Infrared and Raman Spectroscopy*; Academic Press, 1990.

(14) https://www.chemie-biologie.uni-siegen.de/ac/be/lehre/ws1213/ir-ramanlong.pdf.

(15) https://en.wikipedia.org/wiki/Raman_spectroscopy.

(16) Larkin, P. *Infrared and Raman Spectroscopy: Principles and Spectral Interpretation*; Elsevier, 2011.

(17) Hardcastle, F. D.; Wachs, I. E. *Solid State Ionics* **1991**, *45* (3–4), 201.

(18) Ferraro, J.; Nakamoto, K.; Brown, C. *Introductory Raman Spectroscopy*; Elsevier Science, 2003.

(19) Schroeder, S.; Gottfried, M. *Temperature Programmed Desorption (TPD) Thermal Desorption Spectroscopy (TDS)*; 2002.

(20) Falconer, J.; Schwarz, J. *Catal. Rev.* **1983**, *25* (2), 141.

(21) Niwa, M.; Katada, N.; Okumura, K. *Characterization and Design of Zeolite Catalysts*; Springer, 2010.

(22) Cvetanovic, R.; Amenomiya, Y. *Adv. Catal.* **1967**, *17*, 103.

(23) Grimm, R. L. http://cbc41.wpi.edu/research/tpd.

(24) http://www.chem.qmul.ac.uk/surfaces/scc/scat5_6.htm.

(25) Brunauer, S.; Emmett, P. H.; Teller, E. *J. Am. Chem. Soc.* **1938**, *60* (2), 309.

(26) Lowell, S.; Shields, J. E.; Thomas, M. A.; Thommes, M. *Characterization of Porous Solids and Powders: Surface Area, Pore Size and Density*; Springer Science & Business

Media, 2012.

(27) AL-Mahallawi, K. https://www.slideshare.net/BakrYou/water-quality-control-and-treatment-water-treatment.

(28) http://particle.dk/methods-analytical-laboratory/surface-area-bet-2/.

(29) Fagerlund, G. *Mat. Constr.* **1973**, *6* (3), 239.

(30) Matshitse, R. *Brunauer-Emmett-Teller (BET) Surface Area Analysis [Power Point Slides]*.

(31) Connelly, A. https://andyjconnelly.wordpress.com/2017/03/13/bet-surface-area/.

(32) van der Heide, P. *X-Ray Photoelectron Spectroscopy: An Introduction to Principles and Practices*; Wiley VCH Verlag GmbH & Co. KGaA, 2012.

(33) http://xpssimplified.com/.

(34) http://www.chem.qmul.ac.uk/surfaces/scc/scat5_3.htm.

(35) Wagner, J. *X-Ray Photoelectron Spectroscopy*; Nova Science Publishers, 2011.

(36) Chavez, J. https://wiki.utep.edu/pages/viewpage.action?pageId=51217144.

(37) Casa Software Ltd. www.casaxps.com.

(38) Briggs, D.; Seah, M. *Practical Surface Analysis*, 2nd ed.; Wiley VCH Verlag GmbH & Co. KGaA, 1990.

(39) Giorgetti, M.; Stievano, L. *InTechOpen* **2017**, https://www.intechopen.com/books.

(40) Blaha, P. *Core Level Spectroscopy [Power Point Slides]*; TU Vienna.

(41) Koningsberger, D.; Prins, R. *X-Ray Absorption: Principles, Applications, Techniques of EXAFS, SEXAFS, and XANES*; Wiley VCH Verlag GmbH & Co. KGaA, 1988.

(42) http://jolisfukyu.tokai-sc.jaea.go.jp/fukyu/tayu/ACT99E/04/0406.htm.

(43) Newville, M. *Fundamentals of XAFS*; Consortium for Advanced Radiation Sources, University of Chicago, 2004.

(44) Ravel, B.; Kelly, S. D. *AIP Conf. Proc.* **2007**, *882*, 150.

(45) Penner-Hahn, J. A. *X-Ray Absorption Spectroscopy*; 2011.

(46) Duer, M. *Solid State NMR Spectroscopy: Principles and Applications*; Wiley VCH Verlag GmbH & Co. KGaA, 2008.

(47) Kaseman, D.; Iyer, R. S. G. https://chem.libretexts.org/Core/Physical_and_Theoretical_Chemistry/Spectroscopy/Magnetic_Resonance_Spectroscopies/Nuclear_Magnetic_Resonance/Nuclear_Magnetic_Resonance_II.

(48) Hore, P. *Nuclear Magnetic Resonance*, 2nd ed.; Oxford University Press, 2015.

(49) Lewitt, M. *New Techniques in Nuclear Magnetic Resonance*; University of Oxford, 1981.

(50) Canet, D. *Nuclear Magnetic Resonance: Concepts and Methods*; Wiley VCH Verlag GmbH & Co. KGaA, 1996.

(51) Abraham, R. *Nuclear Magnetic Resonance*; Royal Society of Chemistry, 2007.

(52) Soderberg, T. https://chem.libretexts.org/Textbook_Maps/Organic_Chemistry_Textbook_Maps/Map%3A_Organic_Chemistry_with_a_Biological_Emphasis_(Soderberg)/Chapter_05%3A_Structure_Determination_II/5.5%3A_Spin-spin_coupling.

(53) Ashbrook, S. *Introduction To Quadrupolar NMR [Power Point Slides]*; University of St Andrews, 2008.

(54) Kao, H. M.; Yu, C. Y.; Yeh, M. C. *Microporous Mesoporous Mater.* **2002**, *53* (1–3), 1.

(55) Zheng, A.; Huang, S.-J.; Liu, S.-B.; Deng, F. *Phys. Chem. Chem. Phys.* **2011**, *13* (33), 14889.

(56) Khabibulin, D.; Romanenko, K.; Zuev, M.; Lapina, O. *Magn. Reson. Chem.* **2007**, *45* (11), 962.

(57) Papulovskiy, E.; Shubin, A. a; Terskikh, V. V; Pickard, C. J.; Lapina, O. B. *Phys. Chem. Chem. Phys.* **2013**, *15* (14), 5115.

(58) Hanna, J. V.; Pike, K. J.; Charpentier, T.; Kemp, T. F.; Smith, M. E.; Lucier, B. E. G.; Schurko, R. W.; Cahill, L. S. *Chem. - Eur. J.* **2010**, *16* (10), 3222.

(59) Satterlee, J. D. *Concepts Magn. Reson.* **1990**, *2* (3), 119.

(60) Bedson, P.; Prichard, E. *High Performance Liquid Chromatography*; Royal Society of Chemistry, 2003.

(61) Moldoveanu, S.; David, V. *Essentials in Modern HPLC Separations*; Elsevier Science, 2013.

(62) http://www.dyerlabs.com/chemistry/highpressure.html.

(63) Wellings, D. *A Practical Handbook of Preparative HPLC*; Elsevier Science, 2006.

(64) Choudhary, A. http://www.pharmaguideline.com/2016/01/different-types-of-columns-used-in-hplc.html.

(65) Kumar, A. http://technologyinscience.blogspot.co.uk/2011/12/distribution-coefficient-kd-in-gel.html.

(66) Grell, L.; Butarbutar, A.; Burnett, K.; Ghoneim, D. https://en.wikibooks.org/wiki/Proteomics/Protein_Separations_-_Chromatography/Reversed_Phase.

(67) Sedlock, J. https://www.slideshare.net/JordanSedlock/ion-chromatography-sedlock-fall-2014.

(68) Barkovich, M. https://chem.libretexts.org/Core/Analytical_Chemistry/Instrumental_Analysis/Chromatography/High_performance_liquid_chromatography.

(69) Sparkman, O.; Penton, Z.; Kitson, F. *Gas Chromatography and Mass Spectrometry: A Practical Guide*; Elsevier Science, 2011.

(70) Hübschmann, H.-J. *Handbook of GC-MS: Fundamentals and Applications*; Wiley VCH Verlag GmbH & Co. KGaA, 2015.

(71) Poole, C. *Gas Chromatography*; Elsevier Science, 2012.

(72) Lhoest, G. http://www.specmetcrime.com/introduction_%C3%A0_la_gcms.htm.

(73) Snow, N.; Burinsky, D. *Comprehensive Analytical Chemistry*; Elsevier, 2006.

(74) Gruber, L.; A., G. https://www.ivv.fraunhofer.de/en/leistungsangebote/verpackung/stoerstoffanalyse/ms_pages/Introduction_into_mass_spectrometry.html.

(75) McCloskey, J. *Mass Spectrometry*; Academic Press, 1990.

(76) Kim, I. Y.; Suh, S. H.; Lee, I. K.; Wolfe, R. R. *Exp. Mol. Med.* **2016**, *48* (1), e203.

Chapter 3

Experimental and Characterisation Methods

Chapter 3 71
3.1 Catalyst Synthesis 72
3.1.1 Niobium Oxides 72
3.1.2 Decoration of Modified Y Zeolites with Ruthenium and Palladium 74
3.2 Catalyst Characterisation 77
3.2.1 TEM 77
3.2.2 XRD 78
3.2.3 Raman 79
3.2.4 TPD 79
3.2.5 BET 80
3.2.6 XPS 80
3.2.7 XAFS 81
3.2.8 TMP ^{31}P ssNMR 82
3.2.9 ^{93}Nb ssNMR 84
3.2.10 Hammett Indicator Measurements 84
3.3 Catalyst Testing 87
3.3.1 Sugar Conversion to HMF over Niobium Oxides in Water 87
3.3.2 HMF to DMF and Further to Aromatics over Ru/Pd on Modified Y Zeolites in Ethanol 88
3.4 Product Analysis 89
3.4.1 HPLC 89
3.4.2 GC-MS 90
3.5 References 92

3.1 Catalyst Synthesis

3.1.1 Niobium Oxides

All chemicals were obtained in analytical grade of over 99 % purity from Wako Pure Chemical Industries unless stated otherwise. Nb_2O_5 (≥99.9 %) was purchased from Alfa Aesar for means of comparison to the synthesized niobium oxides. The niobium oxide synthesis was performed by Keizo Nakagawa (Kobe University Japan).

Layered bulk HNb_3O_8 was prepared by conventional solid-state reactions in an alumina crucible.[1,2] K_2CO_3 and Nb_2O_5 were mixed in molar ratios of 1.1:3 and calcined at 600 °C for 2 h and 900 °C for 3 h for the synthesis of KNb_3O_8. The obtained KNb_3O_8 was converted to $H_3ONb_3O_8$ by immersion in 6.0 M HCl at 60 °C for 1 week whilst replacing the acid solution with fresh solutions each day. The resulting precipitate was filtered and washed with distilled water repeatedly until the filtrate became neutral and was then dried at 60 °C overnight. The obtained $H_3ONb_3O_8$ was converted to HNb_3O_8 by calcination at 150 °C for 3 h.

The 2D-nanosheet niobium oxide materials hy-Nb (few-layered) and hy-Nb-TEOA (mono-layered) were synthesized by hydrothermal (hy) method in ammonia solution, for hy-Nb-TEOA under the further addition of amine surfactant.[3,4]

For synthesis of hy-Nb-TEOA, 1.989 g of $Nb(OEt)_5$ (0.00625 mol) was mixed with 3.735 g of triethanolamine (TEOA) (0.025 mol), the resulting mixture is stable against hydrolysis at room temperature. 25 mL of aqueous NH_3 was added and the final pH of the mixture was kept at 12.8. The mixture was then transferred to a 45 mL Teflon autoclave and aged at 160 °C for 24 h. The resulting product was centrifuged at 6000 rpm and a colloidal suspension with a small amount of

white precipitate was obtained. After the removal of the precipitate fraction, the yellowish supernatant colloid was collected, filtered and washed with distilled water. The product was dried at 60 °C overnight and was christened hy-Nb-TEOA precursor. Acid treatment of hy-Nb-TEOA precursor was performed using HNO_3 aqueous solution. A 6.0 M HNO_3 aqueous solution was added to hy-Nb-TEOA precursor, forming a colloidal suspension until the pH became 2.0, which resulted in precipitation. The aggregated sample was filtered and washed repeatedly with distilled water until the filtrate became neutral. The product was dried at 60 °C overnight and was christened hy-Nb-TEOA (acid treated).

For hy-Nb, the hydrothermal synthesis of $Nb(OEt)_5$ in aqueous NH_3 was performed in a similar way, but without addition of TEOA. After centrifugation at 3500 rpm for 10 min, a white precipitate with a clear supernatant was collected. The precipitate was then washed with ethanol and dried at 60 °C overnight. The obtained sample was christened hy-Nb precursor. Acid treatment of hy-Nb precursor was performed using HNO_3 aqueous solution. The hy-Nb precursor was stirred in 1.0 M HNO_3 aqueous solution. After several hours, the collected sample was washed with distilled water repeatedly until the filtrate became neutral. The product was dried at 60 °C overnight and was christened hy-Nb (acid treated).

Amorphous mesoporous $Nb_2O_5*nH_2O$ was synthesized using a mixture of niobium(V) ethoxide ($Nb(OEt)_5$), Kojundo Chemical Laboratory, 5.0 g) and distilled water (200 mL) stirred at room temperature for 24 h. The resulting precipitate was filtered, washed with distilled water and soaked in 0.1 M HCl solution overnight. The resulting white precipitate was repeatedly washed with distilled water until the filtrate became neutral and was then dried at 200 °C for 5 h.

All the above niobium oxides (commercial and synthesized) are of white color, with a very light tinge of yellow in the case of hy-Nb-TEOA and mesoporous Nb_2O_5*nH_2O (Figure 3.1).



Figure 3.1 – Commercial Nb_2O_5 and synthesized niobium oxides

3.1.2 Decoration of Modified Y Zeolites with Ruthenium and Palladium

Starting from commercially available acidic HY10 zeolite (Tosoh HUA 350), the following modifications have been made:

NbO/HY10 was synthesized by wet impregnation of HY10 with 5 wt% niobium. Therefore 263.15 mg of ammonium niobate (V) oxalate hydrate (99.99 % from Sigma Aldrich) precursor was mixed with 1 g of HY10 and 1.5 mL of water were added until formation of a slurry (highly viscous dispersion/semi-liquid). The slurry was stirred at about 70 °C for water evaporation until a dry powder was obtained. The white powder was calcined in air at 400 °C for 3 h and christened NbO/HY10.

Weakly basic NaY10 was synthesized from sodium ion exchange of HY10.[5,6] 1 g of HY10 was dispersed in a 50 mL solution of 1 M sodium nitrate for two days under stirring and the solution pH was neutralized with NaOH (aq) over time. The mixture was filtered after and the filtrate was

washed repeatedly with distilled water in order to remove excess sodium nitrate. The obtained NaY10 product was then dried at 60 ℃ overnight.

MgO/NaY10 was synthesized by wet impregnation of NaY10 with 5 wt% magnesium. Therefore 464.52 mg of magnesium acetate tetrahydrate (99.997 % from Alfa Aesar) precursor was mixed with 1 g of NaY10 and 1.5 mL of water were added until formation of a slurry. The slurry was stirred at about 70 ℃ for water evaporation until a dry powder was obtained. The white powder was calcined in air at 400 ℃ for 3 h and christened MgO/NaY10.

The above commercial, ion exchanged and oxide modified Y zeolite supports were decorated with ruthenium and palladium as follows:

Ru/support was synthesized by wet impregnation of the according Y zeolite support with 5 wt% ruthenium. Therefore 69.26 mg of ruthenium (III) chloride (38 wt% Ru content, Alfa Aesar) precursor was dissolved in 1 mL of water and mixed with 500 mg of support to form a slurry. The slurry was stirred at about 70 ℃ for water evaporation until a dry powder was obtained. The brown powder was reduced under hydrogen at 400 ℃ for 3 h and the resulting grey/black powder was christened Ru/support (e.g. Ru/HY10, Ru/NbO/HY10, Ru/NaY10, Ru/MgO/NaY10).

Pd/support was synthesized by wet impregnation of the according Y zeolite support with 5 wt% palladium. Therefore 65.80 g of palladium (II) nitrate (40 wt% Pd content, Alfa Aesar) precursor was dissolved in 1 mL of water and mixed with 500 mg of support to form a slurry. The slurry was stirred at about 70 ℃ for water evaporation until a dry powder was obtained. The brown

powder was reduced under hydrogen at 400 °C for 3 h and the resulting grey/black powder was christened Pd/support (e.g. Pd/HY10, Pd/NbO/HY10, Pd/NaY10, Pd/MgO/NaY10).

The above HY10, NbO/HY10, NaY10 and MgO/NaY10 supports are of white colour, while the final ruthenium and palladium metal decorated supports are of grey/black colour (Figure 3.2).

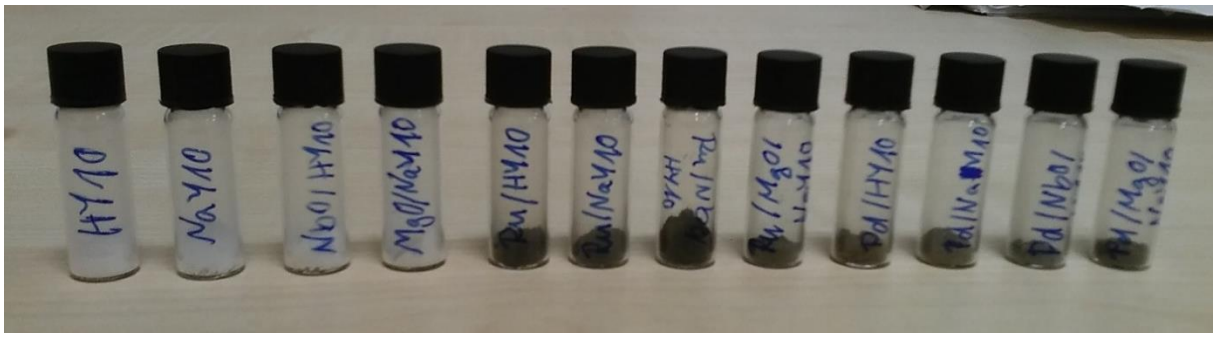


Figure 3.2 – Modified Y zeolite supports before (white) and after decoration with Ru/Pd (black)

3.2 Catalyst Characterisation

3.2.1 TEM

Sample morphology and microstructure were examined by TEM (Transmission Electron Microscopy) using a JEOL 3000F microscope operated at 300 kV. TEM specimens were prepared by pipetting 5 µL of the sample dispersion in ethanol onto holey carbon-coated copper mesh grids (400 meshes). TEM measurements were performed by Elizabeth Raine (University of Oxford).

In the case of Ru and Pd on modified Y zeolites, metal surface areas were further calculated from the obtained TEM particle sizes, assuming a spherical particle conformation. It should be noted that if working with a hemispherical particle model, the resulting metal surface areas per g catalyst stay the same, but surface area, volume and mass per particle would have to be divided by two, while the number of particles per g catalyst would have to be multiplied by two. An exemplary calculation scheme for spherical Ru particles (3 nm) is shown below (Equation 3.1). For Pd metal, surface area calculations were performed using the following parameters: density ρ = 12.0 g cm^{-3}, metal percentage = 5 wt% and according TEM particle diameters.

$$Ru\ metal\ density\ \rho = 12.1\ gcm^{-3}, \qquad metal\ percentage\ of\ catalyst = 5wt\% = 0.05$$

$$average\ particle\ diameter\ d = 3nm$$

$$surface\ area\ A = \pi \times d^2 = 28.27\ nm^2,\ \ volume\ V = \pi \times \frac{d^3}{6} = 14.14\ nm^3$$

$$12.1\ gcm^{-3} \triangleq 12.1 \times 10^{-21}\ gnm^{-3}$$

$$12.1 \times 10^{-21} gnm^{-3} \times 14.14\ nm^{-3} = 171 \times 10^{-21}\ g\ per\ Ru\ particle$$

$$\frac{0.05g}{171\ x\ 10^{-21}g} = 2.92\ \times 10^{17}\ Ru\ particles\ per\ g\ catalyst$$

$$2.92 \times 10^{17} \times 28.27\ nm^2 = 82.66\ nm^2\ per\ g\ catalyst$$

$$\triangleq 8.266\ m^2\ per\ g\ catalyst \qquad Equation\ 3.1$$

3.2.2 XRD

Sample crystallinity was identified by powder XRD (X-Ray Diffraction). A Philips PANalytical X'Pert Pro PW 1710 diffractometer was used, operating in Bragg-Brentano focusing geometry and producing Cu K_α radiation (λ = 1.5418 Å) from a generator operating at 40 kV and 40 mA. Samples were prepared by placing the powders in a fixed depth well on a glass slide and pressing the surface level. XRD spectra were analysed using the program X'Pert High Score with help from Elizabeth Raine.

In the case of Ru and Pd on modified Y zeolites, average metal particle sizes where further calculated from the broadening of the individual metal lattice peaks using the Scherrer equation (Equation 3.2). The metal particle size τ is related to the full peak width at half maximum β as follows, where further λ = 1.5418Å, K = 0.9 and θ = diffraction angle.

$$\tau = \frac{K\lambda}{\beta\cos(\theta)} \qquad Equation\ 3.2$$

3.2.3 Raman

Bond structures of niobium oxides were investigated by Raman spectroscopy. Raman spectra were collected on a Perkin Elmer Raman Spectrum 400F using a laser excitation wavelength of 532 nm and taking 5 scans of exposure time 10 sec for each sample. Before the measurements, the samples were dried at 150 °C.

3.2.4 TPD

TPD (Temperature Programmed Desorption) measurements were performed with NH_3 and CO_2 gas adsorption/desorption to determine sample surface acidity and basicity, respectively. Analyses were performed by Gary G.-Z. Chang (University of Oxford) on a Micromeritics Pulse Chemsorb 2720 equipped with a TCD (Thermal Conductivity Detector) as reported previously by Pudi *et al.*[7] The typical sample size is 100 mg and each sample was weighed accurately before use, for later calculation of acid and base site quantities. After pre-treatment at 450 °C in helium, the sample was saturated with either NH_3 (under the flow of 10 % NH_3 in helium) or CO_2 (under the flow of 100 % CO_2) at room temperature for 1 h. The saturated sample was then purged with helium for 1 h to remove physically adsorbed NH_3 or CO_2. Afterwards the sample was heated to 500 °C at a heating rate of 10 °C min^{-1} under helium flow and the desorption of chemically adsorbed NH_3 or CO_2 was monitored with a TCD. Acid site (measured by NH_3) and base site (measured by CO_2) quantities were calculated from desorption peak area and sample weight.

3.2.5 BET

Specific surface areas were derived from the corresponding adsorption-desorption isotherms, obtained using a conventional BET nitrogen adsorption apparatus (BELSORP18SP, Bell Japan Inc.). The measurements were performed by Keizo Nakagawa (Kobe University). 100 mg of sample were degassed under vacuum at 100 °C for 10 h and weighed, before attaching the sample tube to the volumetric apparatus. An operation temperature of 77 K was used, the boiling temperature of nitrogen. From a vessel with liquid nitrogen, nitrogen was inserted into the sample tube step-wise to give defined relative pressures, while measuring the according volumes of nitrogen adsorbed onto the sample surface. After finishing the adsorption measurement at a relative pressure of 1 (nitrogen liquefaction inside the sample tube), the desorption process was monitored accordingly. Specific surface areas were calculated from a BET plot of the adsorption-desorption isotherm data (see Appendix p.A1-A2 for calculations).

3.2.6 XPS

Atomic oxidation state analysis was performed using XPS (X-ray Photoelectron Spectroscopy). Measurements were conducted by Ashley Shepherd (University of Oxford) on a VG – Escalab X-Ray Photoelectron Spectrometer VGX900 producing aluminium K_α radiation with an energy of 1486 eV and operating at $< 1 \times 10^{-8}$ mbar. The samples were attached to the sample stub by a sticky double sided carbon tape. A wide scan between 0 and 1300 eV was performed to identify all elements present in the sample, using an average of 5 scans with a 1 eV step size, 0.1 second dwell time and 50 eV pass energy. For the regions of interest such as Nb 3d, higher resolution spectra were further collected using an average of 20 scans with a 0.1 eV step size, a 0.2 second dwell time and 20 eV pass energy. Charge neutralization was applied using a combined low energy/ ion flood source. Spectra analysis was conducted afterwards using CasaXPS peak fitting

software and the peak positions were calibrated with the C 1s peak of the carbon tape set to 285.00 eV.[8] Quantitative elemental analysis of the samples was further carried out to determine Nb:O ratios (see Appendix p.A19-A21 for calculation method).

3.2.7 XAFS

Oxidation states and local structures of Nb atoms were probed by XAFS (X-ray absorption fine structure). Measurements were performed by Tai-Sing Wu and Yun-Liang Soo at the beamline BL07A of the National Synchrotron Radiation Research Center Taiwan. A Si (111) Double Crystal Monochromator (DCM) was used to scan the photon energy and the energy resolution ($\Delta E/E$) for incident X-ray photons was estimated to be 2×10^{-4}. Scotch tape was used to sandwich and fixate a small amount of sample. Transmission mode was adopted for Nb K-edge EXAFS measurements and at least two scan sets were collected and compared for each sample. The data analysis was performed by Molly M.J. Li (University of Oxford) using IFEFFIT with Horae packages (Athena and Artemis), working with a combined approach of *ab initio* calculations and model compound fitting. Calibrations were performed using Nb metal as a reference and structural refinements were done using Nb_2O_5 and KNb_3O_8 from the internal program library as model compounds. First shell data analysis was done under the assumption of single scattering with an error estimation given by the correlation factor R between experimental and model result, with values within 2%. Further data fitting parameters were as follows: Rbkg = 1.2, k range = 3 – 12.3, R range = 1.2 – 4 and enot (the shift in absorption threshold position between experimental and model result) with values between ±8. Bond distances to first shell atoms (Nb-O) can be determined with high accuracy of 0.01-0.02Å, while coordination numbers are only accurate to ±1.

3.2.8 TMP ^{31}P ssNMR

Detailed studies on niobium oxide surface acidity were conducted using TMP (trimethylphosphine) adsorption followed by ^{31}P solid state NMR. Due to the variations in interaction strength of the adsorbed TMP molecule with different acid sites, these acid sites can be differentiated by the ^{31}P NMR chemical shift of TMP.[9–11] TMP adsorption and NMR measurements were performed by Yung-Kang Peng (University of Oxford).

150 mg of sample was loaded into a glass tube and pre-treated at 423 K for 2 h under vacuum (10^{-1} Pa). After reaching room temperature, the sample was loaded with 1 mmol TMP per g catalyst and TMP was vaporized under the low pressure conditions (system set-up Figure 3.3). To promote TMP adsorption, the sample tube was then immersed in liquid nitrogen. After about 10 min the pressure of the isolated system reached a plateau, meaning the equilibrium state between gaseous and adsorbed TMP was obtained. Excess TMP was then removed carefully via a short vacuum treatment. The above steps were repeated three times for sample equilibration and a more accurate final TMP adsorption on the sample surface. The glass tube was finally flame sealed for storage and transferred to a Bruker 4 mm ZrO_2 rotor with a Kel-F endcap under nitrogen atmosphere, as a preparation for the NMR measurement.

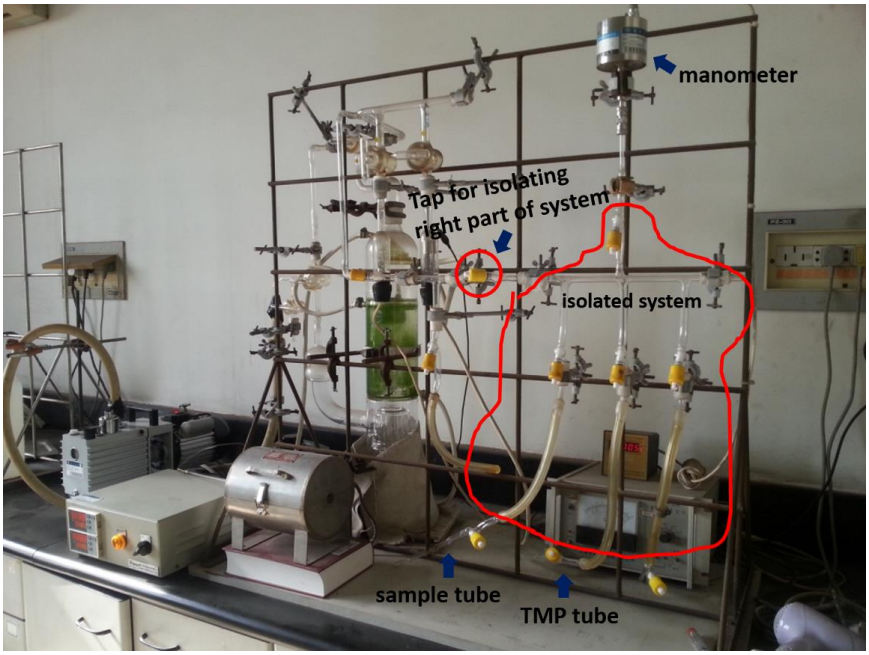
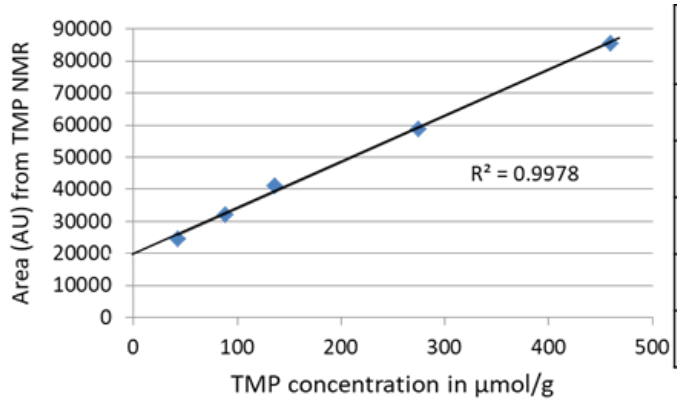


Figure 3.3 – Experimental set-up for TMP adsorption

Solid state magic angle spinning (MAS) NMR experiments were carried out at room temperature using a Bruker Avance III 400WB spectrometer. High power decoupling (HPDEC) was used for quantitative ^{31}P analysis in order to remove additional peak broadening due to proton spin effects. Considering the long relaxation times of ^{31}P nuclei, a 30° pulse with a width of 1.20 μs and 15 s delay time was used. The radiofrequency for decoupling was 59 kHz and the spectra were collected between 200 and −200 ppm, with a scanning number of 800. The ^{31}P chemical shifts were reported relative to 85 % aqueous solution of H_3PO_4 using $NH_4H_2PO_4$ as a secondary standard (0.81 ppm). The quantity of adsorbed TMP molecules was calculated according to the calibration line (Figure 3.4), established by running TMP measurements with standard samples of known solid acid site concentration.



Concentration in µmol/g	Area (AU)
42.4	24385
88.7	31913
136.5	41001
275.1	58800
459.9	85299

Figure 3.4 – NMR peak area calibration line for TMP adsorption

3.2.9 ^{93}Nb ssNMR

^{93}Nb solid state NMR was used to study niobium oxidation states and coordination. The NMR measurements were done by Thomas J.N. Hooper (University of Warwick) using a Bruker Avance II+-600 spectrometer at 14.1 T operating at the ^{93}Nb Larmor frequency of 146.66 MHz. All ^{93}Nb NMR data were acquired using a 5 mm static Bruker probe. A $\pi/2$ pulse length was determined on $K[NbCl_6].CH_3CN$ resulting in a selective $\pi/6$ pulse length of 0.5 µs that satisfied the uniform excitation condition for quadrupolar nuclei[12] where $(I+½)\omega_{rf}t_p \leq \pi/6$. A $(\pi/6)$-τ-$(\pi/6)$ echo sequence was utilised to diminish ringing effects with a τ period of 30 µs and a recycle delay of 0.5 s. All ^{93}Nb chemical shifts were referenced to $K[NbCl_6].CH_3CN$ (δ_{iso}=0.0 ppm).

3.2.10 Hammett Indicator Measurements

The acid strength (pK_a) of a solid acid can be visualized by the color of an adsorbed indicator. A color change of the added indicator occurs upon transfer of the indicator's basic to its conjugate acid form, which happens at an according proton activity/when the solid acid's pK_a is more negative than the indicator's pK_a.[13,14] Since solid acids tend to be very strong acids, they require

the use of indicators with negative pK_a and an extrapolation of the pH scale, the Hammett acidity function H_0. The Hammett acidity function is an extension of the Henderson-Hasselbalch equation (Equation 3.3), which in turn is derived from the acid dissociation constant K_a, where [HA] is the undissociated acid concentration, $[H^+]$ the proton concentration and $[A^-]$ the conjugate base concentration.[15]

$$K_a = \frac{[H^+][A^-]}{[HA]}$$

$$-logK_a = -\log[H^+] - log\frac{[A^-]}{[HA]}$$

$$pK_a = pH - log\frac{[A^-]}{[HA]}$$

$$pH = pK_a + log\frac{[A^-]}{[HA]} \qquad Equation\ 3.3$$

Since the use of pH is only valid for dilute aqueous acid solutions, the Hammett acidity function for concentrated and non-aqueous acids uses the denotation H_0 instead, where H_0 refers to the proton activity a_{H+} rather than the concentration and γ are thermodynamic activity coefficients (Equation 3.4).[13,14,16] Further, the pK_a here is commonly denoted in the conjugate acid and base form, where $[BH^+]$ is the conjugate acid concentration and [B] the base concentration.

$$K_a = \frac{[B][H^+]}{[BH^+]}$$

$$H_0 = -\log\left(a_{H^+}\frac{\gamma_B}{\gamma_{BH^+}}\right) = pK_a + log\frac{[B]}{[BH^+]} \qquad Equation\ 3.4$$

Using an indicator of known pK_a, the H_0 and solid acid's pK_a can be determined by identifying the ratio (color) of the indicator's basic (B) to conjugate acid form (BH^+ for interaction with Brønsted acid sites and BM for Lewis acid sites). A series of indicators with different pKa's in

dilute benzene solution (inert solvent) were therefore added to solid acid samples and the observed colors were noted. A full color change from the indicators basic to conjugate acid form designated the solid acid's pK_a to be more negative than the indicator's pK_a.[13,17] Experiments were performed using the following indicators: dicinnamalacetone (pK_a = -3.0), benzalacetophenone (pK_a = -5.6) and anthraquinone (pK_a = -8.2). 3-4 drops of indicator in benzene solution were added to 10 mg samples of niobium oxide catalyst and color changes were noted.

After determining the acid strength, the samples where the indicator existed in its conjugate acid form were suitable for titration with a base. N-butylamine is a commonly used base in Hammett titrations.[13] Upon addition it replaces the indicator by conjugate acid formation and thereby converts the indicator back to its basic form, resulting in a color change. The end point of the titration is reached upon complete color transition, when the amount of added base is equivalent to the amount of acid sites. Unfortunately no differentiation between Lewis and Brønsted acid sites is possible with n-butylamine. Further difficulties faced with Hammett titrations include full color change/end-point determination, mass transfer limitations and catalyst dispersion.[13,17] Since the catalyst samples did not disperse well in benzene, leading to difficulties in end-point determination upon titration with n-butylamine, further titrations were performed with the samples dispersed in water and methyl red as an indicator.

3.3 Catalyst Testing

3.3.1 Sugar Conversion to HMF over Niobium Oxides in Water

Aqueous solutions of glucose, fructose and sucrose were converted to HMF at elevated temperatures using various types of niobium oxides as solid acid catalysts. 15 mL water containing 150 mg sugar (1wt%) and 150 mg niobium oxide catalyst (1wt%) were charged to a glass liner fitting a Parr autoclave (452HC9 566055 T316 112111, 160 mL, -10°C to 350 °C, up to 200 bar). The autoclave was then sealed under atmospheric conditions and fitted into a ceramic ring heater on a magnetic stirrer (Figure 3.5). The autoclave was heated to 180 °C under stirring, using a thermocouple connection to a temperature controlling unit which adjusted the ring heater accordingly. Reactions were run with the different types of sugar and over various time lengths ranging between 0 to 180 min. Heating up (ring heater) and cooling down (ice bath) periods lasting 30 min and 10 min respectively were not included in the given reaction time lengths. Two reactions were run for each sample mixture to test repeatability of results. Afterwards the reaction mixtures were centrifuged and filtered to remove the catalyst as well as small amounts of solid residues, before analysing the product solutions by HPLC.

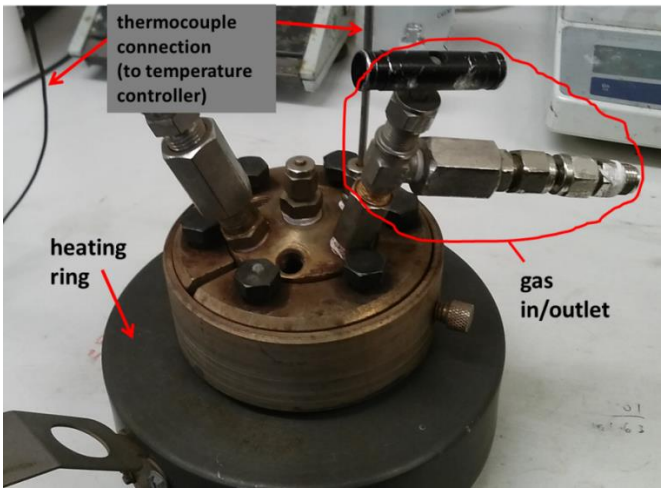


Figure 3.5 – Autoclave reactor set-up

3.3.2 HMF to DMF and Further to Aromatics over Ru/Pd on Modified Y Zeolites in Ethanol

Solutions of HMF in ethanol were converted to DMF and further to aromatics over Ru/Pd on modified Y zeolites at elevated temperatures. A mixture of 250 mg HMF (≥99% Sigma Aldrich), 50 mg catalyst and 15 mL ethanol was charged to a glass liner fitting a Parr autoclave (452HC9 566055 T316 112111, 160 mL, -10°C to 350 °C, up to 200 bar). The autoclave was flushed with nitrogen several times, sealed and fitted into a ceramic ring heater on a magnetic stirrer (Figure 3.5). The autoclave was then heated to 300 °C under stirring, using a thermocouple connection to a temperature controlling unit which adjusted the ring heater accordingly. Reactions lasting 9 h, 12 h and 20 h were performed over the different catalysts. Reaction times included the heating up and cooling down time of 45 min (ring heater) and 15 min (ice bath) respectively. Two reactions were run for each sample mixture to test repeatability of results. Afterwards the reaction mixtures were centrifuged and filtered to remove the catalyst as well as small amounts of solid residues, before analysing the product solutions (1 mL in vial) by GC-MS.

The remaining product solutions from the HMF to DMF conversions were re-charged to the autoclave glass liner with the addition of 100 mg fresh catalyst. All following procedures and conditions are as described above for the HMF to DMF reaction.

3.4 Product Analysis

3.4.1 HPLC

All product solutions from the sugar to HMF conversion were analysed by HPLC (High Pressure Liquid Chromatography) on a Perkin Elmer Series 200 instrument equipped with an autosampler, HPLC pump, column oven and RID (Refractive Index Detector), as shown in Figure 3.6. An Aminex HPX-87H Ion Exclusion Column of 300 mm x 7.8 mm was used for compound separation. The mobile phase was composed of 0.025 M sulfuric acid in HPLC grade water and the pump operated at a mobile phase flow rate of 0.6 mL min^{-1} at 70 bar. The instrument set-up was controlled externally by a computer unit running the HPLC analysis program TotalChrom. Before sample analysis, the RID baseline was equilibrated by running the according HPLC program (0.025 M aqueous sulfuric acid at 0.6 mL min^{-1}) for approximately 1 h until a stable baseline was acquired. Afterwards sample analysis was performed by transferring 1 – 2 mL of clear/filtered product solution to an HPLC vial (2 mL glass vial with a thin plastic cap) which was inserted into the autosampler unit (several vials/injections can be run using the sequence program set-up). Two injection volumes of 5 µL and 100 µL were run per sample to ensure precision of instrumental results. The obtained products were analysed and differentiated according to their retention times. Sugar conversion and HMF yields were calculated using previously established calibration curves. Side product yields and mass balance estimations were done by the division into compound groups and using model compound calibrations. See Appendix p.A4-A9 for experimental HPLC spectra, calibration curves and yield calculations.

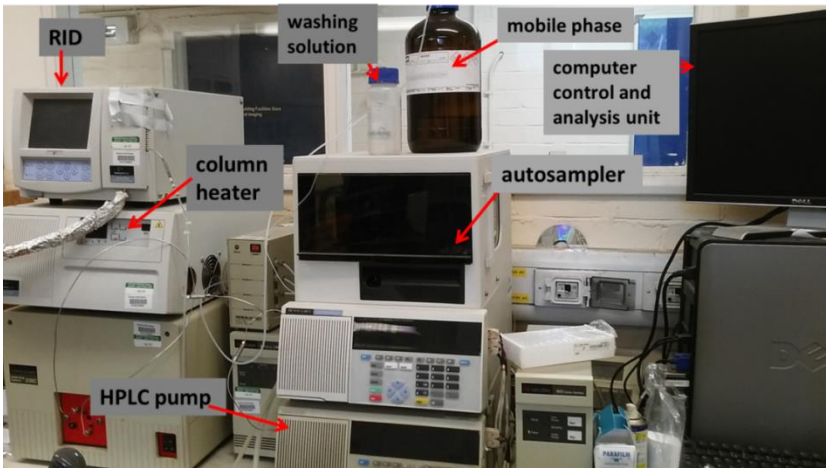


Figure 3.6 – HPLC instrument set-up

3.4.2 GC-MS

All product solutions from the conversion of HMF to DMF and further to aromatics were analysed by GC-MS (gas chromatography coupled with mass spectrometry). An Agilent Technologies 7890B GC System using an HP-INNOWax Column (0 °C – 270 °C) of 30 m x 250 µm x 0.25 µm for product separation was used in combination with a 5977A MSD (mass spectrometry detector) operating at high vacuum (Figure 3.7). Helium gas at a flow rate of 1.2 mL min^{-1} and 1.8 bar was used as the GC mobile phase and the instrument set-up was controlled externally by a computer running the GC-MS analysis program MassHunter. For sample analysis and compound separation the following GC parameters were used: A sample injection volume of 0.2 µL, a split mode inlet at 270°C, a program run time of 30 min with a heat ramp of 10 °C min^{-1} from 50 °C to 250°C and hold mode for 10 min were used. After compound separation by the GC, the gas effluent was directly analysed by the MSD using EI (electron ionization) at an inlet temperature of 250 °C, followed by a single quadrupole detector measuring the according ion fragment patterns. The program internal MS compound library was used for compound identification by comparing known mass spectra to the experimental result. For further

quantification of the products of interest, the GC-MS was calibrated by preparing solutions of different concentrations of commercially available HMF (≥99% Sigma Aldrich), DMF (99% Sigma Aldrich) and triethylbenzene (≥97% Sigma Aldrich). For side product quantification and carbon balance calculation structurally similar products were grouped together and GC-MS calibrations were done for example with 2,5-hexanedione, ethyl levulinate and butanol as model compounds. See Appendix p.A13-A18 for experimental GC-MS spectra, calibration curves and yield calculations.

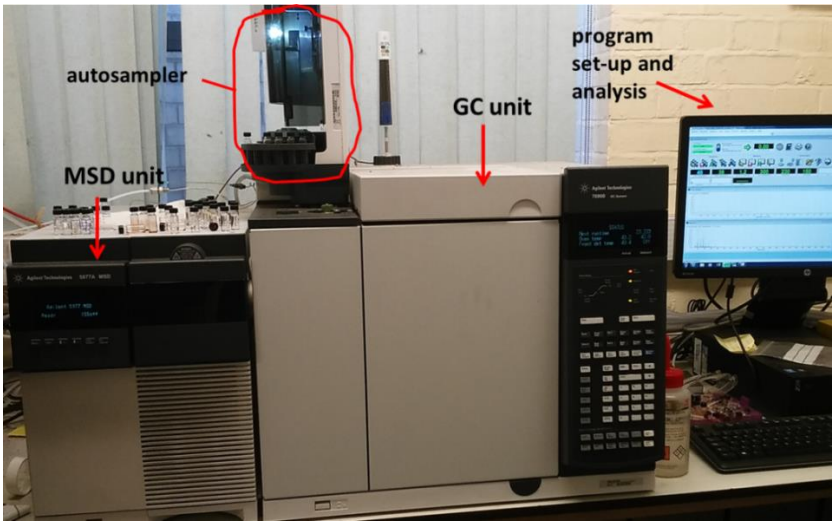


Figure 3.7 – GC-MS instrument set-up

3.5 References

(1) Kim, Y. Il; Atherton, S. J.; Brigham, E. S.; Mallouk, T. E. *J. Phys. Chem.* **1993**, *97* (45), 11802.

(2) Dias, A.; Lima, S.; Carriazo, D.; Rives, V.; Pillinger, M.; Valente, A. A. *J. Catal.* **2006**, *244*, 230.

(3) Nakagawa, K.; Jia, T.; Zheng, W.; Fairclough, S. M.; Katoh, M.; Sugiyama, S.; Edman Tsang, S. C. *Chem. Commun.* **2014**, *50* (89), 13702.

(4) Kreissl, H. T.; Nakagawa, K.; Peng, Y. K.; Koito, Y.; Zheng, J.; Tsang, S. C. E. *J. Catal.* **2016**, *338*, 329.

(5) Ono, Y. *Catal. Today* **1997**, *38* (3), 321.

(6) Ahmed, S.; Chughtai, S.; Keane, M. A. *Sep. Purif. Technol.* **1998**, *13* (1), 57.

(7) Pudi, S. M.; Biswas, P.; Kumar, S. *J. Chem. Technol. Biotechnol.* **2016**, *91* (7), 2063.

(8) Koito, Y.; Rees, G. J.; Hanna, John, V.; Li, M. J. M.; Peng, Y.-K.; Puchtler, T.; Taylor, R.; Wang, T.; Kobayashi, H.; Teixeira, I. F.; Khan, M. A.; Kreissl, H. T.; Tsang, S. C. E. *ChemCatChem* **2017**, *9*, 144.

(9) Lunsford, J. H.; Sang, H.; Campbell, S. M.; Liang, C. H.; Anthony, R. G. *Catal. Letters* **1994**, *27* (3–4), 305.

(10) Chu, Y.; Yu, Z.; Zheng, A.; Fang, H.; Zhang, H.; Huang, S. J.; Liu, S. Bin; Deng, F. *J. Phys. Chem. C* **2011**, *115* (15), 7660.

(11) Zheng, A.; Huang, S.-J.; Liu, S.-B.; Deng, F. *Phys. Chem. Chem. Phys.* **2011**, *13* (33), 14889.

(12) Lippmaa, E.; Samoson, A.; Magi, M. *J. Am. Ceram. Soc.* **1986**, *108* (8), 1730.

(13) Corma, A. *Chem. Rev.* **1995**, *95* (3), 559.

(14) Sanders, W. N.; Berger, J. E. *Anal. Chem.* **1967**, *39* (12), 1473.

(15) Atkins, P.; Overton, T.; Rourke, J.; Weller, M.; Armstrong, F. *Shriver & Atkins' Inorganic Chemistry*; 2010.

(16) Yates, K.; Shapiro, S. A. *Can. J. Chem.* **1972**, *50*, 581.

(17) Walling, C. *J. Am. Chem. Soc.* **1950**, *72* (3), 1164.

Chapter 4

Sugar Conversion to Hydroxymethylfurfural over Niobium Oxides in Water: A Mechanistic Study

Chapter 4 93

4.1 Background 94

4.2 Objectives 99

4.3 Experimental 100

4.3.1 Synthesis of Niobium Oxides 100

4.3.2 Characterisation of Catalyst Acidity 100

4.3.3 Sugar Reactions to HMF over Niobium Oxides 101

4.4 Results and Discussion 102

4.4.1 Catalyst Acidity 102

4.4.2 Sugar Conversion to HMF and Influence of Acidity 108

4.4.3 Reaction Mechanistic Aspects 118

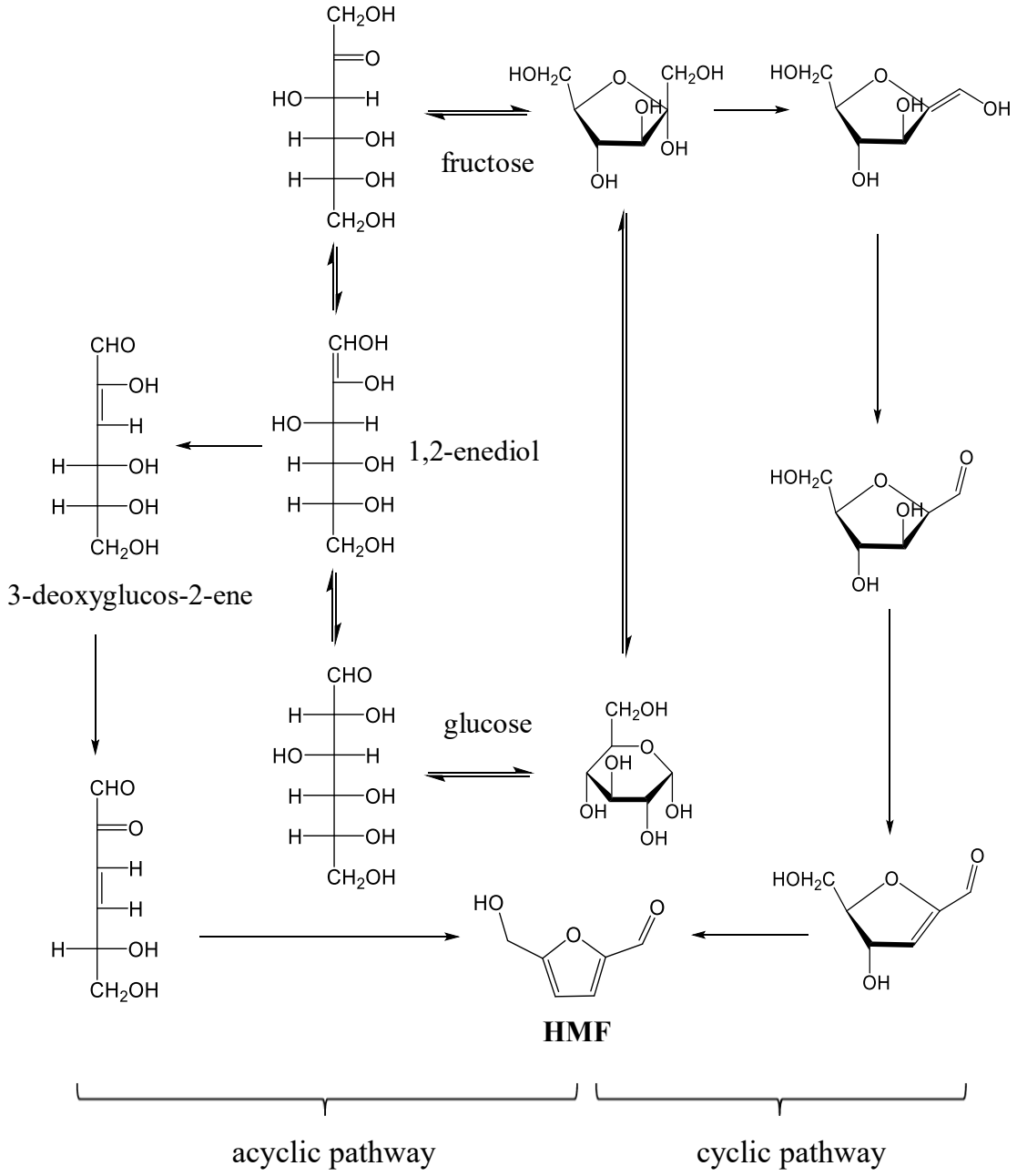
4.5 Conclusions 122

4.6 References 124

4.1 Background

Hydroxymethylfurfural (HMF) is one of the most promising platform molecules in the area of renewable energies and biomass conversion.[1,2] Currently fossil fuels still comprise the main source of energy and platform molecules for the chemical industry, covering almost 80% of the global energy market.[3,4] However, rapidly decreasing fossil fuel reserves and increasing economic demands as well as environmental concerns raise the need for alternative resources, where biomass presents a growing field of interest. Extensive research over past years has led to the establishment of possible routes to convert biomass.[5–8]

HMF is derived from sugar-rich sources such as sugar cane, and further processing yields products such as fuel components, polymers, pharmaceuticals and agrochemicals.[1,9,10] Various acid catalysts, both homogeneous and heterogeneous, have successfully been employed to convert sugars into HMF. Including the use of different solvents, reaction conditions and types of sugar, large amounts of data have been accumulated concerning these processes.[1,2,9,11–13] It has been observed that HMF yield differs significantly with the type of sugar molecule involved. Fructose is generally found to be more reactive and selective towards HMF than glucose. Even though these two sugar molecules are isomers and the same number of water molecules are lost during HMF formation,[2,14] it is not yet clear why there is a significant difference in their rate of conversion. Two main reaction pathways have been proposed in literature, based on different reaction intermediates observed.[1,2] The acyclic pathway proceeds *via* open chain intermediates and involves the formation of 1,2-enediol and 3-deoxyglucos-2-ene from both glucose and fructose.[15,16] The cyclic pathway on the other hand proceeds *via* closed ring intermediates, and glucose conversion proceeds through isomerization to fructose before the further conversion of fructose to HMF (Scheme 4.1).[17–22]



Scheme 4.1 – Acyclic[15,16] *versus* cyclic[17–20] dehydration pathways of glucose and fructose yielding HMF

It has been claimed that catalysts with Lewis and/or Brønsted acid sites are needed to promote the conversion, however there is no agreement amongst researchers which type and strength of acid is required.[21,23,24] For the discussion of cyclic *versus* acyclic pathways, the solvent and its inherent stabilization of cyclic *versus* open-chain forms of the according sugars and

intermediates plays a major role, making comparative mechanistic studies even more complex. In water for example, glucose is almost exclusively present in its pyranose (6-ring) form, while fructose exists in considerable amounts of furanose (5-ring) besides pyranose with fast tautomerisation between the forms, and small amounts of its open-chain form are also present.[1,9] Overall it remains difficult to make a general statement, especially with so many different solvents, reaction temperatures and catalytic materials reported, all of which can influence the on-going reaction mechanism.

In terms of industrial use, the sugar glucose is probably the most interesting starting material for HMF production because of its generally high abundance in biomass feedstocks in the form cellulose.[5,25] Another sugar of relatively low price and ready availability from natural resources is sucrose, found in sugar cane and beet sugar.[26,27] The sucrose molecule consists of a linked glucose and fructose unit and the link can be broken by hydrolysis at elevated temperatures to yield the two monosaccharides.[9,28] Investigating the conversion of sucrose to HMF is therefore closely related to that of glucose and fructose, making it worthwhile to study all three sugars for an in-depth understanding of the mechanisms of conversion.

To find a suitable catalyst for sugar conversion, not only HMF yield and selectivity, but also sustainability and scalability of the production method need to be considered. The use of homogeneous acid catalysts, such as organic acids and ionic liquids, has shown promising results. For example, Zhao *et al.* reported HMF yields of 60 - 70 % through conversion of both glucose and fructose using the catalytic system $CrCl_2$/[EMIM]Cl,[21] and de Souza *et al.* achieved 64 % HMF from fructose in lactic acid.[23] Unfortunately, extensive procedures for product separation and purification are involved in most homogeneous processes.[1,9,11] This makes heterogeneous catalysts industrially more attractive. Regarding solvent use, polar aprotic

solvents and biphasic systems have gained significant interest due to the high HMF yields achieved.[13,17,29,30] Promising results are also shown in combination with heterogeneous catalysts. For example Gallo *et al*. reached 71 % HMF yield from fructose in GVL over Amberlyst-70 and 59 % HMF yield from glucose in GVL (γ-valerolactone) over Amberlyst-70 combined with Sn-ß.[31] Again, the problem with many yield-enhancing organic solvents or extraction phases is difficult product separation due to high boiling points and thermal instability of HMF.[2] On the other hand, using water as solvent does not pose this problem and water is further low in cost and environmentally friendly. Unfortunately, comparably low HMF yields have been obtained so far, mostly due to the low stability of HMF in water.[1,9,11] Niobium oxides have been studied as catalysts in this context, for example de Souza *et al*. obtained 28 % HMF from glucose over NbOH and Carlini *et al*. achieved 29 % HMF from fructose over phosphoric acid-treated NbOH.[23,32] Nakajima *et al.* yielded 12 % HMF from glucose over Nb_2O_5*nH_2O and could increase the yield to 47 % by phosphoric acid treatment of the catalyst, but only at very high catalyst loadings of 10 x the sugar wt%.[33] However, the catalytic processes have not been studied in detail in most works. A better understanding of the on-going reaction mechanisms may help to improve reaction yields, and is worth investigating given the advantages of using water as a solvent.

Niobium oxides are solid acids mostly consisting of interconnected NbO_6 octahedra with varying extents of structural distortions and defects (Figure 4.1a, b). Both Brønsted acid (BA) and Lewis acid (LA) sites are found on niobium oxides, with the individual acidic strength depending on the structural environment.[34–38] In general, BA sites on metal oxides are associated with strongly acidic hydroxyl groups acting as proton donors and LA sites are related to exposed oxygen-deficient cations acting as electron pair acceptors (Figure 4.1c).[33,39–41] In this specific case, LA's are exposed positively charged niobium centers. Depending on the synthetic method, niobium

oxides of different structural features and surface acidity are produced, ranging from bulk to layered to porous materials.[41–43] This results in variations in catalytic activity which, besides influencing product yield and selectivity, can also be useful for the mechanistic study of reactions.

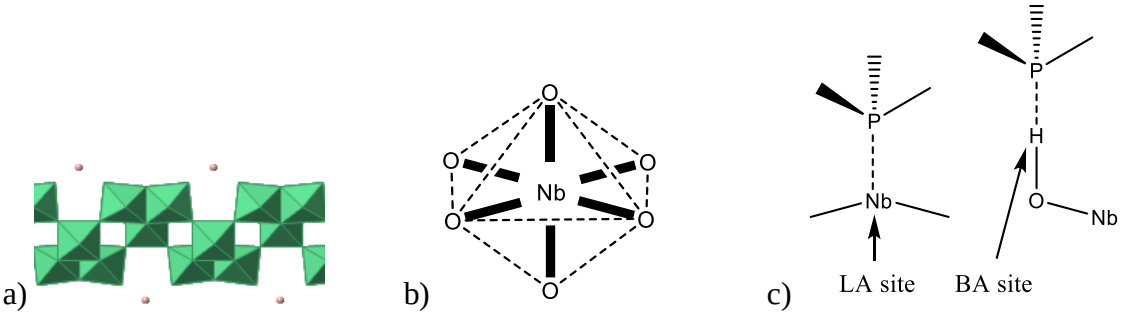


Figure 4.1 – a) Exemplary crystal structure of a niobium oxide (HNb_3O_8) where NbO_6 octahedra are shown in green and protons in pink, b) atomic positions and chemical bonds (in bold) for NbO_6, c) depiction of TMP adsorption to different acid sites

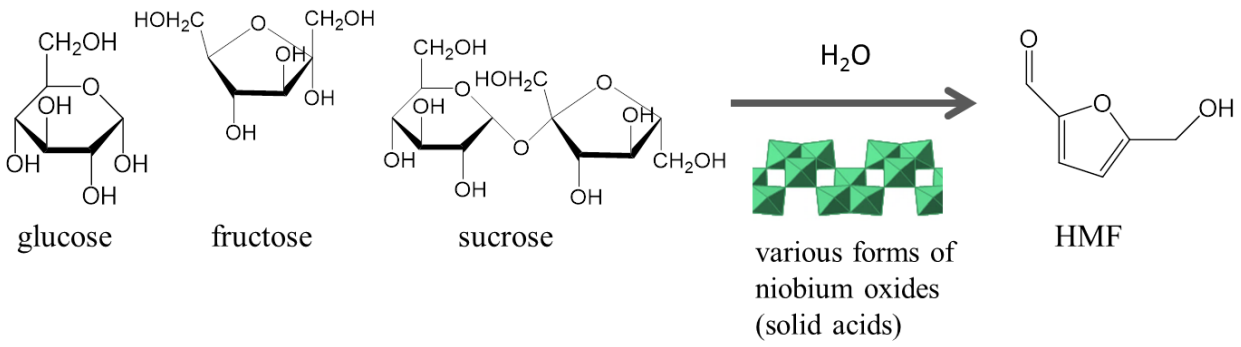
Trimethylphosphine (TMP) ^{31}P NMR is a very useful technique to measure the acid properties of solids. The TMP molecule adsorbs to the acid sites (Figure 4.1c) and, depending on its ^{31}P chemical shift displayed in NMR, the acid type (LA *versus* BA) and acid strength can be determined. Furthermore, the quantification of LA and BA sites is possible from the ^{31}P NMR peak areas.[44–46]

When it comes to catalyzing chemical reactions, Lewis and Brønsted acids can show fundamental differences. The degree to which the activation barrier of a reaction is lowered depends on the interaction strength between the acid and corresponding basic site.[39,47,48] BA's (H^+) are considered hard acids and tend to form stronger bonds with hard bases such as OH^-, H_2O or NH_3 , while soft acids such as Pd^{2+}, Cu^+ or Cd^{2+} react preferably with soft bases such as H^-, CO, R_3P.[49] Consequently, the nature of the cation determines if an LA is hard or soft in character. Besides this intrinsic character, there are other important factors influencing the

interaction strength between acid and base: There are for example steric factors which impact the spatial arrangement, and solvent effects which influence the nature and competitiveness of acid and base. All these effects need to be taken into consideration when it comes to evaluating the catalytic performance of different acids.[39,47,49–51] As discussed previously, this work deals with the surface acidity of niobium oxides and more specifically, the catalytic comparison between BA's (H^+) and LA's (exposed Nb cations) in the conversion of sugars to HMF.

4.2 Objectives

For a scalable and sustainable production of HMF from sugars, catalytic process improvements are needed. This requires both an understanding of the underlying reaction mechanisms and the application of existing knowledge to an industrial and environmental context. In this work, the conversion of glucose, fructose and sucrose to HMF is studied systematically over a variety of structurally related niobium oxides, using water as the solvent (Scheme 4.2). Furthermore, the catalyst acidity is investigated in detail using ^{31}P TMP NMR. The aim is to discover the reaction steps and required catalytic features involved in the conversion of each sugar by relating catalytic activity and acidity. Finally, it is hoped that the results will help to synthesize more efficient catalysts for this reaction in the future.



Scheme 4.2 – Experimental overview: sugar conversion to HMF over niobium oxides in water

4.3 Experimental

This section provides a summary of the experimental procedures used, a detailed description can be found in Chapter 3.

4.3.1 Synthesis of Niobium Oxides

A variety of niobium oxides, ranging from bulk to multi- to monolayer structures, were synthesized by Keizo Nakagawa. The bulk material HNb_3O_8 was prepared by a conventional solid-state reaction of the precursors K_2CO_3 and Nb_2O_5, followed by proton exchange. Few layer niobium oxide (hy-Nb) and monolayer niobium oxide (hy-Nb-TEOA) were synthesized hydrothermally from $Nb(OEt)_5$ in ammonia solution, and in the case of hy-Nb-TEOA under further addition of triethanolamine (TEOA). Both materials were acid treated before use in order to remove the basic surfactant species blocking the surface acid sites. Mesoporous $Nb_2O_5*nH_2O$ (meso Nb_2O_5) was prepared by hydrolysis and condensation of $Nb(OEt)_5$, followed by soaking in acid solution. Detailed synthetic procedures and literature references are given in Chapter 3. For comparison, commercial bulk Nb_2O_5 (Alfa Aesar) was used.

4.3.2 Characterisation of Catalyst Acidity

Acidity measurements were done by two different techniques: The acid sites were first characterised using conventional Hammett indicators. A series of Hammett indicators were used to determine the acid strength (pK_a), followed by titration with n-butylamine for acid site quantification.[37,39,52] A second study, employing trimethylphospine (TMP) adsorption followed by ^{31}P MAS NMR measurements, was conducted by Yung-Kang Peng. The acid type, LA or BA, and acid strength can be clearly differentiated by the ^{31}P chemical shift of TMP due to the

variations in interaction strength of the adsorbed TMP molecule with different acid sites. The acid sites were further quantified by ^{31}P NMR peak area integration.[44–46,53]

4.3.3 Sugar Reactions to HMF over Niobium Oxides

Reactions were performed separately with aqueous solutions of glucose, fructose and sucrose over the different niobium oxides. A mixture of 150 mg sugar in 15 mL water and 150 mg catalyst were charged to a Parr autoclave under atmospheric conditions. The reactions were heated to 180 °C under stirring and were run over different time lengths in a range between 1 and 180 minutes. The formation of HMF and the sugar consumption were monitored over time by analyzing the collected samples using high performance liquid chromatography (HPLC).

4.4 Results and Discussion

For reference, parts of this chapter including figures and tables have been published by the author in Journal of Catalysis, 2016.[54]

4.4.1 Catalyst Acidity

In terms of catalyst characterisation, this chapter focuses on measuring and comparing acid properties of the different niobium oxides. As described in the introduction, surface acidity is relevant for the conversion of sugars to HMF[1,23,24] and the here presented study gives insights into the catalytic mechanisms. Additionally, to help visualize the structural differences amongst the niobium oxides, TEM imaging was used and surface areas were determined by BET nitrogen adsorption measurements (see Appendix p.A1-A2 for BET adsorption-desorption isotherms and surface area calculations).

The niobium oxide samples display significant differences with respect to surface area and similarly large variations are found regarding acidity (Table 4.1 and Figure 4.2). Comparing the TMP NMR acidity and Hammett indicator measurements shows that TMP NMR provides more detailed information. By means of the ^{31}P chemical shift, Brønsted acid (BA) and Lewis acid (LA) sites are easy to differentiate and variations in acid strength of both sites can further be determined. Hammett indicators are useful to visualize the range of acid strengths of the niobium oxides, but they fail to deliver precise values because of the limited number of commercially available indicators within the required pK_a range. Furthermore, a differentiation between BA's and LA's is unfortunately not possible with Hammett indicators. In terms of acid site quantification TMP NMR is also more accurate, since titration with Hammett indicators poses

problems such as color change/end point determination, mass transfer limitations and catalyst dispersion.[37,39,55]

Table 4.1 – Surface area and acid site analysis of the niobium oxide catalysts

Catalyst	SA ($m^2 g^{-1}$)	Acid sites by TMP ^{31}P NMR signal area ($\mu mol\ g^{-1}$)	Acid strength/type by TMP ^{31}P NMR shift (ppm)	Acid strength by Hammett indicator (pK_a)	Acid sites by Hammett titrations ($\mu mol\ g^{-1}$)
Nb_2O_5	3	ND	ND	ND	ND
HNb_3O_8	10	BA (30) no LA	BA: - 2.77	$-5.6 < pK_a < -3.0$	50[a] ; 100[b]
hy-Nb-TEOA	121	BA (171) LA (108)	BA: - 0.36 LA: - 24.98	$-5.6 < pK_a < -3.0$	300[a] ; 200[b]
hy-Nb	166	BA(259) LA(269)	BA: - 0.87 LA: - 42.27	$-5.6 < pK_a < -3.0$	800[a] ; 600[b]
meso Nb_2O_5	142	BA(338) LA(222)	BA: - 5.47 LA: - 25.37	$-5.6 < pK_a < -3.0$	600[a] ; 550[b]

SA: surface area obtained from BET nitrogen adsorption measurements (also see Appendix p.A1-A2),
BA: Brønsted acid site, LA: Lewis acid site
[a] values obtained using dicinnamalacetone indicator in benzene
[b] values obtained using methyl red indicator in water

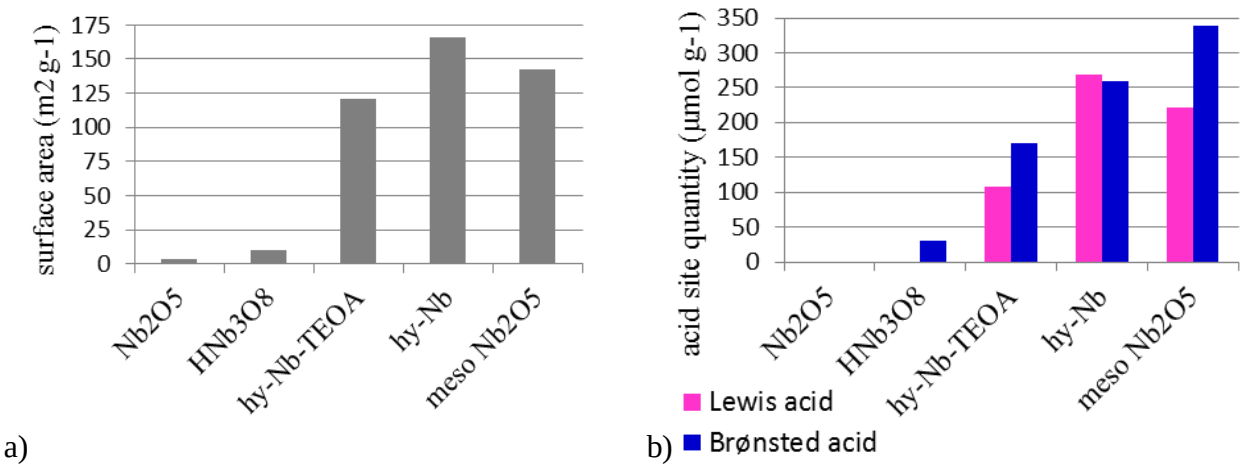


Figure 4.2 – a) Surface areas and b) acid site quantities of the niobium oxide catalysts

Although the values obtained using Hammett indicators are not as precise as those from TMP NMR, both techniques show the same trend: the total amount of acid sites increases in the order of Nb_2O_5 << HNb_3O_8 < hy-Nb-TEOA < hy-Nb < mesoporous Nb_2O_5*nH_2O, which is closely related to their surface areas (Table 4.1 and Figure 4.2). Commercial Nb_2O_5, consisting of interconnected NbO_6 octahedra,[34,41] clearly appears as a bulk material from TEM (Figure 4.3 a). Its low surface area accounts for the fact that the acid site quantity is below the detection limits (about 1 µmol g^{-1}) for both TMP NMR and Hammett measurements. Although HNb_3O_8 (Figure 4.3 b) is also in bulk form, it shows more irregularities on particle edges and a sheet-like structure, resulting in a higher surface area and more acid sites. For hy-Nb (Figure 4.3 c) and hy-Nb-TEOA (Figure 4.3 d), much smaller and thinner nano-sheet like fragments are observed leading to considerably higher surface areas. Previous work has shown that their structures resemble that of bulk HNb_3O_8 with alternating layers of protons and niobate sheets, but in few-layer form for hy-Nb and few- to monolayer form for hy-Nb-TEOA.[42,52,56,57]

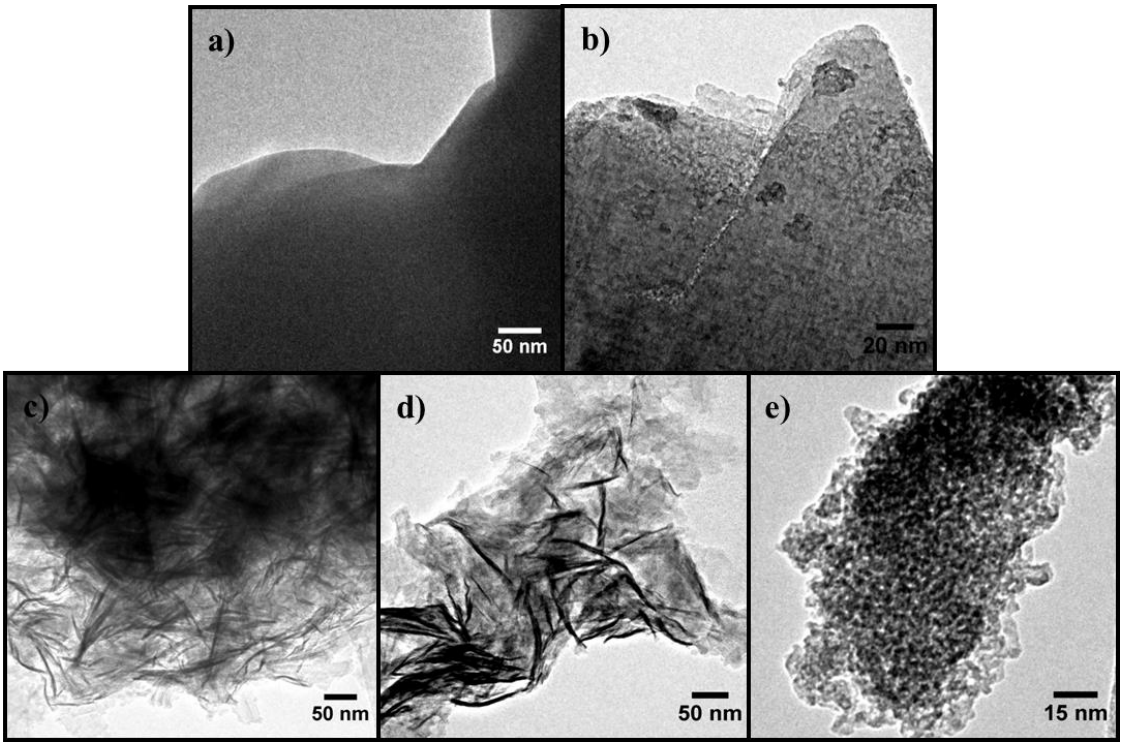


Figure 4.3 – TEM images of a) Nb_2O_5, b) HNb_3O_8, c) hy-Nb, d) hy-Nb-TEOA, e) mesoporous $Nb_2O_5*nH_2O$

Using TEOA as a surfactant during the synthesis can restrict structural growth along the c-axis, which results in down to monolayer formation. However, it should be noted that the hy-Nb-TEOA used in this work was acid treated after the synthesis, resulting in removal of TEOA and the exposure of the catalyst acid sites. This presumably leads to a significant degree of layer re-stacking for hy-Nb-TEOA, explaining the larger surface area and larger acid quantity measured for hy-Nb compared to hy-Nb-TEOA. Finally, mesoporous $Nb_2O_5*nH_2O$ (meso Nb_2O_5, Figure 4.3 e) displays a worm-like structure with many pores and holes in a wide size range of 0.5 – 50 nm diameter, accounting for the amorphous structure with a high surface area and large amount of acid sites (also see Appendix p.A3-A4 for pore size analysis).

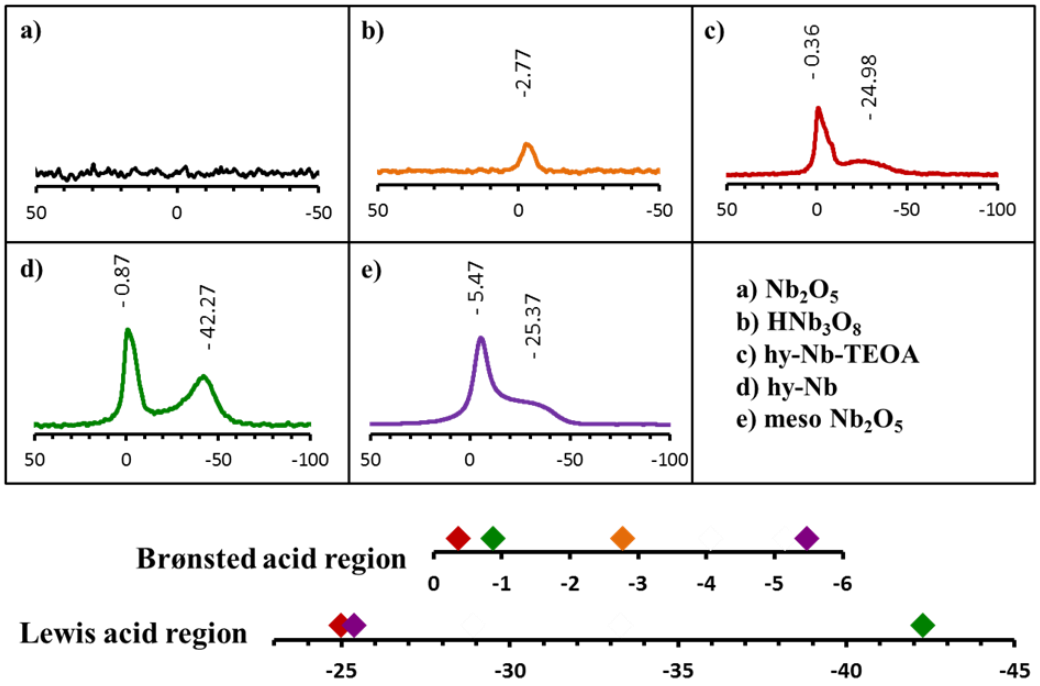


Figure 4.4 – TMP ^{31}P NMR spectra of the niobium oxide catalysts displaying BA and LA strength by means of chemical shift, and BA and LA quantity by peak area

Looking at the TMP NMR data in more detail, it can be seen that there are two separate NMR regions for BA and LA sites, and a further differentiation in acid strength within each region is possible by interpreting the chemical shift (Figure 4.4). In agreement with literature, peaks in the region between about 0 to -7 ppm correspond to BA sites and peaks in the region between about -20 to -50 ppm correspond to LA sites.[44–46] Regarding the differences in acid strength within each region, a less negative shift value signifies a stronger acidity. In the BA region, broad peaks were observed with peak maxima ranging from -0.36 and -0.87 ppm for hy-Nb-TEOA and hy-Nb, to -2.77 ppm for HNb_3O_8, and finally to -5.47 ppm for mesoporous Nb_2O_5*nH_2O.

It should be noted that strongly acidic BA sites on Group IV-VI oxides are generally associated with bridging hydroxyl groups between octahedra with shared edges or faces, while weaker BA sites correspond to terminal hydroxyl groups (Figure 4.5 b, d).[29,32] As a result, the analysis of BA

sites by TMP NMR can reflect the degree of connectivity of NbO_6 octahedra over the different forms of niobium oxides. Mesoporous $Nb_2O_5*nH_2O$ appears to possess mainly corner shared octahedra giving rise to terminal hydroxyls, which is expressed by a comparably weak BA peak at -5.47 ppm. On the other hand, the structure of HNb_3O_8 is reported to contain stacked NbO_6 octahedra with shared edges or faces (Figure 4.5 a).[42,52,56] This can lead to stronger acidic bridging hydroxyls in addition to the weaker acidic terminal hydroxyls (Figure 4.5 b) and HNb_3O_8 shows an overall intermediate chemical shift of -2.77 ppm. Hy-Nb and hy-Nb-TEOA are structurally similar to HNb_3O_8 but with reduced layer thickness, as discussed previously. The increased BA strength of hy-Nb and hy-Nb-TEOA (-0.87 and -0.36 ppm) compared to HNb_3O_8 is likely the result of increased structural distortion and defects due to the layer separation. This could also explain why hy-Nb and hy-Nb-TEOA possess LA sites as opposed to HNb_3O_8. LA sites are formed when the oxygen-surrounded, positively charged niobium centers become exposed, which likely results from distortion or removal of oxygens when downscaling from the bulk to the few-layer materials (Figure 4.5 c, d). Interestingly, hy-Nb possesses LA sites which are more abundant but weaker than hy-Nb-TEOA, indicating some degree of structural difference even amongst the two few-layer materials. Mesoporous $Nb_2O_5*nH_2O$ possesses large amounts of LA sites similar to hy-Nb and its LA strength is comparable to that of hy-Nb-TEOA. Structural distortion or a reduced number of Nb-surrounding oxygens is therefore also expected here. As a side note, structure and acidity are investigated in more detail in Chapter 5.

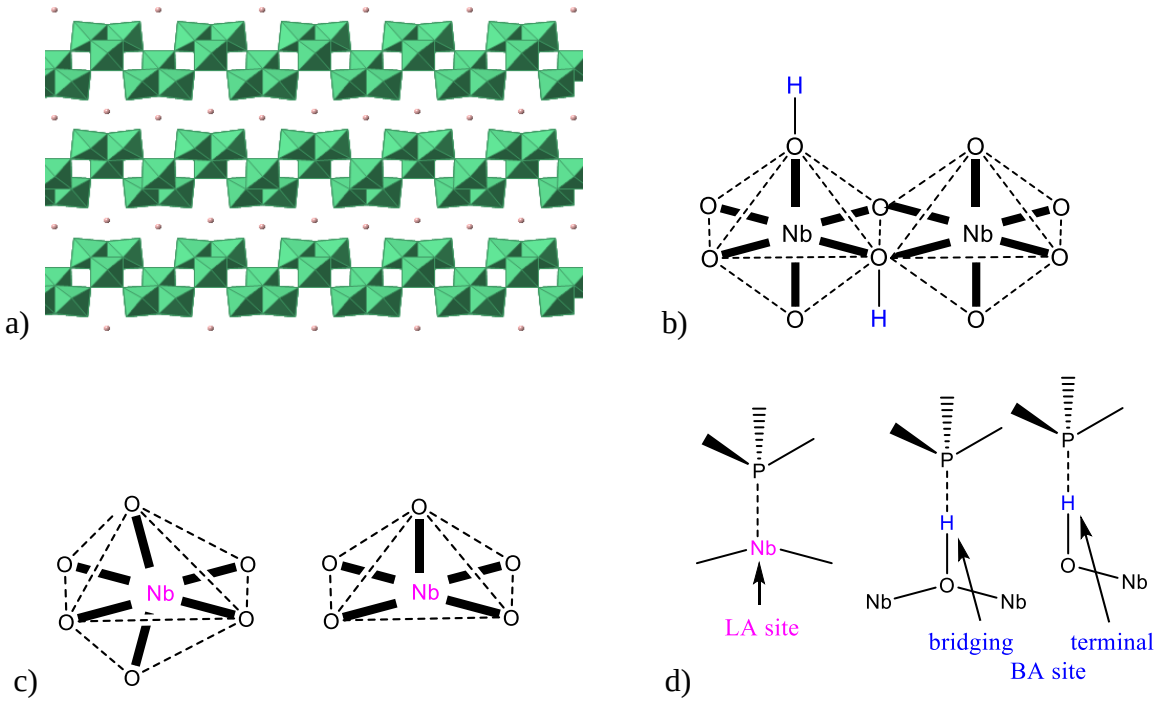


Figure 4.5 – a) Crystal structure of HNb_3O_8: alternating layers of interconnected NbO_6 octahedra and protons
b) Schematic drawing of bridging and terminal hydroxyl groups giving rise to BA sites on interconnected NbO_6 octahedra, atomic bonds in bold
c) Schematic drawing of distorted NbO_6 octahedra and oxygen vacancies giving rise to LA sites by exposure of Nb center, atomic bonds in bold
d) Schematic drawing of TMP adsorption on LA and BA sites

4.4.2 Sugar Conversion to HMF and Influence of Acidity

The HMF yields obtained from sugar conversion over niobium oxides in water are given in Table 4.2. Although HMF is the main product of the catalytic sugar reactions, the overall reaction system is complex and involves the formation of several side products, which is common for this research area. The main side products observed in this work are sugar-derived poly-alcohols and organic acids such as 1,6-anhydroglucose, glyceraldehyde, levulinic acid and formic acid. Some examples of side product yields and according mass balance estimations are given in Table 4.3 (also see Appendix p.A4-A9 for HPLC spectra and yield calculations).

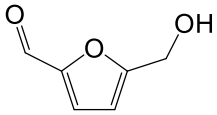
General observations regarding sugar conversion are that fructose is converted faster than glucose under the same reaction conditions, as expressed in the glucose and fructose conversion profiles over time (Figure 4.6 a-f). Fructose also tends to give higher HMF yields than glucose, which is consistent with previous reports in literature.[14–19] It is interesting to note that although the general trend is for fructose to give higher HMF yields, some of the catalysts tested here reach similar yields for both glucose and fructose. This suggests that glucose can be converted to HMF as efficiently as fructose, if the acid catalytic properties are appropriate.

Regarding sucrose conversion, it was found that HMF yields are intermediate to those of glucose and fructose. HPLC analysis further shows that sucrose degradation is fast, with its components glucose and fructose being detected instantly and then decreasing over time, in a manner comparable to the conversion of pure glucose and fructose (Figure 4.6 a-f). This result indicates that sucrose is readily hydrolyzed into its two components glucose and fructose at high temperatures, and that HMF is then formed from both individually. This explains why the HMF yields from sucrose are intermediate to those from glucose and fructose.

As sugar conversion is a very complex process involving the formation of many side products besides the desired product HMF, the calculation of catalytic activity is non-trivial (also see Appendix p.A11-A13): If initial sugar conversion rates were compared to look at catalytic performance, the problem arises that not all sugar molecules are converted to the product of interest, HMF. If instead choosing to monitor initial HMF production, this still poses the difficulty that HMF itself is converted further to products such as levulinic and formic acid. Therefore the catalyst with the highest catalytic activity in HMF formation does not necessarily give the highest HMF yield. For example, a highly acidic catalyst A showing both a fast formation and a fast degradation of HMF, can give a lower maximum HMF yield than a less

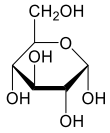
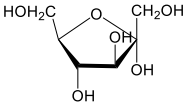
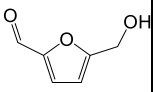
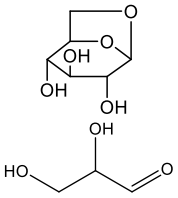
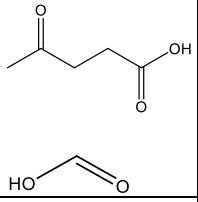
acidic catalyst B with a lower rate of HMF formation but insignificant further degradation. As a result, the maximum HMF yield obtained over each catalyst has been chosen as the method of comparison for catalytic performance in this work.

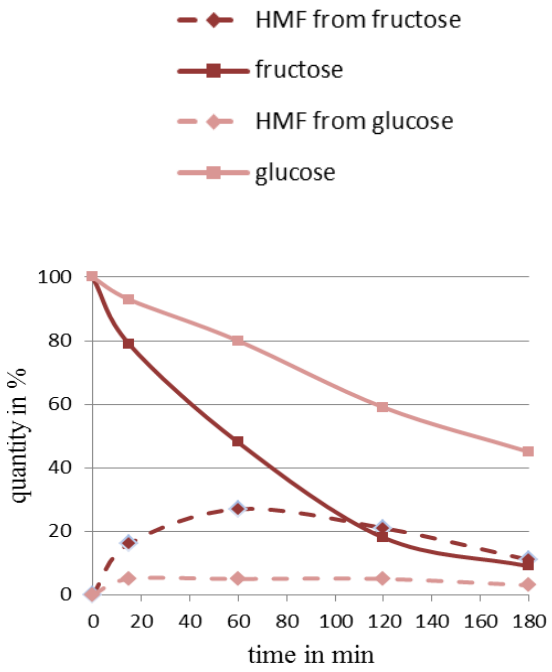
Table 4.2 – Experimental results of sugar conversion over niobium oxides in water

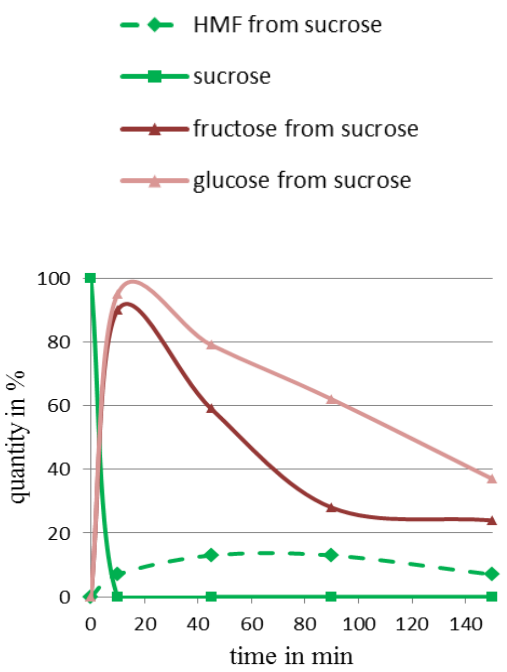
Catalyst	Sugar	Maximum HMF yield (%) 
None	Glucose	5
	Fructose	27
	Sucrose	13
Nb_2O_5	Glucose	13
	Fructose	27
	Sucrose	17
HNb_3O_8	Glucose	18
	Fructose	34
	Sucrose	25
hy-Nb-TEOA	Glucose	28
	Fructose	27
	Sucrose	27
hy-Nb	Glucose	32
	Fructose	30
	Sucrose	32
meso Nb_2O_5	Glucose	36
	Fructose	36
	Sucrose	36

Reactions were performed at 180 °C using 150 mg sugar in 15 mL water with 150 mg catalyst

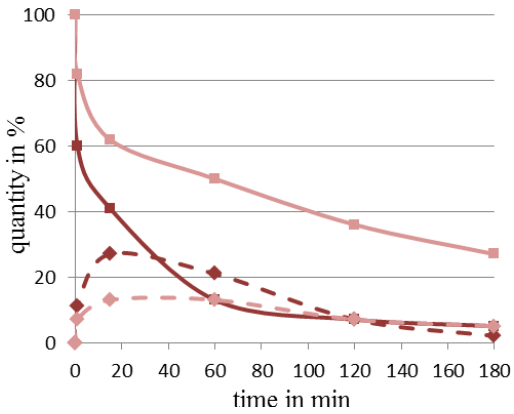
Table 4.3 – Exemplary product distribution and mass balance from sugar reactions

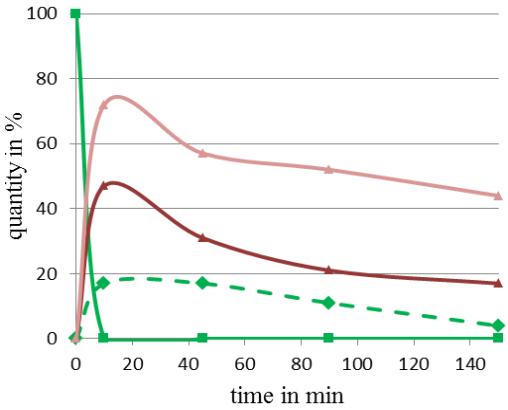
Sugar reaction	Yields of observed products from HPLC					Estimated yield of humins (solid carbon residues)
	Glucose 	Fructose 	HMF 	Poly-alcohols 	Organic acids 	
Glucose over meso Nb_2O_5 after 10 min	3 %	1 %	36 %	30 %	12 %	18 %
Fructose over HNb_3O_8 after 10 min	3 %	23 %	34 %	21 %	5 %	14 %
Sucrose over hy-Nb after 5 min	32 %	10 %	25 %	13 %	5 %	15 %



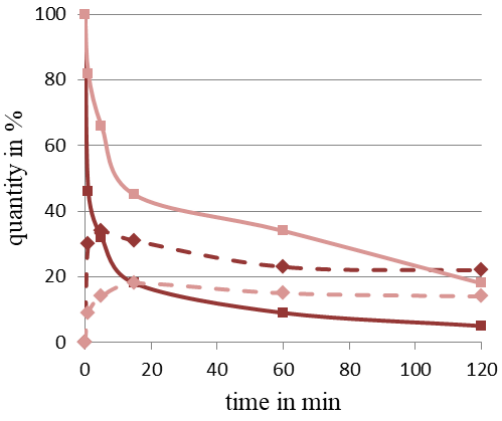


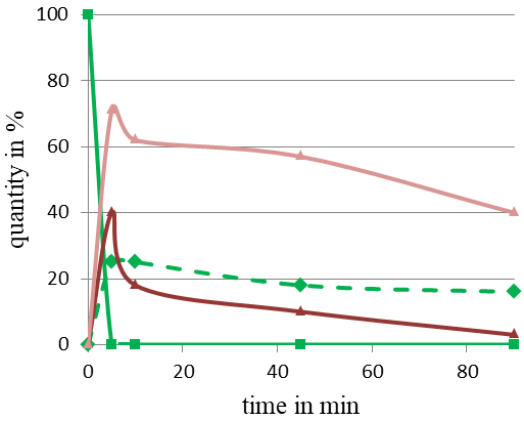
a) **no catalyst**: glucose and fructose conversion sucrose conversion



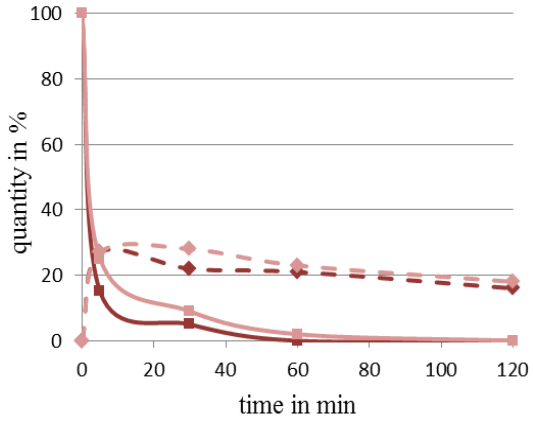


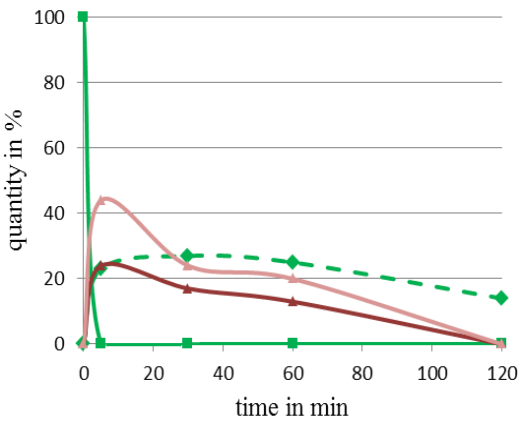
b) **Nb_2O_5**: glucose and fructose conversion sucrose conversion



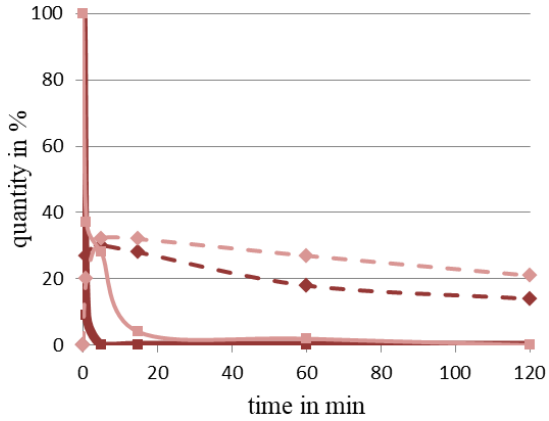


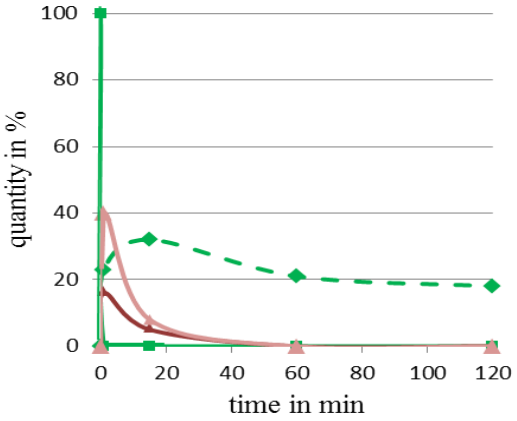
c) **HNb_3O_8**: glucose and fructose conversion sucrose conversion



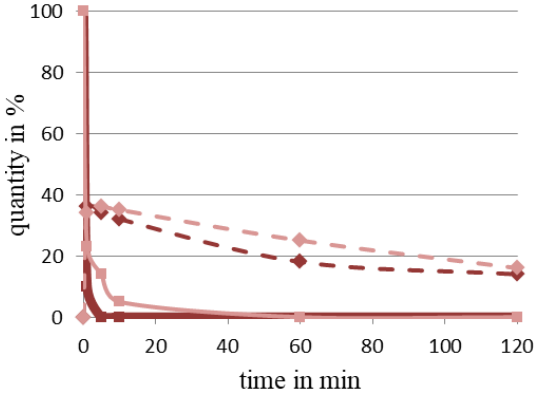


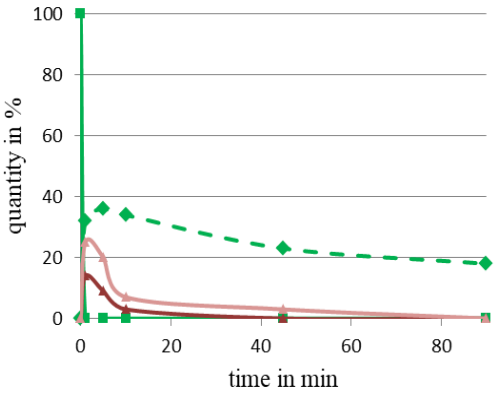
d) **hy-Nb-TEOA**: glucose and fructose conversion sucrose conversion





e) **hy-Nb**: glucose and fructose conversion sucrose conversion





f) **meso Nb_2O_5**: glucose and fructose conversion sucrose conversion

Figure 4.6 – Profiles of sugar conversion over time:
glucose, fructose to HMF and sucrose to glucose, fructose, HMF over
a) no catalyst, b) Nb_2O_5, c) HNb_3O_8, d) hy-Nb-TEOA, e) hy-Nb, f) meso Nb_2O_5

Regarding the maximum HMF yield obtained over each catalyst (Table 4.2 and Figure 4.7), the following order is observed for glucose conversion: mesoporous Nb_2O_5*nH_2O (36 %) > hy-Nb (32 %) > hy-Nb-TEOA (28 %) > HNb_3O_8 (18 %) > Nb_2O_5 (13 %) > no catalyst (5 %). Interestingly, the order for HMF yield from fructose is found to be different from that of glucose, with mesoporous Nb_2O_5*nH_2O (36 %) > HNb_3O_8 (34 %) > hy-Nb (30 %) > hy-Nb-TEOA (27 %) = Nb_2O_5 (27 %) = no catalyst (27 %).

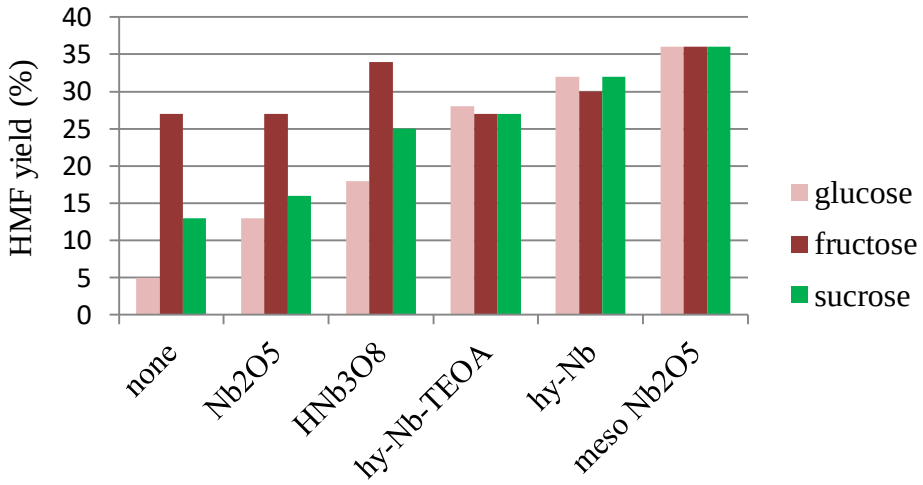


Figure 4.7 – Maximum HMF yields obtained from glucose, fructose and sucrose over the different niobium oxides

For fructose, larger amounts of acid sites have a positive effect on the rate of reaction with faster conversion for higher acid quantities, as would be expected (Figure 4.6 a-f and Table 4.1). Accordingly, the maximum HMF yield is also reached faster for higher acid site quantities. For catalysts of comparable acid site nature it would further be expected that the maximum HMF yield is similar - only reached at different rates - or slightly larger for higher acid site quantities, with conversion processes not taking place on acid sites becoming less kinetically competitive. Experimentally however it is shown that maximum HMF yield varies significantly between 27 % and 36 %, and further does not correlate with acid site quantities. Instead, the key factor for HMF selectivity appears to be the variations in acid site type and strength found among the

catalysts. An inverse correlation between HMF yield and BA strength is noted for fructose: the lower the BA site strength, the higher the HMF yield. For example, hy-Nb-TEOA, with -0.36 ppm TMP ^{31}P NMR chemical shift showing the strongest BA (Figure 4.4), gives only 27 % HMF (the same as without catalyst) < hy-Nb (-0.87 ppm) with 30 % HMF < HNb_3O_8 (-2.77 ppm) with 34 % HMF < mesoporous $Nb_2O_5*nH_2O$ (-5.47 ppm) with 36 % HMF. No apparent correlation can be found for LA strength and even further the presence of LA sites does not seem to significantly affect fructose conversion, for example similar HMF yields are obtained from HNb_3O_8 (no LA) and mesoporous $Nb_2O_5*nH_2O$ (with 222 µmol g^{-1} large LA quantity).

Overall, this leads us to conclude that for fructose conversion, the presence of LA sites does not significantly affect HMF yield while the presence of BA sites increases HMF yield, with weaker BA sites being better promoters than stronger BA sites. This underlines the differences in catalytic nature of LA's (exposed positively charged Nb centers) *versus* BA's (H^+) and even amongst BA's (weak *versus* strong). It appears that in this particular case LA's cannot act as stabilizers for the transition steps from fructose to HMF, while weak BA's can. Strong BA's on the other hand are less selective, likely due to the enhancement of several catalytic processes with more side product formation.

As a control experiment, fructose was converted using HCl (aq), a much weaker BA than those on niobium oxide surfaces, due to the formation of H_3O^+.[58] Indeed, much higher HMF yields were obtained at a comparably low rate of conversion (maximum HMF yield 63 % from 0.01 M HCl after 30 min and 49 % from 0.001 M HCl after 45 min), with the HCl concentration range being comparable to the BA site concentrations of the niobium oxide catalysts. Possible chloride ion interference was ruled out in another control experiment by adding sodium chloride to the sugar solution, which gave the same result as using no catalyst. It is evident that HCl, forming

H_3O^+ and Cl^- in water, with a much weaker Brønsted acidity (pK_a (H_3O^+) = - 1.74)[41] than our solid acid catalysts (-5.6 < pK_a < -3.0, Table 1), is significantly more selective in the conversion of fructose to HMF. A similar example from literature is the hydrolysis of transition metal chlorides in water giving H_3O^+ for high conversion of fructose to HMF.[22] The comparably high HMF yield of 27 % obtained from fructose in water without catalyst might also be due to the enhancing effect of H_3O^+: very small concentrations of H_3O^+ (10^{-14} mol L^{-1} at 25 °C) are present due to the natural dissociation of water, which increases with temperature.[58] Although the H_3O^+ quantities in pure water are very low, the HMF yield from fructose in water is comparable to that obtained over hy-Nb-TEOA with strong but less selective BA, only at a slower rate of reaction. Apart from weaker BA's more effectively promoting HMF selectivity than stronger BA's, another observation was made from these results regarding the nature of niobium oxides in water: even when using water as the reaction medium the strong BA sites (H^+) on niobium oxides remain mostly intact and do not significantly form weak BA adducts with water (H_3O^+). Evidence for this can also be found in literature: niobium oxides, as opposed to many other solid catalysts, retain their acid site activity in water.[36,37,40] For example Nakajima *et al.* have shown BA sites to remain fully intact, and LA sites partially intact.[33]

For glucose, the increase in HMF yield using niobium oxides as compared to no catalyst is much more apparent than for fructose (Figure 4.7). This indicates that different acid catalyzed reaction steps are involved in the conversion of glucose. Glucose conversion over the catalysts is also significantly faster than without catalyst, indicating that non-acid site catalyzed processes are hardly competitive (e.g. accounting for 4/32 = 1/8 of products in the case of Nb_2O_5 and even less competitive for the other niobium oxides, compare reaction rates Appendix p.A12). For catalysts of comparable acid site nature it would therefore be expected that acid quantity dependent rate differences but no large variations in maximum HMF yield are found (max. 13/ (7/8) x 1/8 = 1.9

% more HMF for other catalysts compared to Nb_2O_5). However, as already seen for fructose conversion, there are significant differences in acid site nature (type and strength) among the catalysts. Accordingly large variations in maximum HMF yield are also observed for glucose: HMF yields increase in the order of no catalyst (5 %) < Nb_2O_5 (13 %) < HNb_3O_8 (18 %) < hy-Nb-TEOA (28 %) < hy-Nb (32 %) < mesoporous $Nb_2O_5*nH_2O$ (36 %). As for fructose, a control experiment using 0.01 M HCl (aq) was carried out, yielding 7 % HMF. This is only a small increase in HMF yield compared to no catalyst. When using the much stronger solid BA catalyst HNb_3O_8, significantly more HMF (18 %) can be obtained, indicating that strong BA sites promote glucose conversion, while the effects of weaker BA's are marginal. Even better performances are shown by the niobium oxides which possess LA sites in addition to BA sites - hy-Nb-TEOA yielding 28 % HMF, hy-Nb yielding 32 % HMF and mesoporous $Nb_2O_5*nH_2O$ yielding 36 % HMF (Figure 4.2 b and Figure 4.7). Interestingly for these catalysts, glucose conversion reaches about the same HMF yields as fructose conversion, demonstrating the superior capability of LA's to convert glucose. On the other hand, LA strength does not correlate to HMF yield; it appears that the variations in LA strength present amongst our catalysts are not significant for HMF selectivity (Table 4.1).

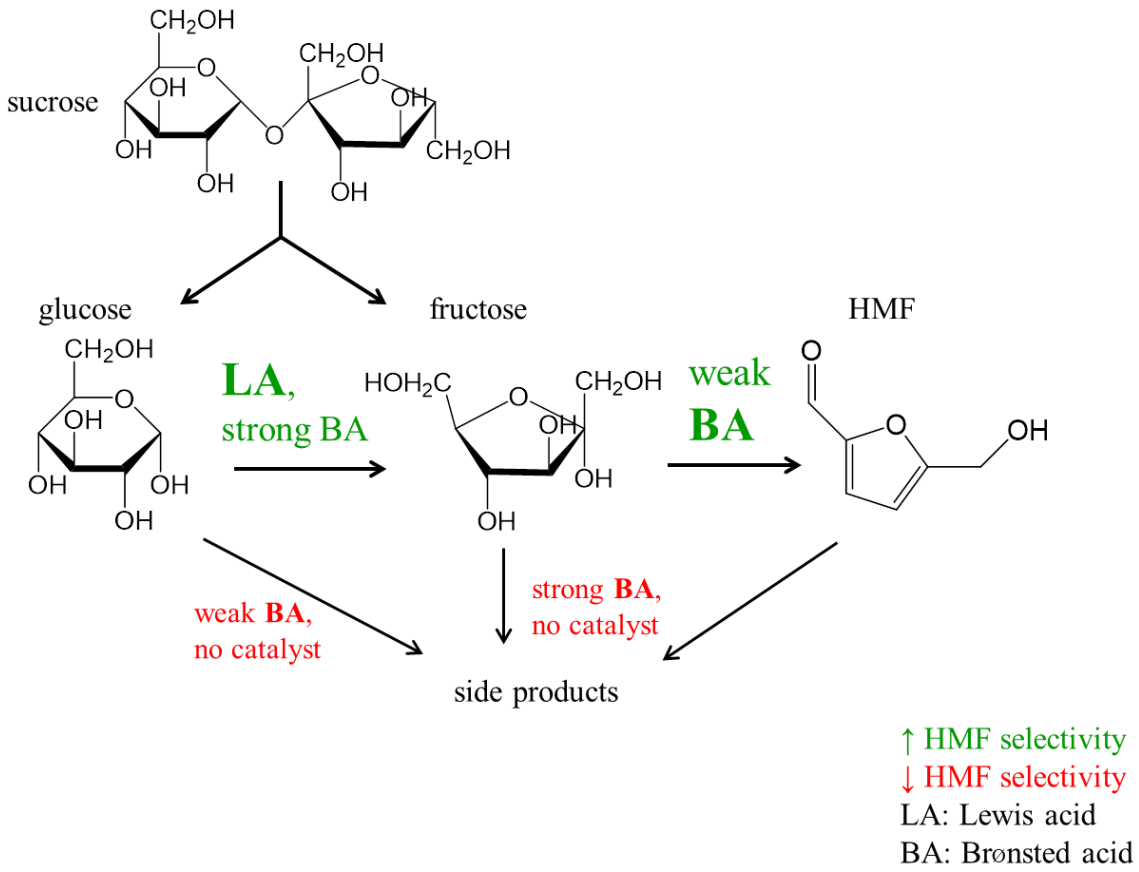
Overall it is shown that glucose conversion is catalyzed primarily by LA sites (exposed positively charged Nb centers) and to a lesser extent by strong BA sites (H^+), with weak BA sites having an insignificant contribution to the activity. Interestingly, the here required catalytic nature is substantially different to that for fructose. Further, for all catalysts HMF yield from glucose can reach up to, but hardly exceeds that from fructose.

4.4.3 Reaction Mechanistic Aspects

The above experimental discussion has shown that the conversion of fructose to HMF is catalyzed by BA's, while glucose to HMF conversion is promoted primarily by LA sites. The acyclic conversion pathways reported in literature suggest the formation of common key intermediates from enol-keto tautomerism for both glucose and fructose,[1,15,16] thus a similar nature of acid sites for acyclic catalytic conversion would be expected. In fact, both glucose and fructose transitions *via* 1,2-enediol and 3-deoxyglucos-2-ene are expected to be base and LA catalyzed (Lobry de Bruyn-Alberda van Ekenstein transformation).[17,58,59] However, this work has shown that fructose conversion to HMF is BA catalyzed. Further, fructose in water is present in considerable amounts (32 %) in cyclic 5-ring form (furanose) which has structural similarity to HMF.[1,60] Both make it likely that fructose conversion to HMF in water proceeds *via* the cyclic pathway proposed in literature rather than the acyclic (Scheme 4.1). For glucose, the cyclic pathways in literature suggest its isomerization to fructose as an additional rate-limiting step before the conversion of fructose to HMF.[17–22] This additional step could explain why different acid catalytic requirements for glucose *versus* fructose conversion were observed in this work. Cyclic conversion routes for both glucose and fructose also appear reasonable from a stability point of view, where the cyclic sugar forms are more stable than the acyclic and dominant in water.[1,60]

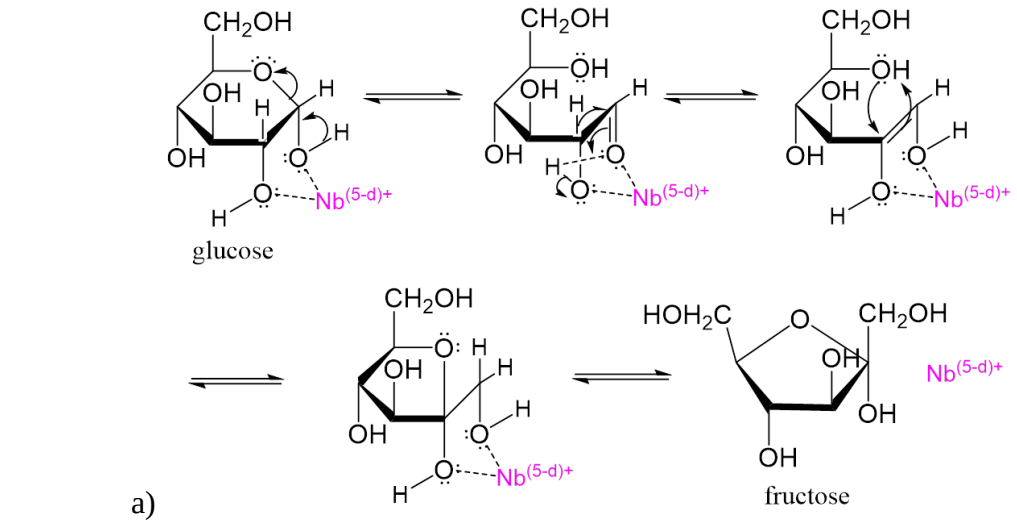
It should also be noted that glucose reaction solutions in HPLC product analysis contained up to 14 % fructose throughout the reaction process, indicating that significant sugar isomerization took place (also see Appendix p.A10). This goes in line with fructose being a reaction intermediate in the formation of HMF, but is no proof yet. However, it was further shown experimentally that HMF yield from glucose can approach, but hardly exceeds that from fructose, which strongly indicates a step-wise conversion with fructose as the key intermediate.

Overall, these observations suggest that glucose and fructose conversions to HMF proceed mainly *via* the cyclic pathway under the given reaction conditions. Scheme 4.3 summarizes the step-wise reaction mechanism: glucose to fructose isomerization is catalysed by strong BA and LA sites, with LA sites being much more selective towards HMF formation. Weak BA's on the other hand are effective for the conversion of fructose to HMF. Sucrose, as shown previously, is easily hydrolysed into its components glucose and fructose at high temperatures and HMF is formed from their further conversion. Unfortunately side reactions still play a significant role in sugar conversion to HMF in water, with up to 50 % side products at maximum HMF yield; therefore they are also included in Scheme 4.3.

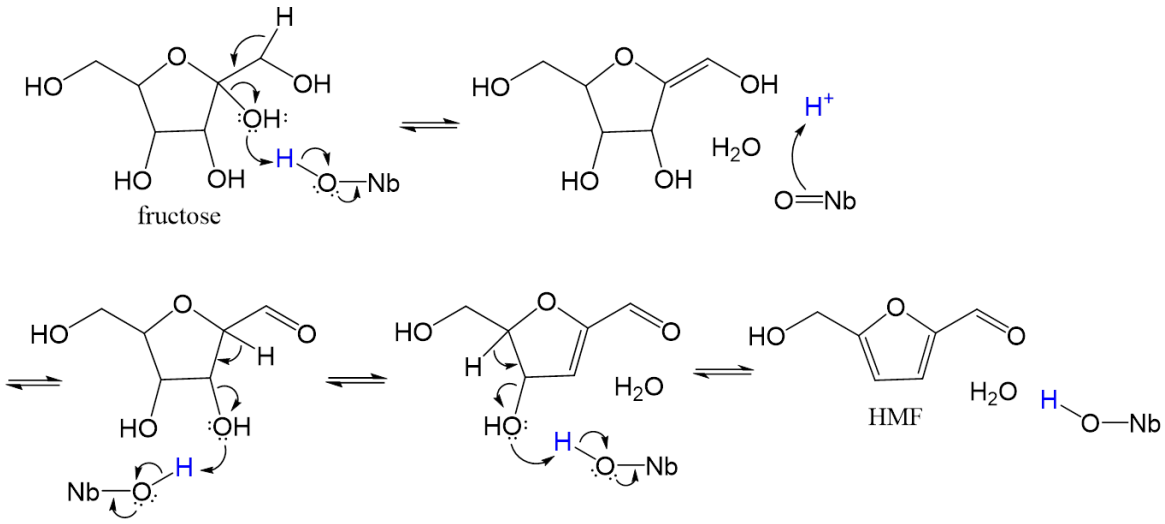


Scheme 4.3 – Catalytic steps of sucrose, glucose and fructose conversion to HMF

Finally, Scheme 4.4 visualizes what the catalytic interactions between sugar molecules and acid sites could look like on a molecular level. The scheme is based on the above findings on catalyst structure and reaction mechanisms, as well as depictions of sugar reactions[14,61–63] in literature. For the glucose to fructose isomerization step (LA catalysed), we propose that the reaction proceeds primarily on exposed $Nb^{(5-\delta)+}$ centres of distorted NbO_6 octahedra (Scheme 4.4 a). This can be rationalized by the Nb centre (LA) stabilizing the 1,2-enediol intermediate by forming a cyclic transition state, which is energetically more favourable than H^+ stabilization due to the larger size of the Nb active site with d-band interaction. On the other hand, the conversion of fructose to HMF is BA catalysed, promoted mainly by weaker acidic terminal hydroxyls (Scheme 4.4 b) while stronger bridging hydroxyls cause increased side product formation. BA sites being better catalysts than LA sites can be explained by the favourable interaction of H^+ as a hard acid with fructose OH groups as hard bases under the formation of water, while the Nb sites as softer acids are less effective.



a)



b)

Scheme 4.4 – a) Glucose to fructose isomerization *via* LA-1,2-enediol intermediate
b) Fructose to HMF conversion catalysed by BA sites

4.5 Conclusions

In summary, this work gave insights into both the catalytic potential and the mechanistic function of niobium oxides in the conversion of sugars, specifically glucose and sucrose, to HMF in water. A combined approach of catalytic testing and acid site analysis of the niobium oxides was employed.

TMP NMR measurements gave detailed information about variations in acid type and strength amongst the different niobium oxide structures. Weaker and stronger BA sites were observed, which are likely to correspond to weaker terminal and stronger bridging hydroxyl groups on the interconnected NbO_6 octahedra. The few-to mono-layered niobium oxides possess particularly strong BA sites compared to the bulk materials, possibly due to more structural flexibility and increased defect formation. This goes in line with the formation of LA sites upon down-scaling from the bulk to few-layer materials, where LA sites arise from exposure of the positively charged niobium center, for example due to structural distortion or oxygen removal. LA sites are also present on amorphous mesoporous $Nb_2O_5*nH_2O$.

Catalytic activities for glucose, fructose and sucrose conversion to HMF in water were tested. Both acid type and strength are closely linked to the catalytic performance: Fructose conversion to HMF is catalyzed by BA sites, with weaker BA sites being more selective towards HMF. By far the highest HMF yield was obtained using the comparably weak BA H_3O^+ rather than solid acids. Glucose conversion to HMF involves the isomerization of glucose to fructose as an additional step before the further conversion of fructose to HMF. This isomerization is catalyzed by both LA sites and strong BA sites, where LA's are much more efficient. In terms of sucrose conversion, the hydrolysis step yielding glucose and fructose is rapid at high temperatures, while

the further formation of HMF is dependent on the individual catalytic conversions of both components.

It was shown that for both glucose and sucrose, of particular industrial interest due to their high abundance in biomass, mesoporous $Nb_2O_5*nH_2O$ gives the highest HMF yield at 36 %. This HMF yield is high compared to previous studies of sugar conversion over niobium oxides with less than 30 % yield under similar reaction conditions.[23,30,32,33] With more acidity tuning and testing of niobium oxides and other groups of solid acids, there is room for further yield improvements. In particular since fructose, intermediate in the conversion of glucose and sucrose, gave much higher HMF yields (63%) using weaker BA's, it should be possible to notably enhance HMF yields from glucose and sucrose by developing a catalyst with the current LA properties but weaker BA sites. After all, the here-presented approach for glucose and sucrose conversion has the worth-while advantage of being both environmentally and cost-friendly.

4.6 References

(1) Van Putten, R. J.; Van Der Waal, J. C.; De Jong, E.; Rasrendra, C. B.; Heeres, H. J.; De Vries, J. G. *Chem. Rev.* **2013**, *113* (3), 1499.

(2) Rosatella, A. A.; Simeonov, S. P.; Frade, R. F. M.; Afonso, C. A. M. *Green Chem.* **2011**, *13* (4), 754.

(3) REN21 Secretariat. *Renewables 2016 Global Status Report*; 2016.

(4) International Energy Agency. *Renewable energy medium-term market report 2015. Market Analysis and Forecasts to 2020 - Executive Summary*; 2015.

(5) Stöcker, M. *Angew. Chemie - Int. Ed.* **2008**, *47* (48), 9200.

(6) Ragauskas, A. J.; Williams, C. K.; Davison, B. H.; Britovsek, G.; Cairney, J.; Eckert, C. A.; Frederick, W. J.; Hallett, J. P.; Leak, D. J.; Liotta, C. L.; Mielenz, J. R.; Murphy, R.; Templer, R.; Tschaplinski, T. *Science* **2006**, *311* (5760), 484.

(7) Saidur, R.; Abdelaziz, E. A.; Demirbas, A.; Hossain, M. S.; Mekhilef, S. *Renew. Sustain. Energy Rev.* **2011**, *15* (5), 2262.

(8) Román-Leshkov, Y.; Barrett, C. J.; Liu, Z. Y.; Dumesic, J. A. *Nature* **2007**, *447* (7147), 982.

(9) Kuster, B. F. M. *Starch - Stärke* **1990**, *42* (8), 314.

(10) Climent, M. J.; Corma, A.; Iborra, S. *Green Chem.* **2014**, *16* (2), 516.

(11) Teong, S. P.; Yi, G.; Zhang, Y. *Green Chem.* **2014**, *16* (4), 2015.

(12) Chheda, J. N.; Huber, G. W.; Dumesic, J. A. *Angew. Chemie - Int. Ed.* **2007**, *46* (38), 7164.

(13) Román-Leshkov, Y.; Chheda, J. N.; Dumesic, J. A. *Science* **2006**, *312* (5782), 1933.

(14) Tong, X.; Ma, Y.; Li, Y. *Appl. Catal. A Gen.* **2010**, *385* (1–2), 1.

(15) Moreau, C.; Durand, R.; Razigade, S.; Duhamet, J.; Faugeras, P.; Rivalier, P.; Ros, P.; Avignon, G. *Appl. Catal. A Gen.* **1996**, *145* (1–2), 211.

(16) Anet, E. F. L. *J. Adv. Carbohydr. Chem.* **1964**, *19*, 181.

(17) Pagán-Torres, Y. J.; Wang, T.; Gallo, J. M. R.; Shanks, B. H.; Dumesic, J. A. *ACS Catal.* **2012**, *2* (6), 930.

(18) Akien, G. R.; Qi, L.; Horváth, I. T. *Chem. Commun.* **2012**, *48* (47), 5850.

(19) Antal, M. J.; Mok, W. S.; Richards, G. N. *Carbohydr. Res.* **1990**, *199* (1), 91.

(20) Assary, R. S.; Redfern, P. C.; Hammond, J. R.; Greeley, J.; Curtis, L. A. *J. Phys. Chem. B* **2010**, No. 114, 9002.

(21) Zhao, H.; Holladay, J. E.; Brown, H.; Zhang, Z. C. *Science* **2007**, *316* (5831), 1597.

(22) Choudhary, V.; Mushrif, S. H.; Ho, C.; Anderko, A.; Nikolakis, V.; Marinkovic, N. S.; Frenkel, A. I.; Sandler, S. I.; Vlachos, D. G. *J. Am. Chem. Soc.* **2013**, *135* (10), 3997.

(23) de Souza, R. L.; Yu, H.; Rataboul, F.; Essayem, N. *Challenges* **2012**, *3* (2), 212.

(24) Weingarten, R.; Tompsett, G. A.; Conner, W. C.; Huber, G. W. *J. Catal.* **2011**, *279* (1), 174.

(25) Sheldon, R. A. *Green Chem.* **2014**, *16* (3), 950.

(26) Economic Research Service. *Sugar : World Markets and Trade Global Production*; 2016.

(27) McConnell, M. https://www.ers.usda.gov/data-products/sugar-and-sweeteners-yearbook-tables.

(28) Reza, M. T.; Wirth, B.; Lüder, U.; Werner, M. *Bioresour. Technol.* **2014**, *169*, 352.

(29) Nikolla, E.; Román-Leshkov, Y.; Moliner, M.; Davis, M. E. *ACS Catal.* **2011**, *1* (4), 408.

(30) Chheda, J. N.; Roman-Leshkov, Y.; Dumesic, J. A. *Green Chem.* **2007**, *9* (4), 342.

(31) Gallo, J. M. R.; Alonso, D. M.; Mellmer, M. A.; Dumesic, J. A. *Green Chem.* **2013**, *15* (1), 85.

(32) C. Carlini, M. Giuttari, G. Raspolli, A. Maria, G. Sbrana, T. Armaroli and G. Busca, Appl. Catal., A. *Appl. Catal. A, Gen.* **1999**, *183*, 295.

(33) Nakajima, K.; Baba, Y.; Noma, R.; Kitano, M.; Kondo, J.; Hayashi, S.; Hara, M. *J. Am. Chem. Soc.* **2011**, *133*, 4224.

(34) Jehng, J.-M.; Wachs, I. E. *Chem. Mater.* **1991**, *3* (1), 100.

(35) Lee, B.; Lu, D.; Kondo, J. N.; Domen, K. *J. Am. Chem. Soc.* **2002**, *124* (38), 11256.

(36) Tanabe, K.; Okazaki, S. *Appl. Catal. A, Gen.* **1995**, *133* (2), 191.

(37) Okuhara, T. *Chem. Rev.* **2002**, *102* (10), 3641.

(38) Nowak, I.; Ziolek, M. *Chem. Rev.* **1999**, *99* (12), 3603.

(39) Corma, A. *Chem. Rev.* **1995**, *95* (3), 559.

(40) Takagaki, A.; Tagusagawa, C.; Hayashi, S.; Hara, M.; Domen, K. *Energy Environ. Sci.* **2010**, *3* (1), 82.

(41) Zhao, Y.; Zhou, X.; Ye, L.; Tsang, S. C. E. *Nano Rev.* **2012**, *3*, 17631.

(42) Murayama, T.; Chen, J.; Hirata, J.; Matsumoto, K.; Ueda, W. *Catal. Sci. Technol.* **2014**, *4*, 4250.

(43) Tanabe, K. *Catal. Today* **2003**, *78* (1–4 SPEC.), 65.

(44) Zheng, A.; Huang, S.-J.; Liu, S.-B.; Deng, F. *Phys. Chem. Chem. Phys.* **2011**, *13* (33), 14889.

(45) Chu, Y.; Yu, Z.; Zheng, A.; Fang, H.; Zhang, H.; Huang, S. J.; Liu, S. Bin; Deng, F. *J. Phys. Chem. C* **2011**, *115* (15), 7660.

(46) Lunsford, J. H.; Sang, H.; Campbell, S. M.; Liang, C. H.; Anthony, R. G. *Catal. Letters* **1994**, *27* (3–4), 305.

(47) Li, Q.; Hunter, K. C.; East, A. L. L. *J. Phys. Chem. A* **2005**, *109* (28), 6223.

(48) Shimizu, K.; Furukawa, H.; Kobayashi, N.; Itaya, Y.; Satsuma, A. *Green Chem.* **2009**, *11* (10), 1627.

(49) Atkins, P.; Overton, T.; Rourke, J.; Weller, M.; Armstrong, F. *Shriver & Atkins' Inorganic Chemistry*; 2010.

(50) Alaerts, L.; Séguin, E.; Poelman, H.; Thibault-Starzyk, F.; Jacobs, P. A.; De Vos, D. E. *Chem. - A Eur. J.* **2006**, *12* (28), 7353.

(51) Akiyama, T.; Itoh, J.; Fuchibe, K. *Adv. Synth. Catal.* **2006**, *348*, 999.

(52) Yang, Z. J.; Li, Y. F.; Wu, Q. Bin; Ren, N.; Zhang, Y. H.; Liu, Z. P.; Tang, Y. *J. Catal.* **2011**, *280* (2), 247.

(53) Zhang, W.; Han, X.; Liu, X.; Bao, X. *J. Mol. Catal. A Chem.* **2003**, *194* (1–2), 107.

(54) Kreissl, H. T.; Nakagawa, K.; Peng, Y. K.; Koito, Y.; Zheng, J.; Tsang, S. C. E. *J. Catal.* **2016**, *338*, 329.

(55) Walling, C. *J. Am. Chem. Soc.* **1950**, *72* (3), 1164.

(56) Takagaki, A.; Lu, D.; Kondo, J. N.; Hara, M.; Hayashi, S.; Domen, K. *Chem. Mater.* **2005**, *17* (10), 2487.

(57) Nakagawa, K.; Jia, T.; Zheng, W.; Fairclough, S. M.; Katoh, M.; Sugiyama, S.; Edman Tsang, S. C. *Chem. Commun.* **2014**, *50* (89), 13702.

(58) Solomons, T. W. G.; Fryhle, C. B. *Organic Chemistry*, 10th editi.; Wiley VCH Verlag GmbH & Co. KGaA, 2011.

(59) Lobry de Bruyn, C. A.; Alberda van Ekenstein, W. *Receuil des Trav. Chim. des Pays-Bas* **1895**, *14*, 203.

(60) Assary, R. S.; Kim, T.; Low, J. J.; Greeley, J.; Curtiss, L. A. *Phys. Chem. Chem. Phys.* **2012**, *14* (48), 16603.

(61) Roman-Leshkov, Y.; Moliner, M.; Labinger, J. A.; Davis, M. E. *Angew. Chemie - Int. Ed.* **2010**, *49*, 8954.

(62) Watanabe, M.; Aizawa, Y.; Iida, T.; Nishimura, R.; Inomata, H. *Appl. Catal. A Gen.* **2005**, *295* (2), 150.

(63) Binder, J. B.; Raines, R. T. *J. Am. Chem. Soc.* **2009**, *131* (5), 1979.

Chapter 5

Niobium Oxides: Structural Studies with Correlation to Acidity

Chapter 5 127

5.1 Background 128

5.2 Objectives 132

5.3 Experimental 133

5.3.1 Synthesis of Niobium Oxides 133

5.3.2 Characterisation of Niobium Oxides 133

5.4 Results and Discussion 134

5.4.1 XRD and TEM 134

5.4.2 Raman Spectroscopy 136

5.4.3 XPS 139

5.4.4 XAFS 144

5.4.5 ^{93}Nb ssNMR 151

5.4.6 Structure and Acidity Correlations 154

5.5 Conclusions 159

5.6 References 161

5.1 Background

In niobium-oxygen systems niobium exists in the oxidation states +2, +4 and +5, giving rise to the following main oxide groups: NbO, NbO_2 and Nb_2O_5. However, niobium oxides also form various non-stoichiometric, metastable and mixed phases, making these systems extremely complex and difficult to study.[1–3] Research literature on niobium oxides goes back over 75 years, with many different and partially contradictory reports on structure. Even with modern analysis techniques a clearer identification of the existing niobium oxides remains difficult due to the great structural variety, some of them hardly differentiable in oxygen content.[4,5]

Many niobium oxide structures are reported to have a stoichiometry between NbO_2 and Nb_2O_5, more specifically between $NbO_{2.4}$ and $NbO_{2.5}$. Although the Nb/O ratios are very similar, these non-stoichiometric structures differ significantly with respect to their electrical conductivity, refractive index and photoelectric behaviour.[1,4,6] These are the properties of importance when it comes to applications of the materials in the semiconductor, photovoltaic, solar device and electronic battery industries. Another significant field of use for niobium oxides is photo and acid catalysis.[7–11] It is therefore of great interest to investigate the relationship between structure and material properties in more detail.

In terms of structural variety, Nb_2O_5 and its closely related non-stoichiometric structures comprise the largest group of niobium oxides. Due to the Nb oxidation state of +5 (or very close to that) with all 4d electrons bound to the 2p band of oxygen, these compounds are generally white powders of low conductivity.[1,4] Further they are all structurally based on interconnected NbO_6 octahedra linked by corner- or edge-sharing with different degrees of distortion.[12,13] As Nb^{5+} is the highest stable oxidation state, NbO_6 units as basic structural feature violates Pauling's electrostatic valence rule.[1,14] In addition to the small Nb^{5+} cation size this is part of the reason for

the structural distortions of edge- and corner-sharing octahedra in Nb_2O_5 compounds. Further the multiple possibilities of linking the octahedra, as well as crystallographic shear where mixing of different linkage regions occurs, play a significant role in distortion and give rise to a large number of existing structures. Additional important factors are impurities and oxygen defects leading to deviations from the regular coordination number of six, resulting in the formation of closely related but non-stoichiometric phases.[1,5,15–17] The Nb_2O_5 compounds reported range from crystalline to amorphous, bulk to nano-size and anhydrous to hydrated forms.

A few of the most common crystalline phases include T-Nb_2O_5, M-Nb_2O_5 and H-Nb_2O_5, named according to the temperatures (German for low, medium, high) they are obtained at.[6,13] H-Nb_2O_5 is monoclinic and thermodynamically the most stable niobium oxide phase. It consists of layered 3x4 and 3x5 blocks of corner-sharing octahedra with adjacent blocks linked by octahedra edges, and there is one recurring tetrahedral site per unit cell (Figure 5.1).[1,6,18] M-Nb_2O_5 has a tetragonal structure described by 4x4 blocks of corner-sharing octahedra which are linked by edge-sharing octahedral (Figure 5.2).[1,6,19] The T-Nb_2O_5 phase is orthorhombic and structurally more complicated, involving six and seven-coordinated Nb atoms which produce distorted octahedra and pentagonal bipyramids respectively. The polyhedra are linked through both corner- and edge-sharing (Figure 5.3).[1,6,20]

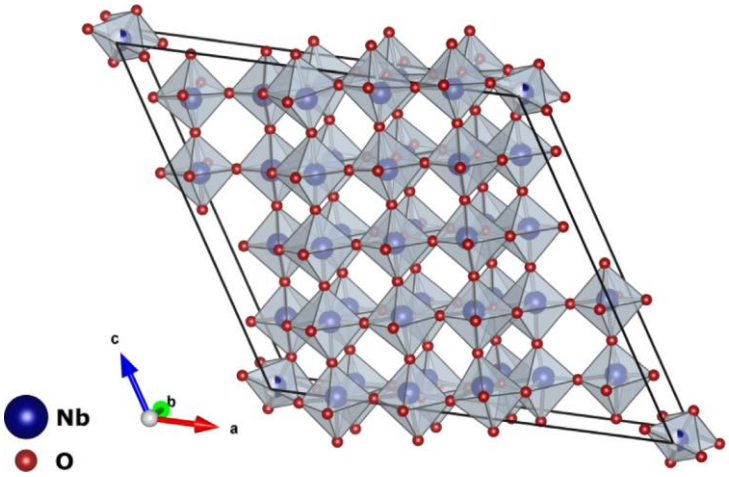


Figure 5.1 – Structure of H-Nb_2O_5 (reprinted from publication[1] (doi 10.1016/j.pmatsci.2016.02.001) with permission from Elsevier)

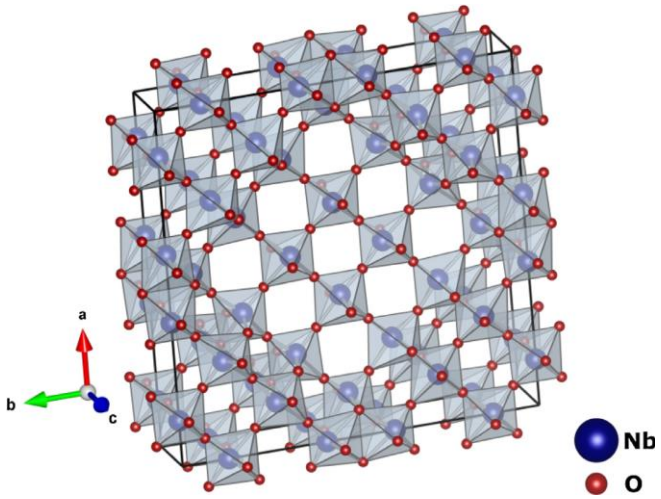


Figure 5.2 – Structure of M-Nb_2O_5 (reprinted from publication[1] (doi 10.1016/j.pmatsci.2016.02.001) with permission from Elsevier)

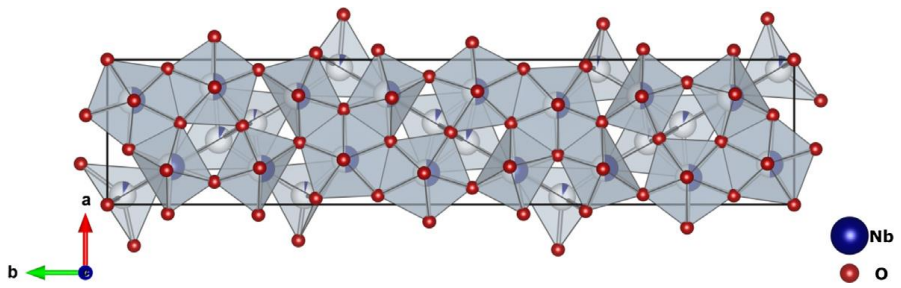


Figure 5.3 – Structure of T-Nb_2O_5 (reprinted from publication[1] (doi 10.1016/j.pmatsci.2016.02.001) with permission from Elsevier)

These are only a few examples, many more phases have been reported in literature.[1,3,5,13,17] It is interesting to note that even samples assigned to the same phase after structural investigation are not always identical: upon heating they undergo different structural transformations. This concept of 'memory of structure' further underlines how many different phases and sub-phases with hardly visible alterations exist within the group of niobium oxides.[1,15]

Synthesis temperature and pressure have a great deal of influence on the niobium oxide phase formed, as do the precursors, reactants and water content. It has been shown that even small amounts of impurities such as OH^- and Cl^- incorporated into the niobium oxide network lead to structural variations and a whole new range of compounds is obtained by the incorporation of water molecules.[6,10,11]

Hydrated forms of Nb_2O_5 are very common, where water molecules are incorporated into the structure by providing O^{2-} as part of the octahedral Nb-O network, while at the same time H^+ acidic sites are formed.[6,21,22] Hydrated niobium oxides have been reported as very strong solid Brønsted acids (BA), containing both terminal and bridging hydroxyls as BA sites. Many of them further contain Lewis acid (LA) sites, which arise from exposure of the electron deficient Nb centers.[6,10,23,24] Some of these hydrated forms are often simply denoted as $Nb_2O_5*nH_2O$, or Nb_2O_5 without reference to water, which can be misleading.

For some of the better studied systems, information on stoichiometry and structure is available, such as for HNb_3O_8 which has a sheet-like structure consisting of alternating layers of protons and niobates/NbO_6 octahedra connected by edge- and corner-sharing (Figure 5.4).[9,21,25,26] Due to their strongly acidic character many of these niobium oxides make good catalysts for esterification, (de)hydration, (de)hydrogenation and redox reactions among others. They have

successfully been applied in the fields of polymer production, photo- and electrochemistry, hydrocarbon conversion and environmental chemistry.[9,11,13,23,24] Again unfortunately the structural details and their relation to acidity remain unclear. In order to design better, targeted catalysts it is therefore important to study structure and acidity in greater detail.

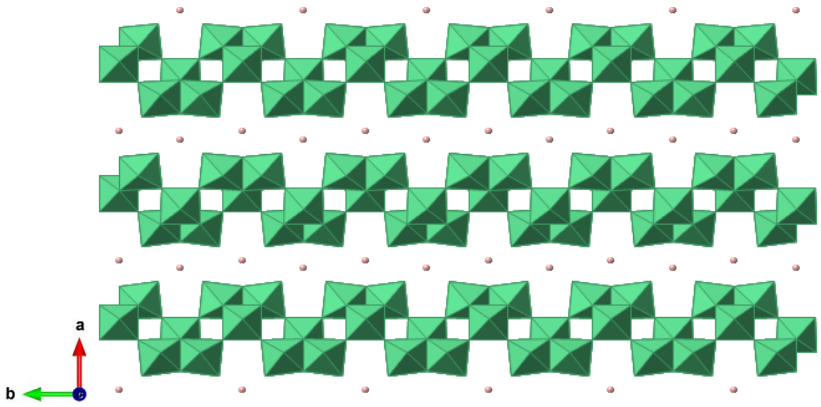


Figure 5.4 – Structure of HNb_3O_8 (NbO_6 octahedra in green, protons in pink)

5.2 Objectives

Various Nb_2O_5 related niobium oxides were studied for the conversion of sugars to hydroxymethylfurfural (HMF), with the results reported and discussed in Chapter 4. Significant variations in acidity amongst these niobium oxides were established, ranging from the type of acidity (Lewis *versus* Brønsted) to the quantity of acid sites and their respective strengths. Because the variations in acidity showed significant impact on the conversion yield and selectivity for the above reaction, this chapter now aims to gain insight into the relationship between structure and acidity. Understanding in greater detail about how certain structures give rise to respective acid sites can help to synthesize more targeted systems and thereby increase the efficiency of future niobium oxide catalysts.

5.3 Experimental

This section provides a summary of the experimental procedures used, a detailed description can be found in Chapter 3.

5.3.1 Synthesis of Niobium Oxides

A variety of niobium oxides, ranging from bulk to multi- to monolayer structures were synthesized by Keizo Nakagawa. The bulk material HNb_3O_8 was prepared by a conventional solid-state reaction of the precursors K_2CO_3 and Nb_2O_5, followed by proton exchange. Few layer niobium oxide (hy-Nb) and monolayer niobium oxide (hy-Nb-TEOA) were synthesized hydrothermally from $Nb(OEt)_5$ in ammonia solution, and in the case of hy-Nb-TEOA under further addition of triethanolamine (TEOA). Both materials were acid treated before use, in order to remove the basic surfactant species blocking their acid sites. Amorphous mesoporous Nb_2O_5*nH_2O (meso Nb_2O_5) was prepared by hydrolysis and condensation of $Nb(OEt)_5$, followed by soaking in acid solution. Detailed synthetic procedures and literature references are given in Chapter 3. For comparison, commercial bulk Nb_2O_5 (Alfa Aesar) was used.

5.3.2 Characterisation of Niobium Oxides

The niobium oxide structures were investigated using XRD, TEM (Elizabeth Raine), Raman spectroscopy, XPS of Nb 3d region (Ashley Shepherd), EXAFS Nb K-edge (Tai-Sing Wu, Yun-Liang Soo, Molly M.J. Li) and ^{93}Nb ssNMR (Thomas Hooper). Detailed information on the analysis procedures can be found in Chapter 3, and descriptions of the individual techniques are given in Chapter 2. Based on the analytical results a comparison between the different structures was done and using the acid site analysis from Chapter 4, parallels between structural features and resulting acid properties were drawn.

5.4 Results and Discussion

For reference, parts of this chapter including figures and tables have been published by the author in JACS, 2017.[27]

5.4.1 XRD and TEM

Comparing the obtained XRD profiles to literature references indicates the commercial Nb_2O_5 used is crystalline H-Nb_2O_5 (Figure 5.5 a), the thermodynamically most stable monoclinic niobium oxide phase which consists primarily of corner- and edge-sharing NbO_6 units. The in-house synthesized HNb_3O_8 also compares well to literature[26,28](Figure 5.5 b), its crystalline structure is known to consist of alternating layers of protons and niobate sheets made of edge- and corner-sharing NbO_6 units. When it comes to hy-Nb-TEOA and hy-Nb, the XRD profiles are considerably broader indicating a significant decrease in crystallinity (Figure 5.5 c). The first synthesis of these two materials was only recently reported and no structural details about Nb-O bonding and crystal structure are available yet.[9] It has been shown however that they consist of many discrete thin layers, in contrast to the bulk materials like commercial Nb_2O_5 and HNb_3O_8, as further evidenced by TEM (Figure 5.6 a-d). Their layer exfoliation is facilitated by the addition of TEOA or ammonia as stabilizers during the hydrothermal synthesis process. The XRD profiles suggest that hy-Nb-TEOA and hy-Nb have structural similarities to HNb_3O_8. The peak broadening and shift to lower angles for the (020) diffraction peak, as well as the shift in relative peak intensities can be explained by the increasing interlayer distance and 2D directional orientation when compared to bulk HNb_3O_8 (Figure 5.5 c). Thus, the layer separation results in less rigid and only partially crystalline structures.

In the case of mesoporous $Nb_2O_5*nH_2O$, no structural information can be obtained from an almost flat XRD profile, except that this material is highly amorphous (Figure 5.5 a). However, the porous structure is clearly shown by TEM (Figure 5.6 e).

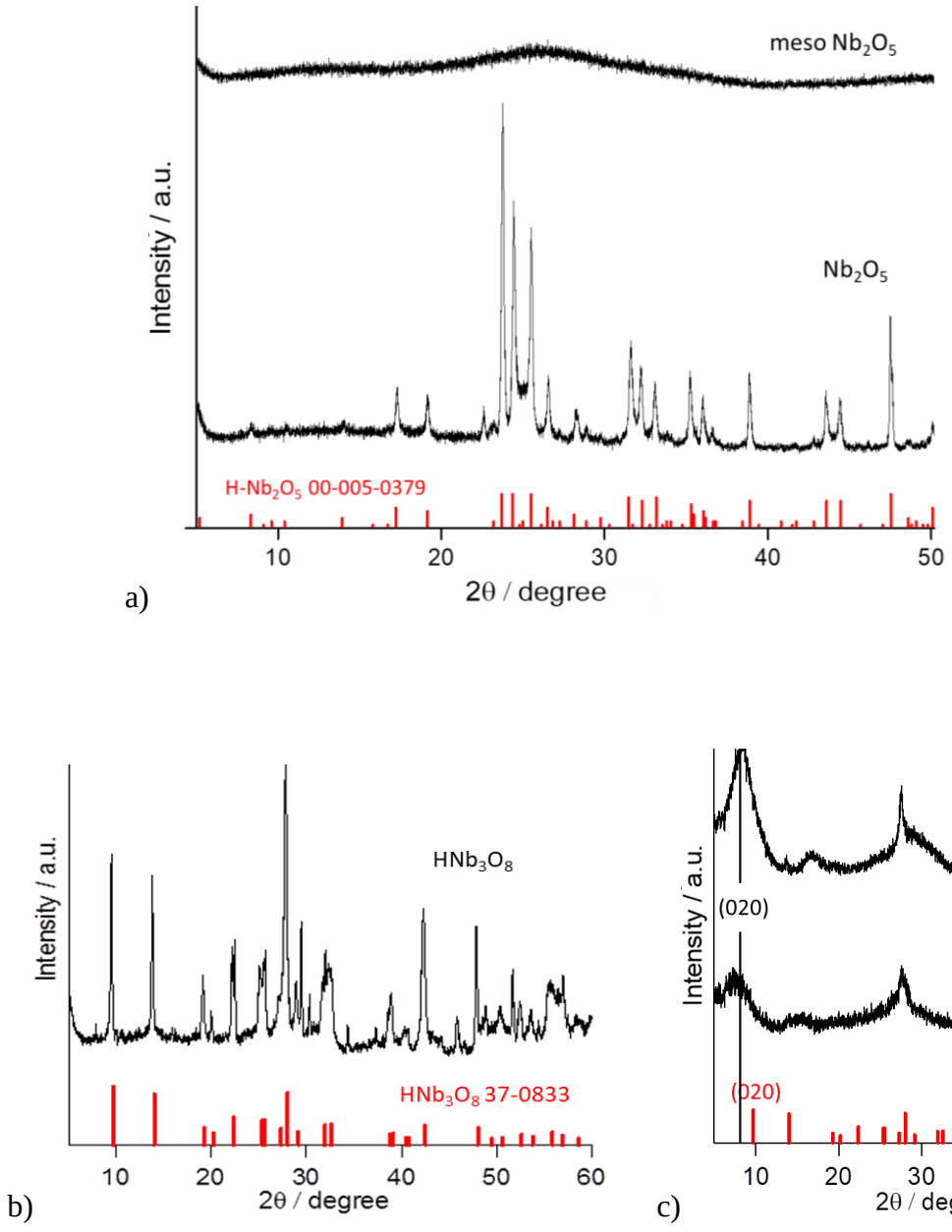


Figure 5.5 – XRD profiles of a) Nb_2O_5 (referenced to H-Nb_2O_5 00-005-0379) and mesoporous $Nb_2O_5*nH_2O$, b) HNb_3O_8 (referenced to HNb_3O_8 37-0833), c) hy-Nb and hy-Nb-TEOA (referenced to HNb_3O_8 37-0833)

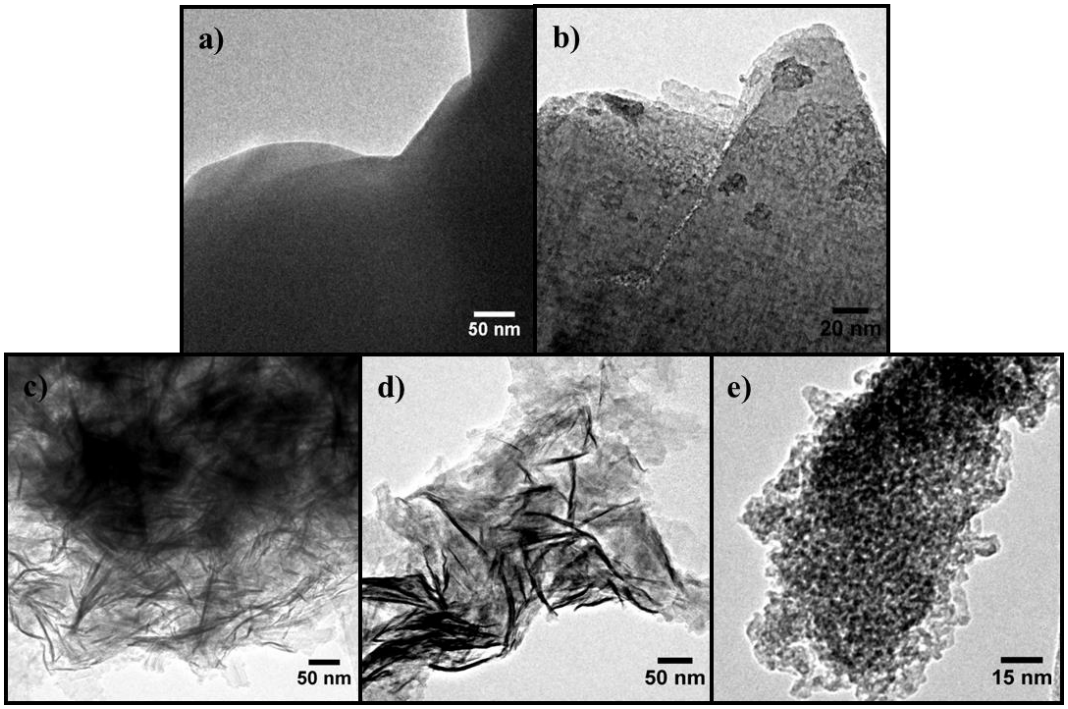


Figure 5.6 – TEM images of a) Nb_2O_5, b) HNb_3O_8, c) hy-Nb, d) hy-Nb-TEOA, e) mesoporous $Nb_2O_5*nH_2O$

5.4.2 Raman Spectroscopy

From Raman spectroscopy the same trend in sample crystallinity is observed as from XRD: commercial Nb_2O_5 and bulk HNb_3O_8 give clear peaks indicating a higher degree of crystallinity while the broader spectra of hy-Nb and hy-Nb-TEOA show a decrease in crystallinity, and finally a very broad spectrum is obtained for the amorphous mesoporous $Nb_2O_5*nH_2O$ (Figure 5.7). As previous analysis of niobium oxide spectra in literature has shown, it is very difficult to assign certain Nb-O stretching modes to specific frequencies in the Raman spectrum. This is due to the high structural complexity of these solids where Nb-O bonds cannot purely be treated as part of perfect and separate NbO_6 octahedra. The observed frequencies are influenced by various factors such as coupling between neighbouring entities, symmetry-related vibrations and degrees of structural distortion.[12,14,29,30] In particular the frequency ranges between 200 - 400 cm^{-1} and 400 - 760 cm^{-1} not only correspond to Nb-O stretching modes of long and intermediate bonds,

but are also caused by symmetry-related vibrations.[29] The frequency range between 760 - 1000 cm^{-1} has been found to be the most consistent and useful for obtaining structural information, it relates to the shortest Nb-O bonds in each system. The following observations have reported in literature: Niobium oxides consisting mainly of corner-shared octahedra are usually found to have their highest frequency stretching mode in the lower end region around 800 cm^{-1}.[14,29] This arises from their crystal structure having a lower degree of bond length variation between 1.9 – 2.0 Å and little distortion and strain. Niobium oxides consisting primarily of edge-shared octahedra, such as H-Nb_2O_5, tend to have their highest frequency stretching mode in the upper end region around 1000 cm^{-1}.[14,29,30] This value is associated with bond length variations between 1.73 – 2.26 Å, including the presence of shorter bonds in a more compact and rigid structure.

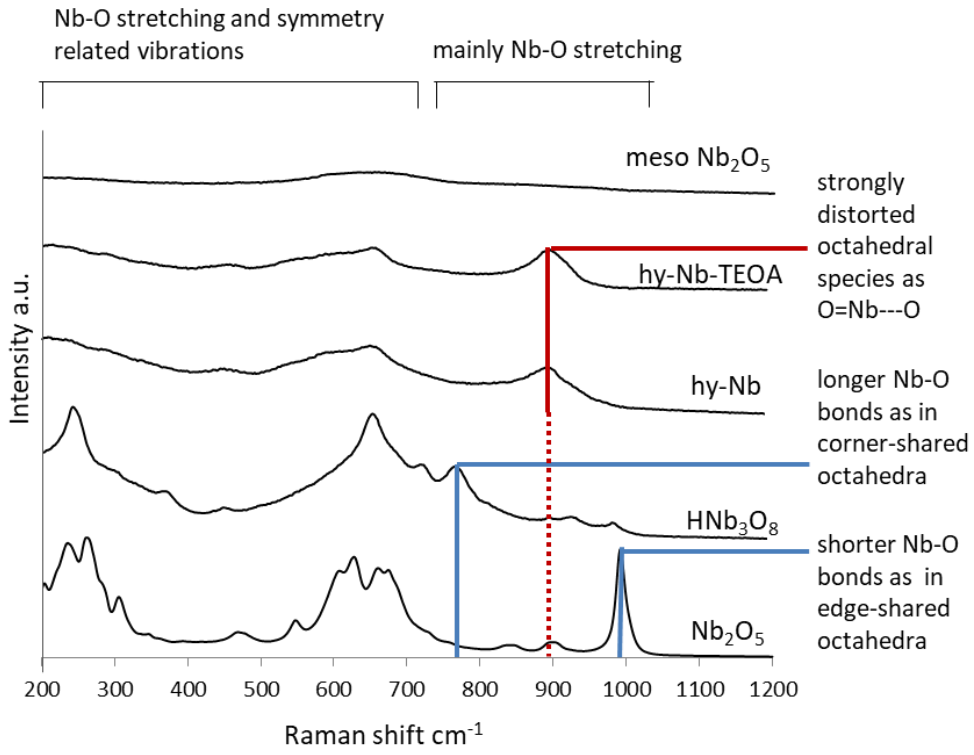


Figure 5.7 – Raman spectra of the different niobium oxides

Regarding the Raman spectra of this work (Figure 5.7), the spectrum of commercial Nb_2O_5 coincides well with that of H-Nb_2O_5 from literature[12,14,30], thus consistent with the XRD result. A

sharp peak is seen at about 1000 cm^{-1}, arising from the significant amount of edge-sharing NbO_6 with many short Nb-O bonds in a closely packed structure. For HNb_3O_8 there is a larger peak at 780 cm^{-1} but only a very small peak at 1000 cm^{-1}, suggesting longer bond lengths and less structural rigidity than for Nb_2O_5. It is known that the crystal structure of HNb_3O_8 consists of considerable amounts of corner- besides edge-sharing octahedra and is further a layered structure with more structural flexibility[9,26,28], which explains the observed longer bond lengths.

A significant Raman peak broadening for hy-Nb and hy-Nb-TEOA compared to the crystalline bulk materials HNb_3O_8 and Nb_2O_5 is further observed. This is expected from the lower crystallinity and higher structural flexibility of these two materials due to increasing interlayer distances and supports the previous observations from XRD and TEM. Besides a broadening of the typical bond regions however, an additional large peak appears at around 900 cm^{-1} for both hy-Nb and hy-Nb-TEOA, which is not evident from the spectra of Nb_2O_5 and HNb_3O_8. It implies that there are some structural differences between HNb_3O_8 and the nanomaterials hy-Nb and hy-Nb-TEOA. The feature around 900 cm^{-1} is believed to arise from octahedral distortions with species such as O=Nb---O, having a double bond-like Nb=O and an elongated Nb-O bond as part of the octahedron.[12,14,29] Due to the high surface areas and structural flexibility, octahedral deformations in the structures of hy-Nb and hy-Nb-TEOA are reasonable.

Finally, the Raman spectrum of mesoporous $Nb_2O_5*nH_2O$ is almost flat, with only a very broad peak in the region of 500 – 750 cm^{-1}, where peaks are also observed for the other niobium oxides. Unfortunately no further information can be obtained as was also the case with XRD, due to the apparently highly amorphous structure and low symmetry of mesoporous $Nb_2O_5*nH_2O$.

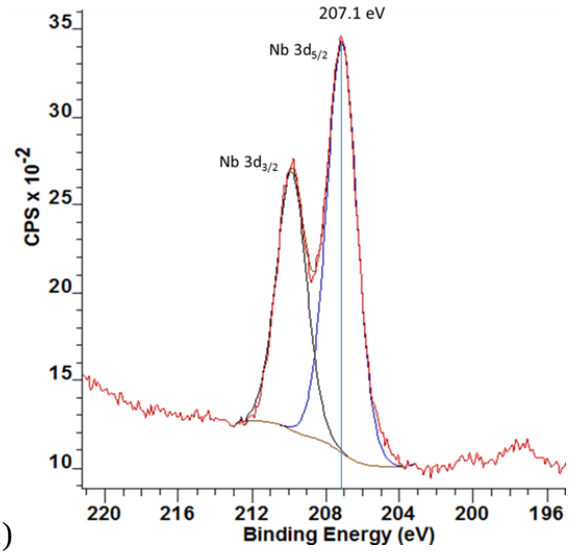
5.4.3 XPS

XPS measurements were performed on the different niobium oxides in order to provide further information about oxidation state and atomic environment within the structures. Literature has shown that for niobium compounds the Nb 3d region is generally the most sensitive and characteristic, while the interpretation of oxygen XPS spectra can provide difficulties due to oxygen impurities from the carbon tape used for sample fixation during measurements.[31–34] The Nb 3d region always shows peak doublets due to spin-orbit coupling of the 3d orbital, giving rise to a Nb $3d_{5/2}$ and a Nb $3d_{3/2}$ peak with an area ratio of 3:2 and a peak separation of 2.72 eV. The doublet position shifts according to oxidation state, with a higher oxidation state causing a shift towards higher binding energies.[31,32,35] The binding energy values representing a sample's Nb 3d region are usually given in the form of Nb $3d_{5/2}$ peak values. Nb_2O_5 with an oxidation state of Nb^{5+} and NbO_2 with an oxidation state of Nb^{4+} have been reported with binding energy values of about 207.4 eV and 206.2 eV, respectively.[35,36] However deviations of up to 0.5 eV are common due to instrument specificities and it is more important to compare the measured values relative to each other.

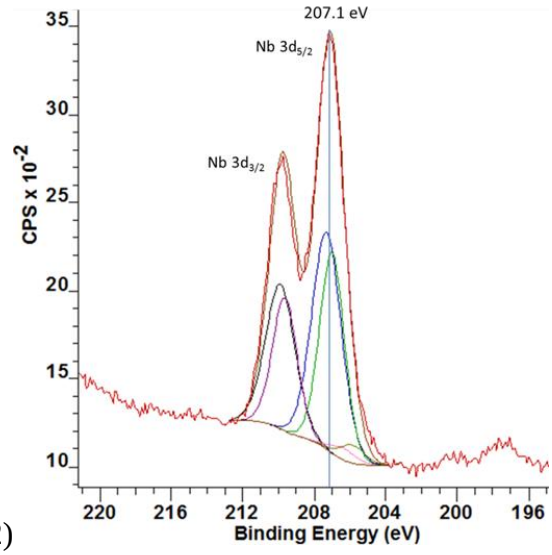
Quantitative elemental analysis of the obtained XPS spectra has been done to determine O:Nb ratios for the niobium oxide samples (for calculations see Appendix p.A19-A21). According to the molecular formulas, the O:Nb ratio for commercial Nb_2O_5 is expected to be 2.5:1, for HNb_3O_8 2.67:1, for hy-Nb and hy-Nb-TEOA similar to that of HNb_3O_8, and for mesoporous $Nb_2O_5*nH_2O$ higher than for commercial Nb_2O_5 due to additional oxygen contribution from water content. Comparing the experimental peak area ratios of the synthesized niobium oxides relative to the one obtained for commercial Nb_2O_5 with an O:Nb ratio of 2.5:1, the following results are obtained: An O:Nb ratio of 2.65:1 for HNb_3O_8, 2.69:1 for hy-Nb, 2.79:1 for hy-Nb-TEOA and 2.78:1 for mesoporous $Nb_2O_5*nH_2O$. These values follow the expected trend of

higher O:Nb ratios around 2.67:1 for the water containing niobium oxides compared to commercial Nb_2O_5. It is however difficult to interpret these results in more detail due to smaller peak area errors, which arise from the additional contribution of oxygen species from the carbon tape used to mount the samples.

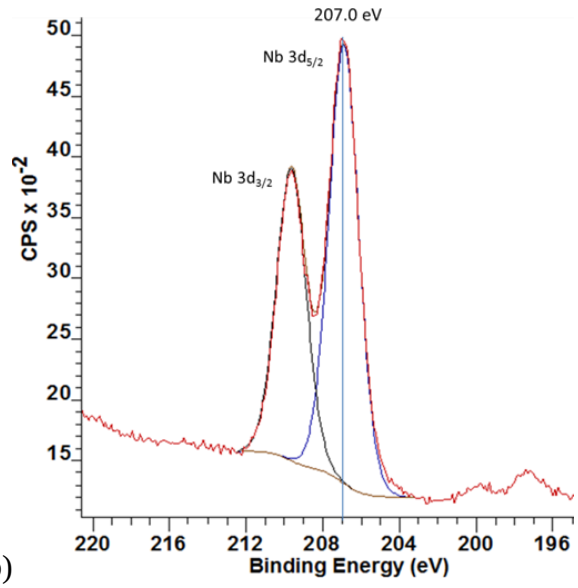
a.1)



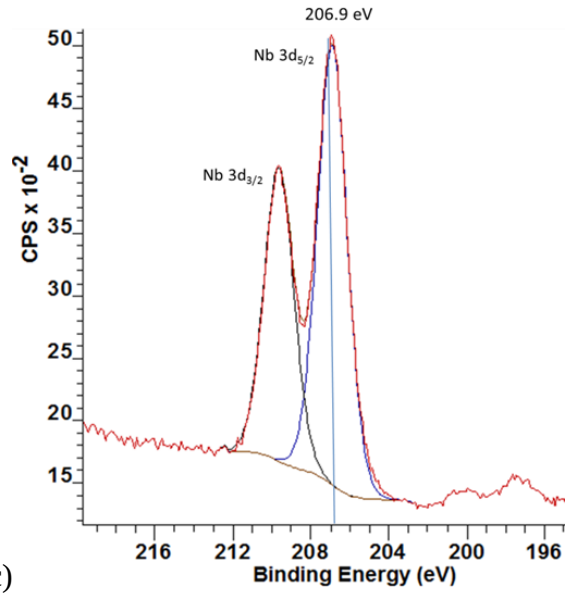
a.2)



b)



c)



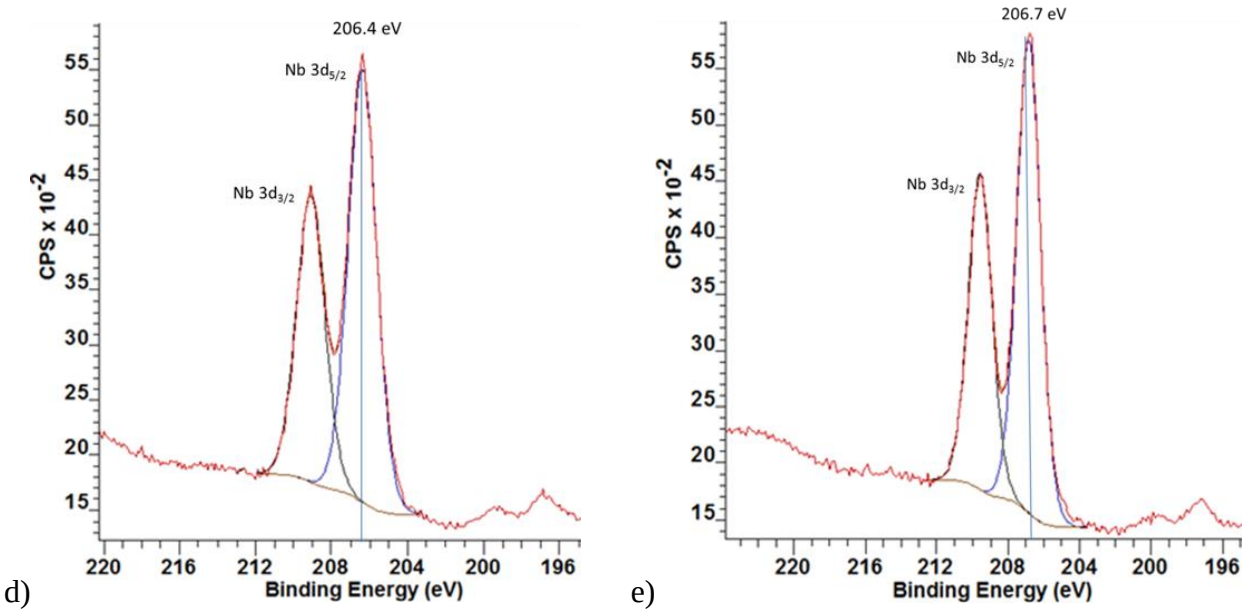


Figure 5.8 – XPS spectra of a.1) Nb_2O_5 single doublet fitting, a.2) Nb_2O_5 triple doublet fitting, b) HNb_3O_8, c) hy-Nb, d) hy-Nb-TEOA, e) mesoporous Nb_2O_5*nH_2O

The XPS Nb 3d spectrum of commercial Nb_2O_5 (H-Nb_2O_5) shows a doublet with a binding energy of 207.1 eV, comparing well with the average literature value of 207.4 eV for Nb^{5+} (Figure 5.8 a.1).[35,36] Since the crystal structure of H-Nb_2O_5 is known to consist of both edge- and corner-sharing octahedra as well as the occasional tetrahedron,[1] all of which provide different Nb environments, strictly speaking 3 sets of doublets would be expected: two large doublets in the Nb^{5+} region and one very small doublet, potentially shifted towards the lower binding energy Nb^{4+} region. Using an XPS peak fitting program (CasaXPS) it is possible to fit the expected 3 doublets (Figure 5.8 a.2), however the peak shifts are too small to get reliable results, the fitting using one doublet is just as good. This suggests that the corresponding binding energies of the three Nb species are too close to separate. Looking at the XPS spectrum of HNb_3O_8 gives a similar result, again there is only one obvious doublet (Figure 5.8 b) although its crystal structure gives rise to at least two Nb environments. Similarly, the remaining samples hy-Nb (Figure 5.8 c), hy-Nb-TEOA (Figure 5.8 d) and mesoporous Nb_2O_5*nH_2O (Figure 5.8 e), whose structures

are yet to be identified, also show only one obvious doublet. Therefore it is not possible to draw conclusions about the number of Nb environments arising from different extents of octahedral distortion or small coordination changes.

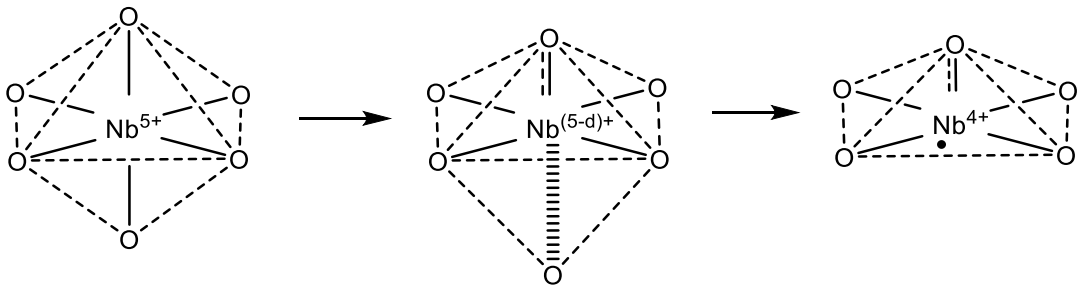
However there is one visible difference amongst the niobium oxide samples: the binding energy shift in the Nb 3d region (Figure 5.8 and Table 5.1). For commercial Nb_2O_5 the Nb 3d region is centred at 207.1 eV > 207.0 eV for HNb_3O_8 > 206.9 eV for hy-Nb > 206.7 eV for mesoporous Nb_2O_5*nH_2O > 206.4 eV for hy-Nb-TEOA. The decreasing binding energy indicates a shift in oxidation state from Nb_2O_5 with mostly Nb^{5+} character to hy-Nb-TEOA with more Nb^{4+} character. A similar shift towards Nb^{4+} has been observed by Xiong *et al.* investigating HNb_3O_8 in comparison to exfoliated/nanosheet-HNb_3O_8.[26] For the bulk materials Nb_2O_5 and HNb_3O_8 the Nb oxidation state of +5 is expected due to their composition of almost purely edge- and corner-sharing octahedra. The few- to monolayered materials hy-Nb and hy-Nb-TEOA have structural similarities to HNb_3O_8 but are less ordered and have significantly more structural flexibility and

Table 5.1 – Nb 3d peak position for the different niobium oxides

Sample	Nb 3d peak region (eV)
Nb_2O_5	207.1
HNb_3O_8	207.0
hy-Nb	206.9
hy-Nb-TEOA	206.4
mesoporous Nb_2O_5*nH_2O	206.7

Peak region given as Nb $3d_{5/2}$ peak center values (common denotation)

surface character, as previously shown by TEM, XRD and Raman spectroscopy. Raman spectroscopy further suggests the presence of a strongly distorted O=Nb---O surface species with one double bond-like and one elongated Nb-O bond. Combining previous and current observations, it appears likely that hy-Nb and especially hy-Nb-TEOA have oxygen vacancies present due to some of the elongated bonds from O=Nb---O species being fully broken. This process resulting in oxygen vacancies in the form of electron-richer five-coordinated Nb^{4+} centers (Scheme 5.1) is likely stabilised by the surfactants used during synthesis of the nanomaterials. In this context, the more pronounced shift towards Nb^{4+} character for hy-Nb-TEOA compared to hy-Nb can be explained by a more enhanced layer exfoliation caused by the addition of TEOA during synthesis, resulting in increased structural flexibility and enhanced oxygen vacancy formation. The lower EXAFS bond coordination numbers for hy-Nb-TEOA compared to hy-Nb (discussed in the next section) support this hypothesis. Interestingly mesoporous $Nb_2O_5*nH_2O$, whose structural analysis had not yielded much information so far, appears to share this increased Nb^{4+} character with hy-Nb and hy-Nb-TEOA.



Scheme 5.1 – Proposed oxygen vacancy formation based on the above Raman and XPS results, supported by EXAFS as follows

As a side note, it is interesting to observe the shift towards Nb^{4+} character for hy-Nb-TEOA and mesoporous $Nb_2O_5*nH_2O$ from XPS, because it suggests the presence of unpaired electrons and therefore coloured samples. For example, NbO_2 of oxidation state Nb^{4+} is blue.[1] However, all

niobium oxide samples studied here are white in colour, leaving two possible explanations: either the amount of Nb^{4+} species could be too small to give a visible colour, or the unpaired electrons could be stabilised by delocalization over the Nb-O d-band structure. Electron delocalization would also explain the shift in total oxidation state towards Nb^{4+} which is depicted by XPS rather than separate signals from distinct Nb^{5+} and Nb^{4+}species. Such network sharing or building of a superstructure for defects present in large amounts has been suggested for metal oxides in previous literature.[17,37]

5.4.4 XAFS

In order to support and supplement the information obtained from XPS, XAFS measurements were conducted on the niobium oxide samples. XAFS gives insights into oxidation state and localized atomic structure, especially with regard to bond distances and to some extent also coordination numbers.[38–42] The obtained XANES Nb K-edge absorption spectra are displayed in Figure 5.9. Generally, a higher oxidation state causes a shift towards higher absorption energies but in the case of Nb^{5+} *versus* Nb^{4+} the energy gap is rather small and can be obscured by the presence of a pre-edge peak and other shape factors.[40,41] Literature further tends to compare niobium oxides by analysis of the pre-edge peak, where Nb^{5+} samples such as Nb_2O_5 tend to display a larger peak size than Nb^{4+} samples such as NbO_2.[38–40] Unfortunately it remains unclear whether the larger pre-edge peak is related primarily to electronic factors (Nb_2O_5 contains a larger density of empty d-states than NbO_2) or rather to geometric factors (Nb_2O_5 is structurally more distorted than NbO_2 and also contains some tetrahedra in addition to octahedra).[38,43,44] Therefore it is difficult to make conclusions about the oxidation state of unknowns without considering geometric factors. Besides the influence of geometric factors, the pre-edge peaks of the measured niobium oxide samples are very close in position, meaning that the peak size order

of Nb_2O_5 > HNb_3O_8 > hy-Nb-TEOA > hy-Nb > mesoporous Nb_2O_5*nH_2O (Figure 5.9) is difficult to interpret with respect to sample oxidation state. The information obtained from XPS, which gave the following order of decreasing Nb^{5+} character starting from Nb_2O_5 > HNb_3O_8 > hy-Nb > mesoporous Nb_2O_5*nH_2O > hy-Nb-TEOA, can be considered more reliable.

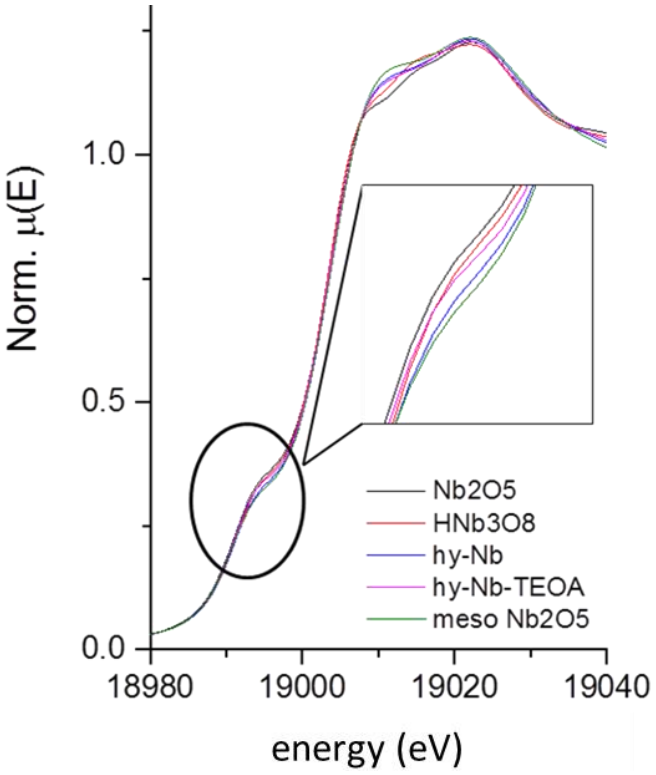
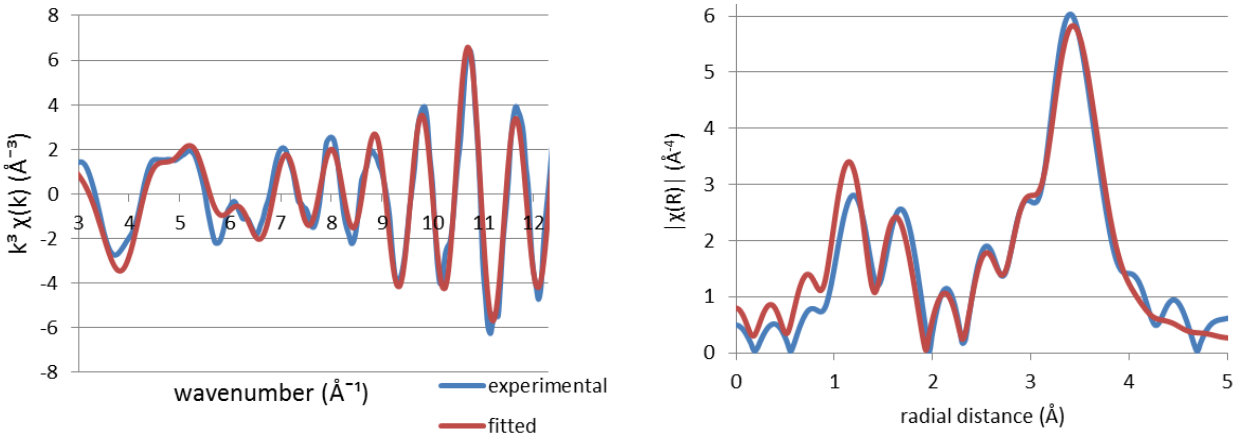


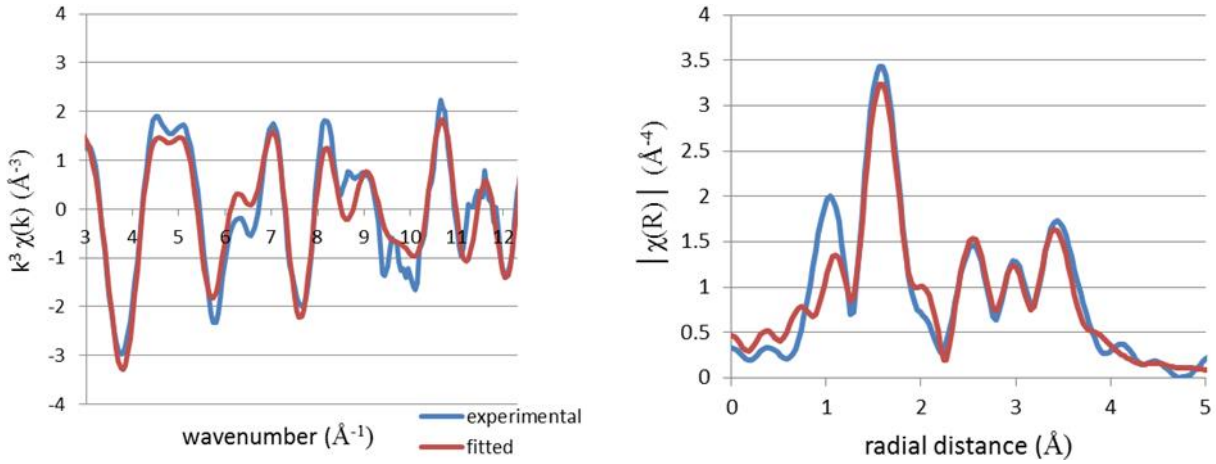
Figure 5.9 – XANES Nb K-edge absorption spectra for the different niobium oxides

Analysis of the Nb K-edge EXAFS region however gives useful information on the niobium environment with respect to Nb-O bond distances, which cannot be achieved by XPS. Bond distance information is obtained by transforming the normalised oscillatory part of the energy absorption coefficient to k space and further to R space, where the R space amplitude relates to the radial distance from Nb at which bonds to neighbouring atoms are present. Using the curve-fitting program IFEFFIT, a combined approach of *ab initio* parameter calculations and fitting to model functions is employed to obtain bond distances and coordination numbers.[39,45,46] In Figure

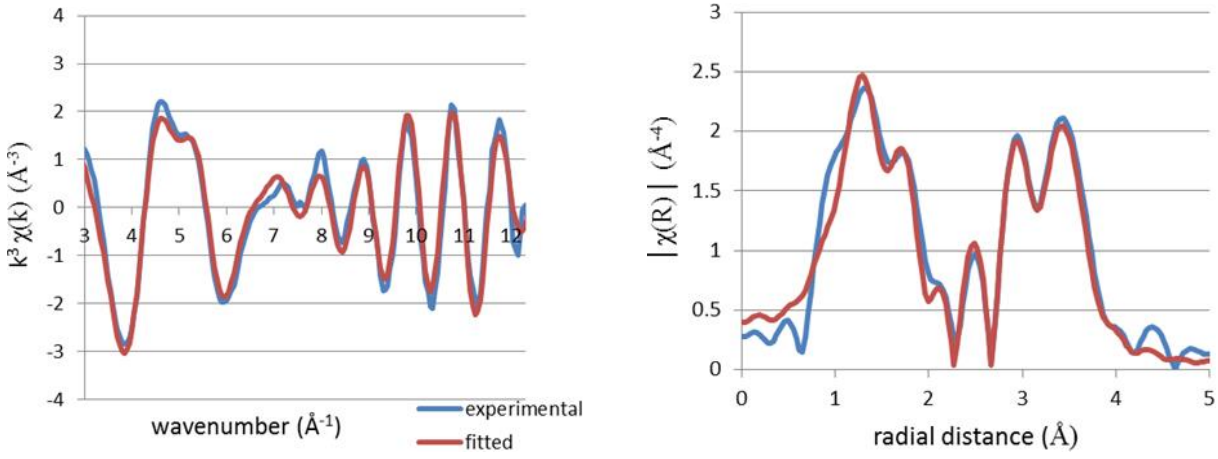
5.10 the fitted k and R ranges for the first and second shell neighbours (Nb-O and Nb-Nb) are displayed for each sample. For valid results the correlation factor R between experimental result and fitting should be within 2% and enot, the difference in absorption threshold energy between experimental and fitted result, should be within ±8. With the above analysis method, first shell Nb-O bond distances were determined with high accuracy of ±0.04Å, while derived coordination numbers of Nb are accurate to ±1. The given numbers are averages over the whole crystal structure, meaning that decimals are common. Both the first shell Nb-O bond lengths and coordination numbers determined from EXAFS are displayed in Table 5.2. For more details on scattering paths and second shell neighbours, see Appendix p.A21-A22. It should further be noted that the FT spectra presented in Figure 5.10 are not phase shift corrected (FT phase shift approx. -0.5Å) due to fitting inaccuracy for compounds of low crystallinity. Similarly, the relation between R space amplitude and coordination number is not always straightforward, as the FT spectrum is not a true radial distribution function due to damping factors.[45] This means that bond distances and coordination numbers cannot easily be read from the FT-spectra, but have been extracted with the help of IFEFFIT and are displayed in Table 5.2.



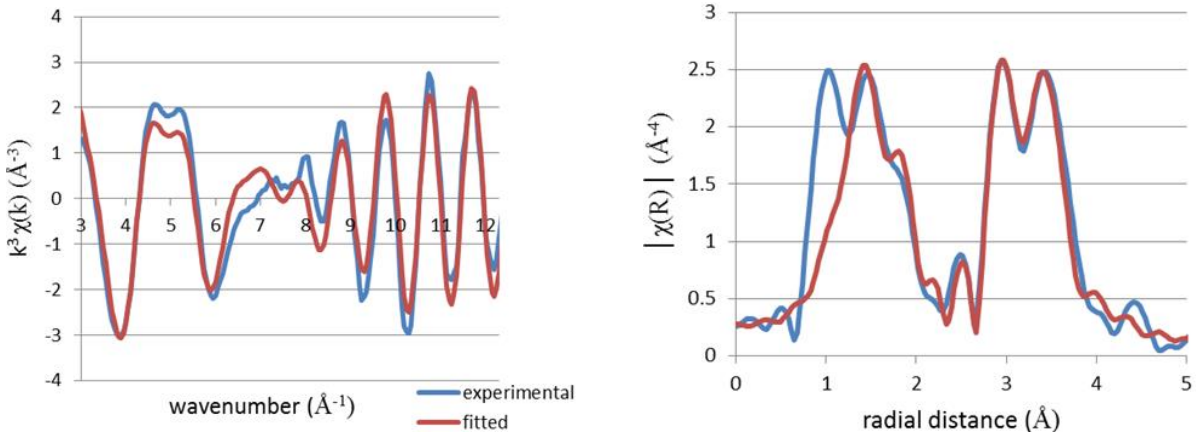
a) Nb_2O_5: R = 2.0 %, k range 3-12.3, R range 1.2-4, enot = -7.6



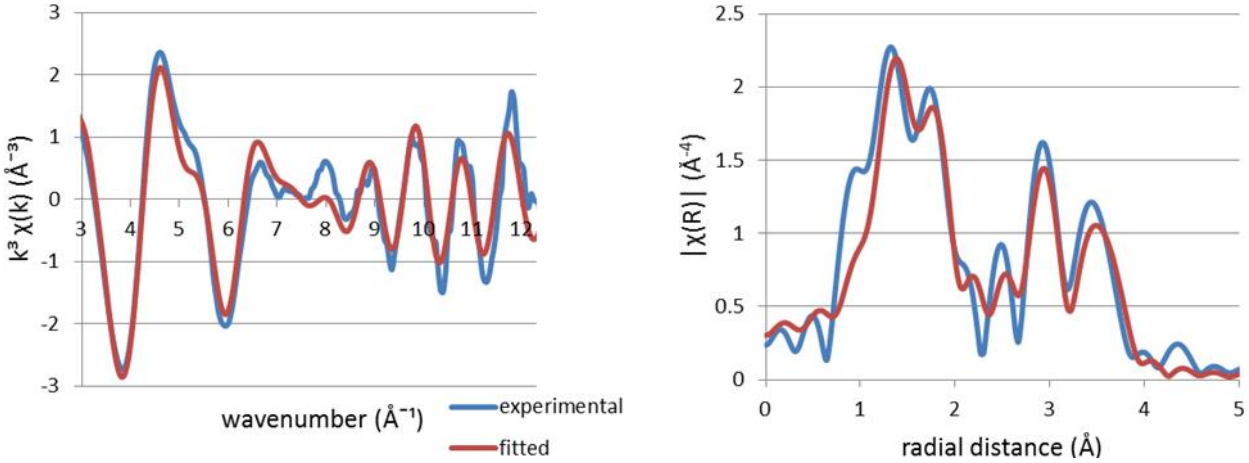
b) HNb_3O_8: R = 1.0 %, k range 3-12.3, R range 1.2-2.8, enot = 2.1



c) hy-Nb: R = 0.5 %, k range 3-12.3, R range 1.2-2.65, enot = 6.3



d) hy-Nb-TEOA: R = 1.1 %, k range 3-12.3, R range 1.2-2.65, enot = 7.6



e) mesoporous Nb_2O_5*nH_2O: R = 2.0%, k range 3-12.3, R range 1.2-4, enot = 6.2

Figure 5.10 – k and R space transformations of Nb K-edge EXAFS spectra of the different niobium oxides for determination of bond distances and coordination numbers

Table 5.2 – Bond distances and coordination number of the different niobium oxides

	Scattering path	Bond length in Å	Coordination number	Total Coordination number
Nb_2O_5	Nb-O1	1.76(1)	1.4(1)	5.7
	Nb-O2	1.96(1)	4.3(2)	
HNb_3O_8	Nb-O1	1.77(1)	1.0(1)	6.2
	Nb-O2	2.02(1)	4.1(1)	
	Nb-O3	2.22(1)	1.1(1)	
hy-Nb	Nb-O1	1.88(1)	0.9(1)	5.6
	Nb-O2	2.07(1)	3.8(1)	
	Nb-O3	2.31(1)	0.9(1)	
hy-Nb-TEOA	Nb-O1	1.93(1)	1.1(1)	4.8
	Nb-O2	2.09(1)	3.4(1)	
	Nb-O3	2.29(4)	0.3(1)	
meso Nb_2O_5	Nb-O1	1.91(1)	0.9(1)	4.5
	Nb-O2	2.10(1)	3.6(1)	

Information obtained from EXAFS k and R space transformations fitted for ^{1st}O-shell

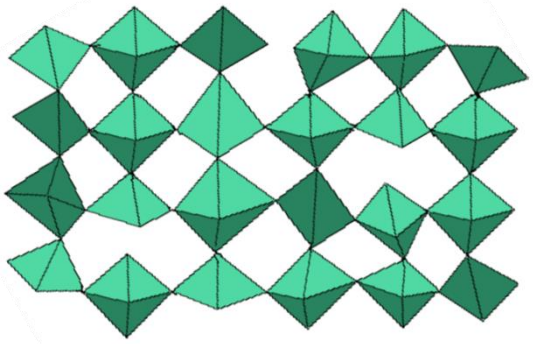
For commercial Nb_2O_5 (H-Nb_2O_5) two Nb-O types with bond lengths of 1.76 Å and 1.96 Å are obtained, with respective Nb coordination numbers of 1.4 and 4.3, giving a total of 5.7. The numbers correlate well with the crystal structure of H-Nb_2O_5 that consists mainly of octahedra and very few tetrahedra, resulting in an average coordination of just below 6. Literature states that corner-shared octahedra consist of rather uniform Nb-O bonds of 1.9 – 2.0 Å, while the more distorted edge-shared octahedra vary in bond lengths between 1.73 – 2.26 Å.[14,29,41] It appears that the measured Nb-O bonds of 1.76 Å represent the shorter edge-sharing octahedral

bonds, while 1.96 Å with a larger average coordination number represents both the longer edge-sharing and the uniform corner-sharing bonds.

For HNb_3O_8 two similar Nb-O bond lengths with respective coordination are obtained, plus a third Nb-O bond of 2.22 Å with a coordination of 1.1. The Nb-O bond lengths correlate well with findings on KNb_3O_8, the precursor of HNb_3O_8 from ion exchange, and also with Crystal Maker data of HNb_3O_8, where the larger numbers of given Nb-O bonds can be grouped to give the bond categories obtained from EXAFS.[47] The total coordination number is 6.2, correlating well with the layered structure known to consist of NbO_6 sheets with a theoretical coordination of 6. The Nb-O bonds of similar nature to Nb_2O_5 are probably again due to the edge- and corner-sharing octahedra present, while the additional longer bond likely arises from the layered structure with a gain in flexibility along the z-axis. The overall increase in bond length and structural flexibility for HNb_3O_8 compared to Nb_2O_5 also compares well with the observations from Raman spectroscopy.

For hy-Nb the trend in bond lengths and coordination numbers is similar to HNb_3O_8, supporting their structural similarities as shown by XRD. The overall longer Nb-O bonds of hy-Nb are a sign of higher structural flexibility due to layer separation as shown previously, and with a total coordination number of below 6 likely includes the formation of some oxygen vacancies as suggested by XPS. These observations get more apparent for the few- to monolayered hy-Nb-TEOA, with even longer Nb-O bonds and a total coordination number of only 4.8. Interestingly, the percentage of the longest Nb-O bond type (Nb-O3) is largely reduced compared to hy-Nb and HNb_3O_8, suggesting the removal of significant amounts of elongated Nb---O bonds, resulting in the formation of oxygen vacancies and a greatly distorted structure with reduced average coordination numbers. This goes in line with the XPS observations of an increased Nb 4+ character for hy-Nb-TEOA (Scheme 5.1).

For mesoporous $Nb_2O_5*nH_2O$, as for Nb_2O_5, there are only two types of Nb-O bonds measured with 1.91 Å and 2.10 Å and respective coordination of 0.9 and 3.6. The overall longer bonds compared to Nb_2O_5 suggest a rather loose and flexible packing of structural units, pointing towards corner-sharing NbO_6. With a coordination number of only 4.5, the structure could be a mix of four-, five- and six-coordinated Nb-O units, which would match its amorphous nature (Scheme 5.2). It is difficult to make a more specific statement on coordination numbers since the calculated numbers are an average representation of the whole structure and involve fitting limitations as mentioned earlier.



Scheme 5.2 – Proposed structure of amorphous mesoporous $Nb_2O_5*nH_2O$ based on EXAFS and XPS results (protons not shown)

5.4.5 ^{93}Nb ssNMR

Further comparison can be drawn from ^{93}Nb solid state NMR spectra of the niobium oxide samples. The high abundance of the ^{93}Nb nucleus and its spin of I = 9/2 are advantageous to NMR measurements, however the large chemical shift anisotropy and quadrupolar coupling lead to significant peak broadening even at high magnetic field strengths.[48–51] Octahedrally coordinated NbO_6 species typically display a convoluted peak signal in the range of -800 to -1500 ppm and the larger the observed peak width, the more chemically distinct NbO_6

environments tend to be present. [48,50,51] Different NbO_6 species are difficult to resolve and even more so NbO_5 species, which are less symmetric and give rise to an even broader peak signal underlying that of NbO_6, in the range of -650 to -1000 ppm.[49] NbO_4 species are again symmetric in character, however they tend to assume the oxidation state of Nb^{4+}, resulting in paramagnetic species whose signal is significantly broadened by paramagnetic interactions.[52] As with NbO_5, the NbO_4 signal is centred downfield compared to NbO_6, in the range of -700 to -900 ppm, but due to signal broadening typically underlies the peak signal of NbO_6.[49,51]

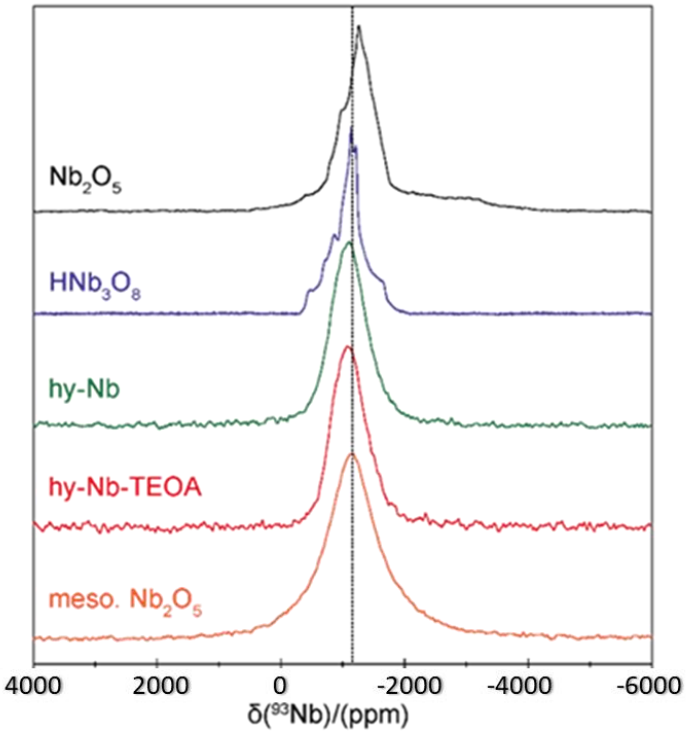


Figure 5.11 – ^{93}Nb static NMR spectra of the different niobium oxides with a dotted line through the center-of-gravity position (δ_{CG}) of mesoporous Nb_2O_5*nH_2O

The static broadline ^{93}Nb NMR data for the niobium oxide samples is shown in Figure 5.11. On first inspection it is apparent that Nb_2O_5 and HNb_3O_8 exhibit more distinct line-shape features than the remaining samples. The HNb_3O_8 spectrum is consistent with that previously reported, where it has been shown to consist of two quadrupolar/chemical shift anisotropy broadened

Table 5.3 – δ_{CG} and full width at half maximum of the NMR resonances for the different niobium oxides

Catalyst	δ_{CG} (ppm)	FWHM (ppm)
Nb_2O_5	-1260 ± 70	650 ± 70
HNb_3O_8	-1130 ± 40	400 ± 40
hy-Nb	-1100 ± 60	590 ± 60
hy-Nb-TEOA	-1100 ± 60	600 ± 60
meso Nb_2O_5	-1150 ± 90	920 ± 90

Determined by Gaussian fitting

resonances, assigned to the chemically distinct edge- and corner-sharing NbO_6 species present.[33] The Nb_2O_5 peak signal is slightly broader than that of HNb_3O_8, which is in agreement with the presence of additional tetrahedral sites and possibly various types of edge- and corner-sharing octahedra, as also indicated by previous NMR studies.[51] The ^{93}Nb spectra for hy-Nb,hy-Nb-TEOA and especially mesoporous Nb_2O_5*nH_2O are of very broad shape, representative of more disordered systems. Therefore the NMR results match the trend in crystallinity of Nb_2O_5/HNb_3O_8 > hy-Nb/hy-Nb-TEOA > mesoporous Nb_2O_5*nH_2O observed from XRD and Raman. Due to the disordered nature of some of the NMR spectra it is difficult to determine more accurate NMR parameters. The center-of-gravity shifts δ_{CG} (Table 5.3) suggest that each system is dominated by NbO_6 moieties, while NbO_4 and NbO_5 species are too broad to be detected by single solid echo experiments. Nb_2O_5 has a significantly more negative δ_{CG} than the other niobium oxides. This could represent a trend in average coordination number/oxidation state from six-coordinate Nb^{5+} species in Nb_2O_5 to an increase in five-coordinate species and Nb^{4+} character for the structurally more disordered materials, as already suggested by XPS and EXAFS.

5.4.6 Structure and Acidity Correlations

In order to look at the relationship between niobium oxide structure and acidity, a summary of the acidity measurements from Chapter 4 is given in Table 5.4. Acid type (Brønsted versus Lewis), strength and quantity for each material were probed by TMP ^{31}P NMR. TMP as an electron donor can form stable adducts with an exposed cation (Lewis acid, LA) or proton (Brønsted acid, BA) of a surface, via coordination of the P atom to the LA or BA center. Due to variations in the ^{31}P chemical shift (ppm) of the surface TMP-LA and TMP-BA complexes, a differentiation between acid type and further strength is possible.[53–55] In general for solid acid metal oxides, BA sites are protonic surface sites in the form of strongly acidic bridging or terminal hydroxyl groups.[54,56] LA sites arise from the exposure of electron deficient metal centres, for example due to lower numbers or distortion of coordinating oxygens.[24,57]

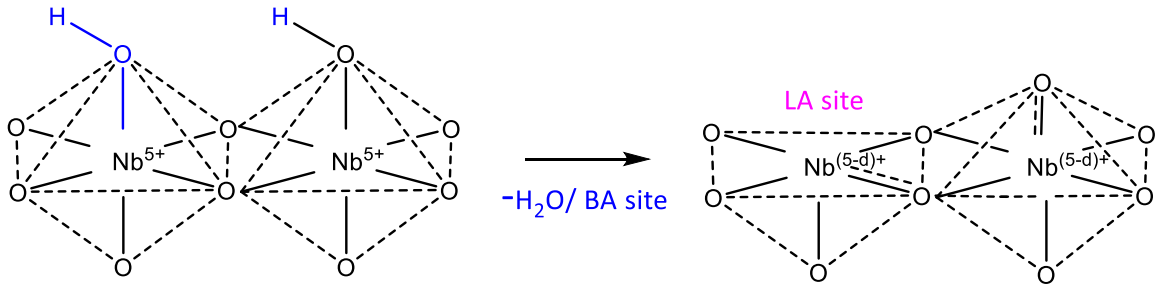
Table 5.4 – Surface area and acid site analysis for the different niobium oxides

Catalyst	Surface area ($m^2 g^{-1}$)	Acid site type and quantity ($\mu mol\ g^{-1}$)	Acid site strength (ppm)
Nb_2O_5	3	ND	ND
HNb_3O_8	10	BA (30) no LA	BA: - 2.77
hy-Nb-TEOA	121	BA (171) LA (108)	BA: - 0.36 LA: - 24.98
hy-Nb	166	BA(259) LA(269)	BA: - 0.87 LA: - 42.27
meso Nb_2O_5	142	BA(338) LA(222)	BA: - 5.47 LA: - 25.37

Surface area obtained from BET nitrogen adsorption measurements,
Acid site analysis (qualitative and quantitative) by TMP ^{31}P NMR, BA region: ~0 to -6 ppm, LA region: ~-20 to -45 ppm, less negative ppm shift means stronger acidity within each region[53,54]

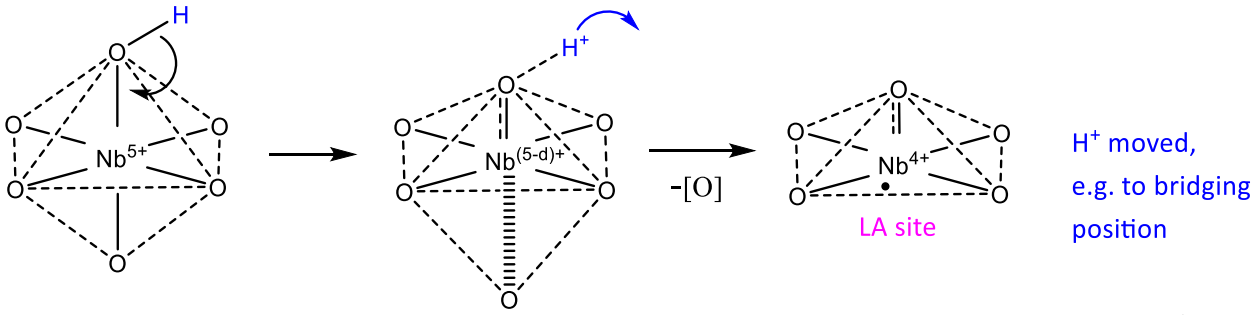
For Nb_2O_5 no acid sites were detected which is consistent from a structural point of view: Protons giving rise to BA sites are not part of the crystal structure of H-Nb_2O_5. Further the rigid network of edge- and corner-sharing octahedra with a highly coordinated niobium center makes the formation of LA sites/TMP-LA adducts difficult. In addition, the surface area of bulk materials is low and the number of possibly formed LA sites is therefore not surprisingly below the detection limit. The same argument applies for HNb_3O_8 regarding LA site formation. BA sites on the other hand were detected on HNb_3O_8, as expected due to the layered structure consisting of alternating proton and niobate sheets.

If few-to monolayer hy-Nb and hy-Nb-TEOA were based on the exact same structural units as HNb_3O_8, an increase in BA sites according to surface area would be expected. However, in both cases the increase in BA sites is less pronounced (only about half) than expected from the increase in surface area (Table 5.4). Instead large amounts of LA sites were detected. It has been suggested that the removal of BA sites in form of water ($2H^+$ and $1O^{2-}$ from the Nb-O network) can result in the formation of LA sites.[6,57] Considering the fact that the reaction between two BA sites in form of a proton and a terminal hydroxyl group yields a water molecule and an oxygen vacancy, one accessible LA site (for TMP adsorption) is created (Scheme 5.3). This process can explain the comparably low amounts of BA sites on hy-Nb and hy-Nb-TEOA, where during synthesis in the presence of stabilisers LA sites were created from the removal of BA sites. The observed coordination numbers of below 6 (EXAFS) further support this type of LA site formation.



Scheme 5.3 – Proposed oxygen vacancy/LA site formation *via* BA site removal in form of water

The above mechanism of water removal/LA site creation can already account for half the quantity of LA sites formed as BA sites removed. But significantly larger LA site quantities than expected from here were measured, indicating that the LA sites present do not entirely arise from the removal of BA sites. Other factors such as the removal of oxygen from Nb-O systems under reducing synthetic conditions in the presence of surfactants likely play a role in LA site formation. As discussed earlier, the formation of oxygen vacancies during surfactant-supported synthesis could proceed *via* breakage of elongated Nb---O bonds in the parent O=Nb---O structure, which creates Nb^{4+} species and allows free access for TMP-LA adduct formation (Scheme 5.4).

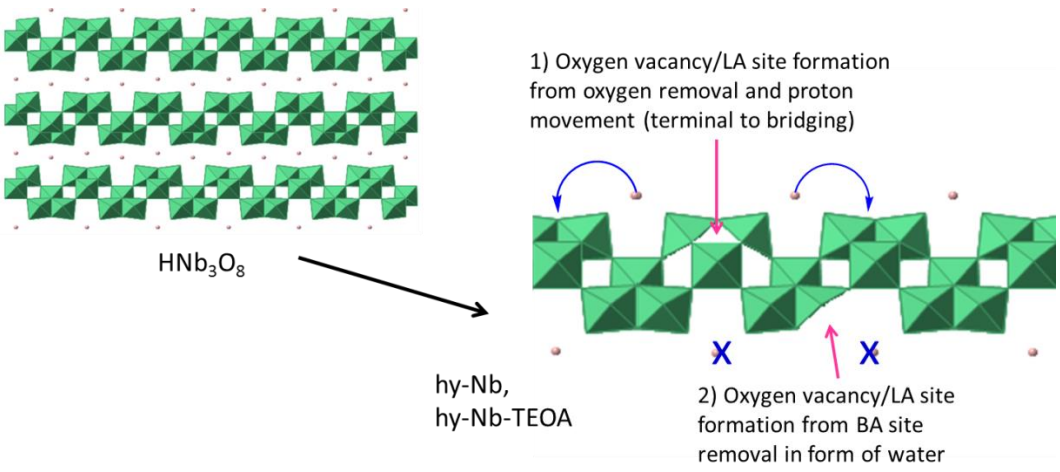


Scheme 5.4 – Proposed oxygen vacancy/LA site formation *via* oxygen removal with Nb^{4+} formation and proton shift

It is further interesting to note that the LA site strength of hy-Nb is lower than that of hy-Nb-TEOA (Table 5.4). This is likely due to the more pronounced Nb^{4+} character (XPS) of hy-Nb-TEOA with an overall lower coordination number (EXAFS), indicating more structural

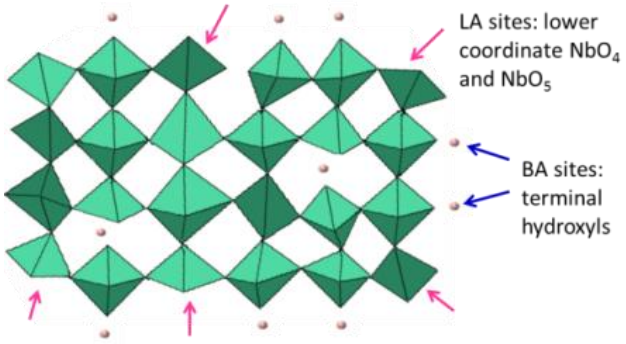
flexibility with more and stronger LA sites, possibly involving charge delocalization as discussed earlier. Previous analysis[9] on the mono-layer structure of hy-Nb-TEOA compared to few-layer hy-Nb also supports this increased structural flexibility and defect formation. At this point it should be noted that the lower acid site quantities and lower surface area measured for hy-Nb-TEOA compared to hy-Nb do not seem to agree with the above observations. However, a significant degree of re-stacking due to monolayer instability of hy-Nb-TEOA upon drying is likely to cause this deviation towards lower surface area and lower exposed than actual acid site quantities. It is to note that after the synthesis, the stabilizers (TEOA and ammonia) are removed by acid treatment.[58] In terms of BA site strength, hy-Nb-TEOA is again more acidic than hy-Nb, which in turn is significantly more acidic than HNb_3O_8. This increase in acid strength for hy-Nb and further hy-Nb-TEOA could be caused by shifts in proton position along the Nb-O network upon few-to monolayer synthesis, where for example oxygen removal/LA site formation could induce such shifts to stronger acidic bridging hydroxyl positions (Scheme 5.4).

Overall, it appears that the complexity of structural changes in hy-Nb and hy-Nb-TEOA compared to bulk HNb_3O_8 is the result of the high structural flexibility of these nanomaterials. At least two processes seem to be involved in LA site formation, where one mechanism gives rise to oxygen vacancies via the removal of two adjacent BA sites in form of water. Another mechanism of oxygen vacancy formation appears to proceed via the reduction process of O=Nb--O with formation of Nb^{4+} species, which could further induce proton shifts as cause for the observed increase in protonic strength (Scheme 5.5).



Scheme 5.5 – Proposed oxygen vacancy/LA site formation upon downscaling from bulk HNb_3O_8 to few- to monolayer hy-Nb and hy-Nb-TEOA

Mesoporous $Nb_2O_5*nH_2O$ also showed large amounts of both BA and LA sites, which can be explained by its high surface area and structural flexibility as for the layered nanomaterials. Its intrinsic porosity (TEM) with loose packing of most likely corner-sharing NbO_4, NbO_5 and NbO_6 units (EXAFS and XPS) is formed during etching/acid-soaking in the synthesis process. Resulting low coordination numbers and oxygen vacancies give rise to significant amounts of LA besides BA sites. The observed LA site strength is comparable to that of hy-Nb-TEOA, which goes in line with their similar properties regarding the increased Nb^{4+} character (XPS) and low coordination numbers (EXAFS). The comparatively low BA site strength suggests the presence of terminal rather than bridging hydroxyls[21,56], which supports a network consisting of lower connectivity corner-sharing rather than edge-sharing Nb-O units (Scheme 5.6).



Scheme 5.6 – Proposed LA and BA site origins in mesoporous $Nb_2O_5*nH_2O$

5.5 Conclusions

Summing up all observations and conclusions made from the above structural analysis (XRD, TEM, Raman, XPS, EXAFS and NMR) supported by acid site analysis, the following characteristics stand out: the crystalline but low surface area/bulk materials Nb_2O_5 (H-Nb_2O_5) and HNb_3O_8 consist primarily of ordered edge- and corner-sharing NbO_6 octahedra with an average oxidation state of Nb^{5+}. Nb_2O_5 has a block structure with acid site quantities below the detection limit (TMP NMR), while HNb_3O_8 is made of layers of niobates interconnected by protons with detectable Brønsted acid (BA) sites as expected. Both Nb_2O_5 and HNb_3O_8 have been studied to detail in literature[1,6,9,28] and were therefore used for comparative study of the remaining niobium oxides.

Hy-Nb and hy-Nb-TEOA have structural similarities to HNb_3O_8 but are few- to monolayered instead of bulk materials. It gives them higher surface areas and more structural flexibility with longer Nb-O bond distances and species such as O=Nb---O arising from distorted NbO_6. Large amounts of Lewis acid (LA) besides BA sites are detected and average coordination numbers of below 6 and a shift in oxidation state towards Nb^{4+} were observed. These observations point towards the presence of oxygen vacancies in hy-Nb and hy-Nb-TEOA, explaining the origin of the observed LA sites. Oxygen vacancies/LA sites appear to be formed during synthesis in the presence of stabilizers, where one possible route involves the removal of BA sites in form of water with the simultaneous formation of NbO_5 species. Another route appears to involve the removal of oxygen from elongated bonds as in O=Nb---O to form NbO_5 species with Nb^{4+} character and to simultaneously induce proton shifts, further reflecting the increased BA strength of hy-Nb and hy-Nb-TEOA.

Overall, the nanostructures hy-Nb and hy-Nb-TEOA consist of NbO_6 composed layers with significant structural flexibility, including distortions and defects. These are formed during synthesis in the presence of surfactants and give rise to large amounts of LA and BA sites compared to bulk layer HNb_3O_8.

For mesoporous $Nb_2O_5*nH_2O$ the structural analysis proved more difficult due to its highly amorphous nature, but some structural insights were still obtained. The rather long and uniform Nb-O bond distances point towards a loosely packed structure consisting of mostly corner-sharing units. With an oxidation state shifted towards Nb^{4+} and an average coordination number of about 5, a mixed structure containing different species such as NbO_4, NbO_5 and NbO_6 is likely for mesoporous $Nb_2O_5*nH_2O$. Again large amounts of LA and BA sites were detected, due to the high porosity and loose network structure formed during acid-soaking in the synthesis process. LA sites show comparable acid strength to that of hy-Nb-TEOA and most likely arise from lower coordinate NbO_4 and NbO_5 units. BA sites of comparably low strength support the presence of a reduced connectivity corner- over edge-sharing network with terminal rather than bridging hydroxyls.

It is hoped that the above structural findings will help to develop better catalysts due to tunable acid properties. With the gain in understanding of how acidity is related to structure, targeted synthesis becomes possible and solid acid catalysts meeting specific catalytic requirements can be developed.

5.6 References

(1) Nico, C.; Monteiro, T.; Graca, M. P. F. *Prog. Mater. Sci.* **2016**, *80*, 1.

(2) Ramakrishna, S.; Le Viet, A.; Reddy, M. V.; Jose, R.; Chowdari, B. V. R. *J. Phys. Chem. C* **2010**, *114* (1), 664.

(3) Schäfer, H.; Schulte, F.; Gruehn, R. *Angew. Chemie - Int. Ed.* **1964**, *76* (12), 536.

(4) Bach, D. EELS Investigations of Stoichiometric Niobium Oxides and Niobium-based Capacitors, 2009.

(5) Anderson, J. S.; Browne, J. M.; Hutchison, J. L. *J. Solid State Chem.* **1972**, *5* (3), 419.

(6) Nowak, I.; Ziolek, M. *Chem. Rev.* **1999**, *99* (12), 3603.

(7) Fang, X.; Hu, L.; Huo, K.; Gao, B.; Zhao, L.; Liao, M.; Chu, P. K.; Bando, Y.; Golberg, D. *Adv. Funct. Mater.* **2011**, *21* (20), 3907.

(8) Katoh, R.; Furube, A.; Yoshihara, T.; Hara, K.; Fujihashi, G.; Takano, S.; Murata, S.; Arakawa, H.; Tachiya, M. *J. Phys. Chem. B* **2004**, *108* (15), 4818.

(9) Nakagawa, K.; Jia, T.; Zheng, W.; Fairclough, S. M.; Katoh, M.; Sugiyama, S.; Edman Tsang, S. C. *Chem. Commun.* **2014**, *50* (89), 13702.

(10) Tanabe, K. *Catal. Today* **2003**, *78* (1–4 SPEC.), 65.

(11) Ushikubo, T. *Catal. Today* **2000**, *57* (3–4), 331.

(12) Jehng, J.-M.; Wachs, I. E. *Chem. Mater.* **1991**, *3* (1), 100.

(13) Zhao, Y.; Zhou, X.; Ye, L.; Tsang, S. C. E. *Nano Rev.* **2012**, *3*, 17631.

(14) McConnell, A. A.; Aderson, J. S.; Rao, C. N. R. *Spectrochim. Acta Part A Mol. Spectrosc.* **1976**, *32* (5), 1067.

(15) Iijima, S. *Acta Crystallogr. Sect. A* **1973**, *29* (1), 18.

(16) Mcqueen, T.; Xu, Q.; Andersen, E. N.; Zandbergen, H. W.; Cava, R. J. *J. Solid State Chem.* **2007**, *180*, 2864.

(17) Marucco, J. F. *J. Chem. Phys.* **1979**, *70* (2), 649.

(18) Gatehouse, B. M.; Wadsley, A. D. *Acta Crystallogr. Sect. A* **1964**, *17*, 1545.

(19) Mertin, W.; Andersson, S.; Gruehn, R. *J. Solid State Chem.* **1970**, *1* (I), 419.

(20) Kato, K.; Tamura, S. *Acta Crystallogr. Sect. B* **1975**, *31* (3), 673.

(21) Takagaki, A.; Lu, D.; Kondo, J. N.; Hara, M.; Hayashi, S.; Domen, K. *Chem. Mater.* **2005**, *17* (10), 2487.

(22) Murayama, T.; Chen, J.; Hirata, J.; Matsumoto, K.; Ueda, W. *Catal. Sci. Technol.* **2014**, *4*, 4250.

(23) Okuhara, T. *Chem. Rev.* **2002**, *102* (10), 3641.

(24) Nakajima, K.; Baba, Y.; Noma, R.; Kitano, M.; Kondo, J.; Hayashi, S.; Hara, M. *J. Am. Chem. Soc.* **2011**, *133*, 4224.

(25) Yang, Z. J.; Li, Y. F.; Wu, Q. Bin; Ren, N.; Zhang, Y. H.; Liu, Z. P.; Tang, Y. *J. Catal.* **2011**, *280* (2), 247.

(26) Xiong, J.; Wen, L.; Jiang, F.; Liu, Y.; Liang, S.; Wu, L. *J. Mater. Chem. A* **2015**, *3* (41), 20627.

(27) Kreissl, H. T.; Li, M. M. J.; Peng, Y. K.; Nakagawa, K.; Hooper, T. J. N.; Hanna, J. V.; Shepherd, A.; Wu, T. S.; Soo, Y. L.; Tsang, S. C. E. *J. Am. Chem. Soc.* **2017**, *139* (36), 12670.

(28) Wang, S.; Liu, C.; Liu, L.; Zhang, X.; Gong, J.; Tong, Z. *Synth. React. Inorganic, Met. Nano-Metal Chem.* **2012**, *42* (2), 251.

(29) Hardcastle, F. D.; Wachs, I. E. *Solid State Ionics* **1991**, *45* (3–4), 201.

(30) Pittman, R. M.; Bell, A. T. *J. Phys. Chem.* **1993**, *97*, 12178.

(31) Hu, Z. P.; Li, Y. P.; Ji, M. R.; Wu, J. X. *Solid State Commun.* **1989**, *71* (10), 849.

(32) Grundner, M.; Halbritter, J. *J. Appl. Phys.* **1980**, *51* (1), 397.

(33) Koito, Y.; Rees, G. J.; Hanna, John, V.; Li, M. J. M.; Peng, Y.-K.; Puchtler, T.; Taylor, R.; Wang, T.; Kobayashi, H.; Teixeira, I. F.; Khan, M. A.; Kreissl, H. T.; Tsang, S. C. E. *ChemCatChem* **2017**, *9*, 144.

(34) Atashbar, M. Z.; Sun, H. T.; Gong, B.; Wlodarski, W.; Lamb, R. *Thin Solid Films* **1998**, *326* (1–2), 238.

(35) www.xpsfitting.com.

(36) www.xpssimplified.com.

(37) Mrowec, S. *Ceramurg. Int.* **1978**, *4* (2), 47.

(38) Morea, R.; Gonzalo, J.; Siegel, J.; Solís, J.; Optica, I. De. *Experiment Title: Structural Assessment of Unconventional Lead Niobium Germanate Glasses with Large Nb Contents by High-Resolution XANES & X-Ray Emission Spectroscopy*; 2012.

(39) Morante, J. R. **2002**, *853*, 2002.

(40) Kodama, R.; Terada, Y.; Nakai, I.; Komaba, S.; Kumagai, N. *J. Electrochem. Soc.* **2006**, *153* (3), A583.

(41) Bizeto, M. A.; Leroux, F.; Shiguihara, A. L.; Temperini, M. L. A.; Sala, O.; Constantino, V. R. L. *J. Phys. Chem. Solids* **2010**, *71* (4), 560.

(42) Ichikuni, N.; Sato, F.; Shimazu, S.; Uematsu, T. *Top. Catal.* **2002**, *18* (1), 101.

(43) Oakton, E.; Tillier, J.; Siddiqi, G.; Mickovic, Z.; Sereda, O.; Fedorov, A.; Copéret, C. *New J. Chem.* **2016**, *40*, 2655.

(44) de Groot, F.; Vankó, G.; Glatzel, P. *J. Phys. Condens. Matter* **2009**, *21* (10), 104207.

(45) Penner-Hahn, J. A. *X-Ray Absorption Spectroscopy*; 2011.

(46) Newville, M. *Fundamentals of XAFS*; Consortium for Advanced Radiation Sources, University of Chicago, 2004.

(47) Gasperin, M. *Acta Crystallogr. Sect. B* **1982**, *36*, 2024.

(48) Khabibulin, D.; Romanenko, K.; Zuev, M.; Lapina, O. *Magn. Reson. Chem.* **2007**, *45* (11), 962.

(49) Papulovskiy, E.; Shubin, A. a; Terskikh, V. V; Pickard, C. J.; Lapina, O. B. *Phys. Chem. Chem. Phys.* **2013**, *15* (14), 5115.

(50) Ashbrook, S. *Introduction To Quadrupolar NMR [Power Point Slides]*; University of St Andrews, 2008.

(51) Hanna, J. V.; Pike, K. J.; Charpentier, T.; Kemp, T. F.; Smith, M. E.; Lucier, B. E. G.; Schurko, R. W.; Cahill, L. S. *Chem. - Eur. J.* **2010**, *16* (10), 3222.

(52) Satterlee, J. D. *Concepts Magn. Reson.* **1990**, *2* (3), 119.

(53) Zheng, A.; Huang, S.-J.; Liu, S.-B.; Deng, F. *Phys. Chem. Chem. Phys.* **2011**, *13* (33), 14889.

(54) Chu, Y.; Yu, Z.; Zheng, A.; Fang, H.; Zhang, H.; Huang, S. J.; Liu, S. Bin; Deng, F. *J. Phys. Chem. C* **2011**, *115* (15), 7660.

(55) Lunsford, J. H.; Sang, H.; Campbell, S. M.; Liang, C. H.; Anthony, R. G. *Catal. Letters* **1994**, *27* (3–4), 305.

(56) Takagaki, A.; Tagusagawa, C.; Hayashi, S.; Hara, M.; Domen, K. *Energy Environ. Sci.* **2010**, *3* (1), 82.

(57) Corma, A. *Chem. Rev.* **1995**, *95* (3), 559.

(58) Kreissl, H. T.; Nakagawa, K.; Peng, Y. K.; Koito, Y.; Zheng, J.; Tsang, S. C. E. *J. Catal.* **2016**, *338*, 329.

Chapter 6

Converting Hydroxymethylfurfural to Dimethylfuran and Further to Aromatic Hydrocarbons

Chapter 6 164

6.1 Background 165

6.2 Objectives 167

6.3 Experimental 169

6.3.1 Catalyst Synthesis: Ru/Pd on Modified Y Zeolites 169

6.3.2 Reaction of HMF to DMF and Further to Aromatics 169

6.3.3 Product Analysis 170

6.4 Results and Discussion 171

6.4.1 Conversion of HMF to DMF 171

6.4.2 Further Conversion of DMF to Aromatic Hydrocarbons 185

6.5 Conclusions 188

6.6 References 190

6.1 Background

Upgrading biomass feedstocks to industrially interesting compounds has become an important research topic over the past several years. Due to diminishing fossil fuel reserves and environmental concerns, renewable energies present a promising alternative.[1–3] Significant advances have been made, but the development of renewable energies still requires progress in order to become more economically viable. In 2016, the renewable energy sector made up about 20 % of the global energy market, 14 % of which is attributed to biomass, while fossil fuels still account for almost 80% of the global energy consumption.[4,5] In the biomass sector compounds with significant potential for further development are so called platform molecules. Hydroxymethylfurfural (HMF) is such a platform molecule; it is obtained from the catalytic conversion of sugar feedstocks and can be upgraded for use in the biofuel, polymer production and pharmaceutical industries.[6,7]

One of the focuses in this project concerns upgrading HMF to aromatics. Currently, aromatics are mainly obtained from the refining of fossil fuels. Aromatics are widely used in the chemical industry, ranging from the production of resins and plastics to solvents and fine chemicals and further to traditional fuel components. Finding sustainable routes to produce aromatics is therefore important.[8–11] Production pathways with as few intermediate steps as possible are aimed for because they reduce both costs and product loss due to separation and purification methods.

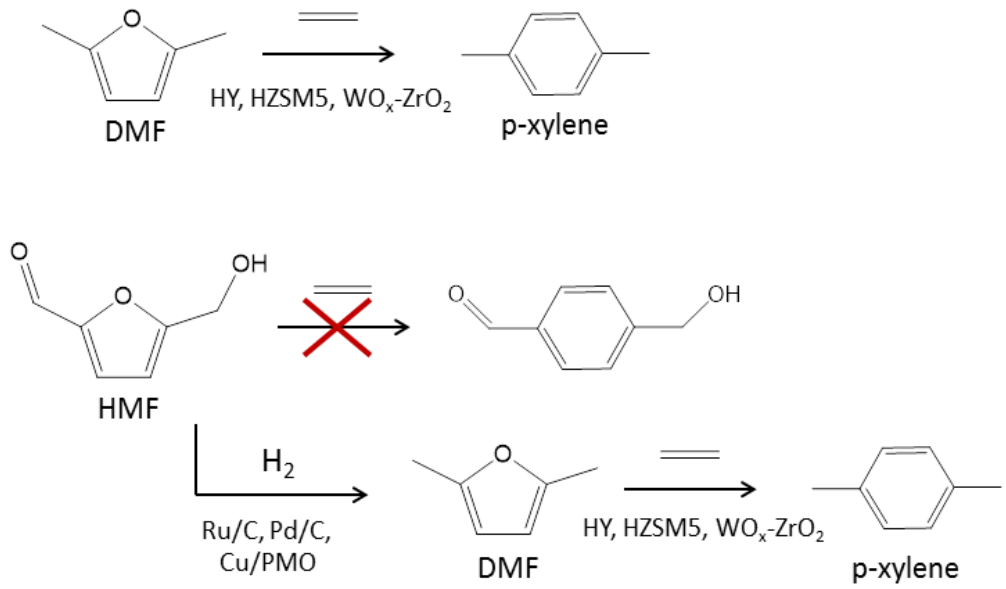
DMF, which is structurally related to HMF, has been widely reported in literature regarding the production of aromatics. The core reaction steps are Diels-Alder cycloaddition of DMF and ethylene and the subsequent dehydration to xylene using an acid catalyst.[12–19] Wang *et al.* reported the production of p-xylene from DMF over WO_x-ZrO_2 with 77 % selectivity at 60 %

conversion.[15] Williams *et al.* achieved a similarly good selectivity of 75 % *p*-xylene at up to 95 % DMF conversion over HY zeolite.[16] Wijaya *et al.* studied the use of silica-alumina aerogels and reached 70 % selectivity,[17] all of which are promising results.

Unfortunately with HMF, which contains an additional keto and hydroxyl group, the direct cycloaddition used to convert DMF has not been achieved.[18] An alternative way to proceed is to convert HMF to DMF before further reaction of DMF to xylene (Scheme 6.1). For HMF to DMF conversion ruthenium, copper and palladium based hydrogenation catalysts have been reported, mostly on carbon supports.[20–23] For example Hu *et al.* obtained 95 % DMF from HMF over Ru/C at 20 bar H_2.[22] Wang *et al.* reported a similarly good yield of 91 % DMF over Ru/Co_3O_4 at 10 bar H_2.[23] Unfortunately though, these reactions require high hydrogen pressures which is neither very economical nor sustainable. A similar problem is encountered during DMF to xylene conversion, where high ethylene pressures are required. Recent work by Teixeira *et al.* though has shown that ethylene can be generated from ethanol *in situ* - over acidic zeolite catalysts which also catalyse the dehydration reaction yielding xylene.[24] Therefore no addition of gaseous ethylene is required and ethanol serves as the solvent for DMF to xylene conversion at the same time. There also have been a small number of reports on non-gaseous hydrogenation in the context of HMF to DMF conversion, using a sacrificial reagent for catalytic hydrogen transfer. Hansen *et al.* achieved a yield of 48 % DMF over Cu/PMO using supercritical methanol[25] and Jae *et al.* reported the use of secondary alcohols yielding up to 80 % DMF over Ru/C.[26]

In order to render the conversion route of HMF to aromatic hydrocarbons industrially relevant, not only individual yields, but also the number of involved processing steps, need to be considered. Separation and transfer steps are time and energy extensive and tend to lower the

overall reaction yield. Having to convert HMF to DMF and DMF to xylene separately under different reaction conditions is therefore not ideal. An efficient one-batch-reaction remains to be developed.

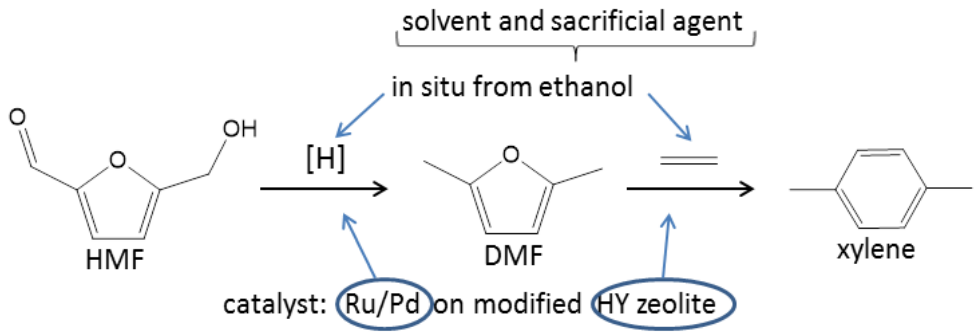


Scheme 6.1 – Conversion pathways and catalysts for DMF and HMF conversion to aromatics

6.2 Objectives

Building on the idea of more economical and sustainable methods of production, this work aims to convert HMF to aromatic hydrocarbons in a one-batch-reaction. Instead of using high pressures of hydrogen and ethylene to subsequently convert HMF to DMF and DMF to xylene, this work uses ethanol to combine the required features in one: it is used as both the solvent and the *in-situ* hydrogen and ethylene source to convert HMF to DMF and further to xylene (Scheme 6.2). On the catalyst side, this work aims to develop a combined hydrogenation and aromatization catalyst, for the purpose of which ruthenium and palladium supported on Y zeolites of varying acidity are synthesized. The variations in support nature are achieved by ion

exchange and doping with different metal oxides, opening up interesting tuning possibilities both on the hydrogenation and aromatization side.



Scheme 6.2 – Aiming to combine the conversions of HMF to DMF and DMF to aromatics into a one-batch process

6.3 Experimental

This section provides a summary of the experimental procedures, detailed descriptions can be found in Chapter 3.

6.3.1 Catalyst Synthesis: Ru/Pd on Modified Y Zeolites

Starting from commercially available HY10 zeolite (Tosoh HUA 350), the following modifications were made:

NbO/HY10: wet impregnation of HY10 with 5 wt% Nb using ammonium niobate(V) oxalate hydrate (99.99 % from Sigma Aldrich), followed by calcination in air at 400 °C for 3 h.

NaY10: ion exchange with 1 M sodium nitrate for two days (pH neutralization with NaOH over time).

MgO/NaY10: wet impregnation of NaY10 with 5 wt% Mg using magnesium acetate tetrahydrate (99.997 % from Alfa Aesar), followed by calcination in air at 400 °C for 3 h.

Support decoration with Ru/Pd: wet impregnation with 5 wt% Ru or 5 wt% Pd using ruthenium(III) chloride (38 wt% Ru content, Alfa Aesar) or palladium(II) nitrate (40 wt% Pd content, Alfa Aesar), followed by reduction under hydrogen at 400 °C for 3 h.

6.3.2 Reaction of HMF to DMF and Further to Aromatics

For the conversion of HMF to DMF, a mixture of 250 mg HMF (≥99 % Sigma Aldrich), 50 mg catalyst and 15 mL ethanol was charged to a Parr autoclave under atmospheric pressure nitrogen. The autoclave was then heated to 300 °C under stirring and reactions lasting 9 h, 12 h and 20 h were performed. Reaction times included the heating up and cooling down times of 45 and 15 minutes, respectively.

In order to confirm the further conversion of DMF to aromatics and minimize catalyst deactivation effects, the reaction mixture from the previous HMF to DMF reaction was centrifuged to remove the old catalyst before being charged to a Parr autoclave, along with 100 mg fresh catalyst under atmospheric pressure nitrogen. The autoclave was then heated to 300 °C and reactions lasting 1 h, 2 h and 4 h were performed. Reaction times included the heating up and cooling down times of 45 and 15 minutes, respectively.

6.3.3 Product Analysis

A gas chromatograph (Agilent GC 7890B, HP-INNOWax column) combined with a mass spectrometer (Agilent MSD 5977A) were used to separate, analyse and quantify reaction products. For product quantification the GC-MS was calibrated by preparing solutions of different concentrations of commercially available HMF (≥99 % Sigma Aldrich), DMF (99 % Sigma Aldrich) and triethylbenzene (≥97 % Sigma Aldrich). The structural identification of side products was done using the internal MS compound library. For side product quantification and carbon balance calculation structurally similar products were grouped together and GC-MS calibrations were done with 2,5-hexanedione, ethyl levulinate and butanol as model compounds.

6.4 Results and Discussion

6.4.1 Conversion of HMF to DMF

This work has investigated ruthenium and palladium on modified Y zeolites as hydrogenation catalysts in the conversion of HMF to DMF. Ethanol was used as both the solvent and sacrificial hydrogenation reagent which gave the significant advantage of not requiring gaseous hydrogen. Together with the use of Y zeolites as the catalyst support, this brought us two steps closer to combining the HMF to DMF reaction with the further conversion of DMF to aromatics, where ethanol was reported[24] as solvent and *in situ* ethylene source using HY zeolite as the catalyst. The effects of modifying the Y zeolite support nature by ion exchange and doping with metal oxides were further investigated regarding DMF yield. TEM images of the catalysts were used to determine ruthenium and palladium particle sizes, and potential effects of variations in the support nature are discussed as follows.

Table 6.1 shows the yields of DMF and derivatives obtained over the different catalysts after reaction times of 9 h, 12 h and 20 h at 300 °C (also see Appendix p.A13-A16 for yield calculations). 'DMF and derivatives' means that every yield given is the combined yield of the main product DMF (dimethylfuran) and its derivatives MF (methylfuran) and MEF (methylethylfuran), which were also obtained during the reaction (Figure 6.1). This is done for simplification, since both derivatives can react further to aromatics *via* cycloaddition and dehydration in a similar fashion to DMF, with the only difference being the attachment of plus or minus one methyl group. The formation of MF and MEF in addition to DMF is most likely due to the elevated temperatures required for HMF to DMF hydrogenation, having C-C bond rearrangement as a side effect. Similar observations were made previously in the context of HMF to DMF hydrogenation over Ru catalysts, especially with regard to MF formation.[22,23,26] DMF

still remains the main product in this work, as it made up ≥70 % of [DMF + MF + MEF] in all reactions presented here. It can be seen from Table 6.1 that the highest yields of DMF and derivatives were obtained after 12 h, and decrease again at longer reaction times of 20 h, indicating that DMF was converted further over time. All reactions showed a complete conversion of HMF, with no HMF left in the product solution even after the shortest reaction time of 9 h. Instead, partially hydrogenated intermediates of HMF to DMF conversion were initially detected, and were further converted to DMF and other products over time.

Table 6.1 – Yields of DMF and derivatives obtained over Ru/Pd on modified Y zeolites

Catalyst	**Total Yield % of DMF and derivatives[a]**		
	9h	**12h**	**20h**
Pd/HY10	33	40	18
Ru/HY10	31	35	11
Pd/NbO/HY10	25	30	9
Ru/NbO/HY10	29	35	10
Pd/NaY10	-	-	-
Ru/NaY10	37	44	8
Pd/MgO/NaY10	30	36	15
Ru/MgO/NaY10	50	61	53

Reaction conditions: 250 mg HMF, 15 mL ethanol and 50 mg catalyst were reacted in a Parr autoclave at 300 °C under stirring.
[a]Total yield given = DMF yield + MF yield + MEF yield, DMF is main product.

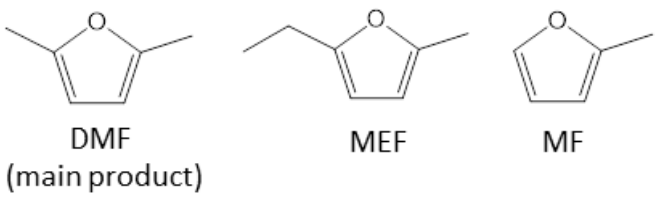
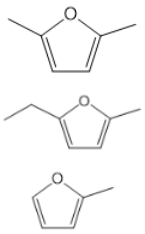
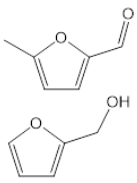
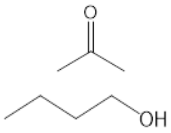
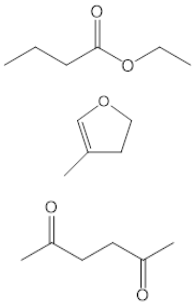


Figure 6.1 – DMF and its derivatives MF and MEF

GC-MS analysis confirmed the presence of various side products besides DMF and derivatives at all reaction times (also see Appendix p.A16-A18 for GC-MS spectra). Exemplary product distributions for the three catalysts with the highest yields of DMF and derivatives (Ru/MgO/NaY10, Ru/NaY10 and Pd/HY10) are given in Table 6.2. Further, oxidation products of ethanol were detected (ethanone and acetal) which confirm the role of ethanol as sacrificial hydrogenation agent for HMF to DMF conversion under the present conditions. Yields of DMF and its derivatives vary significantly among the catalysts, both for Ru *versus* Pd on the same support and between the same metal on different supports (Table 6.1). The highest yield with 61 % was obtained over Ru/MgO/NaY10, while for Pd/NaY10 no detectable amounts of DMF or derivatives were found.

Table 6.2 – Product yield distributions over selected catalysts

Catalyst	**Yield in %**				
	DMF (main), MEF and MF 	Intermediates to DMF, MEF and MF e.g. 	Side products		
			C3/C4 e.g. 	C5/C6 e.g. 	C7-C14 mainly branched aromatics
Ru/MgO/NaY10	61	15	13	15	5
Ru/NaY10	44	13	26	16	7
Pd/HY10	40	9	28	14	10

[a]Yields given as % of starting material HMF after 12 h reaction time at 300 °C, total yield tends to exceed 100 % because side product formation can also result from solvent reactions (also see Appendix p.A13-A16 for yield calculations).

To gain an understanding of the above product yields, the different catalysts were looked at with regard to metal and support nature. Metal particle size and distribution were obtained from TEM images of the catalysts and metal surface areas were further calculated from here (Table 6.3 and Figure 6.2). All Ru catalysts have an even metal particle size distribution with an average particle diameter of 3 nm and an approximate metal surface area of 8.27 m^2 per g catalyst. Therefore metal particle size and surface area should not play a role in the observed differences in DMF yield for the Ru catalysts; instead the differences in support nature are likely to be significant here. For the Pd catalyst however, particle size and surface area differ significantly between the catalysts: Pd/NbO/HY10 and Pd/MgO/NaY10 tend to form particle aggregates with relatively large average diameters of 12 and 13 nm and total metal surface areas of about 2.08 m^2g^{-1} and 1.92 m^2g^{-1}, respectively. Pd/NaY10 and Pd/HY10 on the other hand show an even particle distribution with average particle diameters of 3 and 7 nm and surface areas of 8.31 m^2g^{-1} and 3.57 m^2g^{-1}, respectively. With the differences observed in Pd particle size and surface area as well as support nature, several variables are involved in DMF formation over the Pd catalysts, making it difficult to differentiate here.

Table 6.3 – Average metal particle size and metal surface area obtained from TEM

Catalyst	Metal particle size (nm)	Metal surface area per g catalyst (m^2g^{-1})
Pd/HY10	7	3.57
Ru/HY10	3	8.27
Pd/NbO/HY10	12	2.08
Ru/NbO/HY10	3	8.27
Pd/NaY10	3	8.31
Ru/NaY10	3	8.27
Pd/MgO/NaY10	13	1.92
Ru/MgO/NaY10	3	8.27

For metal surface area calculations see Chapter 3.2.1.

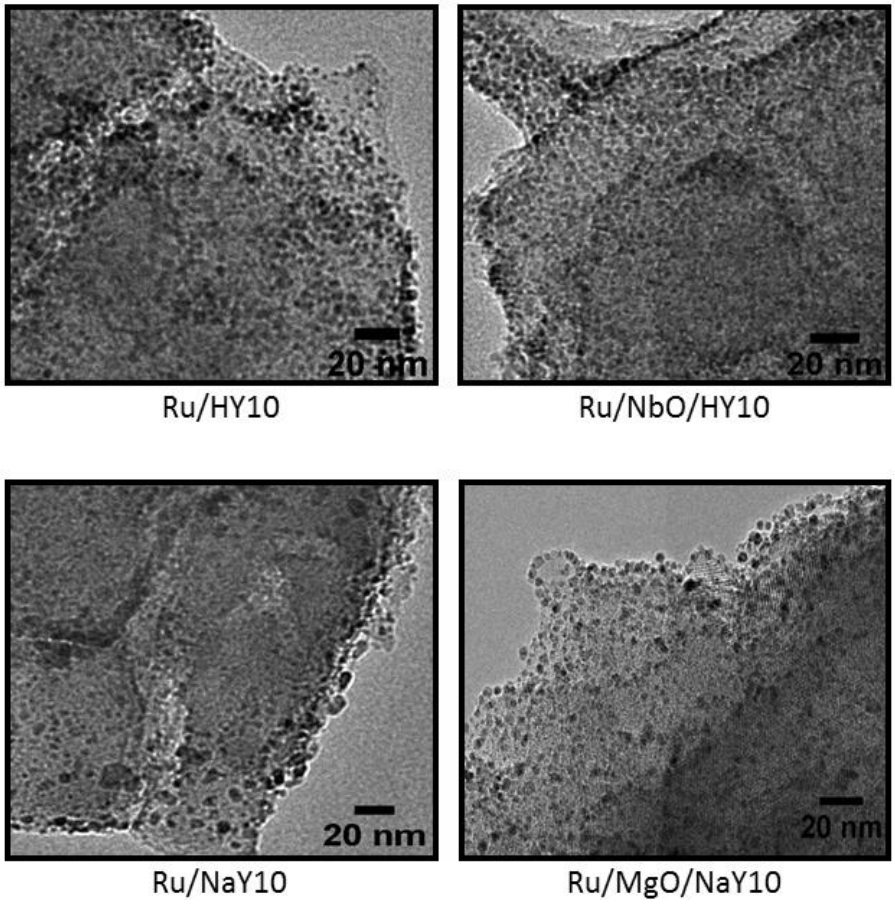


Figure 6.2a – TEM images of Ru on modified Y zeolites

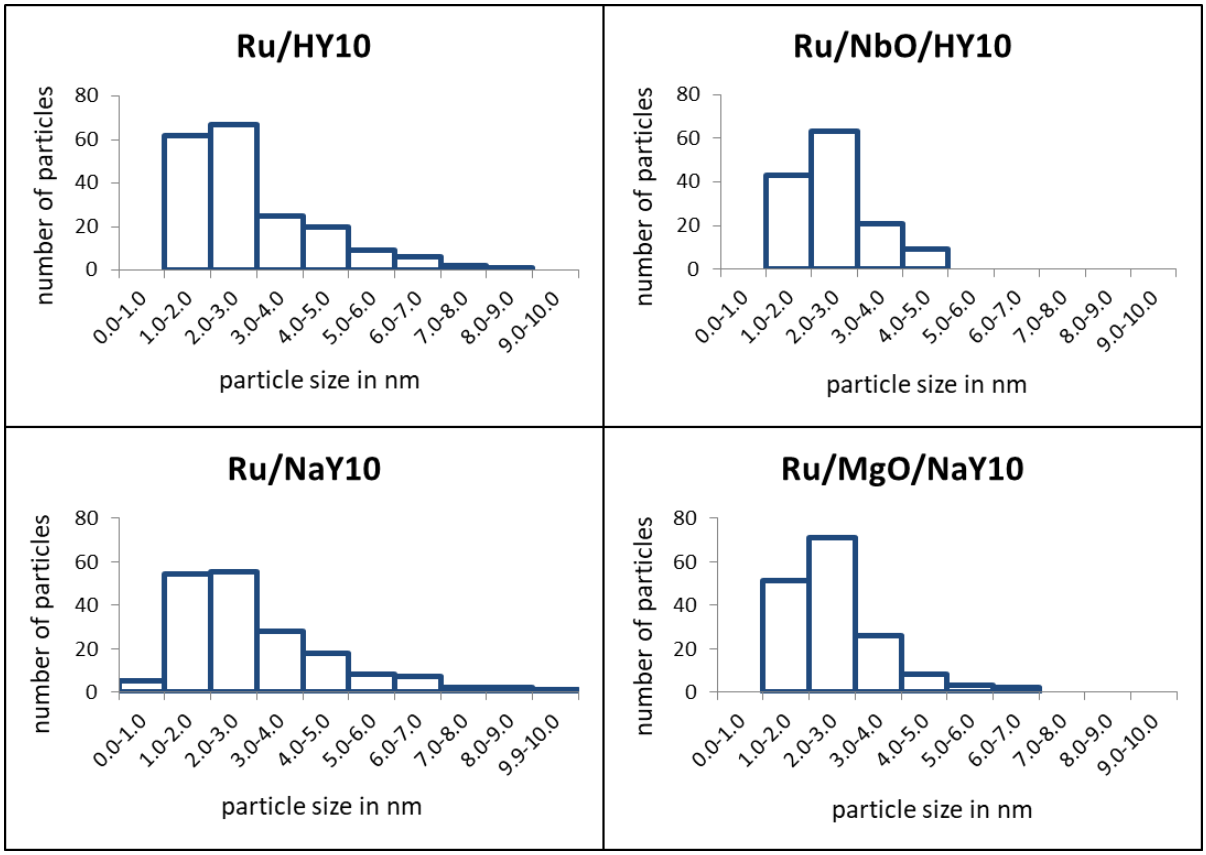


Figure 6.2b – Particle size distributions for Ru on modified Y zeolites from TEM

For all Ru catalysts: average metal particle size = 3 nm,
≥90 % of the measured particles have a diameter between 1 - 5 nm and
the 2 - 3 nm region contains the greatest proportion of particles.
Minimum quantity of particles measured = 150

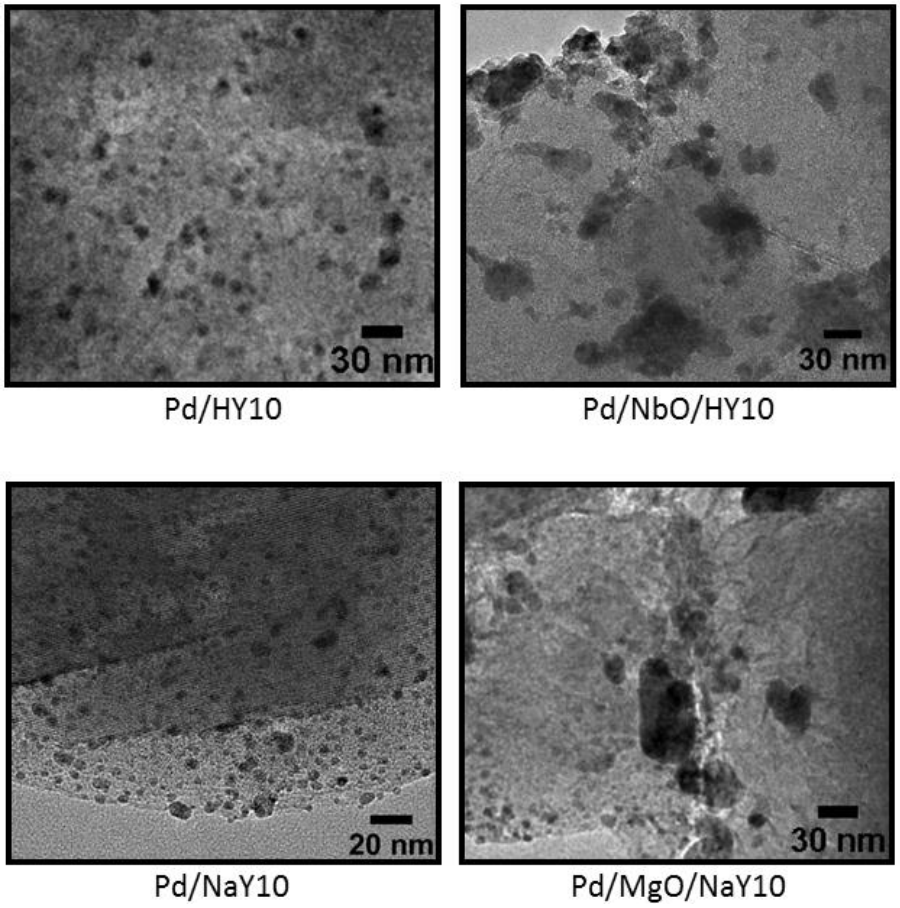


Figure 6.2c – TEM images of Pd on modified Y zeolites

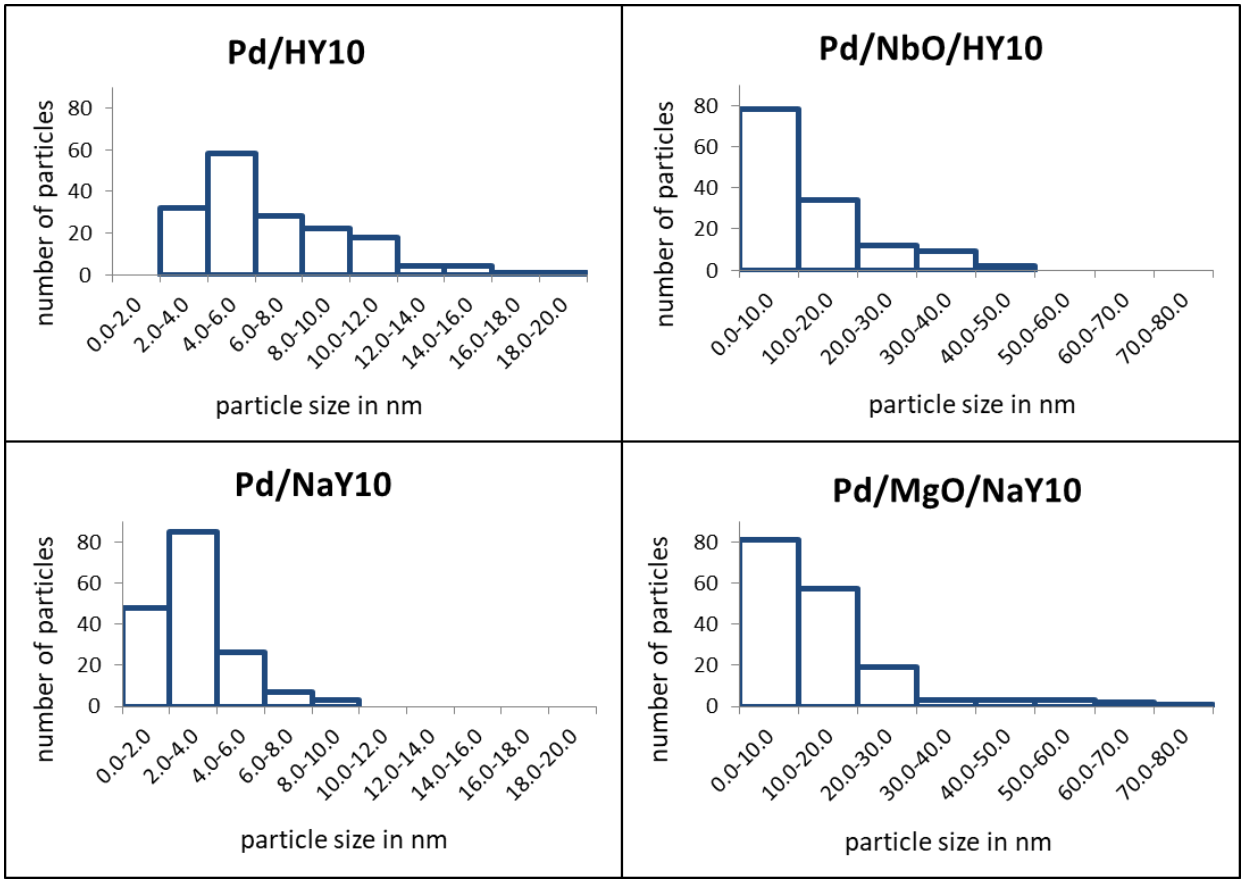


Figure 6.2d – Particle size distributions of Pd on modified Y zeolites from TEM

Average particle sizes: 7 nm for Pd/HY10, 12 nm for Pd/NbO/HY10,
3 nm for Pd/NaY10, 13 nm for Pd/MgO/NaY10.
Only Pd/NbO/HY10 and Pd/MgO/NaY10, both with oxide modified supports,
are comparable with respect to average particle size and distribution.
Minimum quantity of particles measured = 150.

Taking a closer look at the metal particle invariant Ru catalysts (Table 6.3 and Figure 6.2 a,b) reveals information on how DMF yield changes with support nature. Support acidity and basicity measurements were done for the different catalysts using NH_3 and CO_2 TPD (temperature programmed desorption) and the results are displayed in Table 6.4. As expected, commercial HY10 only possesses acid sites. Interestingly, NbO/HY10 showed a neutral surface with neither significant acidity nor basicity, indicating blockage of or reaction with the protonated HY10 sites by NbO. NaY10 has basic properties, which is to be expected from ion exchange where the strongly acidic protons in the HY10 network are replaced by sodium ions. MgO/NaY10 possesses even more basic sites, showing that the addition of MgO further enhances the basicity of the NaY10 support. So far there is unfortunately no deeper understanding of how the metal oxide doping affects the support structurally. The wet impregnation with Mg or Nb precursor followed by calcination in air obviously led to modifications, but no apparent MgO or NbO phases were observed from XRD. XRD profile subtraction of the unmodified from the oxide modified supports only yields background noise, possibly due to variations in the preferential orientation of the zeolite, but no evident peaks can be assigned, while clearly visible peaks arise from Pd and Ru decoration (Figure 6.3). It is therefore unclear if metal oxide particles were formed which are too small to visualize by XRD or if rather than forming a separate phase, the metals were incorporated into the silica-alumina network of the zeolite.

Table 6.4 – Acid and base site quantification for the different supports by NH_3 and CO_2 TPD

Support	**Acid Sites in mmol g^{-1} from NH_3 TPD**	**Base Sites in mmol g^{-1} from CO_2 TPD**
HY10	0.143[a]	-
NbO/HY10	-	-
NaY10	-	0.879[b]
MgO/NaY10	-	1.669[c]

Temperature at which peak desorption is occurring: [a]264 °C, [b]177 °C, [c]157 °C

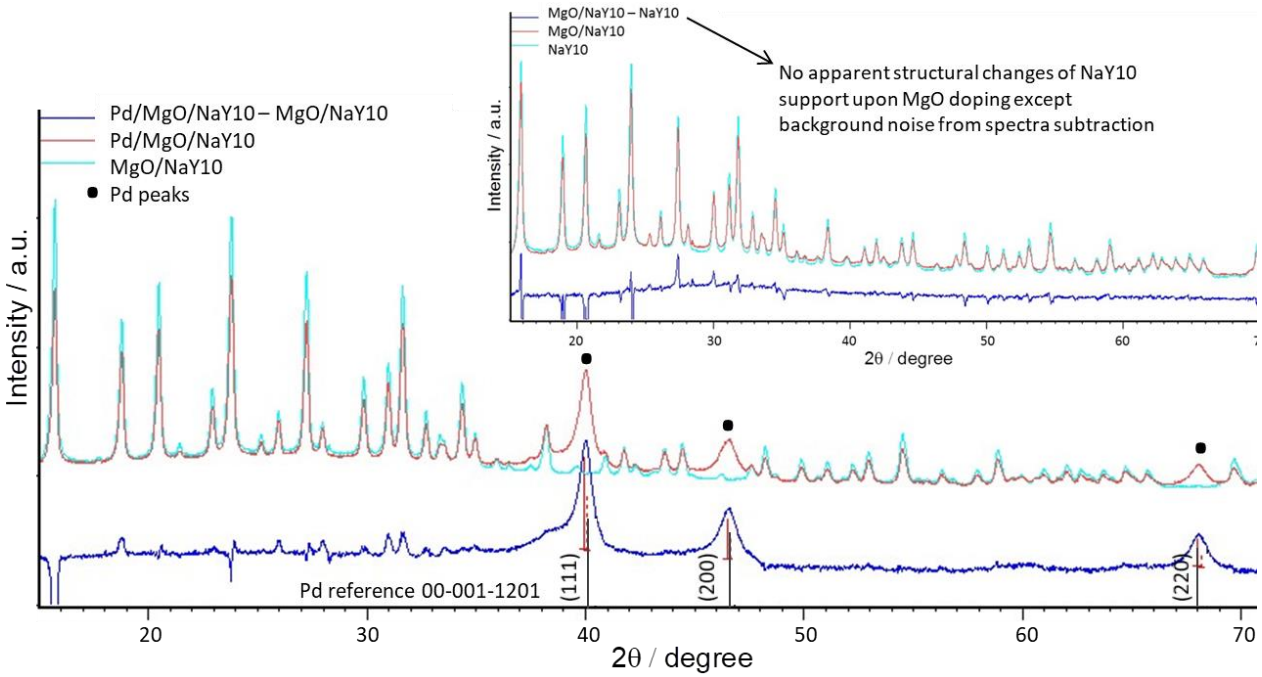


Figure 6.3a – XRD patterns of Pd/MgO/NaY10 and MgO/NaY10 in comparison to NaY10. Average Pd particle size from Scherrer equation = 12 nm (in good agreement with TEM).

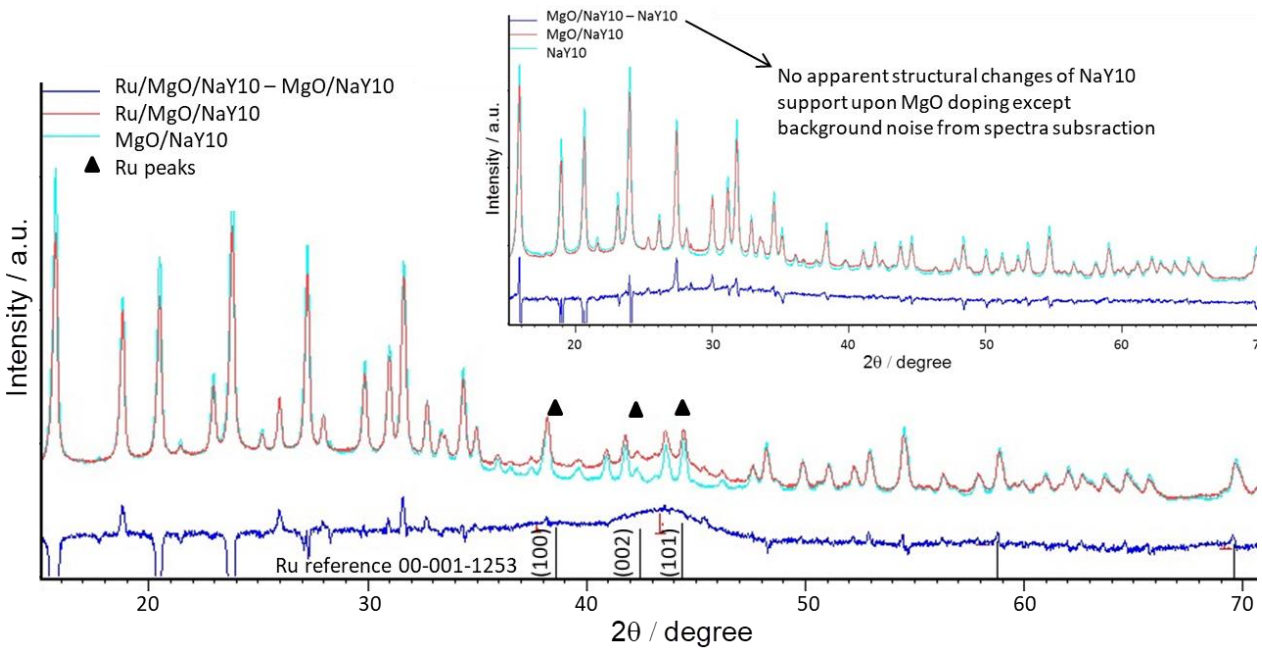


Figure 6.3b - XRD patterns of Ru/MgO/NaY10 and MgO/NaY10 in comparison to NaY10. Average Ru particle size from Scherrer equation = 3 nm (in good agreement with TEM).

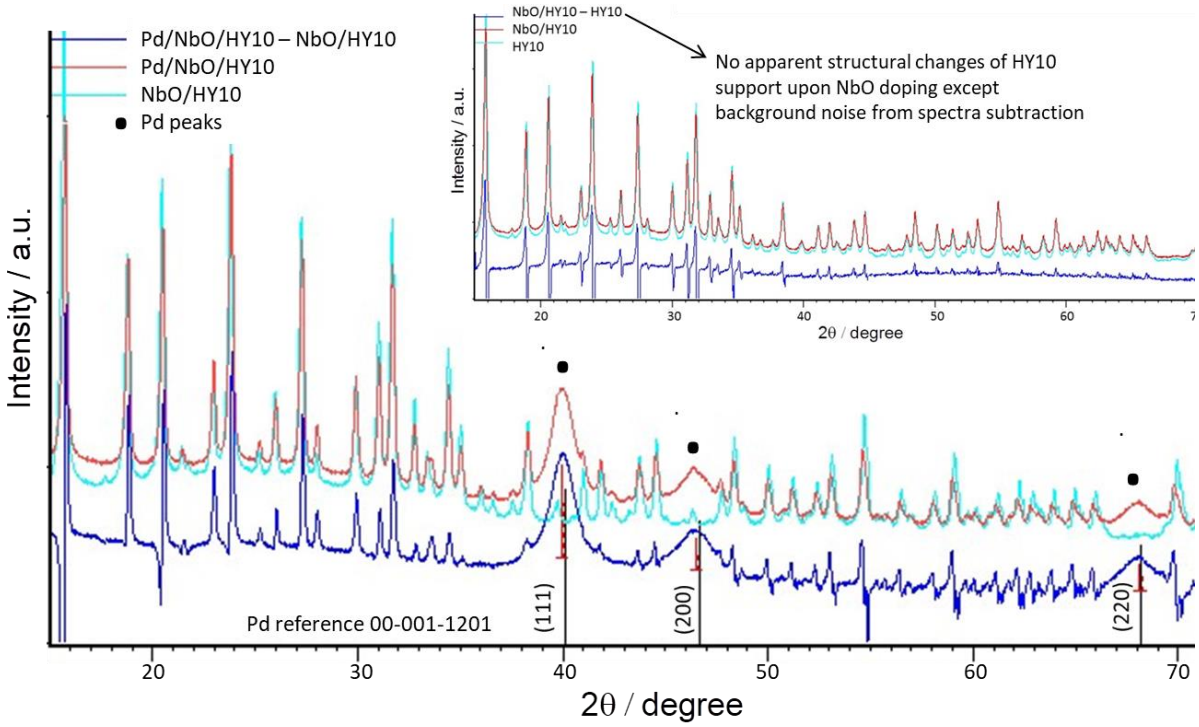


Figure 6.3c – XRD patterns of Pd/NbO/HY10 and NbO/HY10 in comparison to HY10. Average Pd particle size from Scherrer equation = 10 nm (in acceptable agreement with TEM).

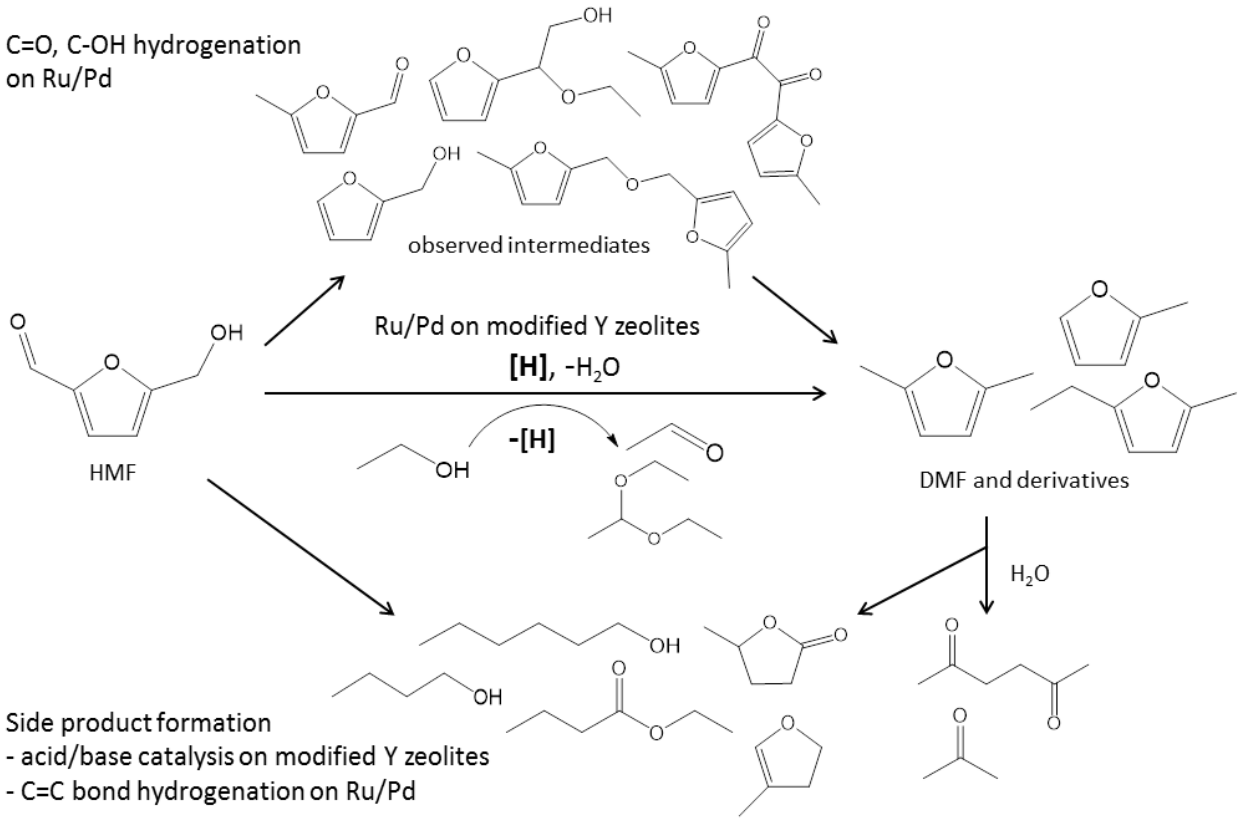
What can be seen is that DMF yield follows the order of support basicity: A yield of 61 % was obtained for Ru/MgO/NaY10 > 44 % for Ru/NaY10 > 35 % for Ru/NbO/HY10 and Ru/HY10 (Table 6.1), showing that a more basic support enhances the yield of DMF and its derivatives. One possible explanation concerns the targeted hydrogenation of HMF: Besides the C-OH and C=O bond that must be hydrogenated in order to form DMF, HMF also contains two C=C bonds which can be hydrogenated, leading to side product formation. It is therefore important to find a catalyst which is more selective towards C-OH and C=O hydrogenation than C=C. Generally, C=C bonds are more easily hydrogenated than C=O, however there are some catalysts, especially Ru and Pt based, which tend to be better C=O activators.[27–29] The support nature plays an important role for the selectivity as well, for example it has been reported that graphitic carbon and carbon nanofibers with increased basic oxygen surface species are more selective towards C=O bond activation.[30,31] Similarly Ru on different ion exchanged Y zeolites has been

reported to be more selective towards C=O bond hydrogenation if the zeolite support is basic in character.[32] Researchers argue that this is due to an increased electron donation from the support to the metal.[30–32] This explanation fits with our experimental observations where Ru on basic modified zeolite supports showed better catalytic results towards DMF and its derivatives than Ru on the neutral or acidic supports.

As mentioned previously, a comparison between the different Pd catalysts is not as straightforward as for the Ru catalysts since the Pd particle size and surface area is not uniform among the catalysts. Pd/NaY10 with an average metal particle size of 3 nm is the only one comparable to the Ru catalysts, while larger particle sizes and smaller metal surface areas were observed for the remaining Pd catalysts (Figure 6.2 c,d and Table 6.3). Interestingly, while HMF was fully converted over all catalysts, Pd/NaY10 showed no DMF amongst the products formed, while Ru/NaY10 yielded 44 % DMF and derivatives. The Pd catalysts overall tend to show worse activity than Ru in the formation of DMF which can be explained by Pd generally being a better C=C bond activator,[28,31] leading to side reactions during the conversion. It is still surprising that no DMF was produced over Pd/NaY10, especially since the other Pd catalysts yielded DMF and its derivatives with 36 % for Pd/MgO/NaY10, 35 % for Pd/NbO/HY10 and 40 % for Pd/HY10. There is no apparent correlation with support acidity here in contrast to the Ru catalysts. When looking at metal particle sizes, average particle sizes of 13, 12 and 7 nm were observed for the Pd catalysts, respectively. Further, the particles on the MgO and NbO modified supports tend to form aggregates. It has been reported that for larger metal particles (>10 nm) electronic support effects are not significant,[27,33] which explains why the DMF yields obtained over Pd/MgO/NaY10 (13 nm) and Pd/NbO/HY10 (12 nm) are very similar in spite of the differences in support basicity. Comparing the oxide modified Pd catalysts with Pd/HY10 and Pd/NaY10, particle size effects on the hydrogenation selectivity of C=C vs C=O bonds cannot be

ruled out either, because surface site ratios and electronic properties of metal nanoparticles change with size.[29,34] In combination with varying support effects, this could explain why DMF yields obtained over the larger particle Pd catalysts differ significantly from that obtained over Pd/NaY10 with 3 nm particles.

For all catalysts the formation of side products in addition to DMF and its derivatives was observed (Table 6.2). After all, HMF was fully converted over the catalysts at 300 °C and although DMF is the main product, several other product types were revealed by GC-MS analysis (also see GC-MS spectra in Appendix p.A16-A18). Side products can result from C=C bond hydrogenation and further from acid/base catalysed ring-opening reactions taking place on the modified zeolite supports (Scheme 6.3). Most of the side products are open chain structures that no longer contain the furan ring unit, meaning that any intermediate structures which could give further clues about the ongoing reaction mechanisms were no longer present. It is therefore difficult to determine mechanistic details of C=O *versus* C=C bond hydrogenation, acid/base catalysis and potentially other reaction processes which cause the differences in DMF yield amongst the catalysts. One observation to be made regarding ongoing reactions besides the targeted C=O and C-OH bond hydrogenation is the rearrangement of C-C bonds, seen for example in the formation of the DMF derivatives MF and MEF, but also in the formation of unwanted side products such as butanol. Regarding the role of ethanol as hydrogen donor in HMF to DMF conversion, it is likely that Ru and Pd, as C=O and C-OH bond activators, can activate not only HMF but also ethanol to facilitate hydrogen transfer between the two. Ru/Pd are certainly crucial to the reaction as no hydrogen transfer was observed in a test reaction using Y zeolite support without Ru or Pd.



Scheme 6.3 – HMF to DMF reaction scheme

Based on observed reaction products, intermediates, side products and catalytic behaviour of Ru/Pd on modified Y zeolites

To sum up, the selectivity of the Ru catalysts, all of which show average metal particle sizes of 3 nm, is determined mainly by support basicity, with the basic zeolite catalysts giving the best DMF yields, in particular Ru/MgO/NaY10 with 61 % of DMF and derivatives. For the Pd catalysts on the other hand, the differences in support nature affect primarily the metal particle size, with larger particles >10 nm formed on the oxide modified supports MgO/NaY10 and NbO/HY10. The metal particle size rather than the support basicity appears decisive for DMF yield in the case of the Pd catalysts.

6.4.2 Further Conversion of DMF to Aromatic Hydrocarbons

The successful conversion of DMF to aromatic hydrocarbons has been reported many times in literature. It is commonly agreed to proceed *via* the cycloaddition of DMF and ethylene followed by a Brønsted acid catalysed dehydration to produce xylene.[14–16,35,36] Most reactions reported require high pressures of ethylene, but recently it was shown that ethanol can be used as solvent for this reaction to produce ethylene *in situ* over HY zeolites, and HY zeolites further catalyse the dehydration to xylene at 300 °C after reacting for 12 h.[24] As mentioned beforehand, this project aims at finding a way to combine the HMF to DMF and DMF to aromatics reactions into one. Taking into account the research findings on DMF to aromatics conversion, we have successfully established a new route of converting HMF to DMF, as detailed above (Scheme 6.3). Ethanol was used as both solvent and hydrogen donor to convert HMF to DMF, and Ru/Pd on modified Y zeolites were employed as catalysts, at a reaction temperature of 300 °C.

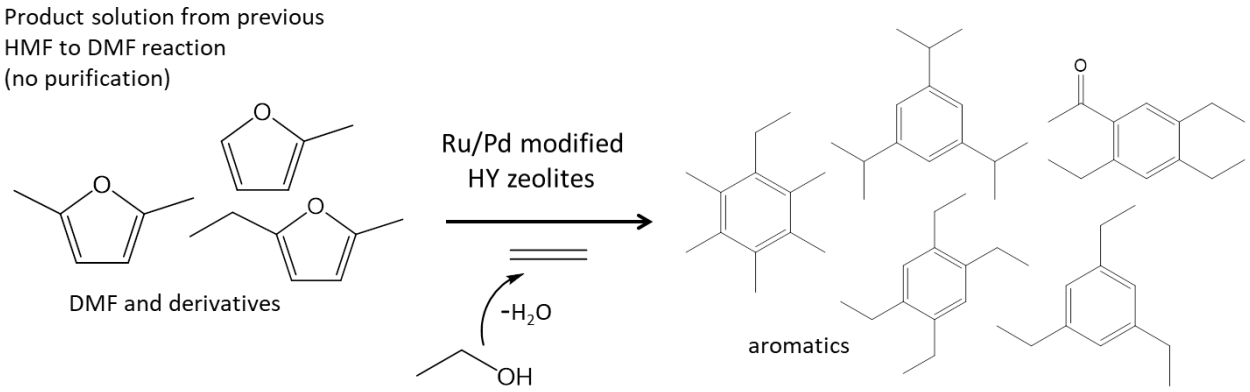
The catalyst giving the highest yield with 61 % of DMF and derivatives is Ru/MgO/NaY10 with a basic zeolite support nature. Since the further conversion of DMF to aromatics is catalysed by acid sites, the low yield of only 5 % aromatics can be explained by the basic nature of the support (Table 6.2). However Pd/HY10 and Ru/HY10 are examples where the zeolite support is acidic in nature, and they yielded 40 % and 35 % of DMF and derivatives, respectively. This should directly lead to the further conversion of DMF into aromatics within the same autoclave reaction, considering the reaction conditions of 300 °C and 12 h. But GC-MS analysis showed that only up to 10 % aromatics are present in the product solution next to DMF/derivatives and side products. It appears that deactivation/coking of the zeolite support during the HMF to DMF step is a problem, as adding fresh catalyst to the product solution led to further formation of aromatics from DMF within 2 h at 300 °C (Table 6.5). Interestingly, aromatics of a higher alkylation degree rather than xylenes were formed (Scheme 6.4, also see Appendix p.A16-A18

for GC-MS spectra). This might be due to reactions with side products from the previous reaction step or the presence of Ru/Pd causing further alkylation *via* C-C bond activation.[37–39] The presence of Ru/Pd and side products also appears responsible for the decrease in aromatic hydrocarbon yield when prolonging reaction times to 4 h, considering the previously reported reaction time of 12 h for the conversion of pure DMF to aromatics over unmodified HY zeolite in ethanol at 300 °C.[24] Reaction times over 2 h tend to yield alkanes and oligomers, where reactive side products from the previous HMF to DMF step or hydrogenation and C-C bond activation by Ru/Pd appear to cause this further conversion of aromatics.

Table 6.5 – Conversion of HMF to aromatics

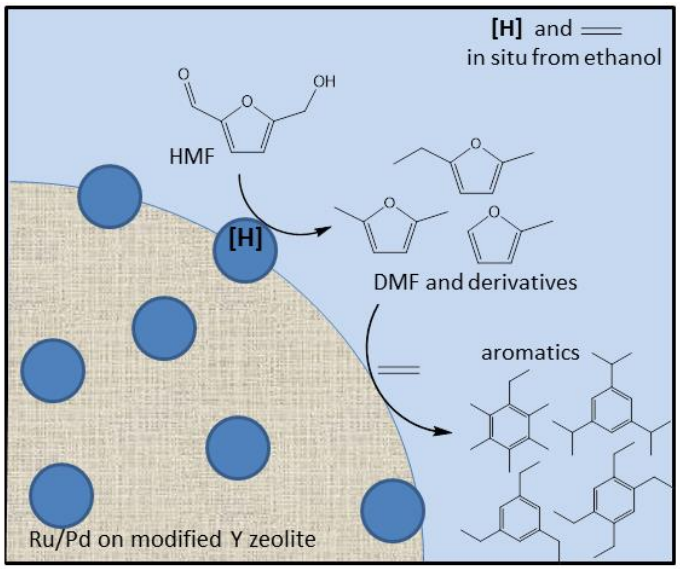
Catalyst		**1. Step: HMF to DMF (300°C, 12h)**		**Addition of fresh/new catalyst**		**2. Step: DMF to aromatics (300°C, 2h)**	
		Yield in %				Yield in % of aromatics	
		DMF	aromatics			From 1. Step DMF	Total[a]
Ru/HY10	**acidic**	35	9	**Ru/HY10**	**acidic**	49	17
Pd/HY10		40	10	**Pd/HY10**		47	19
Ru/MgO/NaY10	**basic**	61	5	**HY10**		43	26

1. Step: HMF to DMF conversion, also compare Table 6.1 and 6.2 for details.
2. Step: DMF to aromatics conversion using product solutions from 1. Step with addition of fresh acidic catalyst.
[a]Total yield of aromatics obtained from HMF by combining 1. and 2. Step.



Scheme 6.4 – Further conversion of DMF to aromatics over Ru/Pd modified HY zeolites

Since most aromatics formed under our reaction conditions are not commercially available, structurally similar triethylbenzene was used for GC-MS calibration and quantification of the obtained aromatics. By this method the amount of aromatics obtained from DMF was estimated to 49 % for Ru/HY10 and 47 % for Pd/HY10 (Table 6.5), with esters and alcohols as side products next to the ones already obtained in the HMF to DMF step. Corresponding total aromatic yields from the initial starting material HMF of 17 % for Ru/HY10 and 19 % for Pd/HY10 are obtained. Ru/MgO/NaY10, due to the basicity of the support, is not a suitable catalyst for the subsequent aromatics step (only 5 % aromatics yielded). Using HY10 to convert the Ru/MgO/NaY10 product solution (containing 61 % DMF and derivatives) to aromatics, a yield of 43 % was obtained. This results in an overall yield of 26 % aromatics from HMF. There is certainly room for improvement regarding reaction yields and catalyst deactivation, but this work has shown useful new features and strategies of how to combine HMF to DMF and DMF to aromatics reaction into one – by using common reaction conditions, a common solvent and sacrificial reagent for both hydrogenation and aromatization, and a catalyst that combines required catalytic features (Scheme 6.5).



Scheme 6.5 – Conversion of HMF to aromatics *via* DMF over Ru/Pd on modified Y zeolite in ethanol at 300 °C

6.5 Conclusions

Advances towards producing aromatic hydrocarbons from hydroxymethylfurfural (HMF), a biomass-based route to help substitute fossil-fuel derived aromatics, have been made in this work. Combining the steps of HMF to DMF and DMF to aromatics conversion into a more economic one-batch-reaction requires a catalyst and solvent suitable for both steps. In recent work it was shown that ethanol can be used as both solvent and *in situ* ethylene source for DMF to aromatics conversion over zeolites, not requiring gaseous ethylene. The here presented approach has shown that ethanol can further be used as both solvent and sacrificial hydrogen donor for HMF to DMF hydrogenation, not requiring gaseous hydrogen and therefore demonstrating a safer and more sustainable production route. Using the same solvent and sacrificial reagent, ethanol, for both HMF to DMF and DMF to aromatics reaction is an important step towards combining the two. On the catalyst side it is shown that zeolites, which are commonly used for the conversion of DMF to aromatics, can successfully be employed as

supports for ruthenium and palladium in the hydrogenation of HMF to DMF. Regarding HMF hydrogenation selectivity, modifying the zeolite support by ion exchange and metal oxide doping before decoration with Ru/Pd has considerable effects. For the Ru catalysts, all of which have average metal particle sizes of 3 nm, a more basic support significantly enhances DMF yield. For the Pd catalysts on the other hand, the differences in support nature affect primarily the metal particle size, with larger particles formed on the oxide modified supports. The metal particle size rather than the support basicity is decisive for DMF yield in case of the Pd catalysts. Overall, the influence of ion exchange and metal oxide doping of the support opens up interesting tuning possibilities.

The catalyst yielding most DMF and derivatives (61 %) is Ru/MgO/NaY10, which due to its basic nature is unfortunately not suitable for the further conversion of DMF to aromatics, where acid sites are required for dehydration. Therefore a second reaction step using the product mixture from the previous HMF to DMF conversion was introduced, using acidic HY10 catalyst under otherwise identical reaction conditions. A yield of 43 % aromatic hydrocarbons from DMF and a corresponding total yield of 26 % aromatics from HMF have been obtained. The acidic catalysts Pd/HY10 and Ru/HY10 on the other hand can directly yield aromatics from HMF in a one-pot-reaction, but due to catalyst deactivation only up to 10 % aromatics have been reached in this work. For catalyst optimization, further structural studies using for example XPS, EDX and synchrotron XRD can help to understand catalyst nature and mechanistic relations. After all, the combination into a one-batch-reaction using a common solvent and sacrificial reagent under common reaction conditions, already presents a promising approach to render the biomass-based production of aromatics economically more viable.

6.6 References

(1) Stöcker, M. *Angew. Chemie - Int. Ed.* **2008**, *47* (48), 9200.

(2) Ragauskas, A. J.; Williams, C. K.; Davison, B. H.; Britovsek, G.; Cairney, J.; Eckert, C. A.; Frederick, W. J.; Hallett, J. P.; Leak, D. J.; Liotta, C. L.; Mielenz, J. R.; Murphy, R.; Templer, R.; Tschaplinski, T. *Science* **2006**, *311* (5760), 484.

(3) Saidur, R.; Abdelaziz, E. A.; Demirbas, A.; Hossain, M. S.; Mekhilef, S. *Renew. Sustain. Energy Rev.* **2011**, *15* (5), 2262.

(4) REN21 Secretariat. *Renewables 2016 Global Status Report*; 2016.

(5) International Energy Agency. *Renewable energy medium-term market report 2015. Market Analysis and Forecasts to 2020 - Executive Summary*; 2015.

(6) Van Putten, R. J.; Van Der Waal, J. C.; De Jong, E.; Rasrendra, C. B.; Heeres, H. J.; De Vries, J. G. *Chem. Rev.* **2013**, *113* (3), 1499.

(7) Rosatella, A. A.; Simeonov, S. P.; Frade, R. F. M.; Afonso, C. A. M. *Green Chem.* **2011**, *13* (4), 754.

(8) Bozell, J. J. *Clean - Soil, Air, Water* **2008**, *36* (8), 641.

(9) Franck, H. G.; Stadelhofer, J. W. *Industrial Aromatic Chemistry*; Springer Science & Business Media, 2012.

(10) Abdel-Shafy, H. I.; Mansour, M. S. M. *Egypt. J. Pet.* **2015**, *25* (1), 107.

(11) Lin, Z.; Nikolakis, V.; Ierapetritou, M. *Ind. Eng. Chem. Res.* **2015**, *54* (8), 2366.

(12) Nikbin, N.; Do, P. T.; Caratzoulas, S.; Lobo, R. F.; Dauenhauer, P. J.; Vlachos, D. G. *J. Catal.* **2013**, *297*, 35.

(13) Chang, C.-C.; Cho, H. J.; Yu, J.; Gorte, R. J.; Gulbinski, J.; Dauenhauer, P.; Fan, W. *Green Chem.* **2016**, *16*, 1368.

(14) Patet, R. E.; Nikbin, N.; Williams, C. L.; Green, S. K.; Chang, C. C.; Fan, W.; Caratzoulas, S.; Dauenhauer, P. J.; Vlachos, D. G. *ACS Catal.* **2015**, *5* (4), 2367.

(15) Wang, D.; Osmundsen, C. M.; Taarning, E.; Dumesic, J. A. *ChemCatChem* **2013**, *5* (7), 2044.

(16) Williams, C. L.; Chang, C. C.; Do, P.; Nikbin, N.; Caratzoulas, S.; Vlachos, D. G.; Lobo, R. F.; Fan, W.; Dauenhauer, P. J. *ACS Catal.* **2012**, *2* (6), 935.

(17) Wijaya, Y. P.; Suh, D. J.; Jae, J. *Catal. Commun.* **2015**, *70*, 12.

(18) Pacheco, J. J.; Davis, M. E. *Proc. Natl. Acad. Sci. U. S. A.* **2014**, *111* (15), 8363.

(19) Do, P. T. M.; McAtee, J. R.; Watson, D. A.; Lobo, R. F. *ACS Catal.* **2013**, *3* (1), 41.

(20) Climent, M. J.; Corma, A.; Iborra, S. *Green Chem.* **2014**, *16* (2), 516.

(21) Gallo, J. M. R.; Alonso, D. M.; Mellmer, M. A.; Dumesic, J. A. *Green Chem.* **2013**, *15* (1), 85.

(22) Hu, L.; Tang, X.; Xu, J.; Wu, Z.; Lin, L.; Liu, S. *Ind. Eng. Chem. Res.* **2014**, *53* (8), 3056.

(23) Wang, J.; Liu, X.; Hu, B.; Lu, G.; Wang, Y. *RSC Adv.* **2014**, *4* (59), 31101.

(24) Teixeira, I. F.; Lo, B. T. W.; Kostetskyy, P.; Stamatakis, M.; Ye, L.; Tang, C. C.; Mpourmpakis, G.; Tsang, S. C. E. *Angew. Chemie - Int. Ed.* **2016**, *55* (42), 13061.

(25) Hansen, T. S.; Barta, K.; Anastas, P. T.; Ford, P. C.; Riisager, A. *Green Chem.* **2012**, *14* (3), 2457.

(26) Jae, J.; Zheng, W.; Lobo, R. F.; Vlachos, D. G. *ChemSusChem* **2013**, *6* (7), 1158.

(27) Kluson, P.; Cerveny, L. *Appl. Catal. A-General* **1995**, *128* (1), 13.

(28) Lashdaf, M.; Lahtinen, J.; Lindblad, M.; Venäläinen, T.; Krause, A. O. I. *Appl. Catal. A Gen.* **2004**, *276* (1–2), 129.

(29) Coq, B.; Figueras, F. *Coord. Chem. Rev.* **1998**, *178–180*, 1753.

(30) Toebes, M. L.; Prinsloo, F. F.; Bitter, J. H.; Van Dillen, A. J.; De Jong, K. P. *J. Catal.* **2003**, *214* (1), 78.

(31) Lashdaf, M.; Hase, A.; Kauppinen, E.; Krause, A. O. I. *Catal. Letters* **1998**, *52* (3–4), 199.

(32) Blackmond, D. G.; Oukaci, R.; Blanc, B.; Gallezot, P. *J. Catal.* **1991**, *131*, 401.

(33) Park, C.; Keane, M. A. *J. Colloid Interface Sci.* **2003**, *266* (1), 183.

(34) Bond, G. C. *Surf. Sci.* **1985**, *156* (PART 2), 966.

(35) Nikbin, N.; Feng, S.; Caratzoulas, S.; Vlachos, D. G. *J. Phys. Chem. C* **2014**, *118* (42), 24415.

(36) Nikbin, N.; Caratzoulas, S.; Vlachos, D. G. *ChemSusChem* **2013**, *6* (11), 2066.

(37) García-Antón, J.; Axet, M. R.; Jansat, S.; Philippot, K.; Chaudret, B.; Pery, T.; Buntkowsky, G.; Limbach, H. H. *Angew. Chemie - Int. Ed.* **2008**, *47* (11), 2074.

(38) Na, Y.; Park, S.; Han, S. B.; Han, H.; Ko, S.; Chang, S. *J. Am. Chem. Soc.* **2004**, *126* (1), 250.

(39) Ritleng, V.; Sirlin, C.; Pfeffer, M. *Chem. Rev.* **2002**, *102* (5), 1731.

Chapter 7

Conclusions and Outlook

Chapter 7 192

7.1 Conclusions and Outlook 193

7.1 Conclusions and Outlook

With diminishing fossil fuel reserves and increasing environmental awareness, the search for alternative energy sources becomes ever more important. The aim is to find both renewable energy sources and environmentally friendly processes to convert these into fuels, electricity and chemicals. A promising area of research is the valorisation of biomass, where the components of biomass are converted to so-called platform molecules, which are precursors for commodity and fine chemicals as well as fuels. The most abundant component of biomass, consisting of roughly 75%, are sugars in the form of cellulose and hemicellulose, which yield the sugar glucose in especially large amounts upon decomposition. By dehydration glucose can be converted into the platform molecule hydroxymethylfurfural (HMF), a promising industrial precursor in the synthesis of plastics, solvents, fuels and fine chemicals.

Part of this work deals with the mechanistic details of glucose, fructose and sucrose conversion to HMF, to help develop more efficient catalysts in the area. Although sugar conversion to HMF was extensively studied over the past years and acids are the catalysts of choice, mechanistic details are largely dependent on the solvent/catalyst system and remain difficult to study and generalise. Looking for an environmentally-, cost- and separation-friendly process to convert sugars into HMF, water and niobium oxides were selected as the solvent and solid acid catalysts, respectively, for study in this project. By comparative study of sugar conversion over different niobium oxides in water, the following mechanistic observations have been made: Sucrose rapidly decomposes into its components glucose and fructose at elevated temperatures and the conversion of fructose to HMF is mainly promoted by weak Brønsted acid (BA) sites on the niobium oxide catalysts. The conversion of glucose on the other hand appears to proceed *via* fructose as an intermediate, where glucose to fructose isomerization is catalysed primarily by Lewis acid (LA) sites, and the further conversion of fructose to HMF is catalysed by weak BA

sites, as described above. As a note on terminology, BA sites on metal oxides are formed by protons from acidic surface hydroxyl groups, while LA sites arise from exposed metal cation centres on the surface, here Nb centres.

As glucose and sucrose are the much more abundant sugars from biomass, they are industrially of bigger interest, but they are also more challenging in their catalytic requirements than fructose due to the different acid site species involved. The best performance in terms of both glucose and sucrose conversion was shown by amorphous mesoporous Nb_2O_5*nH_2O with 36 % HMF yield, due to the combined presence of LA and comparatively weak BA sites. This is a good yield compared to previous studies of sugar conversion to HMF over niobium oxides with below 30 % yield under similar reaction conditions. Further, future yield improvements over solid acid catalysts such as niobium oxides are likely with the given evaluation of catalytic requirements, enabling a more targeted synthesis of catalysts. For example, the synthesis of niobium oxides with LA sites but weaker BA sites than currently has potential, similarly the investigation of other solid acid systems.

Since targeted synthesis of solid acid catalysts is an important feature for yield and selectivity improvements, analysing the relation of structure and acidity is of great interest. Therefore, the structure of the above niobium oxides has been studied to great detail and correlated to according acidity features within this work. For the bulk structures Nb_2O_5 and HNb_3O_8 with their low surface areas, high crystallinity and structural rigidity no LA sites were detected, and only few BA sites in the case of HNb_3O_8, due to water content in the bulk layer structure. The few- to mono-layered forms of hy-Nb and hy-Nb-TEOA show some similarities to HNb_3O_8 in terms of layer structure, but possess much higher surface areas, lower crystallinity and high structural flexibility, which give rise to significant amounts of both BA and LA sites. It appears that LA

sites arise from distortions and defects of the typical NbO_6 structure in such flexible nano-systems synthesized in the presence of stabilisers, where further oxygen vacancies are formed which give rise to NbO_5 units as strong LA sites. The formation of oxygen vacancies goes in line with an increase in Nb^{4+} compared to Nb^{5+} character of these materials, especially in the case of hy-Nb-TEOA and mesoporous Nb_2O_5*nH_2O. Due to its highly amorphous nature mesoporous Nb_2O_5*nH_2O is rather difficult to analyse, but its structure seems to arise from a mixture of loosely connected NbO_4, NbO_5 and NbO_6 units with terminal hydroxyl groups, giving rise to large quantities of LA and weaker BA sites.

The large differences in structure and acidity upon down-scaling from bulk to nano-size materials as shown above are advantageous to the synthesis of catalysts with similar composition but a wide range of properties, opening up new possibilities for catalyst tuning.

As mentioned earlier, HMF obtained from sugars already has a range of application areas and the search for new conversion routes is on-going. Another part of this work deals with the development of a route to convert HMF to aromatic hydrocarbons, which are currently derived from fossil fuels and used as fuel additives and industrial precursors for polymers, resins and solvents. The direct conversion of HMF to aromatics has not yet been achieved, but the conversion of HMF to dimethylfuran (DMF) and further to aromatics has been given new potential by using ethanol as a common solvent and sacrificial reagent to both reaction steps. Ruthenium and palladium on modified Y zeolites are used as catalysts. Firstly, HMF is hydrogenated to DMF with ethanol as solvent and hydrogen source, where the best results are obtained over the basic Ru/MgO/NaY10 catalyst with a 61 % yield of DMF and derivatives. The aromatization of DMF is likely to proceed *via* the established Diels-Alder cycloaddition of DMF with ethylene over acidic zeolite, where in here ethylene is formed *in-situ* from ethanol. The

highest total yield of aromatics with 26 % from HMF was obtained using acidic HY10 during the second reaction step (i.e. 43 % from DMF to aromatics), with the reaction mixture obtained over Ru/MgO/NaY10 from the first step. Interestingly, aromatics of higher alkylation degree than the Diels-Alder reaction-typical xylenes are formed, which might be due to side products present and the modification of the zeolite with Ru/Pd.

Although the obtained aromatic hydrocarbon yield from HMF still needs improvement, the significant advantage of this route is the use of ethanol as a common solvent and sacrificial reagent for both reaction steps involved, with no need for high pressures of hydrogen or ethylene. With future work on the catalyst side, a combination into a one-step reaction is possible. In this context, testing ethanol as solvent in the conversion of sugars to HMF is similarly worth-while, as ideally the same solvent would be used throughout all reaction steps to aromatics, with no product loss or costs from the separation of intermediates.

Overall, this work is based in the area of biomass-derived sugar conversion to industry chemicals and synthetic precursors. More specifically, the conversion of sugars to HMF over niobium oxides in water has been studied as an environmentally- and separation-friendly route. With an emphasis on the study of reaction mechanisms and catalyst structure, new options for targeted synthesis and enhanced catalytic performance have been opened up. Further, the conversion of HMF to aromatics has been addressed using a two-step reaction *via* DMF over modified zeolites, with the advantage of using ethanol as solvent and sacrificial reagent in both steps. Future work suggestions include catalyst optimization and the study of sugar conversion in ethanol, with the possibility to link this route to the production of aromatics.

Appendix

Surface area measurements (BET) and pore data analysis

Specific surface areas of the niobium oxides were derived from N_2 adsorption-desorption isotherms (Figure A.1) using BET plots of the measured data (exemplary BET plot for amorphous mesoporous $Nb_2O_5*nH_2O$ in Figure A.2).

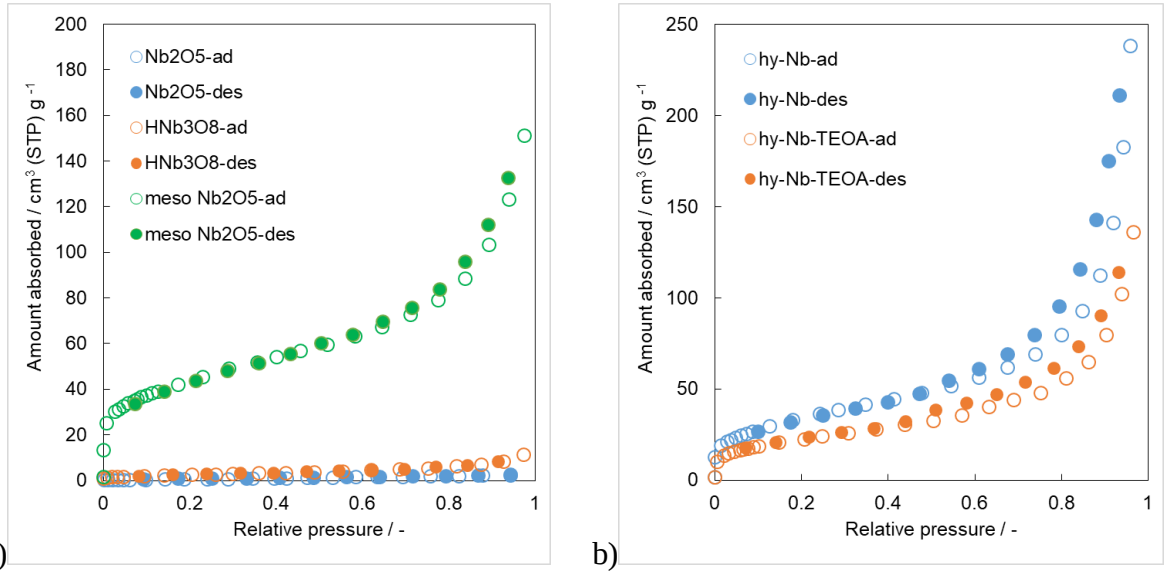


Figure A.1 – a,b) N_2 adsorption-desorption isotherms of the different niobium oxides. Open and closed circles represent adsorption and desorption branches, respectively. Relative pressure is given by p/p_0 where p is the applied pressure and p_0 the saturation pressure (at which nitrogen is liquefied/forms infinite adsorbate layers). Measurements were taken at 77K.

The specific surface area S_{BET} in $m^2\ g^{-1}$ was calculated from the monolayer volume v_{mono} of adsorbed nitrogen in cm^3 (STP) according to the following Equation A.1, where further V is the molar volume of nitrogen in $cm^3\ mol^{-1}$ (STP), m is the sample mass in g, N is Avogadro's number ($6.02 \times 10^{23}\ mol^{-1}$) and a is the area occupied by one adsorbed nitrogen molecule in m^2 ($0.162\ nm^2 = 0.162 \times 10^{-18}\ m^2$).

$$S_{BET} = \frac{v_{mono}\, Na}{Vm} \qquad Equation\ A.1$$

The monolayer volume v_{mono} was obtained from the BET plot, where $p/(v(p_0 - p))$ was plotted against p/p_0, giving rise to a linear plot in the range of about $0.05 < p/p_0 < 0.35$, where v_{mono} is related to the y-intercept I and the slope A of the line by the following Equation A.2.

$$v_{mono} = \frac{1}{I + A} \qquad Equation\ A.2$$

The BET plot is based on the BET equation for multilayer adsorption (for theoretical background see Chapter 2) as shown below (Equation A.3), where further p is the applied pressure, p_0 the saturation pressure, v the volume of adsorbed nitrogen (STP) and C the BET constant.

$$\frac{p}{v(p_0 - p)} = \frac{C - 1}{v_{mono}C}\,\frac{p}{p_0} + \frac{1}{v_{mono}C} \qquad Equation\ A.3$$

$$C = 1 + \frac{A}{I}$$

An exemplary BET plot is shown for amorphous mesoporous $Nb_2O_5{*}nH_2O$ below (Figure A.2), further the obtained specific surface areas for the niobium oxides are as follows: 3 $m^2\,g^{-1}$ for commercial Nb_2O_5, 10 $m^2\,g^{-1}$ for HNb_3O_8, 121 $m^2\,g^{-1}$ for hy-Nb-TEOA, 166 $m^2\,g^{-1}$ for hy-Nb and 142 $m^2\,g^{-1}$ for mesoporous $Nb_2O_5{*}nH_2O$.

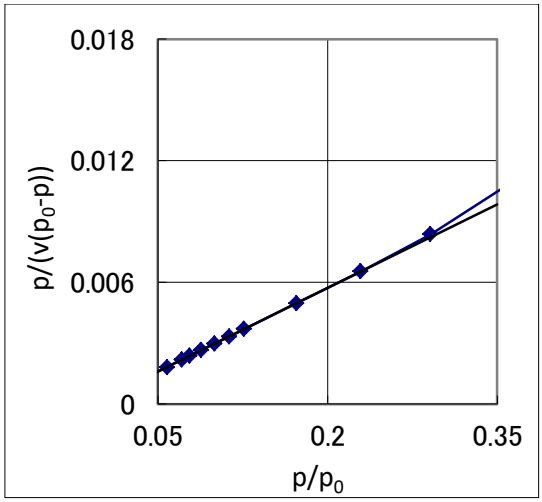


Figure A.2 – BET plot of mesoporous $Nb_2O_5*nH_2O$

Pore size analysis was performed for mesoporous $Nb_2O_5*nH_2O$ from the N_2 adsorption-desorption data using the MP method for analysis of the microporous range (0 – 2 nm, $p/p_0 <$ 0.5) and the Dollimore-Heal method for analysis of the mesoporous range (2 – 50 nm, $p/p_0 >$ 0.5). Both plots are shown below (Figure A.3). It can be seen that mesoporous $Nb_2O_5*nH_2O$ contains pores in a wide size range of 0.5 – 50 nm, which goes in line with its amorphous nature and pore formation via not well defined etching processes (soaking in HCl) during synthesis. A significant pore volume fraction (about ¼) is occupied by micropores besides the mesopores present, which in terms of pore numbers gives mostly micropores. This can also be deduced from the BET adsorption-desorption isotherm, which only shows a modest hysteresis loop in the mesopore region ($p/p_0 > 0.5$) indicating a rather modest number of mesopores. Besides, a not very sharp slope transition in the micropore region at about $p/p_0 = 0.05$ indicates the presence of micropores of about 1 nm, which is in accordance with the MP results.

It is further to note that the BET adsorption-desorption isotherms of hy-Nb and hy-Nb-TEOA indicate the presence of larger amounts of mesopores, which can arise from the interlayer spacing and lamellar interactions of these few- to monolayer materials.

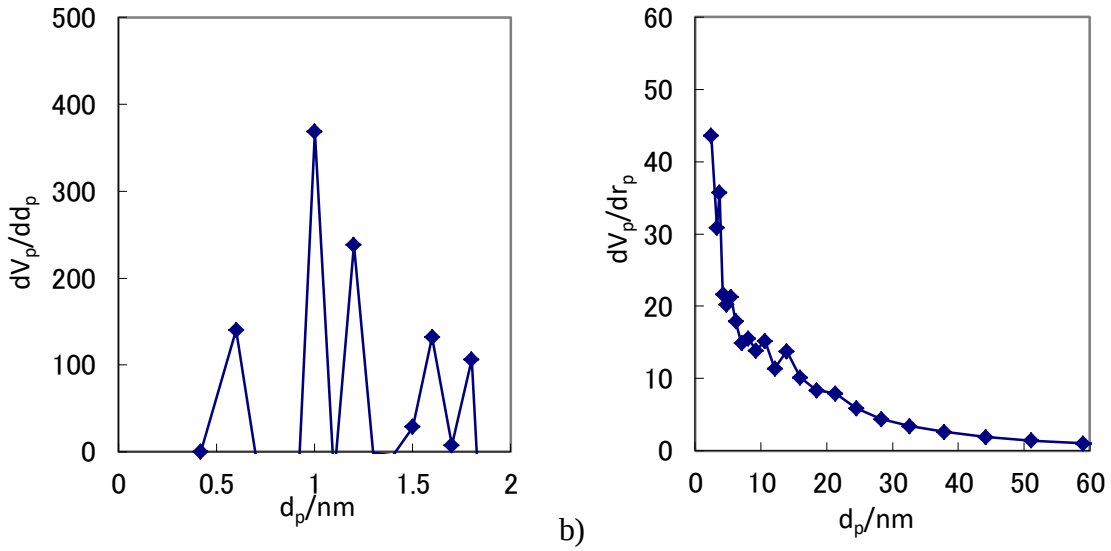
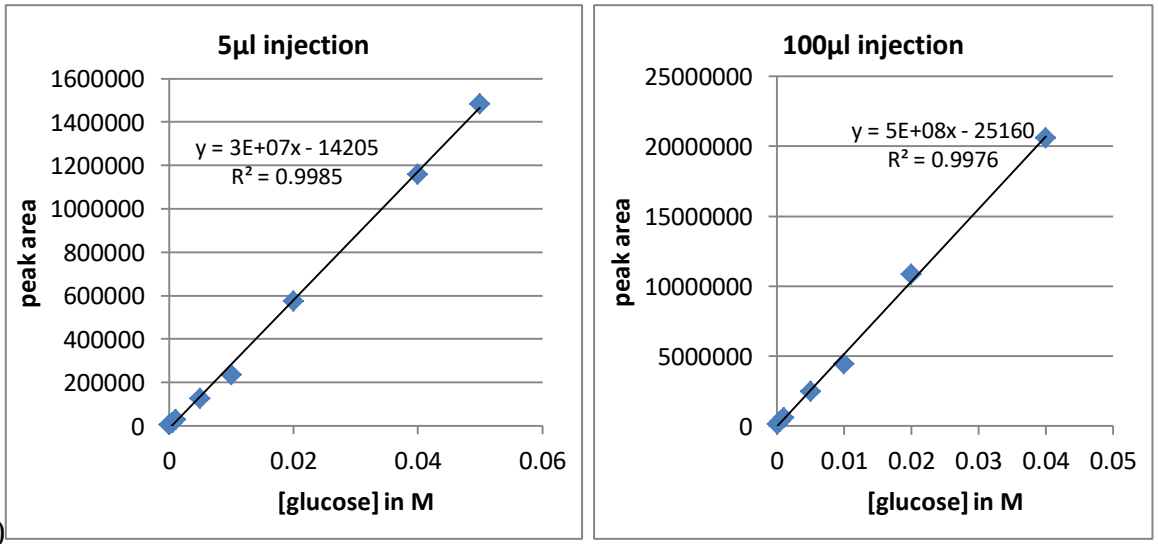


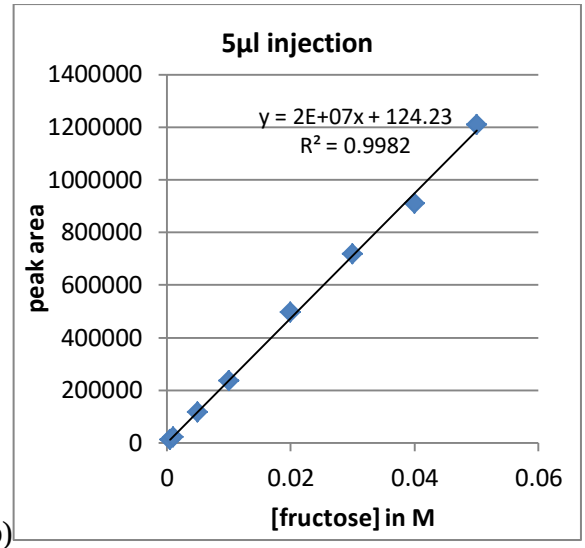
Figure A.3 – Pore size analysis plots of amorphous mesoporous $Nb_2O_5*nH_2O$ for a) microporous region (MP method) and b) mesoporous region (Dollimore-Heal method)

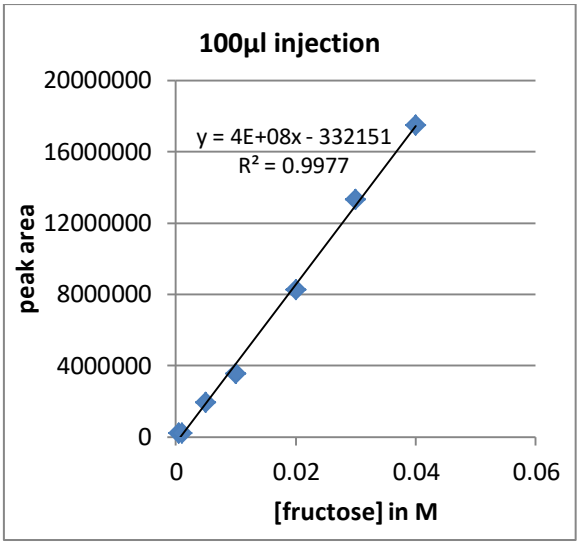
HPLC calibration

Sugar conversion and HMF yields were calculated according to the following calibration curves (Figure A.4). The calibration curves were established by running samples of known compound concentration and plotting the measured peak area against molar concentration.

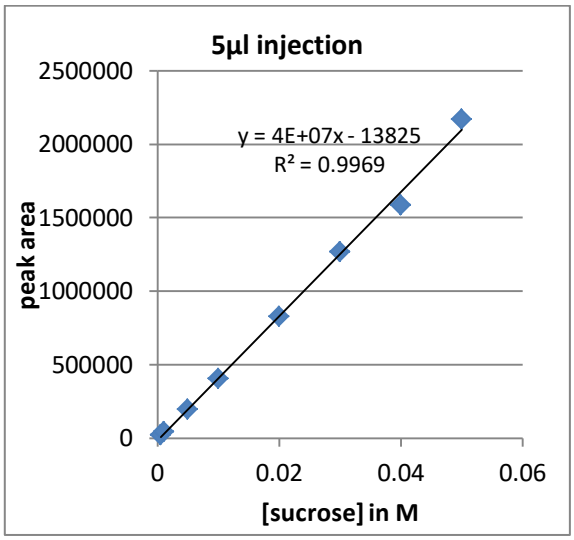


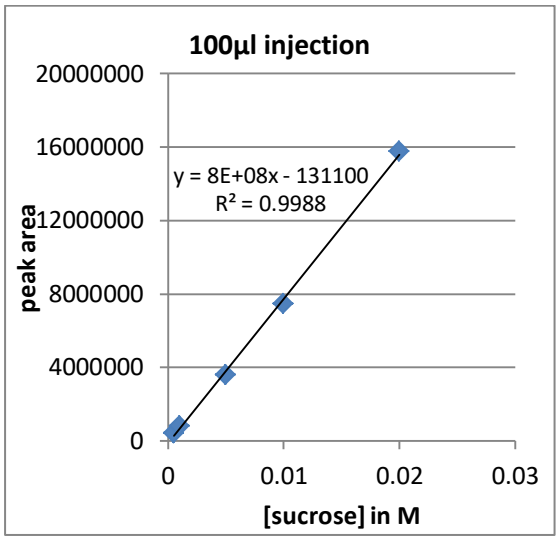
1b)


5µl injection
y = 2E+07x + 124.23
R² = 0.9982
peak area
1400000
1200000
1000000
800000
600000
400000
200000
0
0
0.02
0.04
0.06
[fructose] in M

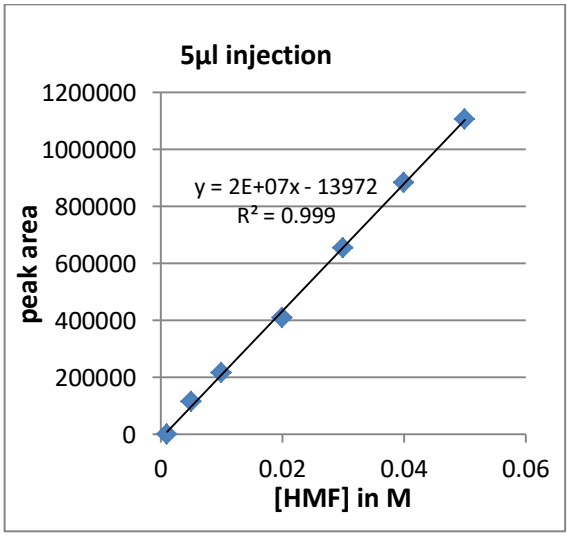

100µl injection
y = 4E+08x - 332151
R² = 0.9977
peak area
20000000
16000000
12000000
8000000
4000000
0
0
0.02
0.04
0.06
[fructose] in M

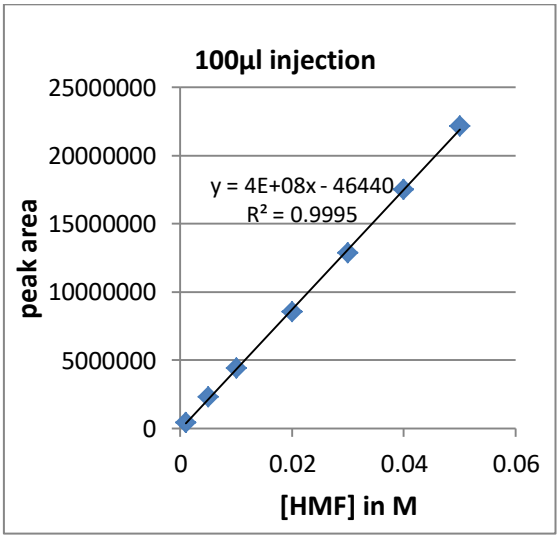
1c)


5µl injection
y = 4E+07x - 13825
R² = 0.9969
peak area
2500000
2000000
1500000
1000000
500000
0
0
0.02
0.04
0.06
[sucrose] in M


100µl injection
y = 8E+08x - 131100
R² = 0.9988
peak area
20000000
16000000
12000000
8000000
4000000
0
0
0.01
0.02
0.03
[sucrose] in M

1d)


5µl injection
y = 2E+07x - 13972
R² = 0.999
peak area
1200000
1000000
800000
600000
400000
200000
0
0
0.02
0.04
0.06
[HMF] in M


100µl injection
y = 4E+08x - 46440
R² = 0.9995
peak area
25000000
20000000
15000000
10000000
5000000
0
0
0.02
0.04
0.06
[HMF] in M

1e)

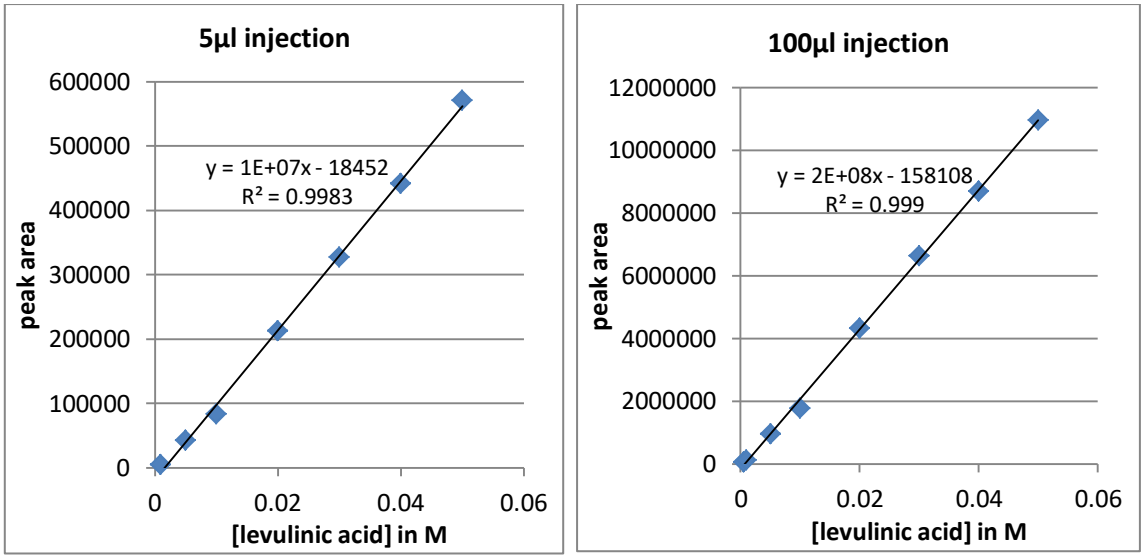


Figure A.4 – HPLC calibration curves for a) glucose, b) fructose, c) sucrose, d) HMF, e) levulinic acid

Yield calculations for sugar conversion to HMF

Reaction product concentrations were determined according to the linear equations shown in Figure A.4, where y is given by the experimentally measured peak area and the concentration x is calculated. For the sugar conversion experiments, 150 mg of glucose or fructose in 15 mL water were used, amounting to a molar concentration of 0.056 M (Equation A.4).

$$\frac{0.15\ g}{180.16\ \frac{g}{mol}}\ x\ 1000\ ml = 0.056\ M\ glucose\ or\ fructose \qquad Equation\ A.4$$

As one equivalent of glucose or fructose is converted to one equivalent of HMF, the HMF yield is given by the following Equation A.5.

$$\frac{[HMF]\ in\ M}{0.056\ M}\ x\ 100\ \% = HMF\ yield\ in\ \% \qquad Equation\ A.5$$

The amount of sugar converted is given by dividing initial minus remaining sugar concentration by the initial concentration (Equation A.6)

$$\frac{0.056\ M - [glucose\ or\ fructose] in\ M}{0.056\ M}\ x\ 100\ \%$$

$$= glucose\ or\ fructose\ conversion\ in\ \% \qquad Equation\ A.6$$

From here, the HMF selectivity can further be calculated using the following Equation A.7.

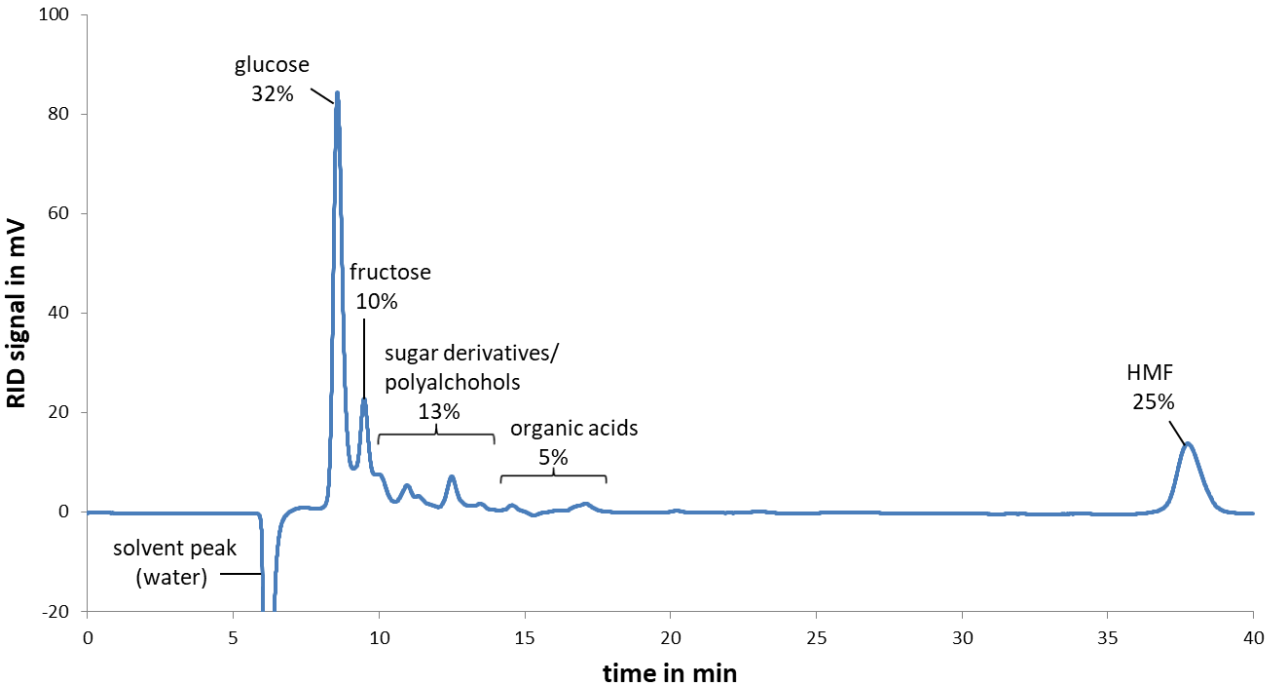
$$\frac{HMF\ yield\ in\ \%}{glucose\ or\ fructose\ conversion\ in\ \%}\ x\ 100\ \%$$

$$= HMF\ selectivity\ in\ \% \qquad Equation\ A.7$$

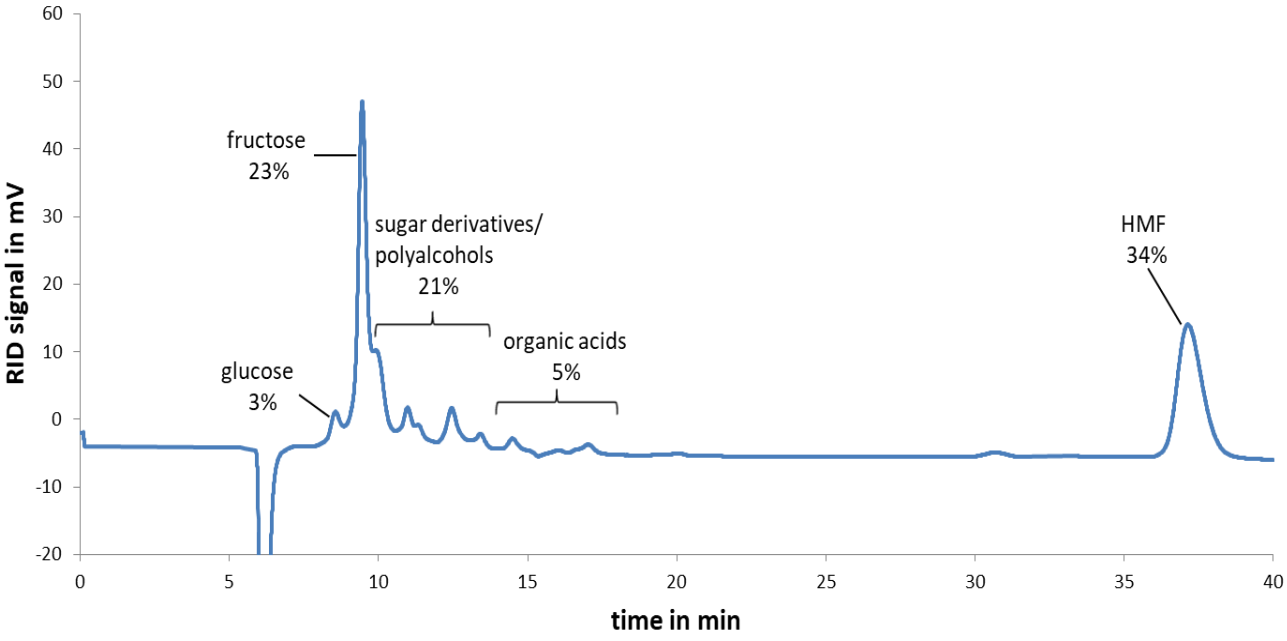
Regarding the conversion of sucrose, the initial sucrose concentration is calculated according to Equation A.4 but using the molar weight of 342.3 g mol^{-1} giving a molar concentration of 0.029 M. As one equivalent of sucrose yields two equivalents of HMF, the HMF yield is calculated by dividing the measured [HMF] in M by 0.058 M (compare Equation A.5). Accordingly, 0.058 M are used as values for sucrose conversion in Equation A.6. The HMF yields given in the main text are averages of the two reactions performed per sample mixture with two HPLC injections each, where the overall yield deviation lies within ±0.5 % HMF. The yields of side products such as levulinic acid and polyalcohols are calculated by dividing [side product] in M by 0.056 M for one-to-one equivalent reactions (Equation A.5), adjustments for other equivalents are made accordingly. Mass balance estimations are done by grouping together compounds of similar nature/retention time and calculating peak areas according to the calibration curve of one representative compound for each group. It should further be noted that the formation of insoluble humins (solid carbon-containing residues) provides a significant contribution to the side products formed and is estimated to account for the remaining % of side products which were not detectable by HPLC.

HPLC spectra for sugar conversion to HMF

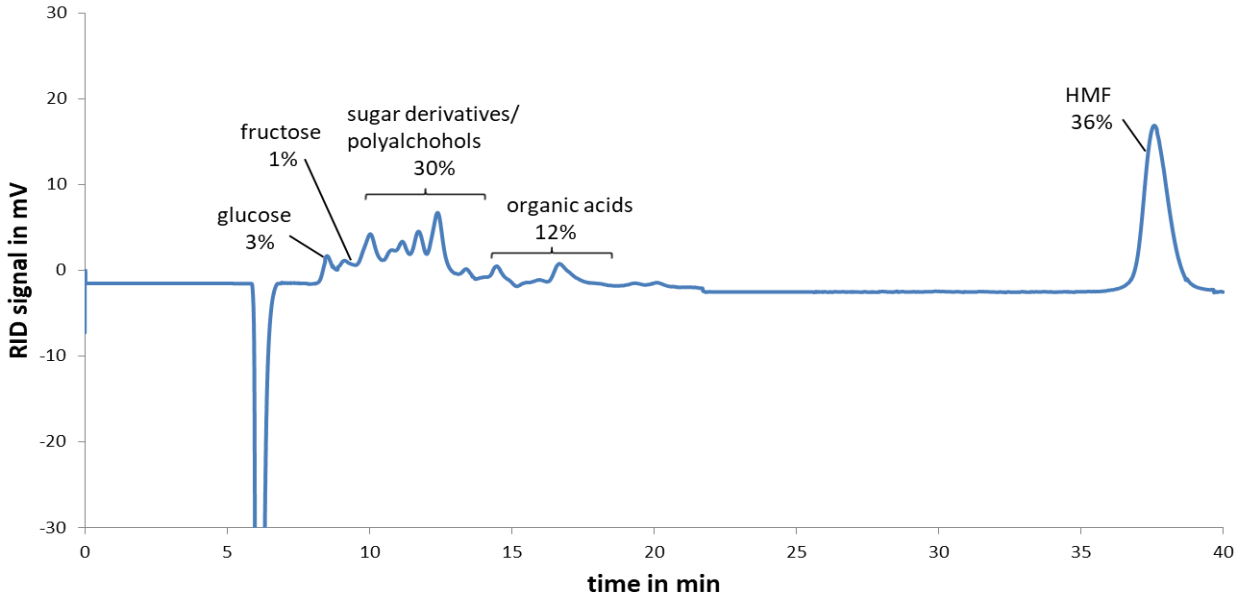
Three exemplary HPLC spectra for sugar conversion to HMF are shown below, indicating compound peaks with retention times and yields (Figure A.5).



a) Sucrose conversion over hy-Nb after 5 min: no sucrose left (fast hydrolysis into glucose and fructose), 32 % glucose and 10 % fructose left, HMF yield 25 % and side products formed (polyalcohols 13 %, organic acids 5 %) adding up to of starting material, estimated formation of insoluble humins 15 %



b) Fructose conversion over HNb_3O_8 after 10 min: 23 % fructose left, isomerization to glucose 3 %, HMF yield 34 % and side products formed (polyalcohols 21 %, organic acids 5 %) adding up to 86 % of starting material, estimated formation of insoluble humins 14 %



c) Glucose conversion over mesoporous Nb_2O_5*nH_2O after 10 min: 3% glucose left, isomerization to fructose 1 %, HMF yield 36 % and side products formed (polyalcohols 30 %, organic acids 12 %) adding up to 82 % of starting material, estimated formation of insoluble humins 18 %

Figure A.5 – a-c) Experimental HPLC spectra for sugar conversion to HMF

Glucose-fructose isomerization

When monitoring glucose and fructose conversion to HMF over time (reaction profiles in main text), it can be seen that fructose is converted at a faster rate and its isomerization yield of glucose formed is always ≤ 3 %. Glucose on the other hand is converted slower and with intermediate fructose yields of up to 14 % (Table A.1). From literature it is further known that the stability of glucose in water is slightly higher than that of fructose, meaning that the isomerization of glucose-fructose would yield ≥ 50 % glucose at equilibrium.[1,2] According to the above observations it can be deduced that in the experiments fructose is readily degraded to other products with little time for isomerization to glucose. The comparably slow conversion of glucose to other products however yields larger amounts of fructose intermediate, where fructose is then readily degraded further. Together with other experimental observations (catalyst comparison in main text) this points towards fructose being an important intermediate in glucose conversion.

Table A.1 – Isomerization yields of fructose during glucose conversion and of glucose during fructose conversion

	Fructose intermediate in glucose conversion	Glucose intermediate in fructose conversion
No catalyst	reaching 12 %, decreasing over time	reaching 2 %, decreasing over time
Nb_2O_5	reaching 12 %, decreasing over time	reaching 2 %, decreasing over time
HNb_3O_8	reaching 13 %, decreasing over time	reaching 3 %, decreasing over time
Hy-Nb-TEOA	reaching 14 %, decreasing over time	reaching 3 %, decreasing over time
Hy-Nb	reaching 12 %, decreasing over time	reaching 3 %, decreasing over time
Mesoporous Nb_2O_5*nH_2O	reaching 14%, decreasing over time	reaching 3 %, decreasing over time

Comparison of the catalytic performance of niobium oxides in sugar conversion to HMF

Turn-over frequency (TOF) calculations and reaction mechanistic considerations

Sugar conversion rates have been estimated based on the amount of sugar converted over the first 5 min of the monitored reaction. Here, it should straightaway be mentioned that these reaction rates cannot be considered initial reaction rates in particular for the catalysts with large amounts of active acid sites (hy-Nb-TEOA, hy-Nb and mesoporous Nb_2O_5*nH_2O) as the reaction has not been monitored over the heating up time of 30 min to 180°C, during which sugar conversion already takes place. Therefore, a comparison of the catalytic activities calculated based on the monitored reaction rates is not viable, as can also be seen by the TOF (moles of sugar converted per mole catalytic sites per minute) values in Table A.2. Low TOF values are obtained for the catalysts with large amounts of acid sites where significant amounts of sugar have already been converted by the time the reaction temperature has reached 180°C. The TOF calculations are shown in Equation A.8.

$$rate\ of\ conversion\ in\ mol\ sugar\ min^{-1} = \frac{\frac{[sugar] in\ M}{1000\ ml}\ x\ 15\ ml}{time\ in\ min} \qquad Equation\ A.8$$

$$TOF\ in\ mol\ sugar\ mol^{-1}\ catalytic\ sites\ min^{-1}$$

$$= \frac{rate\ of\ conversion\ in\ mol\ sugar\ min^{-1}}{[acid\ sites] in\ \mu mol\ g^{-1}\ x\ 0.15\ g\ x\ 10^{-6}}$$

To obtain TOF values corrected for the in-solution processes/conversion without catalyst, the following Equation A.9 was used.

$$corrected\ TOF\ in\ mol\ sugar\ mol^{-1}\ catalytic\ sites\ min^{-1}$$

$$= \frac{rate\ of\ conversion\ in\ mol\ sugar\ min^{-1} - rate\ of\ conversion\ without\ catalyst\ in\ mol\ sugar\ min^{-1}}{[acid\ sites] in\ \mu mol\ g^{-1}\ x\ 0.15\ g\ x\ 10^{-6}}$$

$$Equation\ A.9$$

Table A.2 – TOF values of sugar conversion for the different catalysts

	Rate of conversion in mol sugar min^{-1}		TOF in mol sugar mol^{-1} catalytic sites min^{-1} *	
	glucose	fructose	glucose	fructose
No catalyst	4×10^{-6}	12×10^{-6}	-	-
Nb_2O_5	32×10^{-6}	64×10^{-6}	- [a]	- [a]
HNb_3O_8	56×10^{-6}	104×10^{-6}	11.56	20.44
Hy-Nb-TEOA	120×10^{-6}	136×10^{-6}	2.77	2.96
Hy-Nb	128×10^{-6}	160×10^{-6}	1.57	1.87
Mesoporous Nb_2O_5*nH_2O	144×10^{-6}	160×10^{-6}	1.67	1.76

* corrected for conversion rate without catalyst

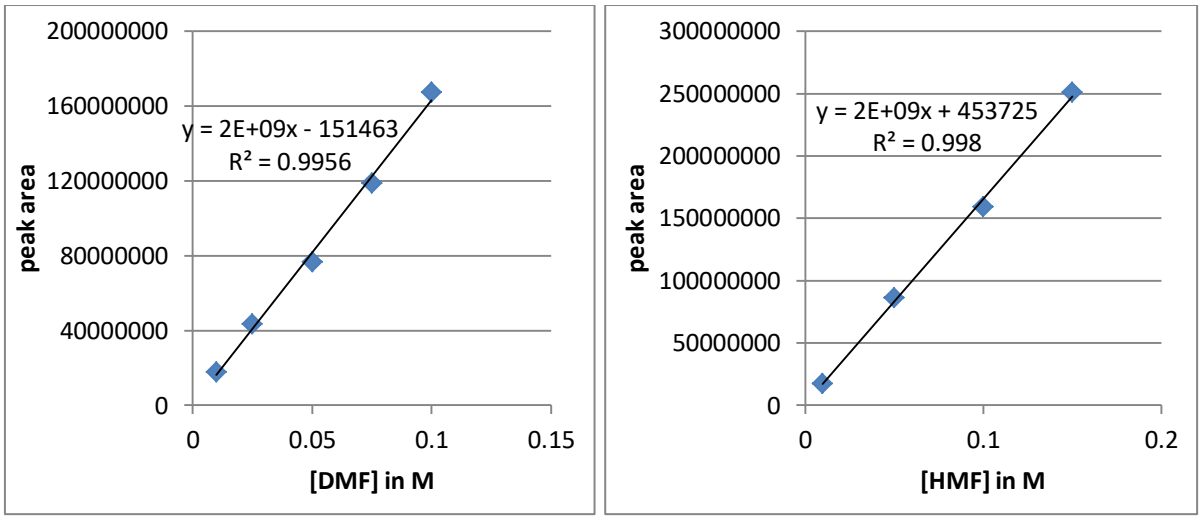
[a] acid site amount below detection limit of TMP NMR technique

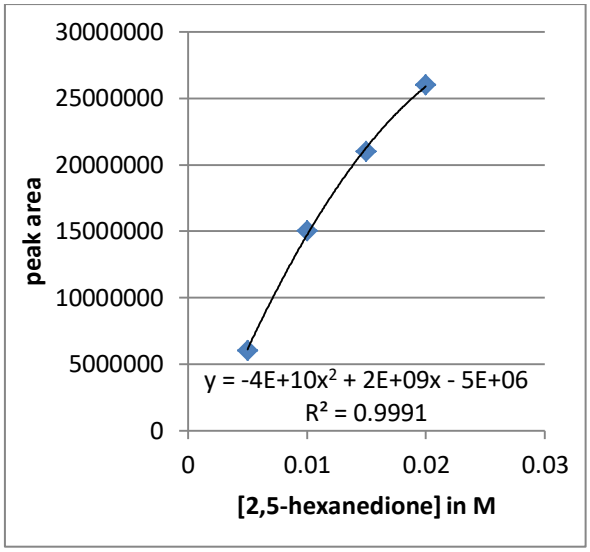
As sugar conversion is a very complex process involving the formation of many side products besides the desired product HMF (see HPLC spectra above), the calculation of catalytic activity is non-trivial: Even if initial reaction rates were measured (e.g. by monitoring the reaction at lower temperatures or using a faster heating up procedure), not all sugar molecules are converted to the product of interest HMF. If instead choosing to monitor initial HMF production to compare catalytic activity, this still poses the difficulty that HMF itself is converted further. This means that the catalyst with the highest catalytic activity in HMF formation does not necessarily

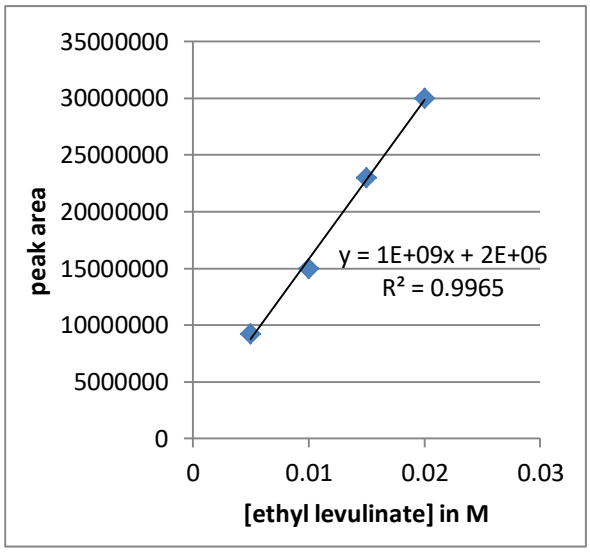
give the highest HMF yield, if it also catalyses the degradation of HMF to a significant extent. For example a highly acidic catalyst A showing both a fast conversion of sugar to HMF and a fast degradation of HMF, can give a lower maximum HMF yield than a less acidic catalyst B with a lower initial rate of HMF formation but insignificant further degradation. Therefore the maximum HMF yield obtained over each catalyst has been chosen as the method of comparison for catalytic performance in this work. From here, a further comparison of catalyst selectivity is possible but will not be discussed in here, as the sugars are fully converted over time. If stopping the reaction at the highest HMF selectivity, HMF extraction from the reaction mixture would be necessary before resuming the reaction in order to improve the overall HMF yield. This work however is looking at the purely aqueous-based catalytic system without extraction solvents.

GC-MS calibration

Reaction product yields from HMF conversion to DMF and further to aromatics were calculated according to the following calibration curves (Figure A.6). The calibration curves were established by running samples of known compound concentration and plotting the measured peak area against molar concentration.







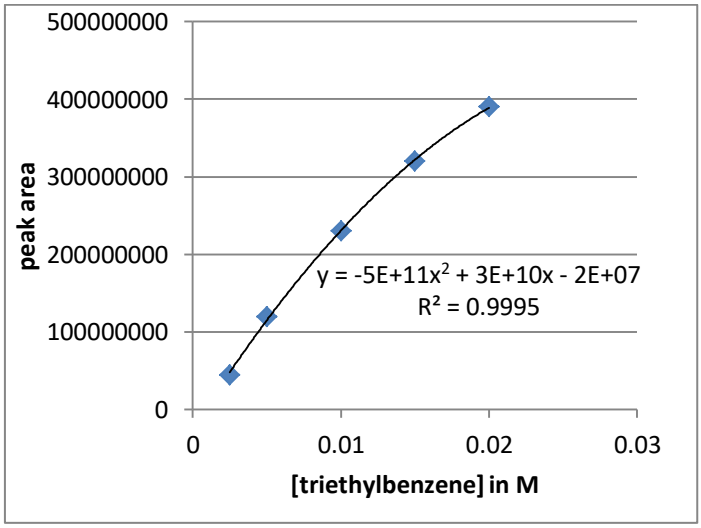


Figure A.6 – GC-MS calibration curves for DMF, HMF, 2,5-hexanedione, ethyl levulinate, triethylbenzene

Yield calculations for HMF conversion to DMF and further to aromatics

DMF and aromatic hydrocarbon yields from HMF conversion were determined using the above calibration curves. The reaction mixtures consisted of 250 mg HMF in 15 mL ethanol (and 50 mg catalyst), amounting to a molar concentration of 0.13 M HMF (Equation A.10).

$$\frac{\frac{0.25\ g}{126.11\ \frac{g}{mol}}}{15\ ml}\ x\ 1000\ ml = 0.13\ M\ HMF \qquad Equation\ A.10$$

One equivalent of HMF is converted to one equivalent of DMF or derivatives (= DMF (main) + MF + MEF), which can be further converted to one equivalent of aromatic hydrocarbons (xylene based). Therefore both DMF and aromatic hydrocarbon yield are given by the following Equation A.11.

$$\frac{[DMF\ or\ aromatics]in\ M}{0.13\ M}\ x\ 100\ \%$$

$$= DMF\ or\ aromatic\ hydrocarbon\ yield\ in\ \% \qquad Equation\ A.11$$

Since mostly DMF and hardly aromatics are formed during the first reaction step (due to either a basic zeolite support or catalyst deactivation), a second reaction step with fresh catalyst is introduced to convert DMF further to aromatics. Therefore the total aromatics yield is given by Equation A.11 as above, and further the aromatics yield from the second step can be expressed as a percentage of DMF formed during the first reaction step (Equation A.12).

$$\frac{[aromatics]in\ M}{[DMF]in\ M}\ x\ 100\ \%$$

$$= aromatic\ hydrocarbon\ yield\ from\ DMF\ in\ \% \qquad Equation\ A.12$$

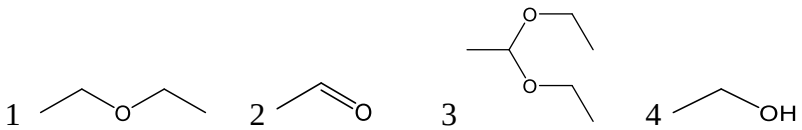
The DMF and aromatic hydrocarbon yields given in the main text are averages of two reaction runs performed per sample mixture with two GC-MS injections each, where the overall yield deviation lays within ±3 % for both DMF and aromatics. Product selectivity has not been calculated since no HMF was left in the analysed reaction mixtures, meaning that yield = selectivity. As mainly branched aromatics (with additional ethyl groups most likely from the

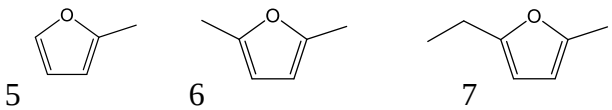
solvent) were formed, which are not commercially available, triethylbenzene was used as model compound for calibration.

The main side products formed are 2,5-hexanedione, levulinic acid and butanol derived compounds (also see GC-MS spectra below), therefore reactions of one-to-one equivalents are assumed (Equation A.11). Mass balance estimations are done by grouping together compounds of similar nature/retention time and calculating peak areas according to the calibration curve of one representative compound for each group. The mass balances obtained tend to exceed 100%, where potential error sources include products from solvent or one-to-two equivalent reactions, and the use of model compounds for calibration.

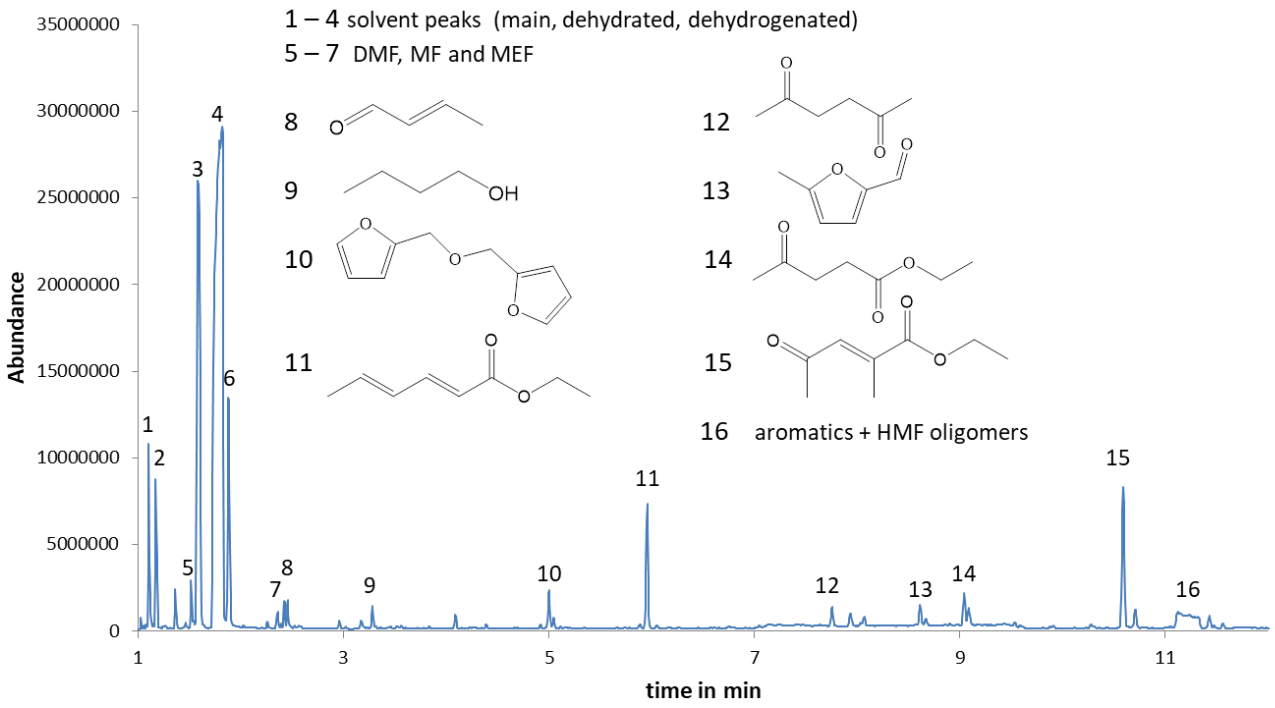
GC-MS spectra for HMF conversion to DMF and further to aromatics

Four exemplary GC-MS spectra for HMF conversion to DMF and further to aromatics are shown below (Figure A.7), indicating compound retention times and product identification.

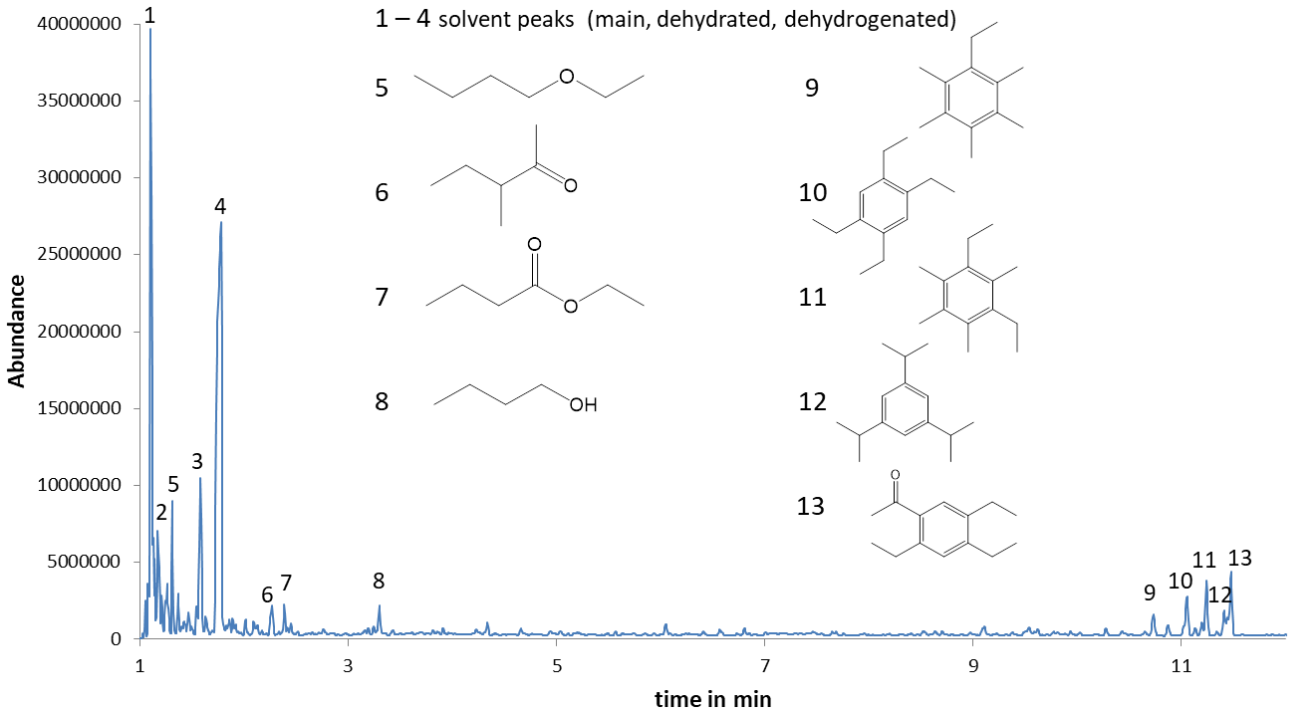




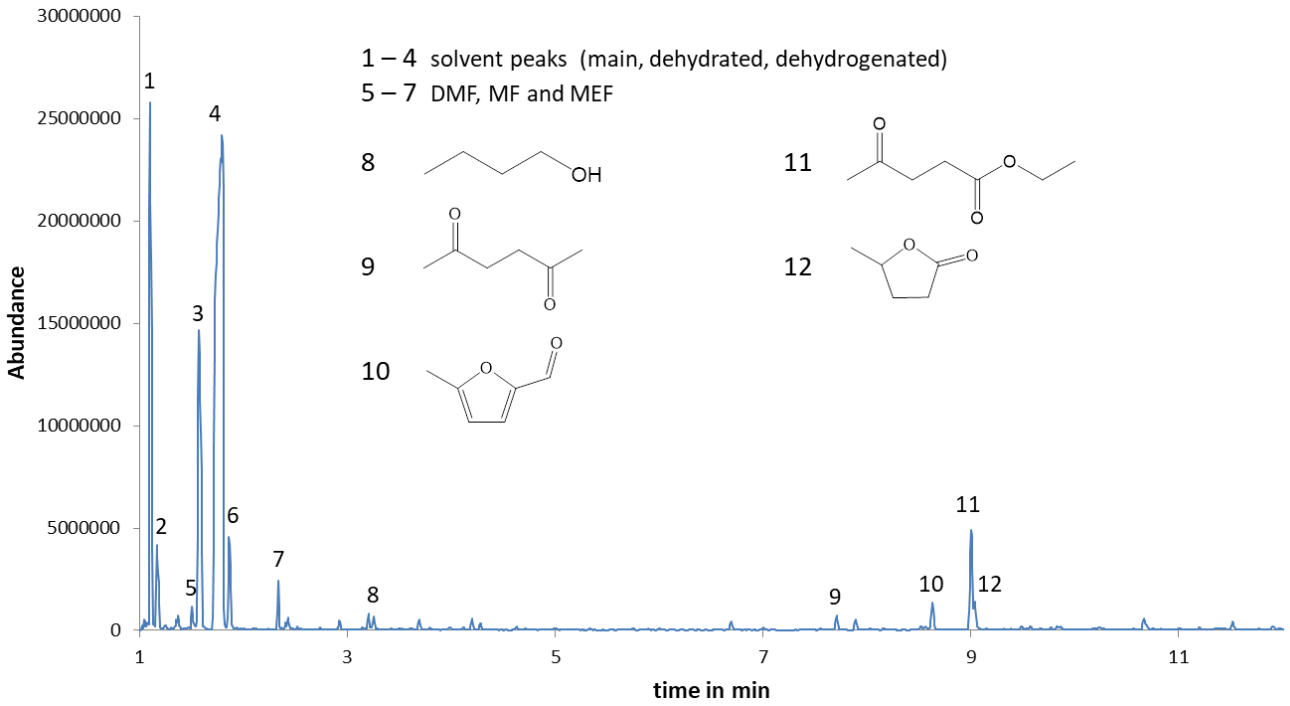
5 6 7 Compounds 1 – 7



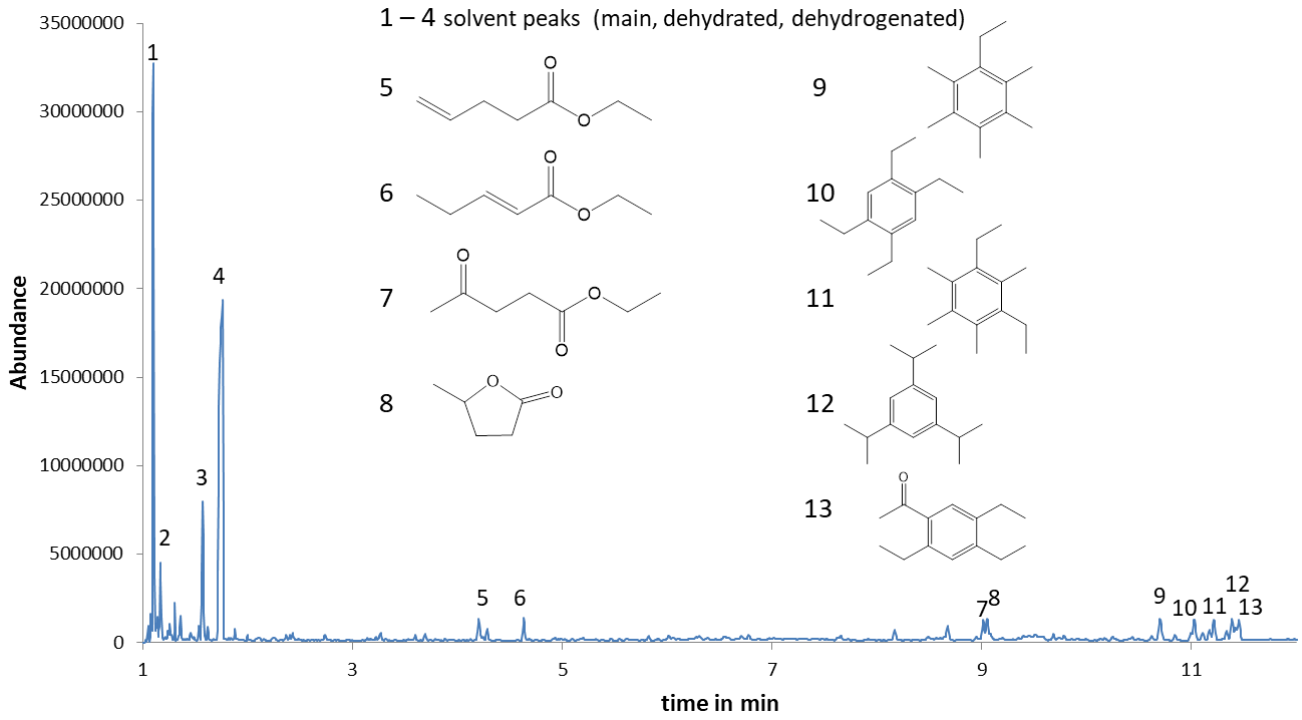
a) Product spectrum of HMF to DMF conversion over Ru/MgO/NaY10 for 12 h at 300°C



b) Product spectrum of further conversion of DMF to aromatics (reaction solution from previous Figure a) with fresh HY10 catalyst for 2 h at 300°C



c) Product spectrum of HMF to DMF conversion over Pd/HY10 for 12 h at 300°C



d) Product spectrum of further conversion of DMF to aromatics (reaction solution from previous Figure c) with fresh Pd/HY10 catalyst for 2 h at 300°C

Figure A.7 – a-d) Experimental GC-MS spectra for HMF conversion to DMF and further to aromatics

XPS elemental analysis of the niobium oxides

Besides the analysis of Nb 3d peak positions for oxidation state comparison (main text), quantitative elemental analysis of the Nb and O species was performed. An exemplary XPS spectrum of (similar spectra for all niobium oxides) is shown in Figure A.8.

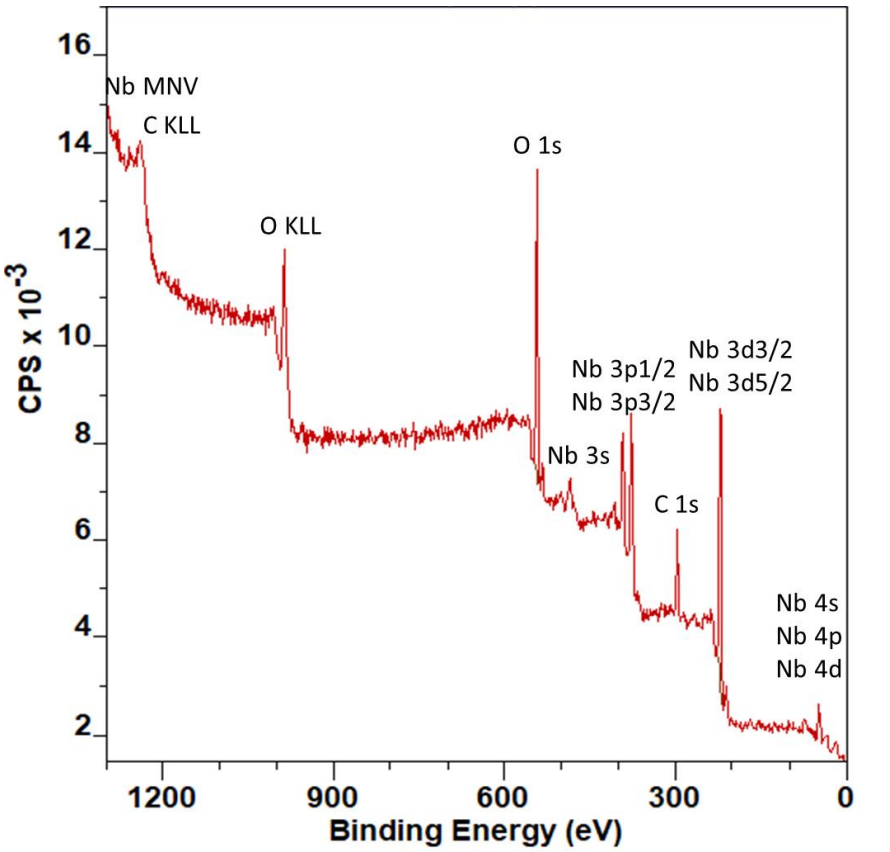


Figure A.8 – XPS spectrum of commercial Nb_2O_5 with assigned element peaks (similar spectra obtained for the other niobium oxides)

As expected and seen from Figure A.8, the niobium oxides samples contain Nb and O, the contribution of C comes from the carbon tape used to mount the samples. Quantitative analysis to determine the O:Nb ratio for each sample has been done by area comparison of the large O1s and Nb3d peaks, using the known ratio of 2.5:1 for commercial Nb_2O_5 as the reference value.

Table A.3 shows the calculated O:Nb ratios for the remaining niobium oxides, using the following Equation A.13:

$$\frac{\frac{5}{2}}{\frac{22922}{27948}} = \frac{unknown\ O{:}\ Nb\ ratio}{\frac{O1s\ peak\ area}{Nb3d\ peak\ area}} \qquad Equation\ A.13$$

Table A.3 – O:Nb ratios calculated for the synthesized niobium oxides using commercial Nb_2O_5 as a reference

	O 1s peak area	Nb 3d peak area	O:Nb ratio
Commercial Nb_2O_5	22922	27948	2.5:1 (known ratio)
HNb_3O_8	51381	59100	2.65:1
Hy-Nb	34429	39061	2.69:1
Hy-Nb-TEOA	55878	61100	2.79:1
Mesoporous Nb_2O_5*nH_2O	52585	57665	2.78:1

Quantitative elemental analysis can also be done using tabulated relative sensitivity factors (RSF) (e.g. taken from the CasaXPS program library). However, the obtained values tend to be less accurate than by using a reference compound of similar nature and known composition, due to instrument specificities and the difficulties involved in background subtraction.[3] For comparison, the O:Nb ratios obtained using the tabulated RSF values of 2.93 for O1s and 8.24 for Nb3d are as follows (calculated by dividing experimental peak area by RSF and dividing corrected O1s by corrected Nb3d peak area): 2.31:1 for commercial Nb_2O_5, 2.45:1 for HNb_3O_8, 2.48:1 for hy-Nb, 2.57:1 for hy-Nb-TEOA and 2.56:1 for mesoporous Nb_2O_5*nH_2O. As can be seen, the ratio obtained for commercial Nb_2O_5 is slightly lower than the actual ratio due to an

error of about 10% involved in using tabulated RSF values, as described above. The ratios for the remaining niobium oxides are influenced accordingly. Therefore, the O:Nb ratios calculated with the more reliable reference compound method (Table A.3) will be given in the main text. A remaining error source is the small additional peak contribution from oxygen species stuck to the carbon tape used during measurement (varies with sample thickness and carbon tape piece).

EXAFS

The bond lengths and coordination numbers calculated for each niobium oxide sample from 1st and 2nd shell fitting of the Nb EXAFS data are displayed in Table A.4 – A.8, as additional information to the EXAFS text in Chapter 5. Only the bond lengths and coordination numbers of main interest (1st shell Nb-O, marked in yellow) are discussed further in Chapter 5.

Table A.4 – EXAFS data for commercial Nb_2O_5

Scattering path	Get scattering path from	Bond length (A)	Coordination number C.N.
Nb-O1	Nb2O5 O21.1	1.76(1)	1.4(1)
Nb-O2	Nb2O5 O19.1	1.96(1)	4.3(2)
Nb-O3	Nb2O5 O19.2	3.25(2)	2.2(4)
Nb-Nb1	Nb2O5 Nb10.1	3.32(1)	0.7(1)
Nb-Nb2	Nb2O5 Nb1.1	3.91(1)	3.5(3)

1st O shell total C.N.=5.7

Table A.5 – EXAFS data for HNb_3O_8

Scattering path	Get scattering path from	Bond length (A)	Coordination number C.N.
Nb-O1	KNb3O8 O2.1	1.77(1)	1.0(1)
Nb-O2	KNb3O8 O5.1	2.02(1)	4.1(1)
Nb-O3	KNb3O8 O4.1	2.22(1)	1.1(1)
Nb-Nb1	NbO Nb1.1	2.80(1)	1.9(2)

1st O shell total C.N.=6.2

Table A.6 – EXAFS data for hy-Nb

Scattering path	Get scattering path from	Bond length (A)	Coordination number C.N.
Nb-O1	KNb3O8 O2.1	1.88(1)	0.9(1)
Nb-O2	KNb3O8 O5.1	2.07(1)	3.8(1)
Nb-O3	KNb3O8 O4.1	2.31(1)	0.9(1)
Nb-Nb1	NbO Nb1.1	2.83(1)	1.0(2)

1st O shell total C.N.=5.6

Table A.7 – EXAFS data for hy-Nb-TEOA

Scattering path	Get scattering path from	Bond length (A)	Coordination number C.N.
Nb-O1	KNb3O8 O2.1	1.93(1)	1.1(1)
Nb-O2	KNb3O8 O5.1	2.09(1)	3.4(1)
Nb-O3	KNb3O8 O4.1	2.29(4)	0.3(1)
Nb-Nb1	NbO Nb1.1	2.83(3)	0.9(2)

1st O shell total C.N.=4.8

Table A.8 – EXAFS data for mesoporous $Nb_2O_5*nH_2O$

Scattering path	Get scattering path from	Bond length (A)	Coordination number C.N.
Nb-O1	Nb2O5 O21.1	1.91(1)	0.9(1)
Nb-O2	Nb2O5 O19.1	2.10(1)	3.6(1)
Nb-O3	Nb2O5 O19.2	3.46(1)	2.4(2)
Nb-Nb1	Nb2O5 Nb10.1	3.52(2)	2.1(4)
Nb-Nb2	Nb2O5 Nb1.1	3.96(1)	1.1(3)

1st O shell total C.N.=4.5

References

(1) Assary, R. S.; Kim, T.; Low, J. J.; Greeley, J.; Curtiss, L. A. *Phys. Chem. Chem. Phys.* **2012**, *14* (48), 16603.

(2) Roman-Leshkov, Y.; Moliner, M.; Labinger, J. A.; Davis, M. E. *Angew. Chemie - Int. Ed.* **2010**, *49*, 8954.

(3) Jablonski, A. *Pol. J. Chem.* **2000**, *74* (11), 1533.